

**High Temperature Fatigue and Fatigue Damage Process
of Aggregate-Asphalt Mixes**

by

Bor-Wen Tsai

**B.A. (National Taiwan University) 1983
M.S. (University of California, Berkeley) 1989
M.Eng. (University of California, Berkeley) 1993
M.A. (University of California, Berkeley) 1999**

A dissertation submitted in partial satisfaction of the

requirements for the degree of

**Doctor of Philosophy
in**

Engineering-Civil Engineering

in the

GRADUATE DIVISION

of the

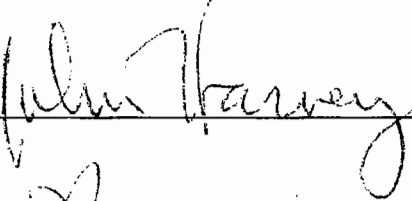
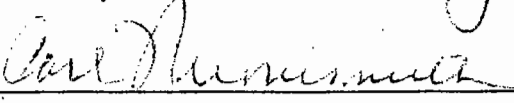
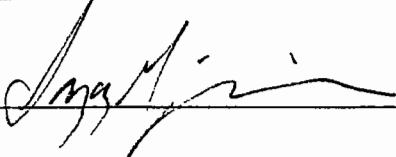
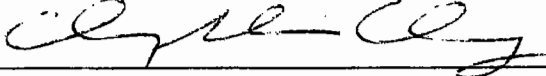
UNIVERSITY OF CALIFORNIA, BERKELEY

Committee in charge:

**Professor John T. Harvey, Co-Chair
Professor Carl L. Monismith, Co-Chair
Professor Sanjay Govindjee
Professor Ching-Shui Cheng**

Fall 2001

The dissertation of Bor-Wen Tsai is approved:

Co-Chair		18 June 01
		Date
Co-Chair		19 June 01
		Date
		19 June 01
		Date
		20 June 01
		Date

University of California, Berkeley

Fall 2001

**High Temperature Fatigue and Fatigue Damage Process
of Aggregate-Asphalt Mixes**

© 2001

by

Bor-Wen Tsai

Abstract

High Temperature Fatigue and Fatigue Damage Process
of Aggregate-Asphalt Mixes

by

Bor-Wen Tsai

Doctor of Philosophy in Civil Engineering

Professor John T. Harvey, Co-Chair

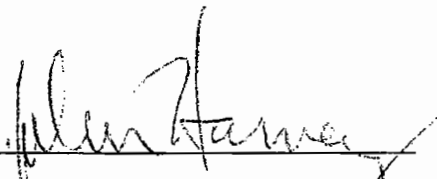
Professor Carl L. Monismith, Co-Chair

The term, “High Temperature Fatigue” has long been identified in mechanical engineering as an important phenomenon that limits the life of metallic components. Asphalt pavement routinely encounters high temperatures in typical California climate regions, yet there has been little study of this phenomenon in the field of asphalt concrete. In this thesis, the effect on fatigue performance of high temperatures (30 °C – 40 °C) in conjunction with trafficking has been studied by placing an aluminum plate under the conventional four-point fatigue test setup and bending the beam upward so as to prevent temperature-induced creep during the test. Thereafter, a dynamic and recursive approach, namely the Weibull dynamic approach, has been used to relate the accelerated laboratory fatigue tests on asphalt concrete to the predicted long term fatigue performance (crack initiation) of in situ pavements.

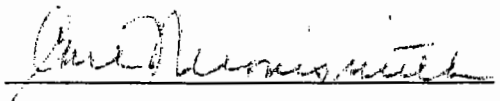
For crack initiation, the Weibull stochastic process was found to successfully describe the fatigue damage process, a process of stiffness deterioration, under any temperature or test conditions. Furthermore, the widely used Weibull proportional

hazards model of survival analysis was recommended as a tool to integrate tests performed under various conditions of strain, temperature, and material variables, including the high temperature fatigue tests and conventional fatigue tests, into a single regression equation. This equation was used as a tool to assess the fatigue damage. A dynamic and recursive fatigue simulation program was developed using the Weibull approach and a layered-elastic theory subroutine to calculate the tensile strain. The Weibull accelerated failure time model was also used to estimate a correction factor to account for the inherent difference of boundary conditions between laboratory test results and in situ fatigue performance.

To verify the Weibull dynamic approach, the Federal Highway Administration (FHWA) sponsored "WesTrack" full-scale accelerated pavement testing project provided a complete and valuable data set containing not only information on various mixes, traffic and wander, pavement temperatures, and laboratory test results, but also the condition survey of fatigue performance. The computer simulation results were compared with the WesTrack condition survey results and validated the feasibility of the Weibull dynamic approach as applied to field fatigue performance prediction.



Professor John T. Harvey, Co-Chair



Professor Carl L. Monismith, Co-Chair

TABLE OF CONTENTS

LIST OF TABLES	viii
LIST OF APPENDIX TABLES	x
LIST OF FIGURES	xii
LIST OF APPENDIX FIGURES	xxiv
1.0 INTRODUCTION	1
1.1 Background	1
1.2 Research Objectives	4
1.3 Literature Review	5
<i>1.3.1 History of Asphalt Concrete Fatigue Model Development</i>	5
<i>1.3.2 Crack Initiation and Crack Propagation</i>	9
<i>1.3.3 High Temperature Fatigue Test</i>	11
<i>1.3.4 Compound Strain-Based Fatigue Loading</i>	13
<i>1.3.5 The Weibull Function</i>	14
<i>1.3.6 Cumulative Fatigue Damage Prediction</i>	15
<i>1.3.7 Full-Scale Accelerated Pavement Tests</i>	16
<i>1.3.8 Shift Factor</i>	18
1.4 Research Organization	21
2.0 DATA SOURCES	29
2.1 WesTrack Project	29
<i>2.1.1 Track Characteristics</i>	30
<i>2.1.2 Mix Characteristics</i>	31
<i>2.1.3 Traffic</i>	32
<i>2.1.4 Temperature</i>	34
2.2 CAL/APT HVS Project	35
<i>2.2.1 503RF Section</i>	35
<i>2.2.2 Trafficking Plan</i>	36
<i>2.2.3 Multi-Depth Deflectometer (MDD)</i>	37
2.3 Laboratory Test Data	38
3.0 TEST PLAN, SPECIMEN PREPARATION, AND TEST SETUP	45

3.1 Test Purpose	45
3.2 Test Setup	46
3.2.1 <i>Conventional Flexural Controlled-Strain Fatigue Test Setup</i>	46
3.2.2 <i>Modified Flexural Controlled-Strain Fatigue Test Setup</i>	47
3.2.3 <i>Instrumentation and Data Acquisition System</i>	48
3.3 Specimen Preparation	50
3.3.1 <i>Gradation Curves of WesTrack</i>	50
3.3.2 <i>Procedure of Specimen Preparation for WesTrack</i>	51
3.4 Test Plan	54
3.4.1 <i>High Temperature Modified Flexural Controlled-Strain Fatigue Test</i>	55
3.4.2 <i>Temperature Susceptibility Fatigue Test with Conventional Setup</i>	55
3.4.3 <i>Fatigue Test with Various Gradation Types</i>	56
3.4.4 <i>Flexural Frequency Sweep Test</i>	56
3.4.5 <i>Varied-Strain Fatigue Test</i>	58
3.4.6 <i>Varied-Temperature Fatigue Test</i>	58
4.0 FATIGUE TEST RESULTS AND ANALYSIS	70
4.1 Background	70
4.1.1 <i>History of Fatigue Life Analysis</i>	70
4.1.2 <i>Interpretation of Weibull Curves</i>	72
4.1.3 <i>Crack Initiation and Weibull Curves</i>	74
4.2 Fatigue Tests at 20°C	75
4.3 Temperature Susceptibility Fatigue Test (Field)	82
4.4 Temperature Susceptibility Fatigue Test (Laboratory)	83
4.5 High Temperature Flexural Controlled-Strain Fatigue Test	84
4.6 Fatigue Test with Various Gradation Types	87
4.7 Pooled Fatigue Tests	88
4.8 Conventional Fatigue Analysis for WesTrack Project	89
4.8.1 <i>Model Selection</i>	89
4.8.2 <i>Mallow's C_p Statistic</i>	90
4.8.3 <i>Data Description</i>	91
4.8.4 <i>A Regression Example: Coarse Gradation</i>	92

4.8.5	<i>Regression Analysis Results</i>	97
4.9	Flexural Frequency Sweep Test	99
4.9.1	<i>Test Results</i>	99
4.9.2	<i>Fitting with Gamma Distribution Function</i>	101
4.10	Varied-Strain Fatigue Test	103
4.10.1	<i>The Strain Effect on Weibull Curves</i>	103
4.10.2	<i>A Hypothesis of Strain-Caused Fatigue Damage</i>	104
4.10.3	<i>Test Results and Analysis</i>	105
4.11	Varied-Temperature Fatigue Test	109
4.11.1	<i>The Temperature Effect on Weibull Curves</i>	109
4.11.2	<i>A Hypothesis of Temperature-Caused Fatigue Damage</i>	110
4.11.3	<i>Test Results and Analysis</i>	111
4.12	Findings and Discussions	113
4.12.1	<i>Findings in Fatigue Test Results and Regression Analysis</i>	114
4.12.2	<i>Fatigue Life versus Temperature versus Strain Level</i>	115
4.12.3	<i>Crack Initiation and Crack Propagation</i>	116
4.12.4	<i>Weibull Curves at Extreme Test Temperatures</i>	116
4.12.5	<i>Coefficients of Weibull Curves</i>	117
4.12.6	<i>Problems of the High Temperature Fatigue Test</i>	117
4.12.7	<i>A General Hypothesis of Fatigue Damage</i>	118
4.12.8	<i>Time Hardening and Strain Hardening</i>	119
5.0	WEIBULL THEORY	167
5.1	Introduction	167
5.2	Survival Analysis	168
5.2.1	<i>Survivor and Hazard Functions</i>	169
5.2.2	<i>Fatigue Damage Process and Survivor Function</i>	171
5.3	Weibull Proportional Hazards Model	172
5.3.1	<i>Weibull Density Function</i>	172
5.3.2	<i>Weibull Proportional Hazards Model</i>	173
5.4	Weibull Equations of WesTrack Project	176
5.4.1	<i>An Example: Fitting the Weibull PH Model</i>	176

5.4.2	<i>Weibull Equation of Coarse Gradation</i>	180
5.4.3	<i>Weibull Equation of Fine and Fine-Plus Gradations</i>	182
5.5	Prediction of Fatigue Performance Using Weibull Theory	184
5.6	Miner’s Law and Weibull Theory	185
5.6.1	<i>Miner’s Law in Explanation with Stiffness Ratio</i>	186
5.6.2	<i>Generalized Miner’s Law</i>	189
5.7	Weibull Accelerated Failure Time Model	191
5.7.1	<i>Introduction</i>	191
5.7.2	<i>Accelerated Failure Time Model</i>	193
5.7.3	<i>Demonstration Example</i>	196
5.7.3.1	<i>Back-Calculation of Layer Moduli for Section 503RF</i>	197
5.7.3.2	<i>Correction Factor and Laboratory Fatigue Test Results for Section 503RF</i>	199
5.7.4	<i>Mode Factor and Controlled-Strain Fatigue Test</i>	200
5.7.5	<i>Findings and Discussions</i>	203
6.0	WESTRACK SIMULATION USING MINER’S LAW	224
6.1	Introduction	224
6.2	WesTrack Data Summary	226
6.2.1	<i>Temperature Distribution</i>	227
6.2.2	<i>Traffic Pattern</i>	228
6.3	Mechanistic-Empirical Models for Stiffness and Fatigue Life	229
6.3.1	<i>Stiffness Models</i>	230
6.3.2	<i>Fatigue Life Models</i>	231
6.4	Stratification of the WesTrack Temperature Data	233
6.5	Tensile Strain Function Using Circly Program	235
6.5.1	<i>WesTrack Pavement Structure and Loading Configuration</i>	235
6.5.2	<i>Circly Program with 110 x 3 x 3 Cases</i>	235
6.5.3	<i>Bi-normal Density Function</i>	236
6.5.4	<i>Regression Analysis for Strain Function</i>	238
6.6	Fatigue Performance Prediction Simulation (Crack Initiation)	241
6.6.1	<i>Simulation Procedures</i>	241

6.6.1.1	Input Matrix and Four-Parameter Strain Function.....	241
6.6.1.2	Tensile Strains with Offset.....	242
6.6.1.3	Fatigue Life with Offset.....	243
6.6.1.4	Repetition Matrix.....	244
6.6.1.5	Fatigue Damage Matrix and Miner’s Law.....	245
6.6.2	<i>Simulation Results</i>	246
6.7	Findings and Discussions	248
7.0	WEIBULL SIMULATION	277
7.1	General Considerations	277
7.1.1	<i>Algorithm of Weibull Program</i>	277
7.1.2	<i>Program Elements and Flow Charts</i>	279
7.1.3	<i>Scope of Simulation</i>	282
7.1.4	<i>Failure Criterion</i>	285
7.1.5	<i>Stiffness, Temperature, and Stiffness Ratio</i>	286
7.1.6	<i>Stiffness as an Input</i>	288
7.1.7	<i>Wander Consideration</i>	288
7.1.8	<i>Vehicle Speed and Stiffness</i>	290
7.1.9	<i>Traffic Wander, Traffic Composition, and Vehicle Speed</i>	291
7.2	Simulation Results of WesTrack	291
7.3	Traffic Pattern and Simulation	296
7.4	Weather and Simulation	299
7.5	Traffic and Weather Effects	300
7.6	Construction Variability and Simulation	303
7.6.1	<i>Degree of Compaction</i>	303
7.6.2	<i>Thickness of the Asphalt Concrete Layer</i>	305
7.6.3	<i>Asphalt Content</i>	307
7.7	Correction Factor and Simulation Results	308
7.8	Findings and Discussions	311
8.0	CONCLUSIONS AND RECOMMENDATIONS	374

APPENDICES	385
APPENDIX A. TABLES	385
APPENDIX B. FIGURES	408
APPENDIX C. FLEXURAL BEAM ANALYSIS AND SPLUS CODE FOR	
CHAPTER 4	486
C.1 Flexural Beam Analysis Using Strain Gage Data	487
<i>C.1.1 Analysis without Aluminum Support</i>	487
<i>C.1.2 Analysis with Aluminum Support</i>	489
C.2 Flexural Frequency Sweep Test	492
<i>C.2.1 Analysis of Without-Support Setup</i>	492
<i>C.2.2 Analysis of With-Support Setup</i>	493
C.3 High Temperature Fatigue Test	495
C.4 Varied-Strain Fatigue Test	499
C.5 Simulation of Correlated Random Variables	502
APPENDIX D. SPLUS CODE FOR CHAPTER 6	506
D.1 Splus Code for Stratification	507
<i>D.1.1 Cellsum() Function</i>	508
<i>D.1.2 Findcell() Function</i>	509
<i>D.1.3 Stratification Output of the WesTrack Field Data</i>	510
D.2 Splus Code for Crack Initiation Simulation	513
APPENDIX E. WEIBULL USER'S MANUAL	516
E.1 General Description	517
<i>E.1.1 Introduction</i>	517
<i>E.1.2 Program Elements and Flow Charts</i>	518
<i>E.1.3 Weibull Theory</i>	521
E.1.3.1 Weibull Density Function	522
E.1.3.2 Weibull Proportional Hazards Model	524
E.1.3.3 Applying the Weibull Proportional Hazards Model	525
<i>E.1.4 Weibull Accelerated Failure Time Model</i>	528
<i>E.1.5 Wander Consideration</i>	532
<i>E.1.6 Stiffness, Temperature, and Stiffness Ratio</i>	532

<i>E.1.7 Vehicle Speed and Stiffness</i>	534
<i>E.1.8 Traffic Wander, Traffic Composition, and Vehicle Speed</i>	534
E.2 Input Data	537
<i>E.2.1 ELSYM5 Input File</i>	537
<i>E.2.2 Environment and Material File</i>	539
<i>E.2.3 Traffic File</i>	540
<i>E.2.4 Stiffness and Weibull Regression Equation File</i>	541
E.3 Output	543
E.4 Examples	543
<i>E.4.1 Example Problem 1</i>	544
<i>E.4.2 Example Problem 2</i>	546
E.5 Source Code	547
<i>E.5.1 Main Program: Weibull_Simulation</i>	547
<i>E.5.2 Module: Strain_Engine</i>	556
<i>E.5.3 Module: Equations</i>	560
<i>E.5.4 Module: ELSYM5_File_Modify</i>	564
<i>E.5.5 Module: Link_List</i>	567
<i>E.5.6 Module: ELSYM5_Program</i>	570
<i>E.5.7 Data Module of ELSYM5_Program</i>	601
REFERENCES	619

LIST OF TABLES

Table 3.1.	WesTrack original construction gradations and laboratory-mixed and laboratory-compacted gradations.	60
Table 3.2.	Laboratory test plan and test purpose.	61
Table 4.1.	Covariates investigated in Chapter 4.	121
Table 4.2.	Summary statistics of WesTrack fatigue tests.	122
Table 4.3.	Model selection of stiffness and fatigue life of the WesTrack project.	123
Table 4.4.	Final regression models of stiffness and fatigue life of the WesTrack project.	124
Table 4.5.	Summary statistics of Weibull coefficients.	125
Table 4.6.	Associated figures and tables for regression analysis.	126
Table 4.7.	Mix properties for the varied-strain fatigue test.	126
Table 4.8.	Mix properties for the varied-temperature fatigue test.	126
Table 5.1.	Temperature susceptibility fatigue test results of WesTrack fine-plus gradation.	208
Table 5.2.	Pavement structure for mode factor simulation.	208
Table 6.1.	Recording and analysis periods of the WesTrack project.	252
Table 6.2.	Sample sizes of fatigue tests for various gradations.	252
Table 6.3 (a).	Results of regression coefficients m_1 of coarse mixes at different temperature gradient intervals.	253
Table 6.3 (b).	Results of regression coefficients m_2 of coarse mixes at different temperature gradient intervals.	253
Table 6.3 (c).	Results of regression coefficients σ of coarse mixes at different temperature gradient intervals.	254
Table 6.3 (d).	Results of regression coefficients A of coarse mixes at different temperature gradient intervals.	254

Table 6.4 (a).	Results of regression coefficients m_1 of fine and fine-plus mixes at different temperature gradient intervals.....	255
Table 6.4 (b).	Results of regression coefficients m_2 of fine and fine-plus mixes at different temperature gradient intervals.....	255
Table 6.4 (c).	Results of regression coefficients σ of fine and fine-plus mixes at different temperature gradient intervals.....	256
Table 6.4 (d).	Results of regression coefficients A of fine and fine-plus mixes at different temperature gradient intervals.....	256
Table 6.5.	Summary table of fatigue performance prediction and condition survey data of WesTrack.	257
Table 7.1.	Mix properties of the WesTrack project as the input of Weibull simulation.....	314
Table 7.2.	Final SR of Weibull simulation of the WesTrack project.	315
Table 7.3.	Condition survey data of fatigue cracking and simulation results.....	316
Table 7.4.	Percentage reduction of air-void contents of WesTrack after 9 months of traffic loading.....	304
Table 7.5.	Decomposition of correction factor.	317

LIST OF APPENDIX TABLES

Table A.4.1.	Fatigue test results and Weibull regression fits at 20 ° C	386
Table A.4.2.	WesTrack temperature susceptibility fatigue test results and Weibull regression fits at various temperatures (field-mixed and field-compacted).	391
Table A.4.3.	WesTrack temperature susceptibility fatigue test results and Weibull regression fits at various temperatures (laboratory-mixed and laboratory-compacted).	392
Table A.4.4.	High temperature fatigue test results and Weibull regression fits.	393
Table A.4.5.	Fatigue test results and Weibull regression fits with various gradation types.	394
Table A.4.6.	Correlation matrix of fatigue tests at 20 ° C	395
Table A.4.7.	Correlation matrix of temperature susceptibility fatigue tests (field-mixed and field-compacted).	396
Table A.4.8.	Correlation matrix of temperature susceptibility fatigue tests (laboratory-mixed and laboratory-compacted).	397
Table A.4.9.	Correlation matrix of high temperature fatigue tests.	398
Table A.4.10.	Correlation matrix of fatigue tests with various gradation types.	399
Table A.4.11.	Correlation matrix of pooled fatigue tests.	400
Table A.4.12.	Correlation matrix of coarse gradation.	401
Table A.4.13.	Correlation matrix of fine gradation.	402
Table A.4.14.	Correlation matrix of fine-plus gradation.	403
Table A.4.15.	Correlation matrix of fine and fine-plus gradations.	404
Table A.4.16.	Range of covariates and response variables of various fatigue tests.	405
Table A.4.17.	Range of covariates and response variables of various gradation types.	406
Table A.4.18.	Summary of frequency sweep tests.	407

Table E.1.	Temperature susceptibility fatigue test results of WesTrack fine-plus gradation.....	526
Table E.2.	The time-varied distributions of wander, traffic composition, and vehicle speed.....	535

LIST OF FIGURES

Figure 1.1.	(a) Fatigue life versus strain with various stiffnesses; (b) and (c) stiffness and tensile strain as a function of temperature; (d) fatigue life versus strain with various temperatures.....	23
Figure 1.2.	Image-and-contour plot of the maximum tensile strains of pavement with a dual-tire traffic load (simulation case: $T_b = 35^\circ\text{C}$, temperature gradient = 0.06).....	24
Figure 1.3.	Crack initiation and crack propagation.	25
Figure 1.4.	Controlled-strain fatigue diagram (after Pell).....	26
Figure 1.5.	Effect of rest period on life ratio (after Raithby).	26
Figure 1.6.	Procedures to predict cumulative loading from results of simple loading test (after Monismith 1975).	27
Figure 1.7.	Methodology followed in the fatigue analysis system to determine ESALs (after Harvey 1997).	28
Figure 2.1.	Layout of WesTrack test track (not to scale).	39
Figure 2.2.	Individual WesTrack gradation curves on a 19 mm nominal size 0.45 power chart.....	40
Figure 2.3.	Individual WesTrack gradation curves on a semi-logarithm chart.....	40
Figure 2.4.	Driverless triple-trailer test trucks.	41
Figure 2.5.	Tractor/trailer configuration.....	41
Figure 2.6.	503RF pavement structure with MDD and thermocouple positioning (after Harvey 1997).....	42
Figure 2.7.	Plan view of test section and location of instruments for data collection (after Harvey 1997).	43
Figure 2.8.	LVDT module of MDD (after CSIR.)	44
Figure 2.9.	Anchor assembly of the MDD installation set in concrete at depth of about 4 meters (after CSIR.).....	44
Figure 3.1.	Conventional fatigue testing machine.....	62

Figure 3.2.	Schematic plots of conventional and modified flexural fatigue test setups.....	63
Figure 3.3.	Modified fatigue test setup with temperature control box.....	64
Figure 3.4.	Modified fatigue test setup: inside view.....	64
Figure 3.5.	Modified fatigue test setup: side view (1).....	65
Figure 3.6.	Modified fatigue test setup: side view (2).....	65
Figure 3.7.	Strain gages attached on beam and aluminum support.....	66
Figure 3.8.	Wheatstone bridge.....	66
Figure 3.9.	Strain gage locations and dimensions of asphalt concrete beam, TEFLON™ sheet, and aluminum support.....	67
Figure 3.10.	Individual WesTrack coarse gradation curves on a 19 mm nominal size 0.45 power chart.....	68
Figure 3.11.	Individual WesTrack coarse gradation curves on a semi-logarithm chart.....	68
Figure 3.12.	Individual WesTrack fine gradation curves on a 19 mm nominal size 0.45 power chart.....	69
Figure 3.13.	Individual WesTrack fine gradation curves on a semi-logarithm chart.....	69
Figure 4.1.	An example of fitting the Weibull survivor function to a fatigue test result in terms of $\ln(-\ln(SR))$ versus $\ln(n)$	127
Figure 4.2.	An example of fitting the Weibull survivor function to a fatigue test result in terms of $\ln(-\ln(SR))$ versus $\ln(\ln(n))$	127
Figure 4.3.	Two parallel Weibull curves.....	128
Figure 4.4.	Two concurrent Weibull curves.....	128
Figure 4.5.	Weibull curves in reversed S shape.....	129
Figure 4.6.	Weibull curve in three phases: (1) Phase I: Heating and arrived at temperature equilibrium, (2) Phase II: Crack initiation developing, and (3) Phase III: Crack propagating.....	129

Figure 4.7.	Pairs diagram for <i>lnstif</i> and <i>lnnf</i> (fatigue tests at 20° C).	130
Figure 4.8.	Pairs diagram for the regression coefficients <i>aa</i> , <i>bb</i> , <i>cc</i> , and <i>dd</i> of the Weibull curves (fatigue tests at 20° C).	131
Figure 4.9.	Scatterplots of 500 independent pairs of bivariate normal random variables with correlation coefficients $\rho = 0.2$, $\rho = 0.4$, $\rho = 0.6$, $\rho = 0.8$, $\rho = 0.0$, and $\rho = 0.99$.	132
Figure 4.10.	Design plot of <i>lnstif</i> (fatigue tests at 20° C).	133
Figure 4.11.	Design plot of <i>lnnf</i> (fatigue tests at 20° C).	133
Figure 4.12.	Design plot of <i>aa</i> (fatigue tests at 20° C).	134
Figure 4.13.	Design plot of <i>bb</i> (fatigue tests at 20° C).	134
Figure 4.14.	Design plot of <i>cc</i> (fatigue tests at 20° C).	135
Figure 4.15.	Design plot of <i>dd</i> (fatigue tests at 20° C).	135
Figure 4.16.	Boxplots for factor <i>grad</i> (fatigue tests at 20° C).	136
Figure 4.17.	Boxplots for factor <i>ac</i> (fatigue tests at 20° C).	136
Figure 4.18.	Boxplots for factor <i>av</i> (fatigue tests at 20° C).	137
Figure 4.19.	Boxplots for factor <i>stn</i> (fatigue tests at 20° C).	137
Figure 4.20.	Boxplots for factor <i>rs4s50</i> (fatigue tests at 20° C).	138
Figure 4.21.	Boxplots for factor <i>m200</i> (fatigue tests at 20° C).	138
Figure 4.22.	Boxplots for factor <i>sa</i> (fatigue tests at 20° C).	139
Figure 4.23.	Boxplots for factor <i>vma</i> (fatigue tests at 20° C).	139
Figure 4.24.	Boxplots for factor <i>vfa</i> (fatigue tests at 20° C).	140
Figure 4.25.	Weibull curves in two strain groups (fatigue tests at 20° C).	141
Figure 4.26.	Test results of high temperature fatigue test for CM mixes.	142

Figure 4.27.	Test results of high temperature fatigue test for FM mixes.	143
Figure 4.28.	Flexural frequency sweep test results for FM mixes at 300 microstrain.	144
Figure 4.29.	Flexural frequency sweep test results for CM mixes at 300 microstrain.	145
Figure 4.30.	Gamma distribution curves with shape parameter $n = 2$ and scale parameters $\beta = 0.1, 0.2, 0.5, 1, 1.5, \text{ and } 2$	146
Figure 4.31.	Gamma distribution curves with shape parameter $n = 5$ and scale parameters $\beta = 0.1, 0.2, 0.5, 1, 1.5, \text{ and } 2$	146
Figure 4.32.	Nonlinear fitting of flexural frequency sweep test using Gamma distribution function (modified fatigue test setup).....	147
Figure 4.33.	Nonlinear fitting of flexural frequency sweep test using Gamma distribution function (conventional fatigue test setup).	147
Figure 4.34.	Weibull curves at various strain levels.	148
Figure 4.35.	Stiffness deterioration curves at various strains in terms of SR versus repetition.	149
Figure 4.36.	Stiffness deterioration curves at various strains in terms of stiffness versus repetition.	149
Figure 4.37.	A 200-400-200 sequential fatigue test.	150
Figure 4.38.	A 400-200-400 sequential fatigue test.	150
Figure 4.39.	A 400-200 sequential fatigue test.	151
Figure 4.40.	A 200-400 sequential fatigue test.	151
Figure 4.41.	A summary of varied-strain fatigue tests in terms of SR versus repetition.	152
Figure 4.42.	A summary of varied-strain fatigue tests in terms of stiffness versus repetition.	153
Figure 4.43.	Cumulative dissipated energy plot for varied-strain fatigue tests.....	154
Figure 4.44.	Weibull curves at various temperatures.	155

Figure 4.45.	Stiffness deterioration curves at various temperatures in terms of SR versus repetition.	155
Figure 4.46.	Stiffness deterioration curves at various temperatures in terms of stiffness versus repetition.....	156
Figure 4.47.	Time needed for internal temperature stabilization of a beam.	156
Figure 4.48.	A 20-30-20 sequential fatigue test.	157
Figure 4.49.	A 30-20-30 sequential fatigue test.	157
Figure 4.50.	A 30-20 sequential fatigue test.	158
Figure 4.51.	A 20-30 sequential fatigue test.	158
Figure 4.52.	A summary of varied-temperature fatigue tests in terms of stiffness versus repetition.	159
Figure 4.53.	Cumulative dissipated energy plot for varied-temperature fatigue tests.	160
Figure 4.54.	Boxplot of fatigue life versus temperature (°C).	161
Figure 4.55.	Boxplot of fatigue life versus strain.	161
Figure 4.56.	Weibull curves at extreme temperatures.	162
Figure 4.57.	Application of time hardening procedure from a low damage state to a high damage state in terms of SR.	163
Figure 4.58.	Application of time hardening procedure from a high damage state to a low damage state in terms of SR.	164
Figure 4.59.	Application of strain hardening procedure from a low damage state to a high damage state in terms of SR.	165
Figure 4.60.	Application of strain hardening procedure from a high damage state to a low damage state in terms of SR.	166
Figure 5.1.	Stiffness deterioration curve fitted with a Weibull survivor function with $\lambda = 0.002$ and $\gamma = 0.412$	209
Figure 5.2.	Weibull density function with $\lambda = 0.002$ and $\gamma = 0.412$	209

Figure 5.3.	Weibull curves for fine-plus gradation at temperature 5 °C	210
Figure 5.4.	Weibull curves for fine-plus gradation at temperature 20 °C	210
Figure 5.5.	Weibull curves for fine-plus gradation at temperature 30 °C	211
Figure 5.6.	Weibull regression fitting and real data for fine-plus gradation.	212
Figure 5.7.	Residual plots of Weibull regression equation for coarse gradation.	213
Figure 5.8.	Residual plots of Weibull regression equation for fine and fine-plus gradations.	214
Figure 5.9.	Change of stiffness ratios along various stiffness deterioration curves.	215
Figure 5.10.	Construction of the compound stiffness deterioration curve with Weibull dynamic approach.	215
Figure 5.11.	Prediction of fatigue life (adapted from Monismith, et al., 1961).	216
Figure 5.12.	Miner's Law in explanation with stiffness ratio and fatigue life.	216
Figure 5.13.	Comparison between Miner's Law and Weibull theory.	217
Figure 5.14.	Weibull accelerated failure time model with different correction factors.....	218
Figure 5.15.	Back-calculated moduli of CAL/APT Goal 1 Section 503RF with test wheel loads of 40 kN and 100 kN subjected to a test temperature of 20 ± 3 °C.	219
Figure 5.16.	Fitted Weibull equation of back-calculated moduli of Section 503RF with a 40 kN test wheel load.....	220
Figure 5.17.	Relationship of $ A / B $ ratio versus MF.....	221
Figure 5.18.	History of maximum tensile strain of Section 503RF.	222
Figure 5.19.	History of mode factor of Section 503RF.....	223
Figure 6.1.	Flow chart of the simulation procedure for fatigue performance prediction (crack initiation time).	258
Figure 6.2.	Temperature spectrum of WesTrack at a depth of 50 mm from 3/3/96 to 10/2/98.....	259

Figure 6.3.	Temperature density function of WesTrack at a depth of 50 mm from 3/3/96 to 10/2/98.	260
Figure 6.4.	Temperature distribution function of WesTrack at a depth of 50 mm from 3/3/96 to 10/2/98.	260
Figure 6.5.	Temperature spectrum of WesTrack at a depth of 150 mm from 3/3/96 to 10/2/98.	261
Figure 6.6.	Temperature density function of WesTrack at a depth of 150 mm from 3/3/96 to 10/2/98.	262
Figure 6.7.	Temperature distribution function of WesTrack at a depth of 150 mm from 3/3/96 to 10/2/98.	262
Figure 6.8.	Spectrum of temperature gradient at WesTrack from 3/3/96 to 10/2/98.	263
Figure 6.9.	Temperature gradient's density function at WesTrack from 3/3/96 to 10/2/98.	264
Figure 6.10.	Temperature gradient's distribution function at WesTrack from 3/3/96 to 10/2/98.	264
Figure 6.11.	Applied traffic at various wander locations of WesTrack.	265
Figure 6.12.	Typical highway wander pattern (after Allen).	266
Figure 6.13.	Bar charts of applied traffic at various wander locations at different periods of WesTrack: (a) 3/3/96-7/15/96: no wander or antenna off, (b) 7/16/96-12/14/96: traffic only at 5R and 5L, (c) 12/15/96-2/18/97: only 135,249 ESALs applied, and (d) 2/19/97-9/3/98: varied wander pattern.	267
Figure 6.14.	Bar chart of applied traffic at various wander locations from 3/3/96-9/3/98.	268
Figure 6.15.	Plot of cumulative ESALs and temperature spectrum at a depth of 150 mm.	269
Figure 6.16.	Maximum tensile strains fitted with a bi-normal distribution functions, $N(0.0010, 0.1361)$ and $N(0.3551, 0.1361)$, with a multiplication factor of $A = 0.0001435$, subjected to the following simulation case: $T_b = 41.10^\circ C$, $g = 0.1091$, $sg = 95.79 \text{ MPa}$, $av = 13.7\%$, and $ac = 6.22\%$	270

Figure 6.17.	Maximum tensile strains fitted with a bi-normal distribution functions, $N(-0.0188, 0.1806)$ and $N(0.3751, 0.1806)$, with a multiplication factor of $A = 0.0000286$ subjected to the following simulation case: $T_b = -2.24^\circ\text{C}$, $g = -0.0518$, $sg = 113.30\text{ MPa}$, $av = 13.7\%$, and $ac = 6.22\%$	270
Figure 6.18.	Illustration of tensile strain calculation with wander.	271
Figure 6.19.	Fatigue performance prediction of crack initiation with and without wander for Section 8.	272
Figure 6.20.	Simulation results of fatigue performance prediction and condition survey of 26 original test sections of the WesTrack project.	273
Figure 6.21.	Simulation results of fatigue performance prediction and condition survey of coarse mixes of the WesTrack project.	274
Figure 6.22.	Simulation results of fatigue performance prediction and condition survey of fine mixes of the WesTrack project.	275
Figure 6.23.	Simulation results of fatigue performance prediction and condition survey of fine-plus mixes of the WesTrack project.	276
Figure 7.1.	“Node-by-node” and “hour-by-hour” algorithm of <i>Weibull</i> program.	318
Figure 7.2.	Module relationship of <i>Weibull</i> program.	319
Figure 7.3.	Flow chart of <i>Weibull</i> main program.	320
Figure 7.4.	Flow chart of <code>process_one_hour()</code> subroutine.	321
Figure 7.5.	Loading configuration, pavement structure, and ELSYM5 input of WesTrack for <i>Weibull</i> simulation.	322
Figure 7.6.	Relationship between initial stiffness and stiffness ratio.	323
Figure 7.7.	A wander example of stiffness deterioration curves arranged in various depths at different offsets of Section 3.	324
Figure 7.8.	Stiffness deterioration of WesTrack Section 3 and WesTrack traffic and environmental factors: (a) temperature and cumulative traffic and (b) stiffness deterioration and cumulative traffic.	325

Figure 7.9.	Image-and-contour plots of SR of WesTrack Section 3 after 21,943 hours of simulation with a correction factor of 1.0: (a) wander and (b) no wander.	326
Figure 7.10.	Image-and-contour plots of SR of WesTrack Section 8 after 21,943 hours of simulation with a correction factor of 1.0: (a) wander and (b) no wander.	327
Figure 7.11.	Stiffness deterioration curves of WesTrack coarse sections at a location of the weakest point of the no-wander case.	328
Figure 7.12.	Stiffness deterioration curves of WesTrack fine sections at a location of the weakest point of no-wander case.	329
Figure 7.13.	Stiffness deterioration curves of WesTrack fine-plus at a location of the weakest point of the no-wander case.	330
Figure 7.14.	The Weibull simulation results and condition survey of coarse mixes of the WesTrack project.	331
Figure 7.15.	The Weibull simulation results and condition survey of fine mixes of the WesTrack project.	332
Figure 7.16.	The Weibull simulation results and condition survey of fine-plus mixes of the WesTrack project.	333
Figure 7.17.	Image-and-contour plots of SR of WesTrack Section 3 with modified traffic pattern: (a) wander and (b) no wander.	334
Figure 7.18.	Stiffness deterioration curves of WesTrack Section 3 with modified traffic pattern.	335
Figure 7.19.	Image-and-contour plots of SR of WesTrack Section 8 with modified traffic pattern: (a) wander and (b) no wander.	336
Figure 7.20.	Stiffness deterioration curves of WesTrack Section 8 with modified traffic pattern.	337
Figure 7.21.	Image-and-contour plots of SR of WesTrack Section 3 with modified weather pattern: (a) wander and (b) no wander.	338
Figure 7.22.	Stiffness deterioration curves of WesTrack Section 3 with modified weather pattern.	339
Figure 7.23.	Image-and-contour plots of SR of WesTrack Section 8 with modified weather pattern: (a) wander and (b) no wander.	340

Figure 7.24.	Stiffness deterioration curves of WesTrack Section 8 with modified weather pattern.	341
Figure 7.25.	Image-and-contour plots of SR of WesTrack Section 3 with modified weather and traffic patterns: (a) wander and (b) no wander.....	342
Figure 7.26.	Stiffness deterioration curves of WesTrack Section 3 with various weather and traffic patterns.....	343
Figure 7.27.	Image-and-contour plots of SR of WesTrack Section 8 with modified weather and traffic patterns: (a) wander and (b) no wander.....	344
Figure 7.28.	Stiffness deterioration curves of WesTrack Section 8 with various weather and traffic patterns.....	345
Figure 7.29.	Image-and-contour plots of SR of WesTrack Section 3 with 2 % less air-void content (10.4 %): (a) wander and (b) no wander.....	346
Figure 7.30.	Image-and-contour plots of SR of WesTrack Section 3 with 2 % more air-void content (14.4 %): (a) wander and (b) no wander.	347
Figure 7.31.	Stiffness deterioration curves of WesTrack Section 3 with various air-void contents.....	348
Figure 7.32.	Image-and-contour plots of SR of WesTrack Section 8 with 2 % less air-void content (6.5 %): (a) wander and (b) no wander.....	349
Figure 7.33.	Image-and-contour plots of SR of WesTrack Section 8 with 2 % more air-void content (10.5 %): (a) wander and (b) no wander.	350
Figure 7.34.	Stiffness deterioration curves of WesTrack Section 8 with various air-void contents.....	351
Figure 7.35.	Image-and-contour plots of SR of WesTrack Section 3 with 5-inch thickness of asphalt concrete: (a) wander and (b) no wander.....	352
Figure 7.36.	Image-and-contour plots of SR of WesTrack Section 3 with 6-inch thickness of asphalt concrete: (a) wander and (b) no wander.....	353
Figure 7.37.	Image-and-contour plots of SR of WesTrack Section 3 with 7-inch thickness of asphalt concrete: (a) wander and (b) no wander.....	354

Figure 7.38.	Stiffness deterioration curves of WesTrack Section 3 with various thicknesses of asphalt concrete.	355
Figure 7.39.	Image-and-contour plots of SR of WesTrack Section 8 with 5-inch thickness of asphalt concrete: (a) wander and (b) no wander.	356
Figure 7.40.	Image-and-contour plots of SR of WesTrack Section 8 with 6-inch thickness of asphalt concrete: (a) wander and (b) no wander.	357
Figure 7.41.	Image-and-contour plots of SR of WesTrack Section 8 with 7-inch thickness of asphalt concrete: (a) wander and (b) no wander.	358
Figure 7.42.	Stiffness deterioration curves of WesTrack Section 8 with various thicknesses of asphalt concrete.	359
Figure 7.43.	Strain history of WesTrack Section 8 with modified traffic pattern.	360
Figure 7.44.	Strain history of WesTrack Section 15 with modified traffic pattern.	360
Figure 7.45.	Differential average tensile strain of Section 15 (fine) and Section 8 (coarse) of WesTrack.	361
Figure 7.46.	Image-and-contour plots of SR of WesTrack Section 3 with 0.5 % less asphalt content (4.47 %): (a) wander and (b) no wander.	362
Figure 7.47.	Image-and-contour plots of SR of WesTrack Section 3 with 0.5 % more asphalt content (5.47 %): (a) wander and (b) no wander.	363
Figure 7.48.	Stiffness deterioration curves of WesTrack Section 3 with various asphalt contents.	364
Figure 7.49.	Image-and-contour plots of SR of WesTrack Section 8 with 0.5 % less asphalt content (4.97 %): (a) wander and (b) no wander.	365
Figure 7.50.	Image-and-contour plots of SR of WesTrack Section 8 with 0.5 % more asphalt content (5.97 %): (a) wander and (b) no wander.	366
Figure 7.51.	Stiffness deterioration curves of WesTrack Section 8 with various asphalt contents.	367
Figure 7.52.	Image-and-contour plots of SR of WesTrack Section 3 with a correction factor of 0.8: (a) wander and (b) no wander.	368
Figure 7.53.	Image-and-contour plots of SR of WesTrack Section 3 with a correction factor of 1.2: (a) wander and (b) no wander.	369

Figure 7.54.	Stiffness deterioration curves of WesTrack Section 3 with various correction factors.	370
Figure 7.55.	Image-and-contour plots of SR of WesTrack Section 8 with a correction factor of 0.8: (a) wander and (b) no wander.	371
Figure 7.56.	Image-and-contour plots of SR of WesTrack Section 8 with a correction factor of 1.2: (a) wander and (b) no wander.	372
Figure 7.57.	Stiffness deterioration curves of WesTrack Section 8 with various correction factors.	373

LIST OF APPENDIX FIGURES

Figure B.4.1. Design plot of <i>lnstif</i> (temperature susceptibility fatigue test, field-mixed and field-compacted).	409
Figure B.4.2. Design plot of <i>lnnf</i> (temperature susceptibility fatigue test, field-mixed and field-compacted).	409
Figure B.4.3. Design plot of <i>aa</i> (temperature susceptibility fatigue test, field-mixed and field-compacted).	410
Figure B.4.4. Design plot of <i>bb</i> (temperature susceptibility fatigue test, field-mixed and field-compacted).	410
Figure B.4.5. Design plot of <i>cc</i> (temperature susceptibility fatigue test, field-mixed and field-compacted).	411
Figure B.4.6. Design plot of <i>dd</i> (temperature susceptibility fatigue test, field-mixed and field-compacted).	411
Figure B.4.7. Design plot of <i>lnstif</i> (temperature susceptibility fatigue test, lab.-mixed and lab.-compacted).	412
Figure B.4.8. Design plot of <i>lnnf</i> (temperature susceptibility fatigue test, lab.-mixed and lab.-compacted).	412
Figure B.4.9. Design plot of <i>aa</i> (temperature susceptibility fatigue test, lab.-mixed and lab.-compacted).	413
Figure B.4.10. Design plot of <i>bb</i> (temperature susceptibility fatigue test, lab.-mixed and lab.-compacted).	413
Figure B.4.11. Design plot of <i>cc</i> (temperature susceptibility fatigue test, lab.-mixed and lab.-compacted).	414
Figure B.4.12. Design plot of <i>dd</i> (temperature susceptibility fatigue test, lab.-mixed and lab.-compacted).	414
Figure B.4.13. Design plot of <i>lnstif</i> (high temperature fatigue test).	415
Figure B.4.14. Design plot of <i>lnnf</i> (high temperature fatigue test).	415
Figure B.4.15. Design plot of <i>aa</i> (high temperature fatigue test).	416
Figure B.4.16. Design plot of <i>bb</i> (high temperature fatigue test).	416

Figure B.4.17. Design plot of <i>cc</i> (high temperature fatigue test).....	417
Figure B.4.18. Design plot of <i>dd</i> (high temperature fatigue test).	417
Figure B.4.19. Design plot of <i>lnstif</i> (fatigue test with various gradations at 20 ° C).	418
Figure B.4.20. Design plot of <i>lnnf</i> (fatigue test with various gradations at 20 ° C).	418
Figure B.4.21. Design plot of <i>aa</i> (fatigue test with various gradations at 20 ° C).	419
Figure B.4.22. Design plot of <i>bb</i> (fatigue test with various gradations at 20 ° C).	419
Figure B.4.23. Design plot of <i>cc</i> (fatigue test with various gradations at 20 ° C).	420
Figure B.4.24. Design plot of <i>dd</i> (fatigue test with various gradations at 20 ° C).	420
Figure B.4.25. Design plot of <i>lnstif</i> (pooled fatigue tests).....	421
Figure B.4.26. Design plot of <i>lnnf</i> (pooled fatigue tests).....	421
Figure B.4.27. Design plot of <i>aa</i> (pooled fatigue tests).....	422
Figure B.4.28. Design plot of <i>bb</i> (pooled fatigue tests).....	422
Figure B.4.29. Design plot of <i>cc</i> (pooled fatigue tests).	423
Figure B.4.30. Design plot of <i>dd</i> (pooled fatigue tests).....	423
Figure B.4.31. Design plot of <i>lnstif</i> (regression: coarse).	424
Figure B.4.32. Design plot of <i>lnnf</i> (regression: coarse).....	424
Figure B.4.33. Design plot of <i>aa</i> (regression: coarse).	425
Figure B.4.34. Design plot of <i>bb</i> (regression: coarse).	425
Figure B.4.35. Design plot of <i>cc</i> (regression: coarse).....	426
Figure B.4.36. Design plot of <i>dd</i> (regression: coarse).	426
Figure B.4.37. Boxplots for factor <i>ac</i> (regression: coarse).....	427
Figure B.4.38. Boxplots for factor <i>av</i> (regression: coarse).....	427
Figure B.4.39. Boxplots for factor <i>temp</i> (regression: coarse).....	428

Figure B.4.40. Boxplots for factor <i>stn</i> (regression: coarse).....	428
Figure B.4.41. Boxplots for factor <i>rs4s50</i> (regression: coarse).....	429
Figure B.4.42. Boxplots for factor <i>m200</i> (regression: coarse).....	429
Figure B.4.43. Boxplots for factor <i>sa</i> (regression: coarse).....	430
Figure B.4.44. Boxplots for factor <i>vma</i> (regression: coarse).....	430
Figure B.4.45. Boxplots for factor <i>vfa</i> (regression: coarse).....	431
Figure B.4.46. C_p plot for the model selection of initial stiffnes (coarse).....	432
Figure B.4.47. Residual plots for the regression model of initial stiffness (coarse).....	432
Figure B.4.48. C_p plot for the model selection of fatigue life (coarse).....	433
Figure B.4.49. Residual plots for the regression model of fatigue life (coarse).....	433
Figure B.4.50. Design plot of <i>lnstif</i> (regression: fine).....	434
Figure B.4.51. Design plot of <i>lnnf</i> (regression: fine).....	434
Figure B.4.52. Design plot of <i>aa</i> (regression: fine).....	435
Figure B.4.53. Design plot of <i>bb</i> (regression: fine).....	435
Figure B.4.54. Design plot of <i>cc</i> (regression: fine).....	436
Figure B.4.55. Design plot of <i>dd</i> (regression: fine).....	436
Figure B.4.56. C_p plot for the model selection of initial stiffness (fine).....	437
Figure B.4.57. Residual plots for the regression model of initial stiffness (fine).....	437
Figure B.4.58. C_p plot for the model selection of fatigue life (fine).....	438
Figure B.4.59. Residual plots for the regression model of fatigue life (fine).....	438
Figure B.4.60. Design plot of <i>lnstif</i> (regression: fine-plus).....	439
Figure B.4.61. Design plot of <i>lnnf</i> (regression: fine-plus).....	439

Figure B.4.62. Design plot of <i>aa</i> (regression: fine-plus)	440
Figure B.4.63. Design plot of <i>bb</i> (regression: fine-plus)	440
Figure B.4.64. Design plot of <i>cc</i> (regression: fine-plus).....	441
Figure B.4.65. Design plot of <i>dd</i> (regression: fine-plus)	441
Figure B.4.66. C_p plot for the model selection of initial stiffness (fine-plus).....	442
Figure B.4.67. Residual plots for the regression model of initial stiffness (fine- plus).....	442
Figure B.4.68. C_p plot for the model selection of fatigue life (fine-plus)	443
Figure B.4.69. Residual plots for the regression model of fatigue life (fine-plus).....	443
Figure B.4.70. Design plot of <i>lnstif</i> (regression: fine and fine-plus)	444
Figure B.4.71. Design plot of <i>lnnf</i> (regression: fine and fine-plus).....	444
Figure B.4.72. Design plot of <i>aa</i> (regression: fine and fine-plus)	445
Figure B.4.73. Design plot of <i>bb</i> (regression: fine and fine-plus)	445
Figure B.4.74. Design plot of <i>cc</i> (regression: fine and fine-plus).....	446
Figure B.4.75. Design plot of <i>dd</i> (regression: fine and fine-plus)	446
Figure B.4.76. C_p plot for the model selection of initial stiffness (fine and fine- plus).....	447
Figure B.4.77. Residual plots for the regression model of initial stiffness (fine and fine-plus)	447
Figure B.4.78. C_p plot for the model selection of fatigue life (fine and fine-plus)	448
Figure B.4.79. Residual plots for the regression model of fatigue life (fine and fine-plus)	448
Figure B.6.1. Simulation result of crack initiation for Section 5 of WesTrack (coarse, AV = 8.1 %, AC = 5.63 %)	449
Figure B.6.2. Simulation result of crack initiation for Section 6 of WesTrack (coarse, AV = 10.8 %, AC = 5.71 %)	449

Figure B.6.3. Simulation result of crack initiation for Section 7 of WesTrack (coarse, AV = 6.9 %, AC = 6.49 %)	450
Figure B.6.4. Simulation result of crack initiation for Section 23 of WesTrack (coarse, AV = 4.9 %, AC = 5.79 %)	450
Figure B.6.5. Simulation result of crack initiation for Section 24 of WesTrack (coarse, AV = 7.2 %, AC = 5.94 %)	451
Figure B.6.6. Simulation result of crack initiation for Section 25 of WesTrack (coarse, AV = 3.7 %, AC = 6.55 %)	451
Figure B.6.7. Simulation result of crack initiation for Section 26 of WesTrack (coarse, AV = 11.0 %, AC = 5.31 %)	452
Figure B.6.8. Simulation result of crack initiation for Section 1 of WesTrack (fine, AV = 8.8 %, AC = 5.35 %)	452
Figure B.6.9. Simulation result of crack initiation for Section 2 of WesTrack (fine, AV = 10.4 %, AC = 4.92 %)	453
Figure B.6.10. Simulation result of crack initiation for Section 3 of WesTrack (fine, AV = 12.4 %, AC = 4.97 %)	453
Figure B.6.11. Simulation result of crack initiation for Section 4 of WesTrack (fine, AV = 6.6 %, AC = 5.12 %)	454
Figure B.6.12. Simulation result of crack initiation for Section 14 of WesTrack. (fine, AV = 9.0 %, AC = 6.05 %)	454
Figure B.6.13. Simulation result of crack initiation for Section 15 of WesTrack (fine, AV = 8.7 %, AC = 5.42 %)	455
Figure B.6.14. Simulation result of crack initiation for Section 16 of WesTrack (fine, AV = 12.2 %, AC = 4.75 %)	455
Figure B.6.15. Simulation result of crack initiation for Section 17 of WesTrack (fine, AV = 11.0 %, AC = 5.74 %)	456
Figure B.6.16. Simulation result of crack initiation for Section 18 of WesTrack (fine, AV = 4.3 %, AC = 6.04 %)	456
Figure B.6.17. Simulation result of crack initiation for Section 9 of WesTrack (fine-plus, AV = 3.9 %, AC = 6.56 %)	457

Figure B.6.18. Simulation result of crack initiation for Section 10 of WesTrack (fine-plus, AV = 11.8 %, AC = 5.28 %)	457
Figure B.6.19. Simulation result of crack initiation for Section 11 of WesTrack (fine-plus, AV = 7.9 %, AC = 5.99 %)	458
Figure B.6.20. Simulation result of crack initiation for Section 12 of WesTrack (fine-plus, AV = 4.6 %, AC = 5.84 %)	458
Figure B.6.21. Simulation result of crack initiation for Section 13 of WesTrack (fine-plus, AV = 5.9 %, AC = 6.51 %)	459
Figure B.6.22. Simulation result of crack initiation for Section 19 of WesTrack (fine-plus, AV = 7.2 %, AC = 5.89 %)	459
Figure B.6.23. Simulation result of crack initiation for Section 20 of WesTrack (fine-plus, AV = 10.9 %, AC = 5.88 %)	460
Figure B.6.24. Simulation result of crack initiation for Section 21 of WesTrack (fine-plus, AV = 4.2 %, AC = 6.75 %)	460
Figure B.6.25. Simulation result of crack initiation for Section 22 of WesTrack (fine-plus, AV = 8.1 %, AC = 5.23 %)	461
Figure B.7.1. Image-and-contour plots of SR of WesTrack Section 1 after 21,943 hours of simulation with a correction factor of 1.0: (a) wander and (b) no wander.	462
Figure B.7.2. Image-and-contour plots of SR of WesTrack Section 2 after 21,943 hours of simulation with a correction factor of 1.0: (a) wander and (b) no wander.	463
Figure B.7.3. Image-and-contour plots of SR of WesTrack Section 4 after 21,943 hours of simulation with a correction factor of 1.0: (a) wander and (b) no wander.	464
Figure B.7.4. Image-and-contour plots of SR of WesTrack Section 14 after 21,943 hours of simulation with a correction factor of 1.0: (a) wander and (b) no wander.....	465
Figure B.7.5. Image-and-contour plots of SR of WesTrack Section 15 after 21,943 hours of simulation with a correction factor of 1.0: (a) wander and (b) no wander.....	466

Figure B.7.6. Image-and-contour plots of SR of WesTrack Section 16 after 21,943 hours of simulation with a correction factor of 1.0: (a) wander and (b) no wander.....	467
Figure B.7.7. Image-and-contour plots of SR of WesTrack Section 17 after 21,943 hours of simulation with a correction factor of 1.0: (a) wander and (b) no wander.....	468
Figure B.7.8. Image-and-contour plots of SR of WesTrack Section 18 after 21,943 hours of simulation with a correction factor of 1.0: (a) wander and (b) no wander.....	469
Figure B.7.9. Image-and-contour plots of SR of WesTrack Section 9 after 21,943 hours of simulation with a correction factor of 1.0: (a) wander and (b) no wander.	470
Figure B.7.10. Image-and-contour plots of SR of WesTrack Section 10 after 21,943 hours of simulation with a correction factor of 1.0: (a) wander and (b) no wander.....	471
Figure B.7.11. Image-and-contour plots of SR of WesTrack Section 11 after 21,943 hours of simulation with a correction factor of 1.0: (a) wander and (b) no wander.....	472
Figure B.7.12. Image-and-contour plots of SR of WesTrack sSection 12 after 21,943 hours of simulation with a correction factor of 1.0: (a) wander and (b) no wander.....	473
Figure B.7.13. Image-and-contour plots of SR of WesTrack Section 13 after 21,943 hours of simulation with a correction factor of 1.0: (a) wander and (b) no wander.....	474
Figure B.7.14. Image-and-contour plots of SR of WesTrack Section 19 after 21,943 hours of simulation with a correction factor of 1.0: (a) wander and (b) no wander.....	475
Figure B.7.15. Image-and-contour plots of SR of WesTrack Section 20 after 21,943 hours of simulation with a correction factor of 1.0: (a) wander and (b) no wander.....	476
Figure B.7.16. Image-and-contour plots of SR of WesTrack Section 21 after 21,943 hours of simulation with a correction factor of 1.0: (a) wander and (b) no wander.....	477

Figure B.7.17. Image-and-contour plots of SR of WesTrack Section 22 after 21,943 hours of simulation with a correction factor of 1.0: (a) wander and (b) no wander.....	478
Figure B.7.18. Image-and-contour plots of SR of WesTrack Section 5 after 21,943 hours of simulation with a correction factor of 1.0: (a) wander and (b) no wander.	479
Figure B.7.19. Image-and-contour plots of SR of WesTrack Section 6 after 21,943 hours of simulation with a correction factor of 1.0: (a) wander and (b) no wander.	480
Figure B.7.20. Image-and-contour plots of SR of WesTrack Section 7 after 21,943 hours of simulation with a correction factor of 1.0: (a) wander and (b) no wander.	481
Figure B.7.21. Image-and-contour plots of SR of WesTrack Section 23 after 21,943 hours of simulation with a correction factor of 1.0: (a) wander and (b) no wander.....	482
Figure B.7.22. Image-and-contour plots of SR of WesTrack Section 24 after 21,943 hours of simulation with a correction factor of 1.0: (a) wander and (b) no wander.....	483
Figure B.7.23. Image-and-contour plots of SR of WesTrack Section 25 after 21,943 hours of simulation with a correction factor of 1.0: (a) wander and (b) no wander.....	484
Figure B.7.24. Image-and-contour plots of SR of WesTrack Section 26 after 21,943 hours' simulation with a correction factor of 1.0: (a) wander and (b) no wander.....	485
Figure C.1. Flexural beam analysis with different tensile and compressive moduli.	504
Figure C.2. Stress and strain relationship of a supported beam.	505
Figure E.1. Module relationship of <i>Weibull</i> program.	603
Figure E.2. Flow chart of <i>Weibull</i> main program.	604
Figure E.3. Flow chart of the <code>process_one_hour()</code> subroutine.	605
Figure E.4. "Node-by-node" and "hour-by-hour" algorithm of <i>Weibull</i> program.	606

Figure E.5.	Weibull curves for fine-plus gradation at temperature 5 ° C	607
Figure E.6.	Weibull curves for fine-plus gradation at temperature 20 ° C	607
Figure E.7.	Weibull curves for fine-plus gradation at temperature 30 ° C	608
Figure E.8.	Weibull regression fitting and real data for fine-plus gradation.	609
Figure E.9.	Weibull accelerated failure time model with different correction factors.....	531
Figure E.10.	Illustration of tensile strain calculation with wander.....	610
Figure E.11.	Relationship between initial stiffness and stiffness ratio.....	611
Figure E.12.	Plot of traditional flexural frequency sweep test at various reference temperatures.	612
Figure E.13.	Using a uniform distribution U(0,1) to generate a set of random numbers with a given distribution function.	613
Figure E.14.	Assignment of random numbers to the nearest discrete number.	613
Figure E.15.	Loading configuration, pavement structure, and ELSYM5 input of WesTrack for Weibull simulation.....	614
Figure E.16.	Image-and-contour plot of stiffness ratio after the last application of traffic loading of example 1 with wander.....	615
Figure E.17.	Image-and-contour plot of stiffness ratio after the last application of traffic loading of example 1 with no wander.....	615
Figure E.18.	Stiffness deterioration curves at offset 14 in. and depth 5.99 in. for both wander and no wander cases for example 1.	616
Figure E.19.	Image-and-contour plot of stiffness ratio after the last application of traffic loading of WesTrack (example 2: with wander).	617
Figure E.20.	Image-and-contour plot of stiffness ratio after the last application of traffic loading of WesTrack (example 2: with no wander).	617
Figure E.21.	Stiffness deterioration curves for example 2.	618

ACKNOWLEDGMENTS

I would like to give my sincerest thanks to the following people who have contributed their efforts to the completion of this thesis and Doctoral degree.

It is difficult to find the words to express my deep gratitude to my advisor, Professor Carl L. Monismith. Without his helpful advice, strong support, and encouragement throughout my graduate studies, it would not have been possible for me to complete the Doctoral degree. My heartfelt thanks go as well to Professor John T. Harvey, for he has been, and continues to be, the first person to whom I turn for counsel and assistance. Our rapport of “like teacher, like brother” encourages me to ask for his help with any problems I come up against without hesitation. I appreciate his warmth and unflagging patience with me. I would also like to thank the other professors on my committee, Professor Sanjay Govindjee and Professor Ching-Shui Cheng, for their time, their help, and their suggestions.

Additionally, I would like to recognize the fellows working in the Pavement Research Center for the dedication of their time, labor, and help, as well as their friendship, throughout my dissertation study: Dave Hung for his help with the testing setup, David Kim for his enthusiasm in purchasing materiel, Hector Matha for his expertise in specimen preparation, Irwin Guada for his aid in debugging, and Ed Nicks for keeping the testing equipment running. Special thanks to Maggie Paul and Manuel Garcia for their time and effort in editing and readying this dissertation.

Finally, I would like to thank my wife, Wen-Yu Tsai, for her support in all ways possible.

1.0 INTRODUCTION

1.1 Background

“High Temperature Fatigue” has long been identified as an important phenomenon that limits the lifetime of metallic components in mechanical engineering application. However, little has been studied in the field of asphalt concrete under these conditions. The lack of popular attention to this matter might be attributed to the “common wisdom” that fatigue cracking occurs at an intermediate temperature of around 20°C, whereas when the temperature rises above 40°C or higher, the distress mode of asphalt concrete is predominated by the rutting mechanism, i.e., the asphalt concrete tends to flow out as viscoelastic materials do at high temperatures. The fatigue tests used by many researchers (e.g., Monismith, Deacon, Epps, Tayebali, and Harvey) to generate fatigue life regression equations have been conducted at temperatures ranging only from 5°C to 30°C.

In 1995, a project named “WesTrack” which was sponsored by Federal Highway Administration (FHWA) and headed by the Nevada Automotive Test Center was to continue to develop the asphalt aggregate mix performance-related specifications prepared in earlier studies (Kennedy 1994, Witczak 1997) and to validate the Superpave Mix design method. A 2.9 km oval track including 26 test sections was built to evaluate the effect of variations in binder content, gradation, and density on the Superpave Design system. Pavement temperatures were recorded hourly at different depths of the pavement structure from March 1996 to October 1998. During the trafficking of the test section, the proportion of temperatures above 30°C at the bottom of the asphalt concrete layer

was about 20 % of the total recorded time. Serious fatigue cracking had been observed within some test sections. The realities of fatigue distress and the high temperature found at the bottom of asphalt concrete have motivated the study of “high temperature fatigue” conducted herein to verify the existence of fatigue damage in asphalt concrete at the elevated temperatures.

Based on the high temperature distribution and the observed fatigue distress that occurred at WesTrack, three questions come to mind: (1) How much of the fatigue distress occurs at high temperatures? (2) How does the temperature affect the fatigue damage process? and (3) Does high temperature have a more deleterious effect in terms of fatigue damage than does low temperature?

This study of fatigue at high temperatures has been limited to a temperature range of 30°C to 40°C. The conventional repetitive simple shear test at constant height is usually conducted at temperatures higher than 40°C because very little permanent shear deformation is developed below 40°C. Using the conventional fatigue testing machine and methodology, it is very difficult to obtain the fatigue response at a temperature higher than 30°C. Most mixes will creep and sag during the installation and during testing; as a result, it is almost impossible to conduct a controlled-strain fatigue beam test.

Monismith et al. (1985) have suggested a relationship of fatigue life as a function of maximum tensile strain and initial mix stiffness,

$$N_f = A(1/\epsilon_t)^a (1/S_{mix})^b, \quad (1.1)$$

where: ϵ_t = tensile strain, S_{mix} = initial mix stiffness, N_f = fatigue life, and A , a , and b are experimentally determined coefficients.

From Figure 1.1a, it will be noted that the fatigue life at a specified strain level decreases as the stiffness of the mix increases. In equation 1.1, the ϵ_t and S_{mix} are the functions of temperature (as shown in Figures 1.1b and 1.1c); in other words, the fatigue equation can then be transferred as a function of temperature (as shown in Figure 1.1d). It should be noted that the fatigue life as a function of temperature depends highly on the rate change of ϵ_t and S_{mix} , especially at high temperatures. The magnitude of the fatigue life depends on the interaction between the effect of the temperature on the rate change of S_{mix} contributed to the term $(1/S_{mix})^b$ and the effect of the temperature on the rate change of ϵ_t contributed to the term $(1/\epsilon_t)^a$. Hence, it is worthwhile to study the fatigue response at an elevated temperature.

Figure 1.2 displays an image-contour plot of the computed maximum tensile strains occurring in a pavement structure under the load application of dual tires. This simulation case assumes a 35 °C bottom temperature and a positive temperature gradient that is defined as $(T@150mm - T@50mm)/100mm$; in other words, the pavement temperature near the surface is lower than that found at the bottom of the asphalt concrete layer. The calculations of maximum tensile strain were based on a layered-elastic program named Circly (Wardle 1977). From the results, it can be observed that the maximum tensile strain occurred at the bottom of the asphalt concrete layer.

A designed traffic pattern, i.e., the wander pattern, was applied on the WesTrack track. As a result of the wander pattern and environmental factors, the pavement

experienced a compound-strain loading history. The following question is then how to apply the laboratory simple fatigue test results to describe the cumulative fatigue damage caused by the compound-strain loading history.

It should be noted that the WesTrack pavement was designed to accumulate about ten million 80 kN (18 kips) equivalent single axle loads (ESALs) in two years with fatigue cracking occurring for the average construction quality conditions originally planned. It was found that several sections deteriorated much faster than should be expected. During the WesTrack project, there were two winters, hence it was suspected that the cold weather accelerated the crack propagation for those sections seriously cracked. To explore the possible reasons for the deterioration, it is very important to fully understand the fatigue damage process experienced by the asphalt concrete under the combination effect of material, traffic and environmental factors. Within the context of this study, the term “stiffness deterioration process” is the synonym of the term “fatigue damage process” because the stiffness ratio is utilized as an index of the fatigue damage.

1.2 Research Objectives

The scope and the objectives of this project were to:

- Explore the fatigue behavior of asphalt concrete subjected to high temperatures, defined as the range of 30°C to 40°C.
- Explore the use of the Weibull proportional hazards model to describe the stiffness deterioration process of asphalt concrete subjected to various

material and testing variables and to use this model in the Weibull dynamic approach to predict fatigue performance.

- Determine whether it is possible to predict the fatigue performance, especially the crack initiation, of real pavement in laboratory simple fatigue tests through the introduction of the Weibull dynamic approach and hence to improve and specify the performance-oriented mix design which will ensure longer service life with economy.
- Provide an affordable and feasible computer program based on the developed Weibull dynamic approach to simulate the fatigue performance with the input of traffic and temperature spectra, laboratory fatigue test results, and pavement structure. In doing so, it might be expected to accelerate the efficiency of pavement design and reduce the extensive amount of computation effort required to an acceptable level.
- Identify and subdivide the correction factor, conventionally recognized as “shift factor”, into several sub-correction factors which are related to mix properties, traffic wander, temperature, rest periods, crack propagation time, and boundary conditions of pavement structure; in addition, potential correction factors related to traffic composition and vehicle speed are also discussed.

1.3 Literature Review

1.3.1 History of Asphalt Concrete Fatigue Model Development

Fatigue cracking is one of the three major modes of distress considered in pavement design. The other two modes are permanent deformation and thermal cracking, which are beyond the scope of this study. Investigation by Hveem (1955) demonstrated the concept that fatigue cracking has a higher propensity to occur on the pavement when the pavement experiences a larger deflection and a higher loading frequency. This work had an impact on developing laboratory fatigue tests to describe the phenomenon of fatigue failure. Accordingly, two equations (Monismith et al. 1971, Pell 1973) were developed to define the fatigue response of asphalt concrete as shown in the following:

$$N_f = A(1/\varepsilon_t)^B \quad (1.2)$$

or

$$N_f = C(1/\sigma_t)^D,$$

where N_f = number of repetitions to failure, ε_t = tensile strain repeatedly applied, σ_t = tensile stress repeatedly applied, and A, B, C, and D are experimentally determined coefficients.

Monismith et al. (1985) proposed a more applicable formula for the fatigue life, already shown in equation 1.1. This equation was used in the Shell (1978 and 1985) and the Asphalt Institute (1981) design procedures; the coefficients were determined by considering the amount of cracking, mix type, and the thickness of the asphalt-bound layer. Following the development of this laboratory fatigue relationship, Deacon (1965) demonstrated the applicability of a cumulative fatigue damage hypothesis by using it to consider the development of damage resulting from a range in strains. This relationship

is termed the linear summation of cycle ratios, or Miner's Law (1945). Miner's hypothesis for cumulative fatigue damage has been widely used to predict fatigue cracking. The hypothesis is stated as follows,

$$\sum_{i=1}^n \frac{n_i}{N_i} \leq 1, \quad (1.3)$$

where n_i = number of actual traffic load applications at strain level i and N_i = number of allowable traffic load applications at strain level i . Fatigue failure is defined as when the linear summation of cycle ratios reaches one. It is assumed that the fatigue failure is independent of loading sequence. Monismith et al. (1987) proposed an analytically-based approach to predict the fatigue life and stressed that the tensile strains on the underside of an asphalt concrete layer must be calculated for the expected range of traffic loads, materials, and environmental conditions.

Van der Poel (1954) first referred to a loosely defined (not shear, bulk, elastic, or complex) quotient of stress and strain as the stiffness. Monismith (1969) reinforced van der Poel's concept, stating that the time of loading and temperature must be well defined when the term stiffness is used. This indicates that the stiffness of aggregate-asphalt mixes is a relative quantity rather than an absolute quantity and the term is meaningful only when the temperature and loading time are specified.

The work done by Deacon (1965) and Epps (1968) has contributed significantly to identifying the factors in pavement design that affect fatigue performance and minimize fatigue cracking. Finn and Epps (1980) indicated the possible causes of fatigue cracking as structural deficiency, excessive air voids, change in properties of asphalt with

time, aggregate gradation, stripping, construction considerations, and drainage. Harvey and Tsai (1996) also showed that the air-void content and asphalt content have significant effects on the fatigue performance of asphalt concrete.

An alternative approach to a strain-based fatigue analysis in pavement design is to utilize the concept of dissipated energy. This concept can be traced to the work done by van Dijk et al. (1972) on thin bitumen films. Van Dijk (1975) and van Dijk and Visser (1977) extended the concept to the fatigue of bituminous mixes. The dissipated energy was recognized as a leading factor in fatigue analysis, particularly of visco-elastic material, by Pronk and Hopman (1990). Van Dijk and Visser (1977) reported the following energy relationship which is independent of test method, testing conditions, loading frequency, or rest periods:

$$W_{FAT} = A(N_{FAT})^Z, \quad (1.4)$$

where N_{FAT} is the load repetitions to fatigue failure; W_{FAT} is the total dissipated energy per unit volume obtained by summation for $i = 1$ to N_{FAT} , i.e., $W_{FAT} = \sum_{i=1}^{N_{FAT}} W_i$; A and Z are experimentally determined and mix-dependent. To relate this energy relationship obtained from the laboratory to the pavement structure, it is necessary to calculate the dissipated energy that occurs in a pavement structure under traffic load. It is possible to compute the dissipated energy by using a dynamic algorithm, such as is found in the program SAPSI (Sousa et al. 1988, Chen 1987).

In the Strategic Highway Research Program (SHRP) project A-003, Tayebali et al. (1994) also proposed an energy-dependent surrogate fatigue model:

$$N_f = A \cdot \exp(B \cdot VFB) \cdot (w_0)^C, \quad (1.5)$$

where N_f = fatigue life, w_0 = initial dissipated energy per cycle, psi, VFB = percent voids filled with bitumen, and A and B are experimentally determined coefficients.

The strain-based fatigue analysis mainly utilizes equation 1.1 and Miner's Law (equation 1.3). Equation 1.4 is the primary relationship used for the energy-based fatigue analysis. Both of these approaches have long been used in evaluating pavement fatigue design, yet neither approach considers information on the fatigue damage before pavement failure.

1.3.2 Crack Initiation and Crack Propagation

Conventionally, the term fatigue is used to mean tensile fatigue rather than shear fatigue in pavement engineering. In this regard, the fatigue resistance of an asphalt mix is defined as the capacity to prevail against repeated bending without fracture. Fatigue failure manifests itself in the form of cracking that consists of a series of interconnecting cracks on the pavement surface caused by repeated traffic loading. Fatigue cracking occurs at places of high tensile strain or at locations with high tensile stress concentrations in the asphalt concrete layer.

In general, fatigue can be described as a two-phase process, i.e., a crack initiation process followed by a crack propagation process. In places where a high tensile strain

repetitively occurs in the asphalt concrete, microcracks start to initiate; hence, a lost area, where the microcracks develop, increases gradually as a result of the accumulating microcracks. Consequently, the tensile stress increases relatively and causes the development of macrocracks. Majidzadeh et al. (1971) postulated that the fatigue life of asphalt mixes could be described by three processes: damage initiation, growth, and final failure. Therefore, the fatigue life could be represented accordingly by the following form,

$$N_f = f(c_0, (A, n, K), K_C).$$

In this equation, c_0 is associated with the process of crack initiation and considered as the “starter flaw” from which the crack will propagate. The (A, n, K) set expresses the process of crack growth and is the parameters of the Paris equation (Paris 1964):

$$\frac{dc}{dN} = AK^n, \text{ where } K \text{ is the stress intensity factor and the } A \text{ and } n \text{ are the material}$$

constants. The K_C is the critical stress-intensity factor which is proportional to the critical strain energy release rate and Young’s modulus. Both notched and unnotched specimens were utilized to determine these constants. Salam and Monismith (1972) also conducted a series of fracture tests using notched specimens and examined the tensile fracture characteristics of asphalt mixes using the Paris equation.

Little et al. (1997) asserted that the mechanisms of crack initiation and propagation should be governed by the same Paris law. This crack-based fatigue analysis

differs markedly from the phenomenological-and-statistical fatigue analysis as discussed in this thesis.

However, some fatigue performance models have defined the crack initiation as the first appearance of longitudinal, transverse, or alligator cracks of a minimum length of 0.5 m under the wheel paths. Accordingly, several models have been proposed such as the PARIS model (1999), and the HDM-4 model (1997). Ullidtz (1987) proposed a progressive way to predict the crack propagation time in the Mathematical Model of Pavement Performance (MMOPP). However, it should be noted that the study of crack propagation is not included in this thesis.

Huang (1993) also pointed out a finding of the AASHO Road Test: “more surface cracking occurred during periods when the pavement was in a relatively cold state than during periods of warm weather.” His statement suggests the possibility that cold weather actually favors the crack propagation phenomenon.

It was found that the fatigue failure that occurred at WesTrack was from the bottom layers up to the surface, justifying further study of the prediction of this “bottom-up” type of cracking.. As illustrated in Figure 1.3 repetitive trafficking loads cause both tensile and shear strains to occur on or near the surface and mainly tensile strains at the bottom of the asphalt layer. Once the accumulated fatigue damage exceeds the fatigue-resistant capacity of the asphalt layer, the crack initiation develops and the crack starts to propagate. It might be conjectured that the propagation is accelerated by the shrinkage of the asphalt layer in a cold winter and the tensile strain caused by the temperature drop.

1.3.3 High Temperature Fatigue Test

The examination of “high temperature fatigue” within the context of this study is limited to a temperature range of 30°C to 40°C. Pell (1963) reported a set of fatigue test results of asphalt mixes, as illustrated in Figure 1.4, containing tests conducted from -9.5°C to 40°C and showing that the fatigue life at a given strain level is seen to increase as the temperature increases.

Hofstra and Valkering (1972) concluded that, “elastic theory can be used to describe the behavior of flexible pavements subjected to moving wheels even at the highest temperatures that are likely to be experienced in pavements.” They measured the stresses and strains imposed by a moving wheel load using the laboratory test track and then compared the results with the theoretical results from the BISTRO computer program (Peutz et al. 1968). The temperatures of test pavements were varied from 20°C to 60°C.

Raithby and Sterling (1972) conducted direct cyclic tensile and compressive fatigue tests with a constant stress on a specimen sawed from a “rolled carpet” with a loading consisting of sinusoidal loading and various rest periods at three test temperatures: 10°C, 25°C, and 40°C. The relation of rest period to the fatigue performance at various temperatures was the major concern of this paper. A life ratio, defined as the ratio of the mean life to failure with rest periods to the mean life under continuous cycling (no rest periods) for the same cyclic stress conditions, was used to estimate the rest period effect. From these findings (as shown in Figure 1.5) it can be concluded that: (1) the life ratios were not significantly different at 10°C and 25°C; (2) the life ratios at 10°C and 25°C were about 5 to 6 times larger than those at 40°C for the rest periods greater than 0.2 seconds; (3) the rest periods resulted in a longer fatigue

life; and (4) the application of test results with no rest periods would seriously underestimate the fatigue performance of the in-situ condition that has rest periods. In addition to their findings of how fatigue life is affected by rest periods, Raithby and Sterling also found that rest periods affect the dynamic stiffness. When rest periods are included, the dynamic stiffness falls rapidly initially, as is the case without rest periods; thereafter the change of stiffness is much more gradual than in the case without rest periods.

From Figure 1.5, it can be seen that the life ratios at 10°C and 25°C were about 5 to 6 times larger than those at 40°C for rest periods greater than 0.2 second. This observation contradicts the understanding that the healing of asphalt concrete at high temperatures should elongate the fatigue life.

It is suspected that the early quick drop in stiffness in a laboratory fatigue test is due in part to the test beam moving to a temperature equilibrium after a 2 to 3°C temperature increase from energy dissipation (Pronk 1996).

1.3.4 Compound Strain-Based Fatigue Loading

The ultimate goal of conducting laboratory fatigue tests is to predict the in-situ pavement fatigue performance. From the point of view of a strain-based analysis, it is recognized that compound fatigue loading always exists in the pavement as caused by the combination of traffic and environmental factors. Usually, a simple fatigue test (same deformation or load, temperature, load duration, rest period) is conducted in the laboratory. Therefore, it is important to comprehend the fatigue damage process of compound fatigue loading using the simple fatigue test results. Monismith, et al. (1975)

reported that neither the “time-hardening” and the “strain-hardening” procedures used in calculating the permanent deformation, as illustrated in Figure 1.6, provided a solution that agreed quantitatively with the experimental results. Ullidtz (1987) used the strain-hardening procedure to calculate the permanent strain in the MMOPP model. Although it seems that the strain-hardening and the time-hardening are usually applied in calculating the permanent deformation, in this study the feasibility of applying these two procedures to the fatigue damage process in terms of stiffness ratio will be evaluated.

Actually, this compound strain loading is pertinent to the microscopic mechanism of how the stiffness deterioration process behaves under various temperature or environmental factors; therefore it is very important to further confirm this mechanism in the future.

1.3.5 The Weibull Function

In the late 1930s, Weibull introduced his ideas about the statistical distributions of material strength with the publication of two important papers: “A Statistical Theory of the Strength of Materials” (Weibull 1939a) and “The Phenomenon of Rupture in Solids” (Weibull 1939b). Since then, the Weibull function and the Weibull distribution have found wide application in many fields. However, there has been little application of the Weibull function in describing the fatigue damage process in asphalt concrete. Garcia-Diaz, A. (1984) developed several performance models using an “S-shaped” survivor curve, instead of a Weibull survivor function, for predicting pavement performance in terms of three indices, present serviceability index, distress area index, and the distress

severity index. Little et al. (1997) suggested that a microcrack length distribution can be described as a Weibull distribution with the following form:

$$p(c) = \lambda\gamma(\lambda c)^{\gamma-1} \exp(-(\lambda c)^\gamma)$$

where c = microcrack length, γ = a shape parameter, and λ = a scale parameter. The parameters were further assumed to change with load repetitions. This crack-based approach is an alternative way to inspect the fatigue damage.

1.3.6 Cumulative Fatigue Damage Prediction

Cumulative fatigue damage theory is usually referred to by Miner's Law, shown in equation 1.3. Actually, Palmgren (1924) first introduced the hypothesis of cumulative fatigue damage for the testing of ball bearings. However, it was Miner (1945) who advanced a similar proposal and made it more popular for his testing of aluminum alloy specimens. Two aspects of this Palmgren-Miner hypothesis should be mentioned: (1) the accumulation of fatigue damage is assumed to be linear and equal to one at failure, and (2) The required number of loads to fail and the applied number of loads are obtained in terms of stress level instead of strain level. It is generally agreed that the allowable number of load repetitions is related to the tensile strain at the bottom of the asphalt concrete layer. Deacon (1965) proposed the linear summation of cycle ratios (sometimes referred to as Miner's hypothesis) to determine the cumulative fatigue damage using strain-based test results. However, Ioannides (1997) inspected the Miner's hypothesis

and found evidence in the literature suggesting the concepts of cumulative damage theory should be abandoned.

A specific phenomenological probabilistic model, namely the B-model, of cumulative damage of fatigue, fatigue crack growth, and wear was published in Bogdanoff's book (1985). In addition to this probabilistic model, Oh (1991) characterized the fatigue life of specimens with variable amplitude loads by using a nonlinear cumulative damage model.

Many researchers (e.g., Croney 1990, Ullidtz 1987, Wang and Larson 1978), from their studies on experimental and in-service pavements, found that there is a significant relationship between long-term pavement performance and changes in the transition deflections of the pavement surface. In a model of long-term pavement performance, i.e., MMOPP, Ullidtz (1987) characterized the aforementioned relationship as a reduction in the elastic modulus of the asphalt concrete with progressive fatigue damage. Collop (1994) also indicated that it is important to consider the modulus degradation mechanism in pavement design, and that it should be included in calculations when predicting long-term flexible pavement performance. Ullidtz (1998) asserted that, "the interaction of structural damage, climate effects, aging and traffic loading may accelerate the deterioration."

1.3.7 Full-Scale Accelerated Pavement Tests

Metcalf (1996) gives us this definition of full-scale accelerated pavement tests: "the controlled application of a prototype wheel loading, at or above the appropriate legal load limit to a prototype or actual, layered, structural pavement system to determine

pavement response and performance under a controlled, accelerated, accumulation of damage in a compressed time period.”

As pointed out by Monismith (1992), the following four historical events had significant influence before 1962, the recognized starting point of analytically based design: (1) early work done by Burmister (1945), (2) the development of the Benkelman beam during the WASHO Road Test (1954 and 1955), (3) the research on pavement deflection and fatigue failure by Hveem (1955), and (4) the AASHO Road Test (1962)

The most important concept of the AASHO test (1962) that was performed in the early 1960s in Illinois was that the damaging effect of the passage of an axle load can be represented by a number of 18-kip equivalent single axle loads (ESAL's). Huang (1993) stated that, “one important contribution of the AASHO Road Test was the development of the pavement serviceability concept together with the equations relating serviceability, load, and thickness design of both flexible and rigid pavements.”

Dai (1997) inspected the test results from the Mn/Road project and found that the linear elasticity assumption seems to be acceptable when calculating the peak strains in the bottom of an asphalt concrete layer at an average temperature of up to 40°C. Additionally, it was found that the peak strain in the bottom of the pavement continuously decreased as the truck speed increased on a smooth pavement. However, for a relatively rough pavement, the strain decreased as the truck speed increased up to about 65 km/hr, then strain started to increase when the speed further increased from 65 up to 103 km/hr, which could be attributed to the dynamic load. Therefore, the higher vehicle speed results in less loading time and thus decreases the tensile strain level at the bottom of the pavement.

Sebaaly et al. (1989) demonstrated that most of the stiffness of asphalt-bound layers may be lost when cracking appears on the surface of the pavement. They determined the modulus of asphalt concrete using the Falling Weight Deflectometer (FWD) data during a FHWA experiment with the Accelerated Loading Facility (ALF).

Recently, Kim and Kim (1997) used the technology named Spectral Analysis of Surface Waves (SASW) to decide the modulus of asphalt concrete related to the number of load applications. Accordingly, several findings of pavement deterioration have been summarized by them: (1) a rather rapid deterioration rate, during which one third of the initial stiffness is lost. This is then followed by a much slower deterioration rate to a final level of about 15-20 % of initial stiffness, (2) the first appearance of cracking was observed at about 70 % stiffness deduction, and (3) a rapid increase in cracking occurred at about 80 % stiffness deduction.

1.3.8 Shift Factor

Within the context of this study, the term “correction factor” rather than shift factor is used, for it is recognized that the shift factor is actually affected by a host of correction factors that account for wander, mix properties, boundary conditions, temperature conditions, pavement structure, crack propagation, and the trafficking load. To apply the laboratory fatigue test results to predict in-situ fatigue performance, it is necessary to apply a shift factor. A shift factor of 10 means that the damage to a test beam caused by one repetition is equivalent to the same damage caused by 10 load repetitions as accumulated in an asphalt pavement.

A large variety of shift factors can be expected, owing to the differences in material properties, test methods, field conditions, pavement structure, and structure models. Pell (1987) indicated that the shift factor might range from 5 to 700. Deacon et al. (1994) in the SHRP A-003 studies recommended a shift factor ranging from 10 to 14 depending on the amount of surface cracking that can be tolerated. Many shift factors have been proposed by the Asphalt Institute, the Shell design method, Thompson (1987), Powell et al. (1984), and Verstraeten et al. (1982). One commonality is that all these shift factors relate the hot mix asphalt (HMA) tensile strain to the allowable number of load repetitions. Finn et al. (1977) showed that a shift factor of about 13 was required for laboratory fatigue test results to match the fatigue performance of the AASHO Road Test. Raithby and Sterling (1970) demonstrated that rest periods of a uniaxial tensile cyclic test would affect the fatigue lives by a factor of 5 or more as compared with the specimen tested without rest periods. Gerritsen and Koole (1987) suggested a shift factor ranging from 5 to 25 (including the considerations of the rest periods between the loads, lateral distribution of the wheel loads and the temperature gradient in the asphalt layer) should be multiplied to the laboratory-derived fatigue criterion to meet the in-situ fatigue performance. In recent studies, Harvey et al. (1997) also proposed a strain-based shift factor for use in a reliability-based mix design system for mitigating fatigue distress as seen in Figure 1.7.

Several findings from the above literature review are summarized in the following:

1. Historically, the various conventional fatigue approaches and models do not take into consideration the entire fatigue damage process, only the end points of crack initiation and propagation.
2. It seems to be acceptable to apply the linear layered-elastic programs, e.g., Circlly or ELSYM5 (Ahlborn 1972), based on the linear elasticity assumption in calculating the strains of pavement structure at high temperatures.
3. The fatigue cracking appearing on the surface of an asphalt concrete pavement is caused not only by the crack initiation but more importantly by the crack propagation that is mostly attributed to the cyclic thermal strain and shrinkage as well.
4. Caution should be exercised in applying the results of simple fatigue tests, either in controlled-strain or controlled-stress loading modes, to interpreting the cumulative fatigue damage caused by compound loading.
5. Full-size accelerated pavement testing provides an effective but expensive way to validate the correction factors needed for applying the laboratory fatigue test results to predict fatigue performance in field pavement.
6. Stiffness deterioration of asphalt concrete must be considered in pavement design.

Keeping these facts in mind, a Weibull dynamic approach will be developed in this study. In this approach, the fatigue damage process is described by using a two-parameter Weibull function; furthermore, a Weibull proportional hazards model is adopted to represent all the material and environmental variables in one comprehensive

regression equation. A Weibull accelerated failure time model is used to correct for the effect of boundary conditions between the laboratory and field. In conducting the simulation, it is presumed that the linear elastic theory is appropriate at high temperatures; hence, the linear layered-elastic program ELSYM5 will be used as the “strain engine” in computing the strains occurring inside the asphalt concrete layer.

1.4 Research Organization

This dissertation is divided into 8 chapters. Chapter 2 provides a brief introduction of the available data resources from the WesTrack and CAL/APT HVS projects. The laboratory test plan is described in Chapter 3 to supplement the incompleteness of currently available data and explore the effects of environmental and material variables on the fatigue damage process. The specimen preparation is also described in detail in Chapter 3.

Chapter 4 contains a detailed analysis of laboratory fatigue test results performed for this study, including the identification of significant factors that affect the stiffness, fatigue life, and fatigue damage process, regression analysis of stiffness and fatigue life for various WesTrack mixes, and the exploration of a compound stiffness deterioration curve subjected to changes of strain level and temperature.

The theoretical derivation of a Weibull dynamic approach for predicting fatigue performance is described in Chapter 5, mainly containing the Weibull proportional hazards model and the Weibull accelerated failure time model. In addition, some discussion of the relation of predictions from Weibull and Miner’s Law is also included.

A methodology for simulating the fatigue performance of WesTrack based on the Miner's approach is proposed in Chapter 6.

Chapter 7 contains the fatigue performance simulations utilizing the Weibull dynamic approach. Several variables including traffic pattern, weather pattern, construction variability, and correction factor that affect the fatigue damage process are also inspected. Conclusions and perspectives are presented in Chapter 8.

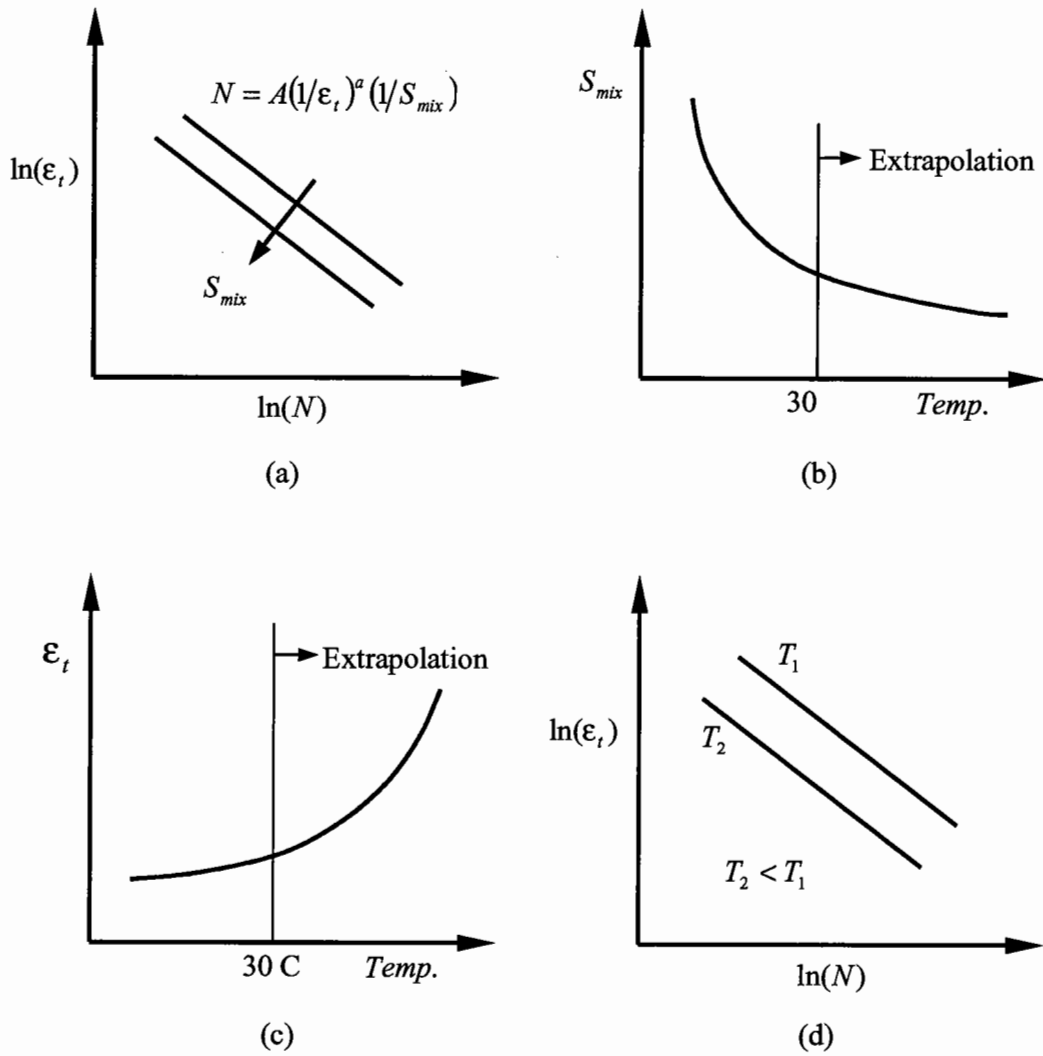


Figure 1.1. (a) Fatigue life versus strain with various stiffnesses; (b) and (c) stiffness and tensile strain as a function of temperature; (d) fatigue life versus strain with various temperatures.

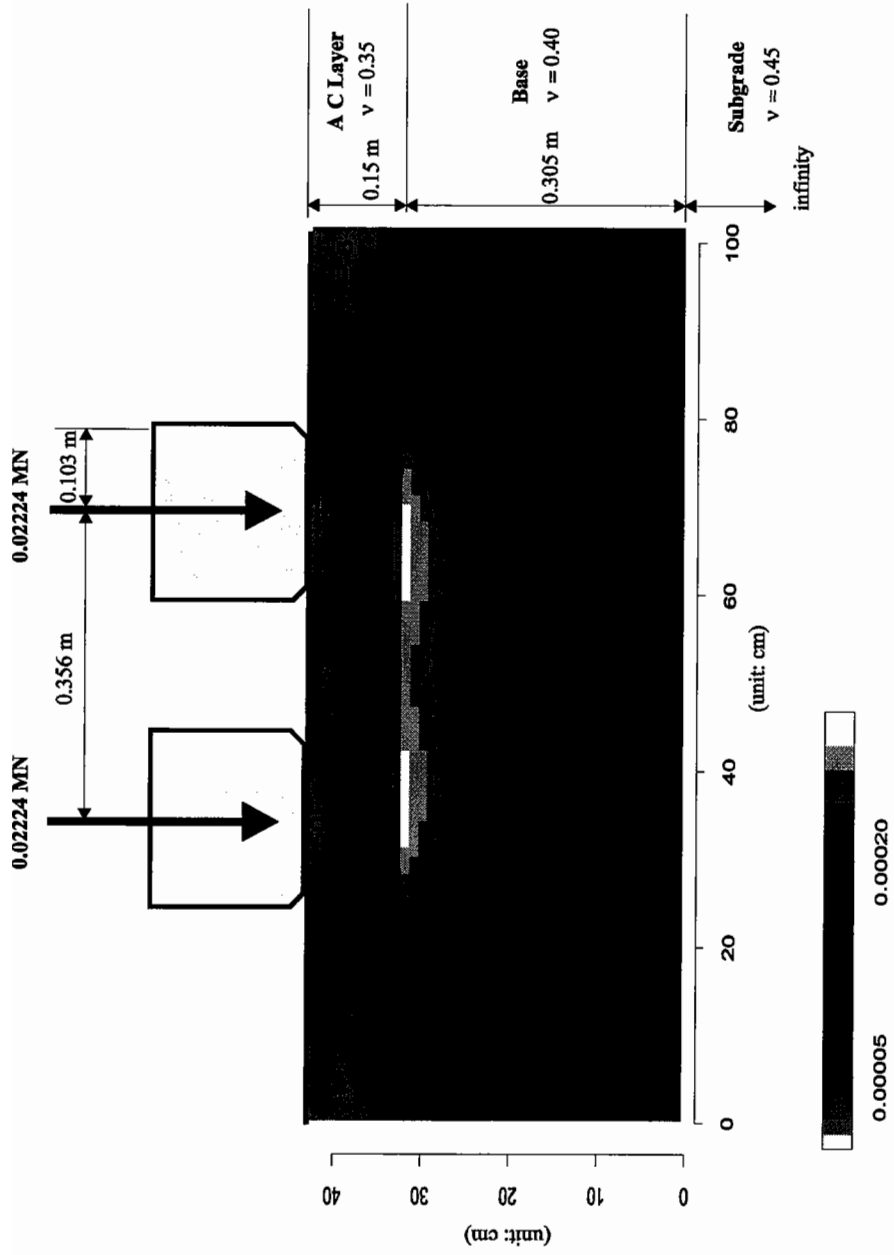
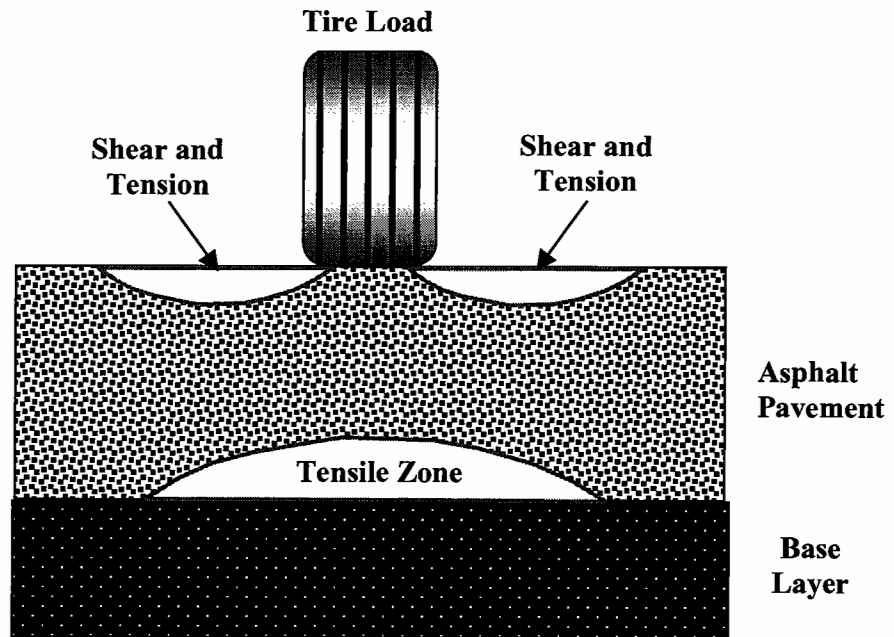
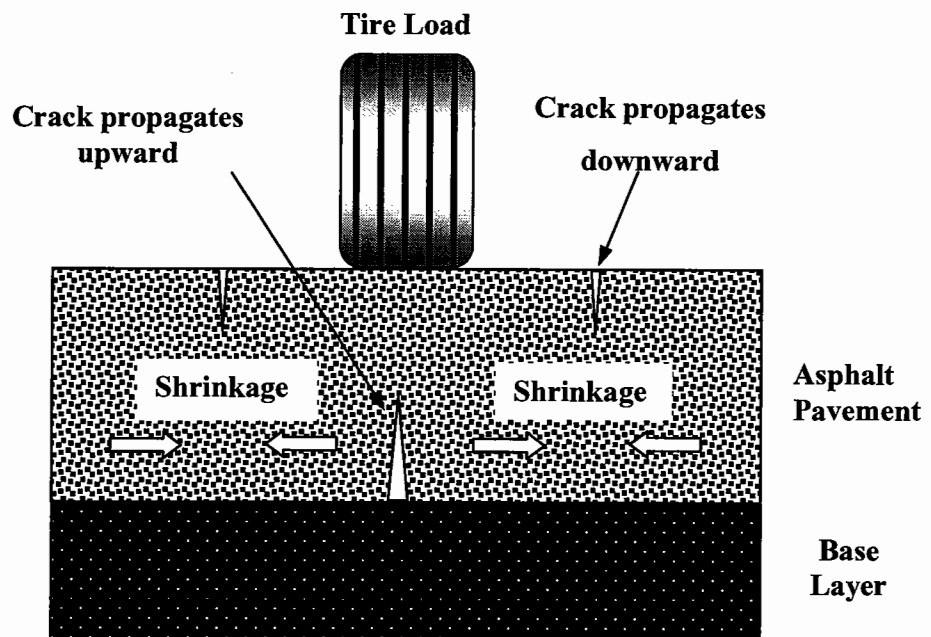


Figure 1.2. Image-and-contour plot of the maximum tensile strains of pavement with a dual-tire traffic load (simulation case: $T_b = 35^\circ\text{C}$, temperature gradient = 0.06)



(a) Crack Initiation



(b) Crack Propagation

Figure 1.3. Crack initiation and crack propagation.

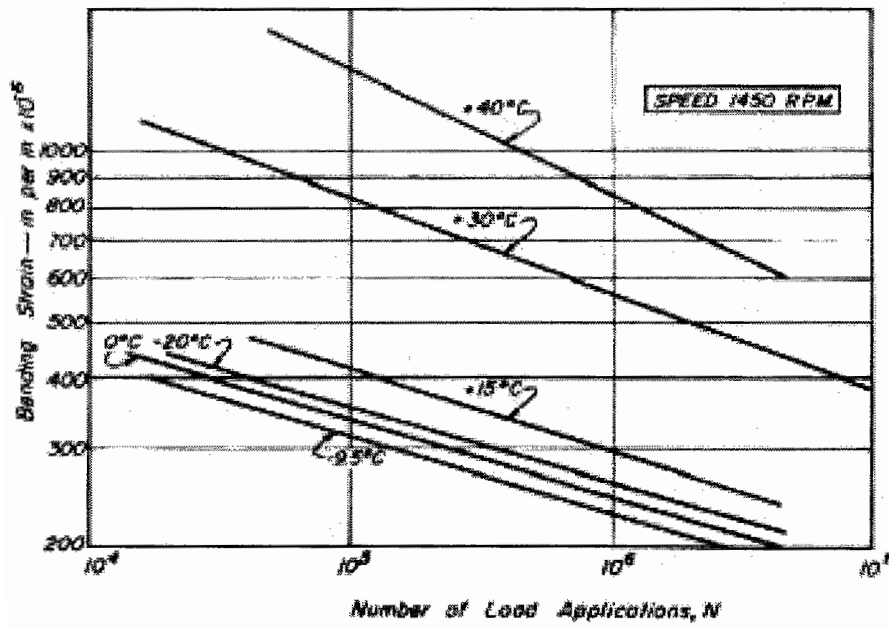


Figure 1.4. Controlled-strain fatigue diagram (after Pell).

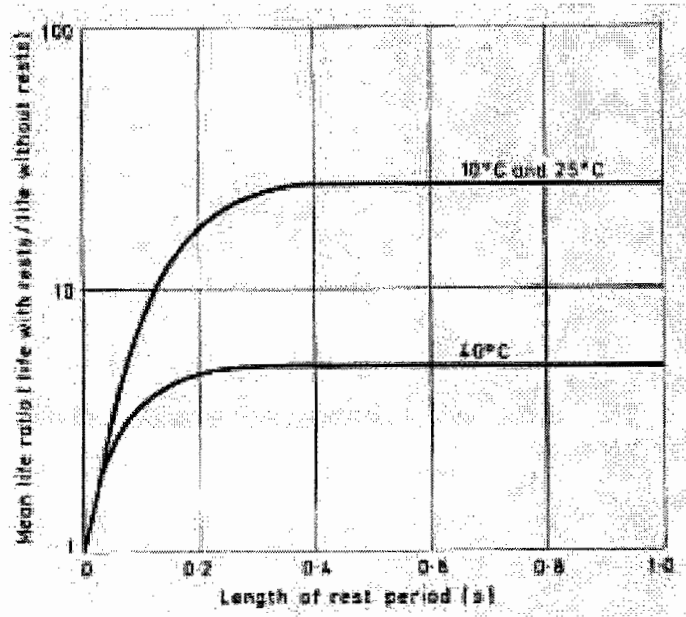
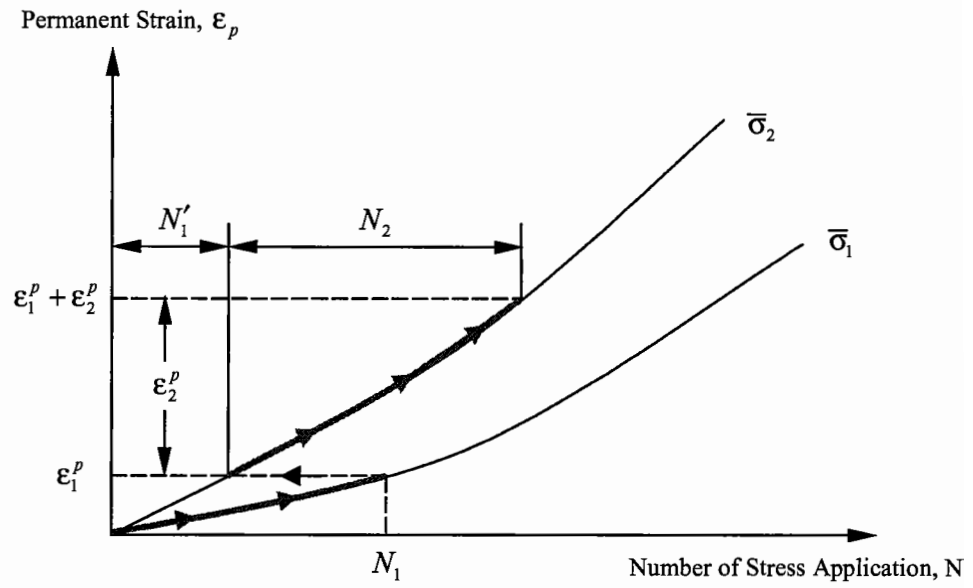
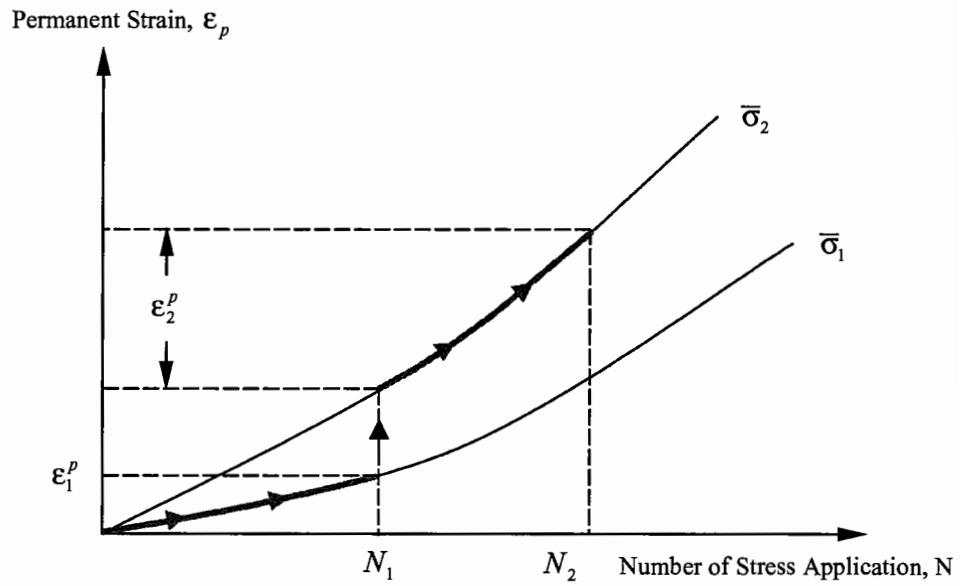


Fig 5. Effect of Rest Period on Life Ratio

Figure 1.5. Effect of rest period on life ratio (after Raithby).



(a) Time Hardening Procedure



(b) Strain Hardening Procedure

Figure 1.6. Procedures to predict cumulative loading from results of simple loading test (after Monismith 1975).

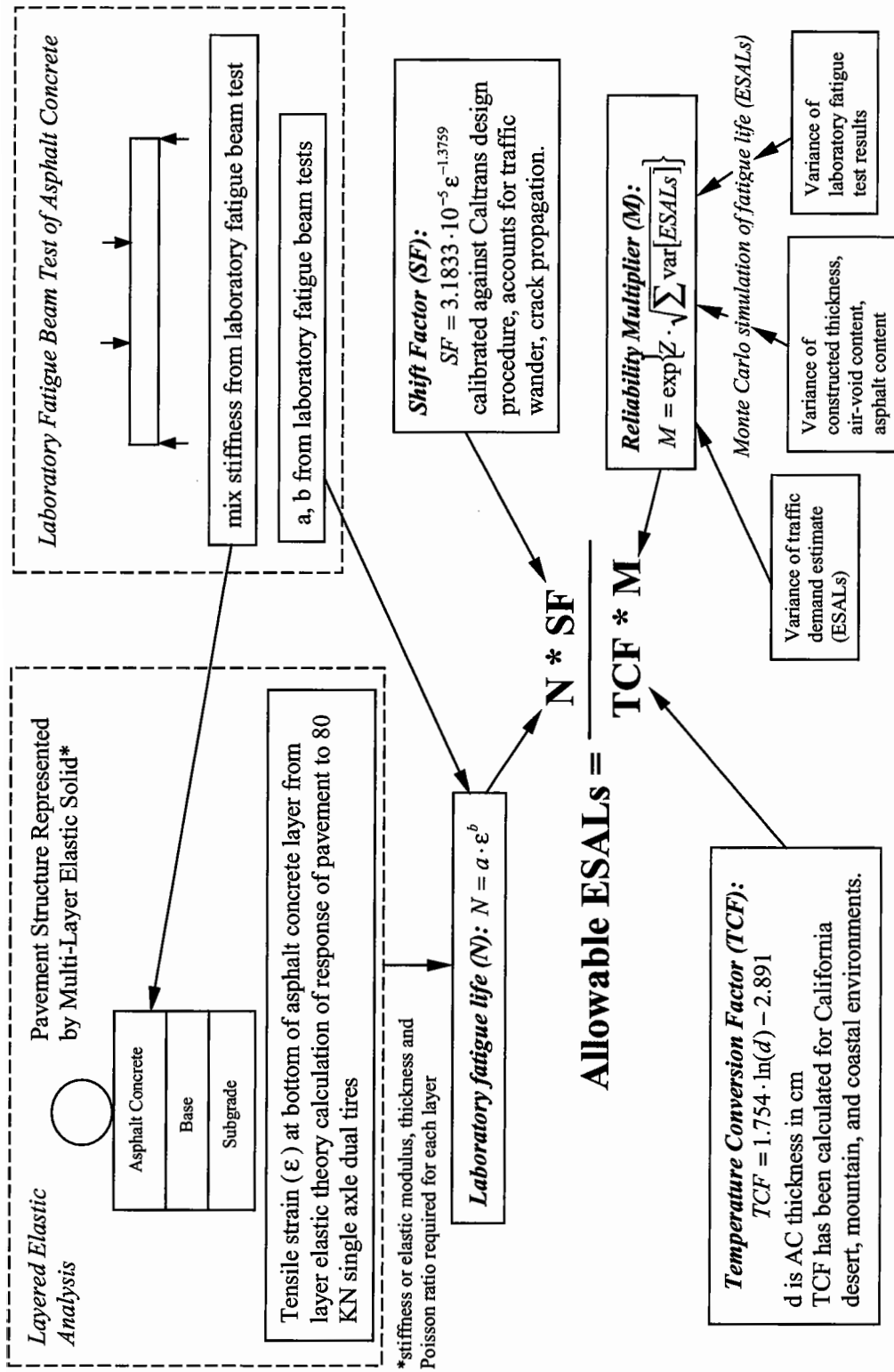


Figure 1.7. Methodology followed in the fatigue analysis system to determine ESALs (after Harvey 1997).

2.0 DATA SOURCES

In keeping with the objectives discussed in Chapter 1, a primary task is to integrate the laboratory fatigue test results with the condition survey and field data by introducing the Weibull dynamic approach as well as several correction factors to correct the effects caused by, for instance, traffic wander, temperature variation, and boundary conditions. To achieve this goal, it is necessary not only to incorporate the laboratory test results with the field data but also to ensure that the laboratory tests can cover the data range encountered in the field. Accordingly, the laboratory test plan put forth in the next chapter is such that the test results obtained can further extend the currently existing database. This database is briefly discussed in the paragraphs to follow, as well as the WesTrack project, CAL/APT HVS project, and the laboratory fatigue tests associated with each of these projects.

2.1 WesTrack Project

WesTrack was a \$15 million full scale accelerated pavement testing facility sponsored by the FHWA of the U.S. Department of Transportation and the National Cooperation Highway Research Program (NCHRP), located approximately 100 kilometers southeast of Reno, Nevada. The test pavements were designed and constructed from October of 1994 to October of 1995.

The main objectives of the WesTrack project were to define the effects of construction variability on the asphalt mix performance, to further expand the performance-related specifications of aggregate-asphalt mixes that had been developed in

the Strategic Highway Research Program (SHRP), and to validate the Superpave Mix Design method.

The papers and reports (e.g., WesTrack Team 1996, and Hand 1998) of the WesTrack project have been published and discussed in detail elsewhere. A brief summary of the WesTrack project is included here to provide a background understanding for the prediction of fatigue performance based on the Miner's hypothesis and the Weibull dynamic approach presented in Chapters 6 and 7.

2.1.1 Track Characteristics

A 2.9-km oval track, constructed in November of 1995, consists of 26 test sections, as seen in Figure 2.1. As stated above, one of the objectives of WesTrack was to assess the construction variability of binder content, gradation, and density on performance using mixes designed according to the Superpave mix design system. To achieve this goal, mixes of three different aggregate gradations, termed coarse, fine, and fine-plus, each with three asphalt contents and air-void contents were arranged at various locations of track. Sections 5, 6, 7, 8, 23, 24, 25, and 26 were coarse mixes, sections 1, 2, 3, 4, 14, 15, 16, 17, and 18 were the fine mixes, and sections 9, 10, 11, 12, 13, 19, 20, 21, 22 were the fine-plus mixes.

The pavement structure for these 26 original sections was all the same, consisting of an asphalt concrete layer of 6 inches (150 mm), a base layer of 12 inches (304 mm), and a subgrade layer. This identical pavement structure of the original WesTrack sections made it impossible to investigate the effect of pavement thickness on the fatigue

performance. Because of failures, 9 sections were replaced in June 1997. However, only the originally constructed 26 sections are considered in the later simulation.

2.1.2 Mix Characteristics

The WesTrack coarse gradation was produced from partially crushed gravel and screenings. The WesTrack fine gradation was obtained from the same crushed material with additional local natural sands. The addition of 3 % of baghouse material, or material passing the 0.075 mm sieve, to the fine mix defined a fine-plus mix. All the mixes utilized a nominal maximum aggregate size of 19 mm and used an unmodified PG 64-22 binder. According to the American Association of State Highway and Transportation Officials (AASHTO) specification MP-1 (1996), the binder will have appropriate properties to a high temperature of 64 °C and a low temperature of -22 °C.

The individual gradation curves of WesTrack are shown in Figure 2.2, which plots the percent passing against the 0.45 power of sieve size. As seen in this figure, the fine and fine-plus curves are plotted above the Superpave restricted zone and the maximum density line; the coarse curve is plotted below the Superpave restricted zone and the maximum density line. Notice that the fine-plus gradation is almost parallel shifted upward from the fine gradation curve. The same grading information is also plotted in terms of percent passing against the logarithm of sieve size as illustrated in Figure 2.3.

The aggregate gradation in the Superpave specification is controlled by two criteria (1) the control points and (2) the restricted zone, as shown in Figure 2.2. The control points form the master range through which the proposed trial blends must pass.

It is recommended by the Superpave mix design method that the trial blends gradations not pass through the restricted zone to ensure that the trial blends do not have an excess of fine sand in relation to total sand. With these specifications, it is believed that a distribution of aggregate particle sizes can be developed to form a tough aggregate skeleton to resist rutting and maintain sufficient VMA (voids filled with aggregate) for durability.

2.1.3 Traffic

The trafficking load for the WesTrack project was generated by four autonomous (driverless) tractor/triple-trailer vehicles under an automated vehicle guidance system designed and installed in March 1996. For each truck, two two-single-axle trailers were towed and attached to a typical 3-axle tractor/single-axle semi-trailer, as shown in Figure 2.4. In addition to the 54 kN load of the steering axle, each axle carried 89 kN; as a consequence, it resulted in the application of 10.5 ESALs with each truck pass. The 295/75R22.5 truck tires were inflated to 700 kPa (100 psi). The speed of the trucks was maintained at 64 kilometer per hour or 40 miles per hour. Ten million 80 kN (18 kips) equivalent single axle loads (ESAL) were planned to be applied to the pavements in two years; accordingly, the WesTrack pavement structure was designed to serve this requirement.

The trafficking load of WesTrack was applied at 11 wander positions designated as 5L, 4L, 3L, 2L, 1L, CENTER, 1R, 2R, 3R, 4R, and 5R, where the “xL” stands for x inches to the left of central position and “yR” means y inches to the right of central position. In addition, a wander case named “OFF” was applied on the track at times. It

means that the truck guiding system was shut off and the truck was manually maneuvered. When the trafficking loads were documented as being applied in the “OFF” situation, it was considered that the traffic was evenly distributed over the 11 wander positions because no recorded data were available in finding the real wander distribution of the “OFF” situation.

Instead of using ESAL as a simulation base, the load repetitions of an 89 kN axle load, resulting in 5000 lb. for each tire in a dual-tire setup, will be utilized in the simulation of fatigue performance. For this purpose, it is necessary to convert the ESAL-based traffic data into a repetition-based traffic data. As visualized in Figure 2.5, from a mechanical point of view, the truck configuration can be categorized into three types of load configurations: namely one 54 kN steering axle (two tires per axle), a 89 kN per axle tandem axle (four tires per axle and two axles), and a 89 kN single axle (four tires per axle and one axle) with dual tires. After inspecting the tensile strain calculated by the ELSYM5 program when subjected to several environmental conditions, no distinct differences were perceived among the maximum tensile strains occurring at the bottom of the asphalt concrete layer for those three load configurations. The tandem is spaced enough to act like two singles. It was then decided to assume that the fatigue damage caused by each axle has the same effect. Since this truck configuration results in an application of 10.5 ESALs, a multiplication factor of 0.763 (8 axles divided by 10.5 ESALs) has been applied to convert the ESALs into load repetitions.

Inspection of the traffic data indicates that almost one-tenth of the traffic was applied on the track with very little wander, i.e., applied mostly at the central position. This is unrealistic as compared to normal highway trafficking. This traffic pattern was

later modified by author so as to evaluate the wander effect caused by this specific WesTrack traffic pattern. It was observed at WesTrack that, likely due to the radial tires of the trucks, once the initial deformation (or rutting) was established in the wheel path, the following trailers, instead of following the guiding cab vehicle, tended to follow the initial ruts. Therefore, there were differences between the “documented and well-controlled” traffic data and the actual trafficking. The traffic data was recorded hourly according to the wander positions that apply.

2.1.4 Temperature

Temperature sensors for WesTrack were installed in sections 12, 19, and 25, and temperatures were recorded hourly. For each section, there were 18 sensors installed below the surface; sensors 1 to 3 were placed in the AC layer at depths: 25.4, 76.2, and 127 mm, respectively. Another fifteen sensors were also placed at spacing of 18, 94, 172, 246, 322, 476, 627, 782, 933, 1087, 1240, 1392, 1544, 1696, and 1847 mm below the top of the base layer. It is the temperatures in the asphalt concrete layer that are of primary interest for this study. The pavement temperatures at 50 mm were obtained by interpolating the temperatures of sensors 1 and 2; the pavement temperatures at 150 mm were calculated by extrapolating from the temperatures of sensors 2 and 3. The temperature gradient, g , was defined based on the temperatures at these two depths and is expressed as $g = \frac{T_{50} - T_{150}}{100}$. It was found that the temperatures recorded from section

19 deviated somewhat from those recorded at sections 12 and 25. As the temperatures obtained from sections 12 and 25 were reasonably consistent, the representative pavement temperatures for WesTrack were determined utilizing the average temperatures

of sections 12 and 25. An input file containing the pavement temperatures at 50 mm and 150 mm and the induced temperature gradients was utilized in the *Weibull* program to predict the fatigue performance as described later.

2.2 CAL/APT HVS Project

Since 1995, the California Department of Transportation (Caltrans) Accelerated Pavement Testing Program (CAL/APT) has used the Heavy Vehicle Simulator (HVS) system technology, both in a controlled experimental setting at the University of California at Berkeley's Richmond Field Station (RFS) and on selected field sites throughout California.

The primary intent to using the data from the CAL/APT HVS project is to verify the feasibility of applying the Weibull accelerated failure time model (described in Chapter 5) to estimate the correction factor caused by the differences of boundary conditions between laboratory tested specimens and asphalt pavement in the field. For this study a back-calculation algorithm utilizing data from multi-depth deflectometer (MDD) measurements at Section 503RF was adopted to estimate stiffness deterioration with trafficking.

2.2.1 503RF Section

Section 503RF was the fourth of four pavement test sections as part of Goal 1 of the CAL/APT Strategic Plan (Caltrans 1995); this section as well as the other three were designed and constructed according to Caltrans procedures. Section 503RF was a full-

scale pavement containing an asphalt concrete pavement with a conventional aggregate base and was tested with the HVS at the RFS.

The primary objective of the Section 503RF test was to quantitatively verify Caltrans' existing design methodology for the conventional aggregate base pavement pertinent to failure under repetitive trafficking at a moderate temperature, which was maintained at a level of $20 \pm 3^\circ\text{C}$ at the pavement surface. Thermocouples were utilized to record air and pavement temperatures; their installation positions are shown in Figure 2.6.

The pavement structure of Section 503RF, as seen in Figure 2.6, was designed to follow the specification of Caltrans procedures (Caltrans 1991), containing a dense-graded asphalt concrete surface, an untreated aggregate base and subbase and a clay subgrade. The design layer thicknesses of Section 503RF were 137 mm for asphalt concrete, 274 mm for aggregate base, and 229 mm for the aggregate subbase. It was found, however, from a few cores that the as-built thicknesses of the asphalt concrete layer and aggregate subbase were 162 mm and 305 mm respectively. Accordingly the layer thicknesses used in the verification of the Weibull accelerated failure time model are those actually measured.

2.2.2 Trafficking Plan

The HVS trafficking of Section 503RF was started in March 1996 and completed in September 1996 with a total of more than 1.91×10^6 load repetitions. The trafficking plan of Section 503RF was conducted in three stages. A dual-wheel load of 40 kN was applied for the first 150,000 repetitions to avoid excessive initial deformation. In the

second stage, a dual-wheel load of 80 kN was applied for 50,000 repetitions. After this, the dual-wheel load was increased to 100 kN and maintained at this level for the rest of test to accelerate pavement cracking. The HVS was programmed to simulate the wander over 1 m width as happens on a normal highway with the bias-ply truck tires inflated to a pressure of 690 kPa (100 psi). Trafficking was bi-directional as opposed to uni-directional at WesTrack and in the field.

2.2.3 Multi-Depth Deflectometer (MDD)

The MDD is a device that can measure both elastic deformation and permanent deformation in the pavement. It consists of several Linear Variable Differential Transducers (LVDT) installed at various depths of pavement.

Generally, the MDD system can be summarized in two aspects:

1. the LVDT module has a special housing that can be tightly attached and integrated with the pavement as a whole, i.e., any movement of pavement is exactly what the LVDT module “feels”; and
2. an anchor system is installed at a minimum depth of 3 meters and forms a rigidly fixed reference system, which serves as a reference point for the movement of the LVDT modules. In other words, the movement of pavement (or the reading of LVDT modules) is measured relatively to the anchor.

Figures 2.8 and 2.9 show photos of the LVDT module and the anchor respectively. More detailed information on the MDD can be found in “Guideline to the Use and Operation of the Heavy Vehicle Simulator (HVS)” (CSIR 1995). The

installation depths of Section 503RF are shown in Figure 2.6. The MDD data from MDD 4 (Figure 2.7) was utilized to back-calculate the stiffness.

2.3 Laboratory Test Data

The currently existing database of laboratory flexural fatigue beam testing of WesTrack consists of 151 fatigue tests at 20°C and a total of 35 test results from temperature susceptibility fatigue tests at various temperatures (5°C, 20°C, and 30°C). Tables A.4.1 and A.4.2 list the pertinent details of mix information and the test results. All these test beams were sawed from the field-mixed and field-compacted slabs from various original test sections (sections 1 through 26) of WesTrack prior to trafficking.

As for the CAL/APT HVS project, in addition to the field collected MDD data, a small set of laboratory fatigue tests with the same mixes (field-mixed and field-compacted) have been utilized to verify the feasibility of the Weibull accelerated failure time model.

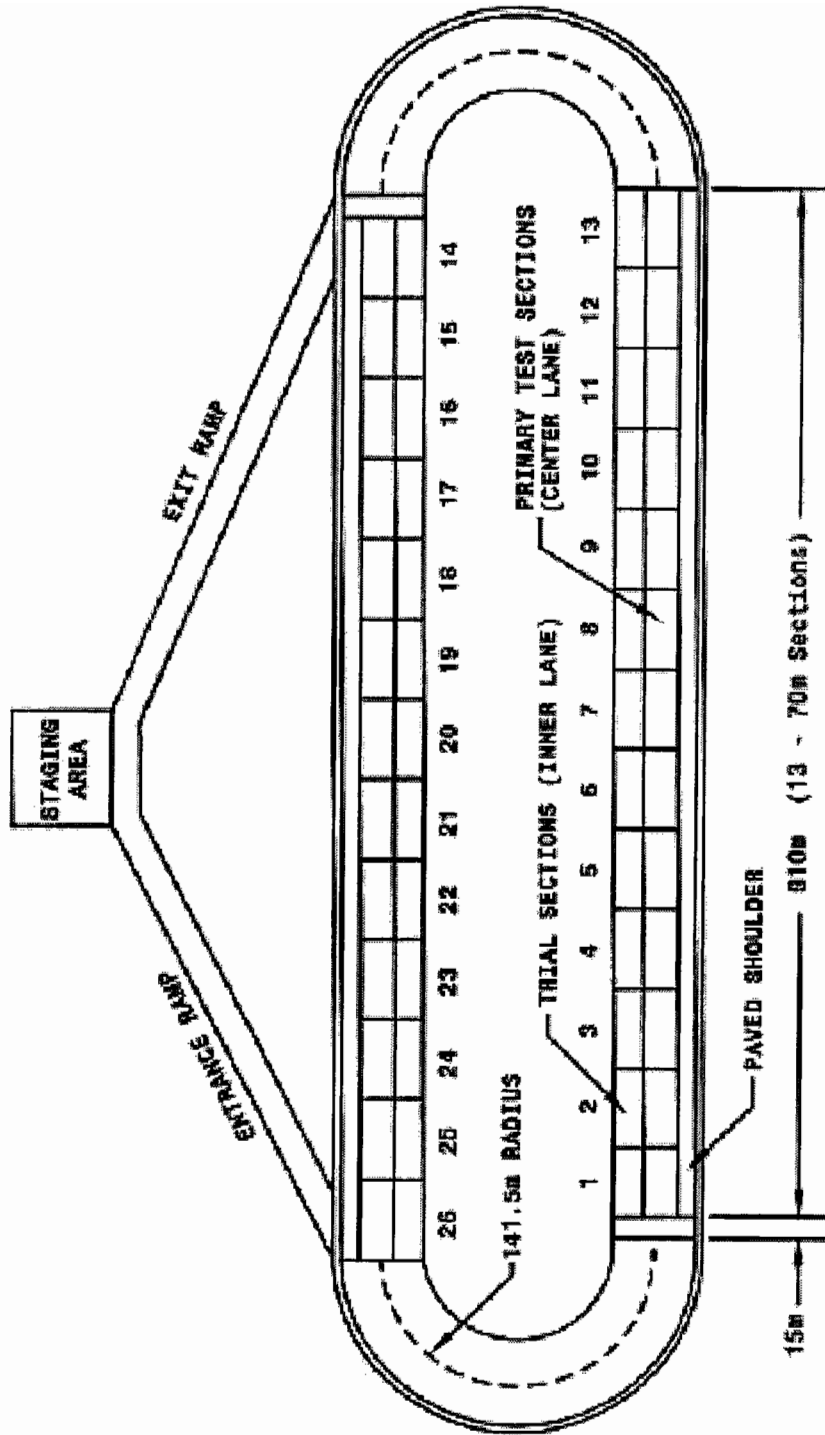


Figure 2.1.1. Layout of WesTrack test track (not to scale).

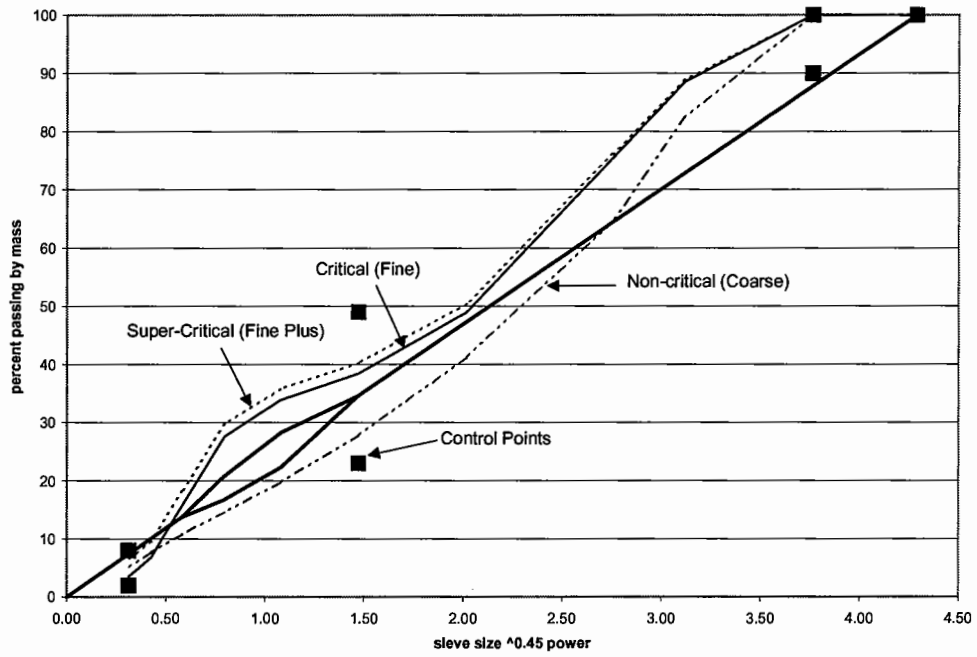


Figure 2.2. Individual WesTrack gradation curves on a 19 mm nominal size 0.45 power chart.

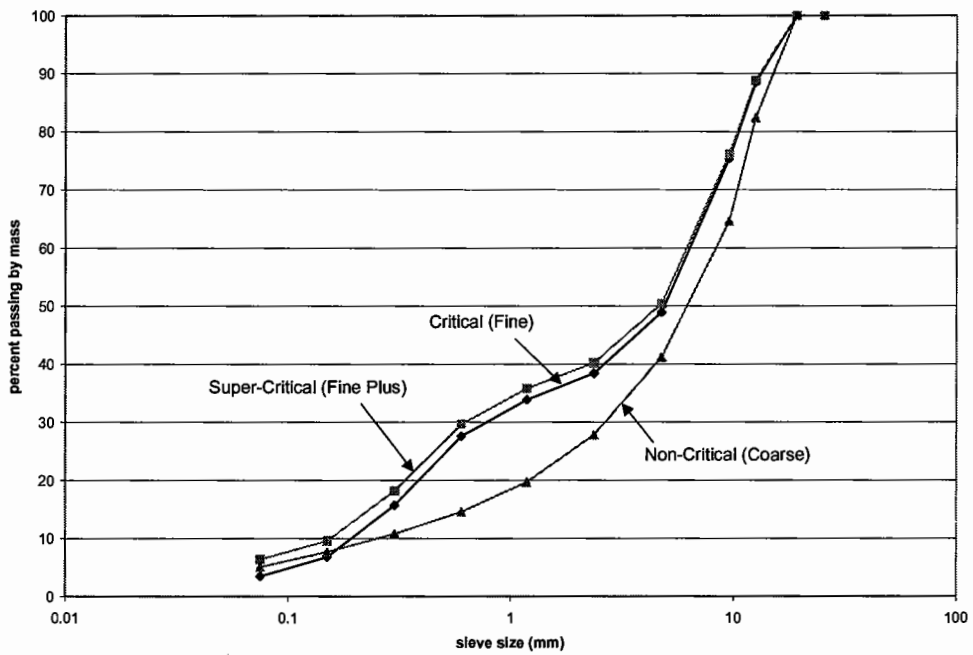


Figure 2.3. Individual WesTrack gradation curves on a semi-logarithm chart.

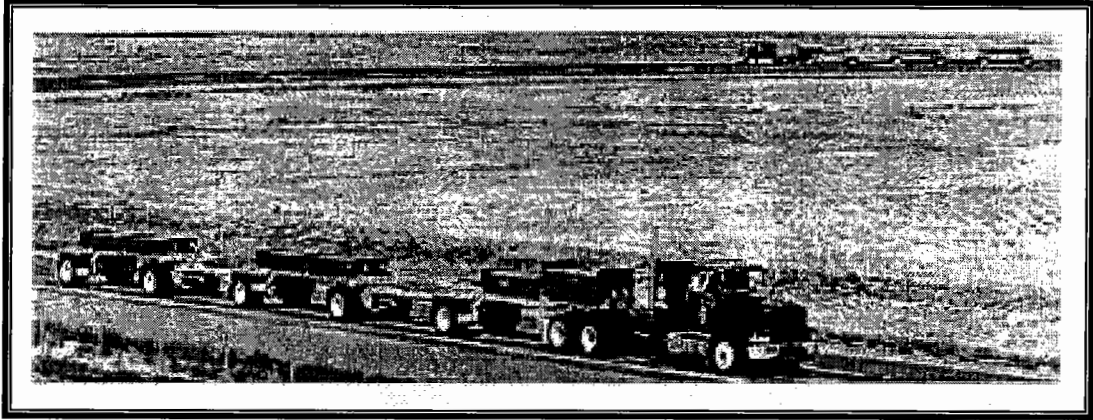


Figure 2.4. Driverless triple-trailer test trucks.

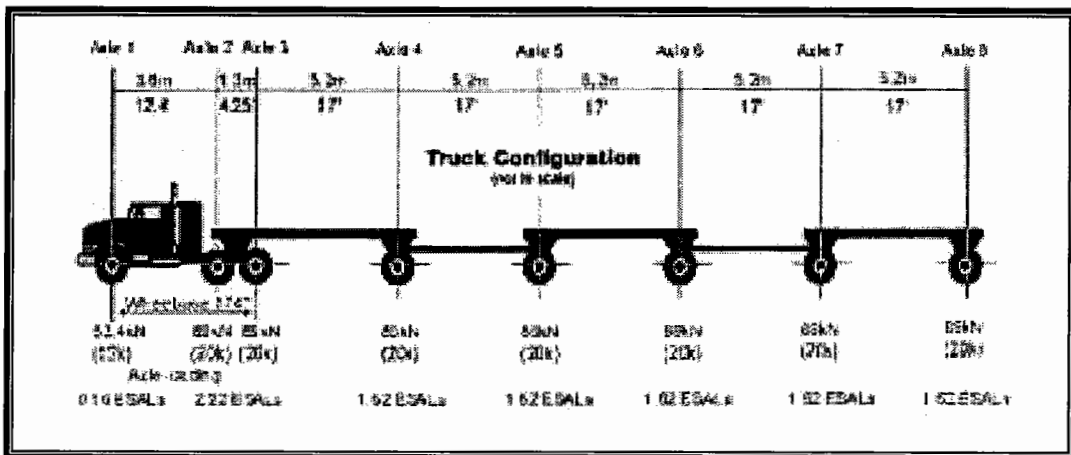


Figure 2.5. Tractor/trailer configuration.

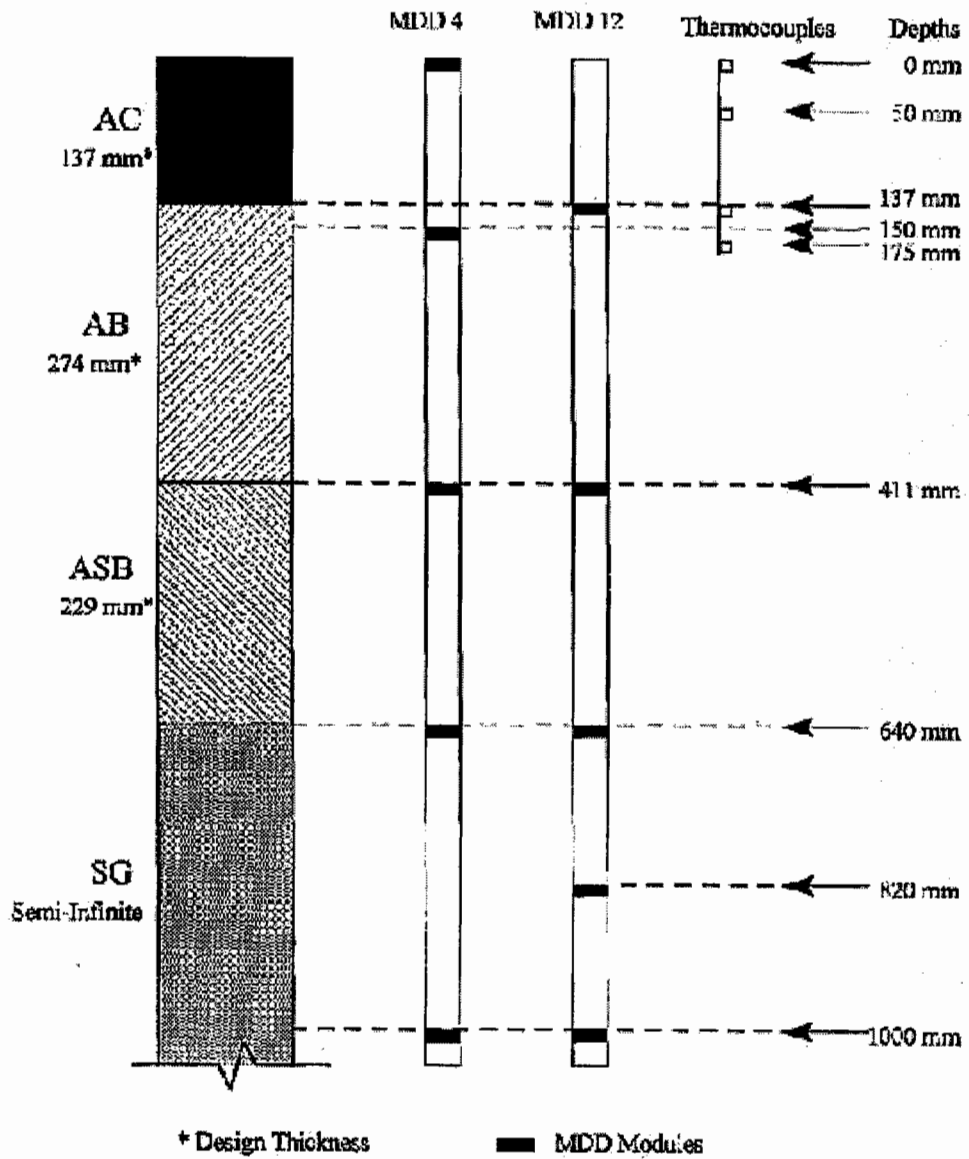


Figure 2.6. 503RF pavement structure with MDD and thermocouple positioning (after Harvey 1997).

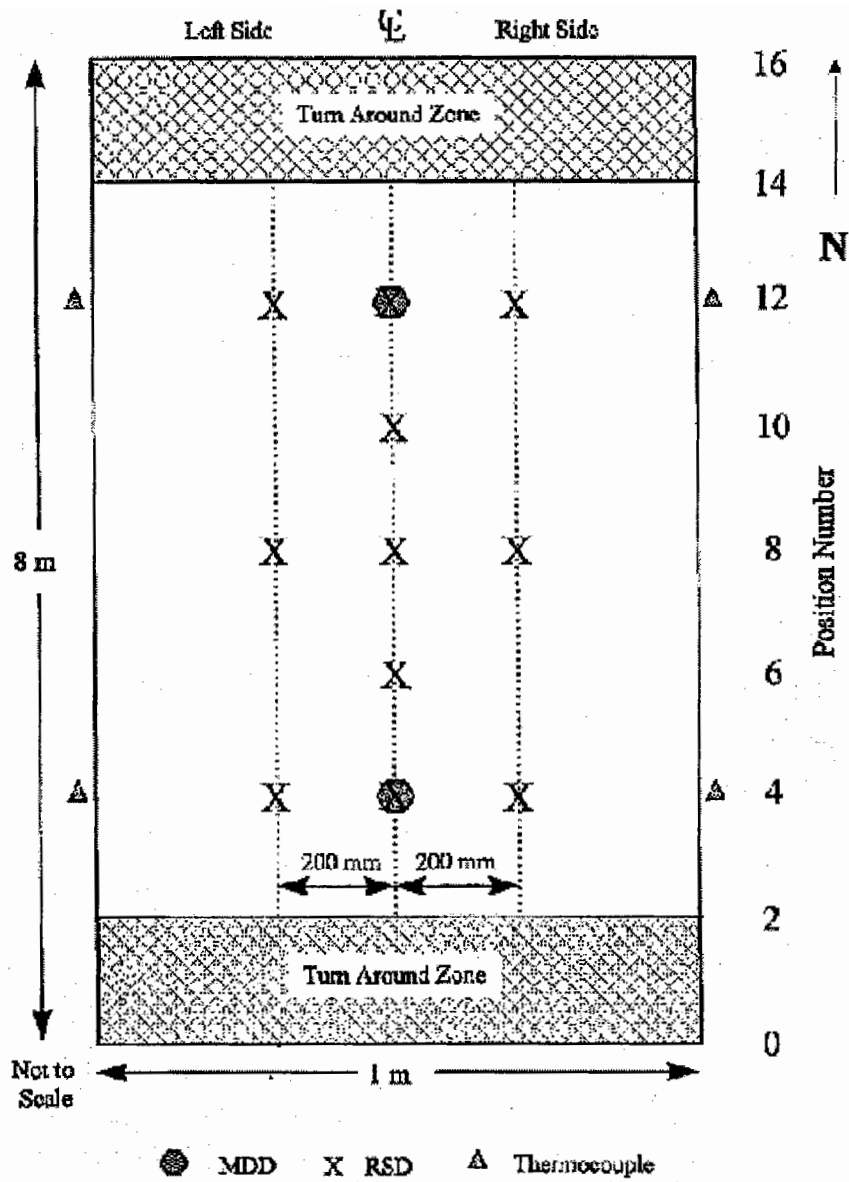


Figure 2.7. Plan view of test section and location of instruments for data collection (after Harvey 1997).

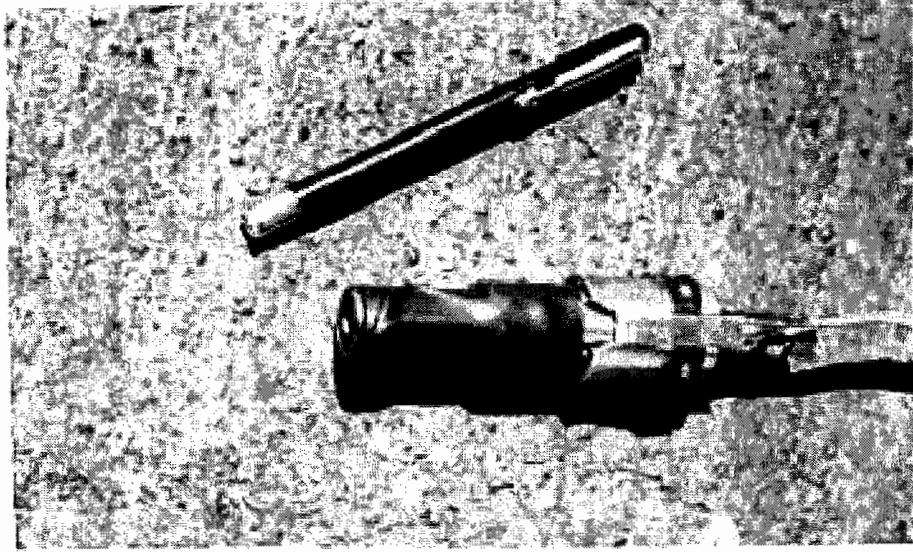


Figure 2.8. LVDT module of MDD (after CSIR.).

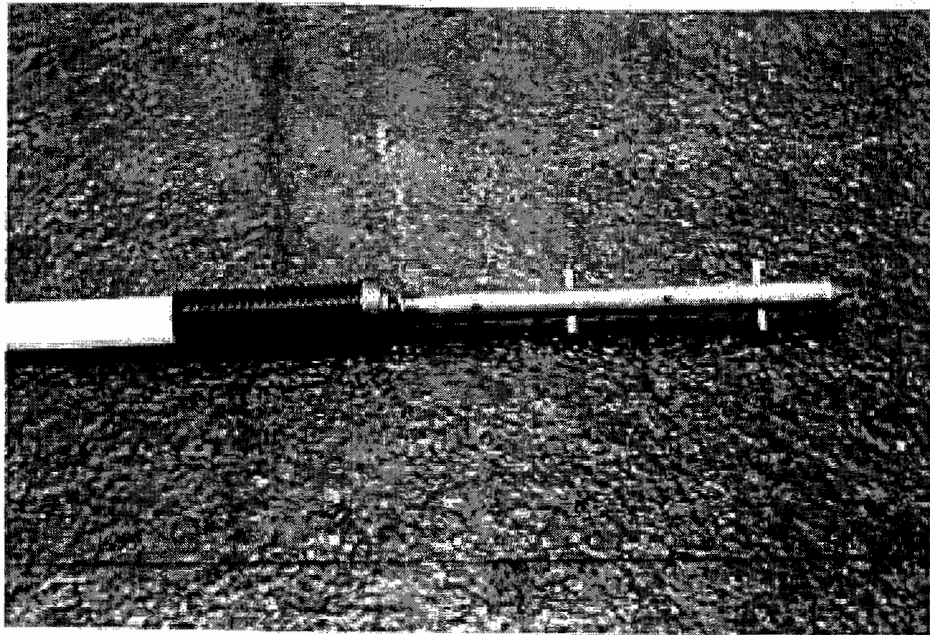


Figure 2.9. Anchor assembly of the MDD installation set in concrete at depth of about 4 meters (after CSIR.).

3.0 TEST PLAN, SPECIMEN PREPARATION, AND TEST SETUP

3.1 Test Purpose

The questions raised in Chapter 1: “Is high temperature fatigue an important problem?” and, “How does temperature affect the fatigue damage process?” motivated this study of how to use laboratory fatigue test results to predict the in situ fatigue performance. To accomplish this, a test plan with various experiments was necessary.

The objectives of the test plan for this thesis are to:

1. Investigate the effects on fatigue damage and cracking of temperature, including temperatures greater than 30°C as well as the effects of tensile strain levels, and the effects of traffic repetitions.
2. Validate the stiffness deterioration hypothesis postulated in the Weibull dynamic approach and the corresponding relationship of stiffness deterioration with loading frequency, strain level, and temperature, and,
3. Assess the feasibility of applying the Weibull dynamic approach to long term fatigue performance prediction.

To achieve the test plan objectives, a modified flexural fatigue test setup was proposed to overcome the problems encountered at high temperatures with a conventional flexural fatigue test setup. In the following paragraphs, the modified flexural fatigue test setup and its related instrumentation and data acquisition system are discussed. Before discussing any specific test types, the specimen preparation procedure as well as the gradations used in the test plan are presented.

3.2 Test Setup

It has long been recognized that test temperatures greater than 30°C are a restricted zone for a conventional flexural controlled-strain fatigue test. The viscoelastic properties of asphalt concrete at high temperatures produce practical difficulties to installing the test specimen and running the test with a four-point flexural controlled-strain fatigue beam setup. As a result of these practical difficulties, no reliable laboratory fatigue data were collected at high temperatures by the WesTrack project. Consequently, an inaccurate prediction of fatigue performance is unavoidable when the extrapolation of the fatigue performance without the information in this restricted zone is applied. In light of this, before any further exploration of high temperature fatigue behavior or discussion of the Weibull dynamic approach, overcoming the limitations of the test setup at high temperature becomes the first priority. The difference between the conventional and modified flexural fatigue setups is briefly discussed here. The instrumentation and data acquisition systems of both setups are also explained.

3.2.1 Conventional Flexural Controlled-Strain Fatigue Test Setup

The conventional flexural controlled-strain fatigue test is a four-point bending test and is usually conducted at a temperature ranging from 0°C to 30°C. It is believed that within this range the asphalt concrete beam behaves like a viscoelastic material but with sufficient stiffness to support beam for test duration within a limited strain range of interest and linear relation of deformation and load. Therefore, the desired test strain level can be achieved by controlling the maximum deformation based on the elastic beam

theory. However, this calculated strain level is an assumed strain under the elastic beam theory. Strictly speaking, instead of calling it a “controlled-strain” fatigue test, it should more accurately be called a “controlled-deformation” fatigue test. One of the advantages of the four-point bending fatigue test is that the middle one-third part of the beam is theoretically subjected to ‘pure’ bending without any shear deformation. The conventionally used accelerated fatigue test machine, shown in Figure 3.1, was developed by the SHRP A-003 project.

3.2.2 Modified Flexural Controlled-Strain Fatigue Test Setup

In this thesis the terms “modified fatigue test setup” and “conventional fatigue test setup” are used to differentiate the two setups. The modified flexural controlled-strain fatigue test setup deviates from the conventional setup in three aspects. First, an aluminum (type 6061-T6) support is placed below the specimen to prevent the creep effect from occurring due to specimen self-weight while subjected to high temperatures. A thin TEFLON™ sheet between the two provides a virtually frictionless interface. The aluminum support should be stiff enough to withstand the weight of a test beam.

Second, instead of being sinusoidally bent downward, the modified setup bends the beam upward; otherwise the test could not induce any tension and therefore no cracking. Third, another deviation from the conventional test setup is that, instead of utilizing LVDTs to control the tensile strain level, the modified flexural fatigue beam test is controlled by a strain gage that is attached on the extreme tensile surface of the asphalt concrete.

Figure 3.2 is a schematic plot showing the differences between the modified and conventional flexural fatigue setups. As can be visualized in Figure 3.2a, the conventional test setup bends the asphalt concrete beam downward to a position that generates the designed tensile strain at the bottom surface of the beam and then returns it to its original position following a sinusoidal-wave deformation control shifted so that a peak of the sinusoidal-wave is the original unloaded position. In Figure 3.2b, the modified test setup bends the beam upward to a position that generates a desired tensile strain at the top surface of the beam and then returns it to its original position following a sinusoidal-wave strain control, directly controlled by the strain gage.

The reason for developing the modified flexural controlled-strain fatigue test is mainly to conduct high temperature fatigue tests at 40°C. Having devised a setup, a temporary temperature control unit was subsequently built. The test machine along with the temperature control unit is shown in Figure 3.3. Inside the temperature control box, a heating element was placed at the back of the fatigue module to generate enough heat to maintain the desired temperature. Three fans were installed in the box to ensure good air circulation and a uniform temperature; as shown in Figure 3.4, two fans hang at the back and one is seated in the front. Notice that in Figure 3.4 the aluminum support can be seen just underneath the beam. A side view of the setup, without the side panels of the temperature box in place, is shown in Figure 3.5. A closer side view of the LVDT and the aluminum support is shown in Figure 3.6.

3.2.3 Instrumentation and Data Acquisition System

One deviation separating the conventional setup from the modified setup is that the modified setup utilizes a strain gage to control the tensile strain rather than using LVDT control. Figure 3.7 shows the strain gages attached to both the aluminum support and the asphalt concrete beam. Two long strain gages, EA-06-20CBW-120/option w from Measurements Group, Inc., with a gage length of 50.80 mm are separately attached to the top and bottom of the asphalt beam using the M-Bond AE-10 adhesive kit (also from Measurements Group, Inc.). The placement of these long strain gages is dependent upon the roughness of the asphalt concrete surface and also the extent to which their wires will interfere with the test setup. Ideally, if possible, the strain gages should be affixed to the top and bottom surfaces and aligned centrally in both the lengthwise and widthwise directions. However, this is not the case usually encountered, for oftentimes roughness or cavities are present on the surface of the beam. Therefore, most of the time the center position along the lengthwise direction can be maintained but the position along the widthwise direction must be adjusted to avoid the cavities or the interference of wires. It is usual to have to affix the bottom strain gage close to the edge to avoid the wires' interference. To ensure the quality and durability of gluing, an appropriate clamping pressure must be applied during the curing stage of gluing. The strain gages on the asphalt concrete are approximately two times longer than the maximum aggregate size in the mix.

Two short strain gages, EA-06-250BG-120/option p from Measurements Group, Inc., with a gage length of 6.35 mm are placed on surfaces of the aluminum plate with an instant glue, CN-E cyanoacrylate adhesive from Tokyo Sokki Kenkyujo Co., which is an instant-type glue that will bond in roughly 2 minutes with only finger-tight pressure on

the glued elements needed. Since the surfaces of the aluminum support are very smooth, the bottom strain gage was glued in the central position at both directions; the top strain gage, next to the TEFLON™ sheet, was placed in the center of the lengthwise direction and close to the edge in a widthwise direction.

The strain gage on top of the asphalt concrete beam is utilized as the command channel in a closed-loop control system, namely the Automated Testing System (ATS) from the SHRP Equipment Co. The rest of strain gages are utilized as the monitoring channels so that it is possible to analyze the mechanics of this fatigue setup. In addition to the strain gages, a conventional LVDT is still used to monitor the deflection of the beam, and the load cell reading is recorded as usual. The temperature is controlled but not recorded. A Wheatstone bridge, as seen in Figure 3.8, was connected between the signal conditioner and strain gage to amplify the signal. Figure 3.9 illustrates the locations of strain gages and gives detailed dimensions of the asphalt concrete beam, TEFLON™ sheet, and aluminum support.

3.3 Specimen Preparation

3.3.1 Gradation Curves of WesTrack

The individual gradation curves used for the original WesTrack mixes, namely coarse, fine, and fine-plus, have been described in Chapter 2. The same mixes were used in the preparation of test beams so as to extend the existing database of WesTrack for use in this study. In addition to the original WesTrack mixes, several gradation curves were selected to estimate the gradation variability. Two additional gradation curves,

designated as coarse high (CH) and coarse low (CL), based on the original WesTrack coarse gradation (coarse medium, CM), were created by shifting the CM gradation upward and downward as depicted in Figures 3.10 and 3.11. The other two gradation curves, designated as fine high (FH) and fine low (FL), based on the original WesTrack fine gradation (fine medium, FM), were generated by moving the FM gradation up and down as depicted in Figures 3.12 and 3.13. The corresponding percentage passing information is listed in Table 3.1.

3.3.2 Procedure of Specimen Preparation for WesTrack

In general, the specimen preparation for WesTrack consisted of sieving, wet sieving, batching, mixing, rolling, cutting and air-voiding. Each activity is described briefly below.

- Sieving:

Five different bins were received: ¾", ½", 3/8", Wadsworth sand, and Rockdust. Each was oven dried prior to sieving. Then, each bin was individually sieved and stored in buckets by sieve size. Later the sieved aggregate were combined to meet the batching criteria for various gradation requirements.

- Wet sieving:

The purpose of this activity is to verify whether the batched gradation matches the designed gradation. The test standards utilized are ASTM C117 (wet sieve analysis) and ASTM C136 (dry sieve analysis). In this study, six gradations were chosen for the

laboratory-mixed and laboratory-compacted mixes. They are CH, CM, CL, FH, FM, and FL. The coarse gradations were composed of material from the ¾", ½", and rock dust bins. The fine gradations consisted of material from all five bins.

- **Batching:**

Once the composition percentage was set from the wet sieving results, a 7-kilogram batch was prepared for each of the six gradations.

- **Mixing:**

Prior to mixing with binder, hydrated lime was added to the aggregate blends. The hydrated lime was used in the WesTrack project to prevent the stripping of mixes. Before placing 1.5 % hydrated lime by weight of aggregate into the aggregate blend, the aggregate blend was thoroughly mixed with 2 % to 5 % water by weight of aggregate. After mixing of the hydrated lime, the mix was then placed in the oven overnight to remove the water introduced during the mixing phase.

In order to obtain a homogeneous mix of aggregate blend and asphalt binder, it is necessary to heat up both materials before mixing. The aggregate blend with the hydrated lime was heated at 144 °C for four hours and the asphalt binder for at least two hours or until the asphalt binder became consistent and workable enough to stir. The suitable amount of asphalt binder was then poured into the heated aggregate and hydrated lime blend. The mixing time is 5 minutes or until the aggregate is completely covered with asphalt binder. It should be noted that the mixing bowl and blades should be pre-heated with infrared heat lamps to avoid sticking.

- Rolling:

The purpose of rolling is to reach the desired air-void content by pouring a certain mass of loose mix into a certain volume ingot and then compacting it with passes of the rolling wheel until the desired volume for the specimen is obtained. Prior to compaction, the mix is placed in the oven at 135°C for four hours for the short-term oven aging process. After the four hours' curing time, the temperature was raised to its compaction temperature of 138°C for two to four hours. At the same time the compaction molds are being heated with infrared heat lamps. Before being poured into the molds, the loose mix is weighed carefully to achieve the desired mass and therefore the desired air-void content.

Half of the loose mix is poured into the ingot and tamped with a rod; the other half is placed on top of the first half and tamped with a rod in the same way. The rolling wheel then starts to roll over the mix in such a way that the center of the wheel is directly over the mix. This is done ten times. The next ten compaction passes are conducted such that the left edge of the rolling wheel runs over the center of the mix. After those ten passes, another ten are applied to the center. The following ten passes are performed such that the right edge of the rolling wheel runs over the center of the mix. Then ten more passes are applied at the center. This sequence of passes is repeated until the surface of the mix is flush with the surface of the platform. After finishing compaction, the ingot is left in place overnight to allow it to cool.

- Cutting:

A circular masonry bit saw is used to cut the ingot into fatigue beams. The dimensions of beam specimens are 50.8 mm (2 inch) in height, 63.5 mm (2.5 inch) in width, and 381 mm (15 inch) in length.

- **Air-voiding:**

This is the final activity to take place before any testing starts. The procedure followed is that of “Procedure—Bulk Specific Gravity of Compacted Bituminous Mixtures Using Parafilm-Coated Specimens” from Chevron Research Company (Del Valle 1985). Prior to testing, all specimens are weighed in water and in air for the air-void measurement. Specimens are first soaked in 25 °C water and then dried with compressed air to a saturated surface dry (SSD) state. The weight in air is then recorded. Parafilm is used to wrap the specimen and its weight is taken in air. Then the weight of the specimen with parafilm is recorded in water and finally the parafilm is removed to record the weight of specimen in water.

3.4 Test Plan

Once the goal has been determined, the specimens can accordingly be prepared following the aforementioned preparation procedure. Generally, all beams tested here have the original WesTrack gradations, the same binder, PG64-22, and the same aggregate sources. Based on the objectives of the test plan mentioned above, a series of various types of flexural fatigue tests were subsequently designed and conducted as listed in Table 3.2.

3.4.1 High Temperature Modified Flexural Controlled-Strain Fatigue Test

This test was designed to be a full factorial experiment with four factors each at two levels. The four factors were air-void content, aggregate gradation, test temperature, and strain level. The two levels for air-void content are $6.6 \pm 1\%$ and $11.2 \pm 1\%$, coarse medium and fines medium for gradation, 30°C and 40°C for test temperature, and 200 and 400 microstrain for test strain level. The total number of tests run was 16 (2^4) with no replicates. With this additional information at temperatures 30°C and 40°C , the test database was used to investigate the fatigue behavior of asphalt concrete at high temperatures and the use of the Weibull proportional hazards model. The test setup utilized herein is the modified fatigue test setup with a loading frequency of 10 Hz.

The theoretical derivation of the high temperature flexural controlled-strain fatigue test is based on the flexural beam analysis with aluminum support which is included in Appendix C. The analysis described in Appendix C is used to calculate the tensile complex modulus of asphalt concrete and thus monitor its stiffness deterioration process at high temperatures.

This set of test data was conjugated with the available WesTrack temperature susceptibility data (Appendix A: Table A.4.1 to Table A.4.4) to derive an integrated regression equation to represent the fatigue damage process while subjected to various testing conditions.

3.4.2 Temperature Susceptibility Fatigue Test with Conventional Setup

The purpose of this test was to extend the database of temperature susceptibility fatigue behavior of WesTrack mixes with the laboratory-mixed and laboratory-

compacted specimens. This test consisted of 24 beams with two gradation types (CM and FM), two asphalt contents (5.7 % and 5.4 %), three temperatures (5 °C , 20 °C , and 30 °C), and two strain levels (200 and 400 microstrain). The test setup utilized was the conventional fatigue test setup with a loading frequency of 10 Hz.

3.4.3 Fatigue Test with Various Gradation Types

This is a test to verify the fatigue performance difference caused by various gradation types. A total of 16 specimens were tested. Four aforementioned gradation types designated as CL, CH, FL, and FH were used in the test. There were four beams of each gradation type of which two were tested at one strain level (300 microstrain) and two at another strain level (500 microstrain). Note that there was one replicate per gradation per strain. The gradation types CL and CH have a 5.7 % asphalt content; FL and FH have a 5.4 % asphalt content. All tests were conducted at a temperature of 20 °C , with a 10 Hz loading frequency, and using the conventional fatigue setup. For purposes of statistical analysis, another 8 test results (four tests of CM and four tests of FM) at 20 °C from the temperature susceptibility fatigue test for laboratory-mixed and laboratory-compacted specimens are included, although the test strain levels are different.

3.4.4 Flexural Frequency Sweep Test

The objectives of conducting a flexural frequency sweep test are threefold:

1. to explore the relationship of loading frequency (or loading time) and the complex modulus of asphalt concrete while subjected to various temperatures,

2. to verify the feasibility of using strain gages in calculating the stiffness at high temperatures,
3. and to explore the possibility of integrating the results into the simulation program to characterize asphalt concrete stiffness under different vehicle speeds.

The loading frequencies utilized in this study are 15, 10, 5, 2, 1, 0.5, 0.2, 0.1, 0.05, 0.02, and 0.01 Hz. The 15 Hz upper limit is a constraint imposed by the capabilities of the test machine. The temperatures 40°C, 30°C, and 20°C were applied sequentially for the modified fatigue test setup, and 30°C, 20°C, and 5°C for the conventional fatigue test setup. The general principles for conducting frequency sweep tests are "Quick to Slow in loading frequency and Hot to Cold in temperature" to minimize damage to the specimen. The number of repetitions applied varies with loading frequency and ranges from 5 periods for 0.01 Hz to 300 periods for 15 Hz so as to obtain a stable measurement.

For the conventional fatigue test setup, the test is controlled by the LVDT to a deflection level that can generate 300 microstrain at the bottom surface of the asphalt concrete, whereas, for the modified fatigue test setup, the tensile strain is directly controlled by the strain gage at a 300 microstrain level. However, for the conventional fatigue test setup, the tensile strain occurring at the extreme fiber of the asphalt concrete will also be monitored by strain gages.

In addition to shedding light on the relationship among loading frequencies, complex moduli, and temperatures, another intent of conducting this test was to verify

whether the test results obtained from the modified fatigue test setup match the results obtained from using the conventional fatigue test setup, especially at the common temperatures of 20 °C and 30 °C. Since thorough comprehension of complex moduli versus various temperatures and loading frequencies is not a major concern of this project, only a few beams were set aside for this type of test. To wit, four beams with the same asphalt content (5.7 %), similar air-void content (around 9 %), and with two gradations (WesTrack fine and coarse gradations) were used.

3.4.5 Varied-Strain Fatigue Test

The purpose of this experiment is to explore the behavior of fatigue damage under various patterns of strain levels and investigate the applicability of the wander effect of tires to fatigue life. These goals were to be achieved by using four varied-strain fatigue tests, consisting of a 200, 400, and 200 microstrain test, a 400, 200, and 400 microstrain test, a 400 and 200 microstrain test, and a 200 and 400 microstrain test. These tests will be referred to, respectively, as the 200-400-200 test, the 400-200-400 test, the 400-200 test and the 200-400 test. The 200-400-200 and 400-200-400 tests had two replicates, whereas the 400-200 and 200-400 tests had only one replicate because of the limited number of test beams. All these tests were conducted at 20 °C in a conventional fatigue setup with a 10 Hz loading frequency. The mix used here is coarse medium with an air-void content of 6.6 ± 1 % and an asphalt content of 5.7 %.

3.4.6 Varied-Temperature Fatigue Test

To explore the relationship between initial stiffness and the fatigue damage process is the major concern of this experiment's design. It is recognized that the stiffness of asphalt concrete varies with the change of temperature. Thus, in this experiment design, two temperatures, 20°C and 30°C, were selected to represent the change of temperature. To simplify the number of factors, only one strain level (200 microstrain) was used. The varied-temperature fatigue tests consisted of,

1. a 30°C, 20°C, and 30°C test,
2. a 20°C, 30°C, and 20°C test,
3. a 30°C and 20°C test, and
4. a 20°C and 30°C test.

These tests will be hereafter referred to, respectively, as the 30-20-30 test, the 20-30-20 test, the 30-20 test, and the 20-30 test. The 30-20-30 tests had two replicates. The 30-20 and 20-30 tests had only one replicate. All these tests were conducted at a 400 microstrain level with a 10 Hz loading frequency. The mix used here was coarse medium with an air-void content of 6.6 ± 1 % and an asphalt content of 5.7 %.

Table 3.1. WesTrack original construction gradations and laboratory-mixed and laboratory-compacted gradations.

Sieve Size		WesTrack Target Gradations			WesTrack Lab-mixed and Lab-compacted Gradations					
		Fine	Fine-plus	Coarse	CL	CM	CH	FL	FM	FH
(US)	(mm)									
1"	25.4	100.0	100.0	100.0	100.0	100.0	100.0	100.0	100.0	100.0
3/4"	19.0	100.0	100.0	100.0	100.0	100.0	100.0	100.0	100.0	100.0
1/2"	12.5	88.5	88.8	82.4	68.0	82.5	88.0	73.0	89.0	91.0
3/8"	9.5	75.4	76.1	64.6	55.0	64.0	80.0	60.0	75.0	85.0
#4	4.75	48.9	50.4	41.2	34.0	41.0	47.0	43.0	49.0	54.5
#8	2.36	38.4	40.2	27.8	22.0	28.0	32.0	33.0	38.5	43.0
#16	1.18	33.9	35.8	19.7	15.0	19.5	25.0	29.0	34.0	39.0
#30	0.6	27.6	29.7	14.6	9.0	14.0	19.0	22.5	27.5	32.5
#50	0.3	15.7	18.2	10.8	7.0	10.5	14.0	12.5	16.0	19.0
#100	0.15	6.8	9.6	7.7	5.0	7.5	10.0	3.5	7.0	10.0
#200	0.075	3.5	6.4	5.1	3.0	5.0	7.0	1.0	3.5	5.5

Table 3.2. Laboratory test plan and test purpose.

No.	Test Type	Test purpose	Test setup	No. of Tests
1	High temperature modified flexural controlled-strain fatigue test	Verify the fatigue behavior of asphalt concrete at temperatures greater than 30 °C	Modified fatigue test setup with strain gage	16
2	Temperature susceptibility fatigue test (laboratory-mixed and laboratory-compacted)	Extend the database of temperature susceptibility fatigue response of WesTrack	conventional	24
3	Fatigue test with various gradation types	Assess the difference of fatigue performance due to the change of gradation	conventional	24
4	Flexural frequency Sweep Test	Verify the correctness of the modified fatigue setup and explore the relationship among initial stiffness, temperature, and loading frequency	Modified for 40 °C - 30 °C - 20 °C series Conventional for 30 °C - 20 °C - 5 °C series	4
5	Varied-strain fatigue test	Validate the stiffness deterioration hypothesis caused by various strain levels.	conventional	6
6	Varied-temperature fatigue test	Validate the stiffness deterioration hypothesis caused by various temperatures.	conventional	6

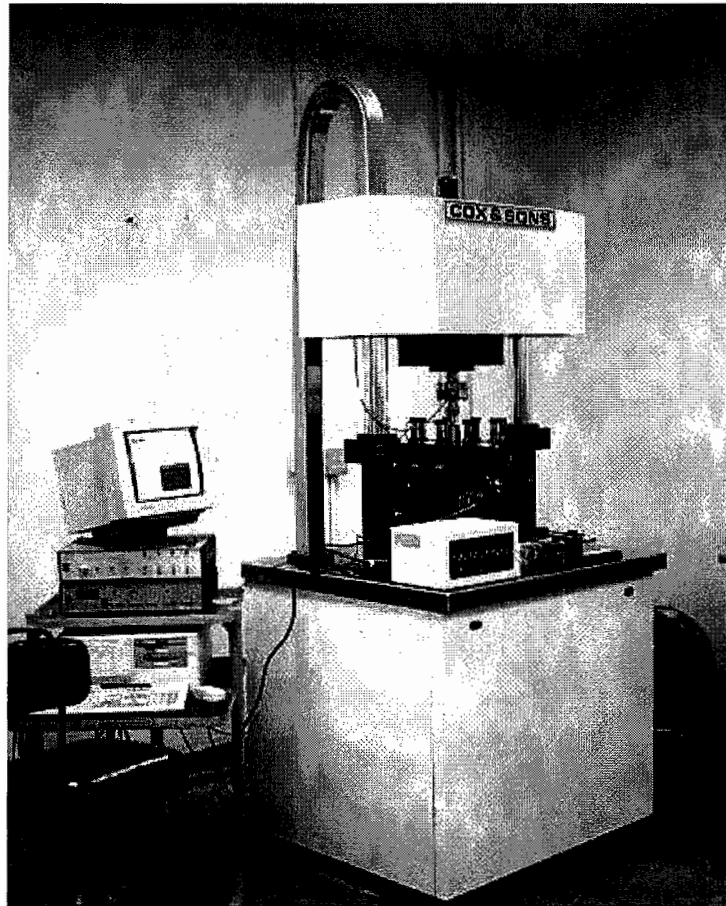
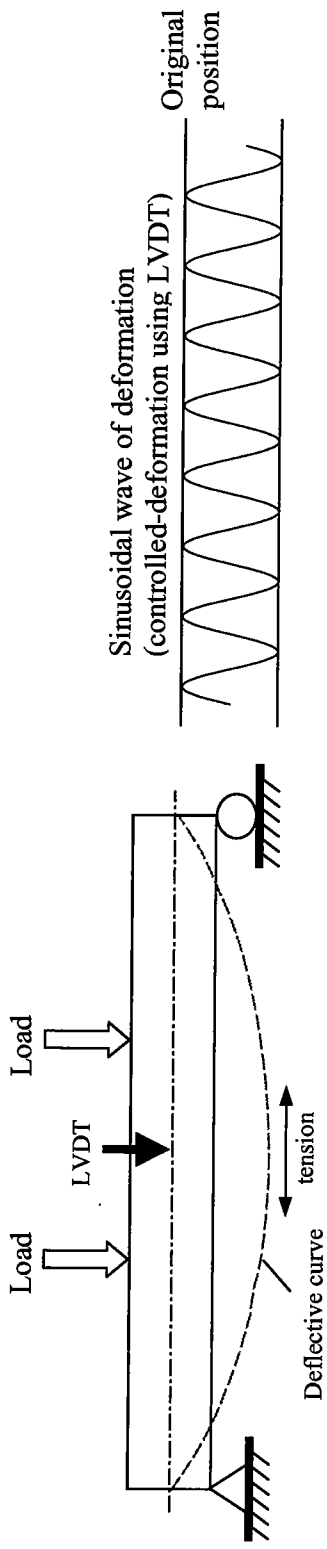
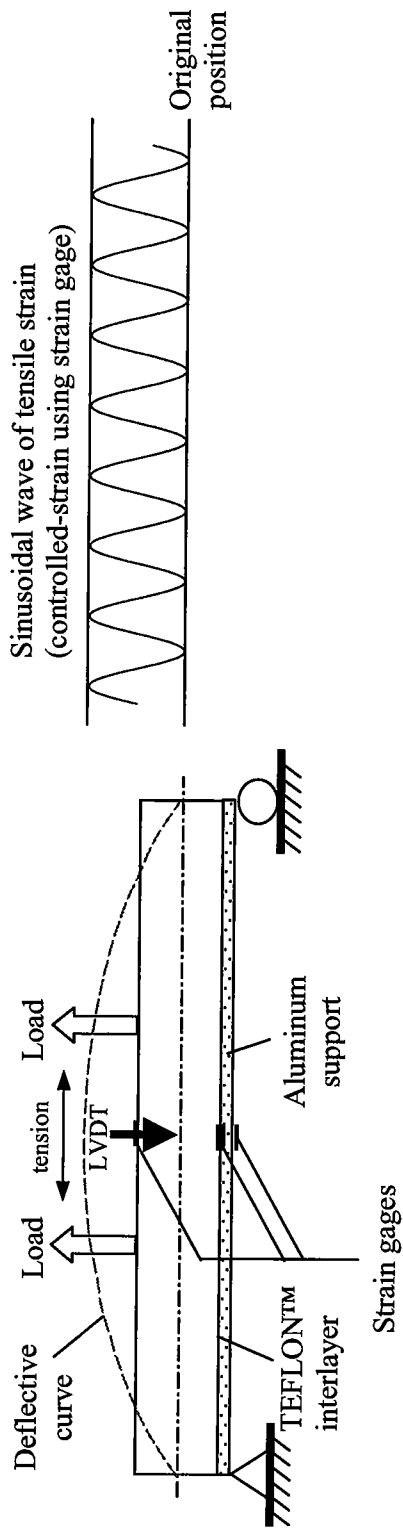


Figure 3.1. Conventional fatigue testing machine



(a) Conventional flexural fatigue test setup



(b) Modified flexural fatigue test setup

Figure 3.2. Schematic plots of conventional and modified flexural fatigue test setups.

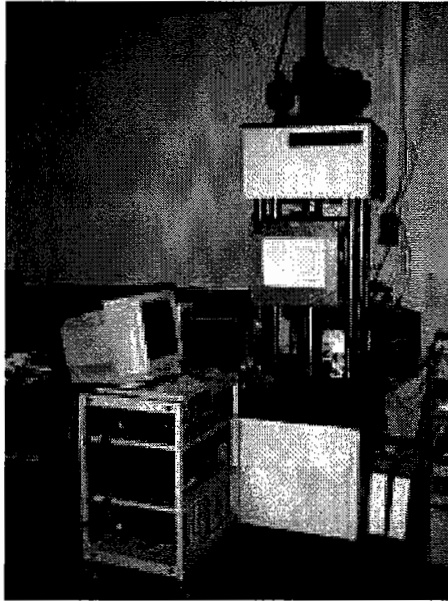


Figure 3.3. Modified fatigue test setup with temperature control box.

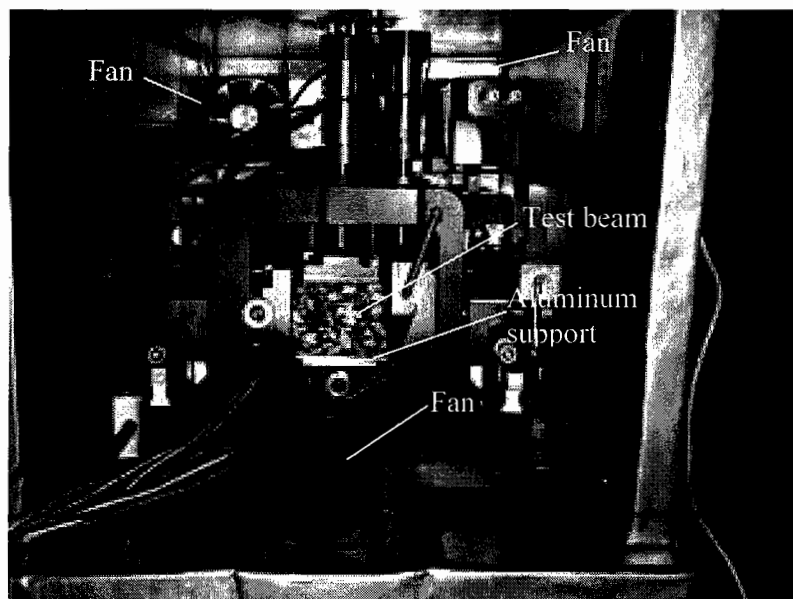


Figure 3.4. Modified fatigue test setup: inside view.

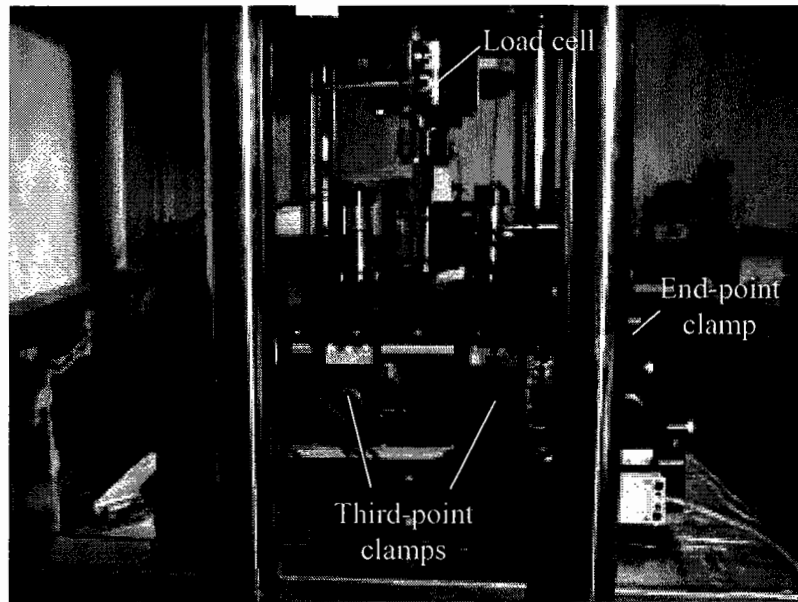


Figure 3.5. Modified fatigue test setup: side view (1).

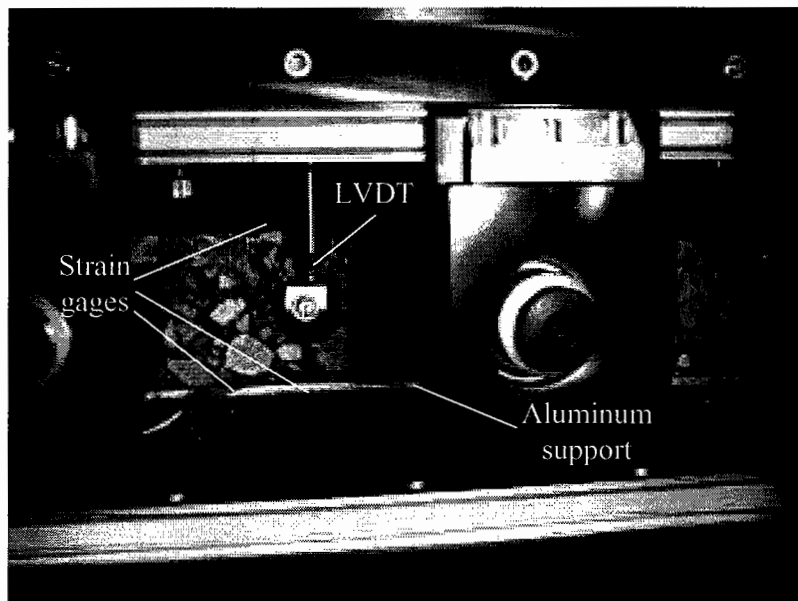


Figure 3.6. Modified fatigue test setup: side view (2).

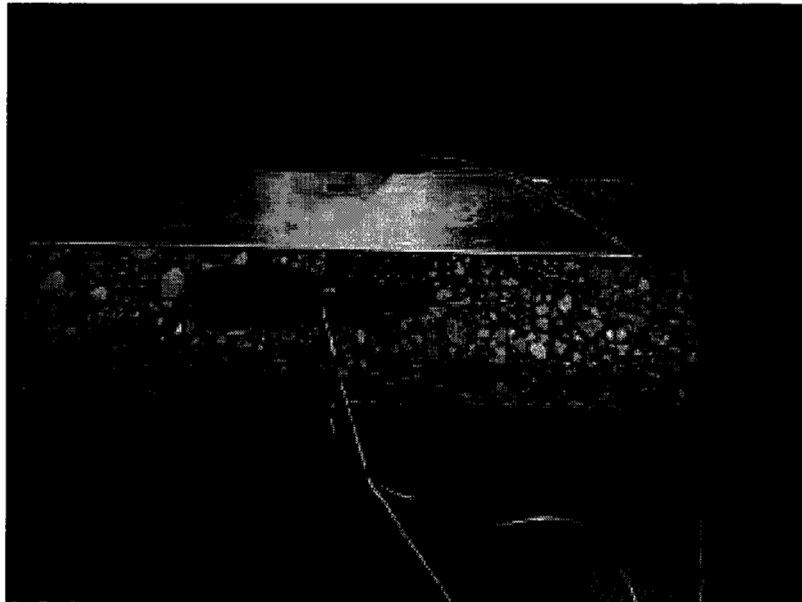


Figure 3.7. Strain gages attached on beam and aluminum support.

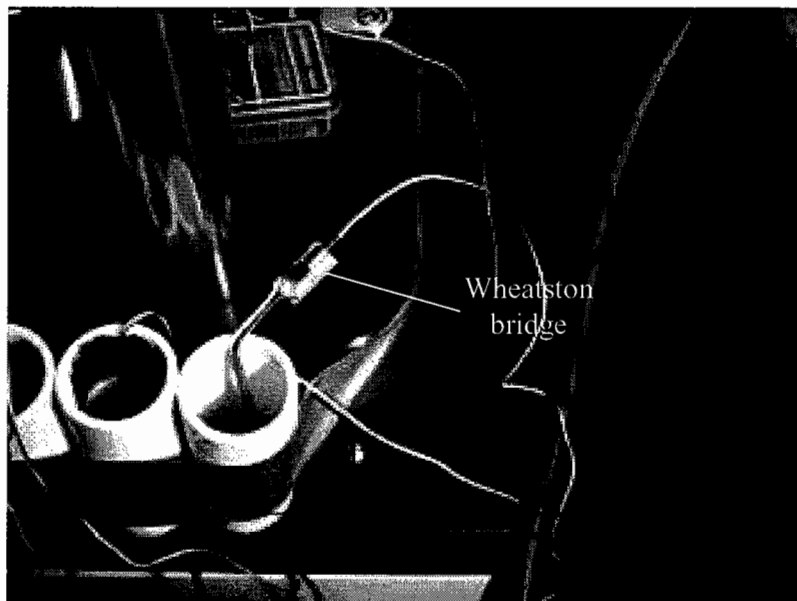
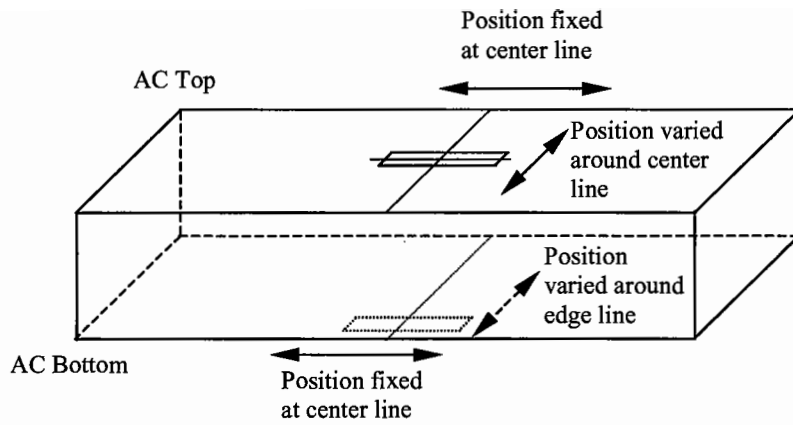
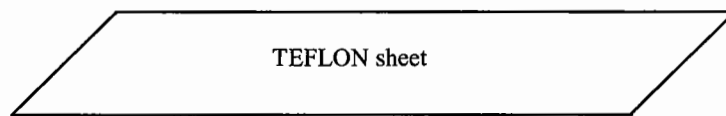


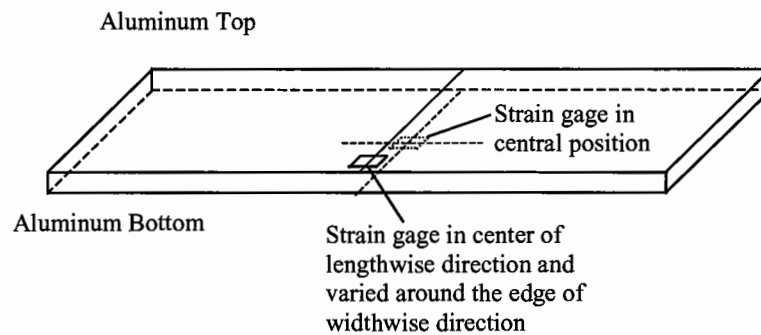
Figure 3.8. Wheatstone bridge.



Asphalt concrete beam: 381.0 mm. (L) x 50.8 mm. (H) x 63.5 mm. (D)



TEFLON™ sheet: 381.0 mm. (L) x 2.39 mm. (H) x 63.5 mm. (D)



6061-T6 Aluminum support: 381.0 mm. (L) x 3.18 mm. (H) x 63.5 mm. (D)

Figure 3.9. Strain gage locations and dimensions of asphalt concrete beam, TEFLON™ sheet, and aluminum support.

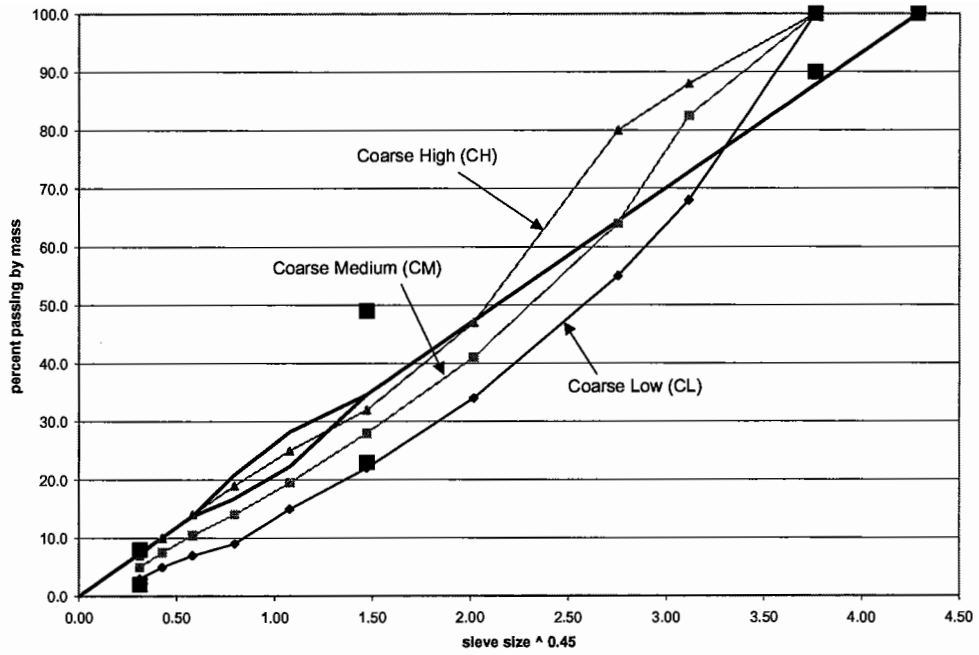


Figure 3.10. Individual WesTrack coarse gradation curves on a 19 mm nominal size 0.45 power chart.

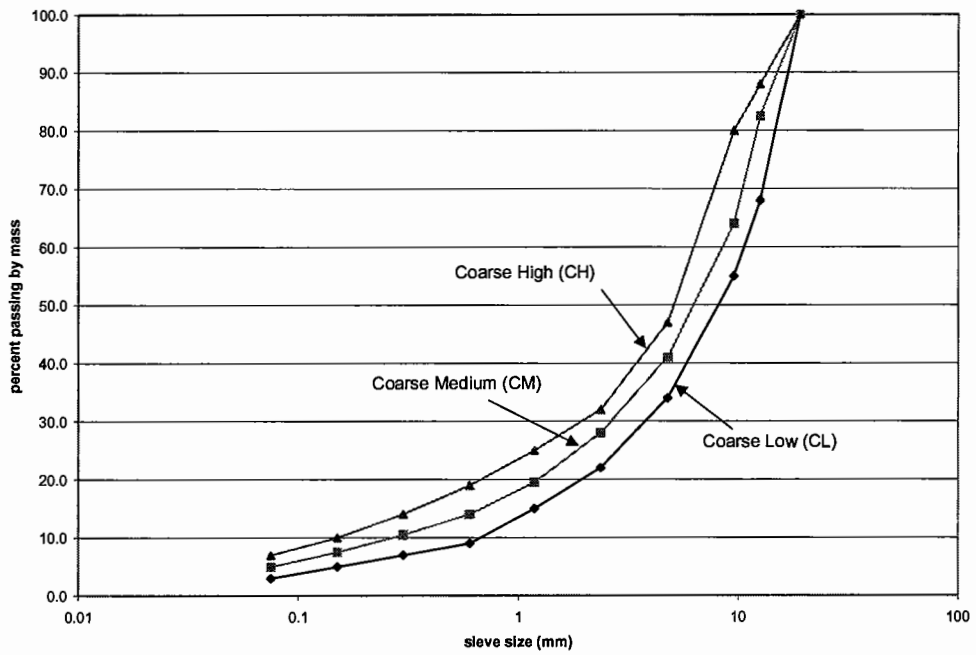


Figure 3.11. Individual WesTrack coarse gradation curves on a semi-logarithm chart.

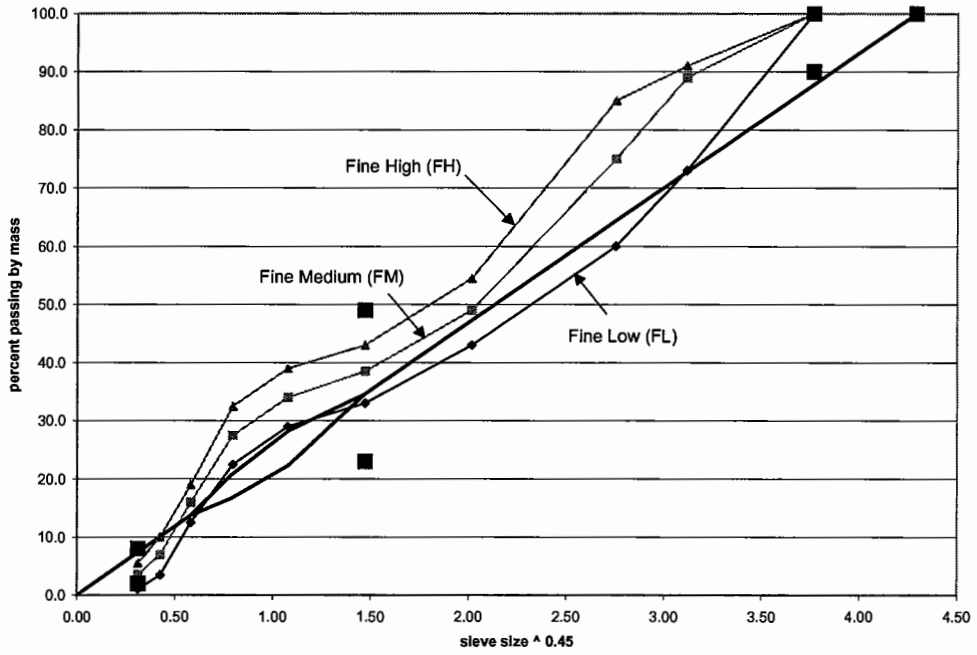


Figure 3.12. Individual WesTrack fine gradation curves on a 19 mm nominal size 0.45 power chart.

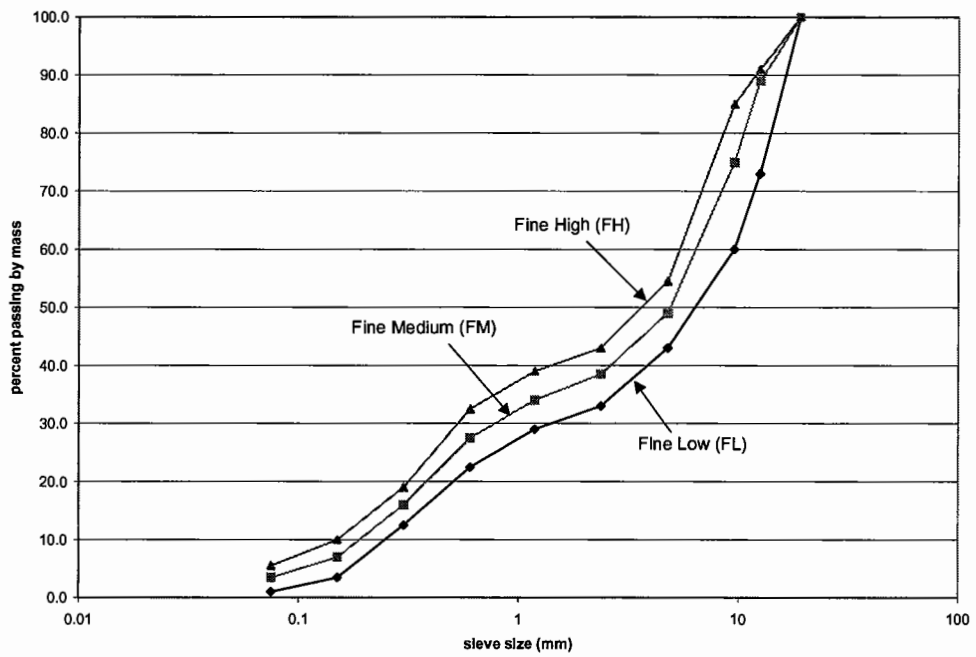


Figure 3.13. Individual WesTrack fine gradation curves on a semi-logarithm chart.

4.0 FATIGUE TEST RESULTS AND ANALYSIS

4.1 Background

4.1.1 History of Fatigue Life Analysis

It has long been acknowledged that the fatigue behavior of asphalt-aggregate mixes can be characterized by equation 1.2,

$$N = A(1/\epsilon_t)^B. \quad (1.2)$$

Monismith et al. (1985) suggested a more applicable model to describe the fatigue behavior of asphalt-aggregate mixes in general (as shown in equation 1.1)

$$N_f = A(1/\epsilon_t)^a (1/S_{mix})^b. \quad (1.1)$$

In this formula, the relation of initial stiffness to the fatigue life has been taken into consideration. Strain-based models have been used to predict pavement fatigue life in most of the literature (Finn et al. 1977, SHELL 1978, Asphalt Institute 1981). Taking the logarithm of both sides of equations 1.1 and 1.2 presents a linear relationship. Equation 1.2 is a linear line and equation 1.1 a linear surface in three-dimensional space. According to the conventional definition of laboratory fatigue life—cumulative load repetitions until a 50 % reduction of the initial stiffness (S_0), each equation yields only

one data point per test strain level. It is obvious that these equations fail to describe the fatigue damage process other than its beginning (S_0) and end (N_f).

Other researchers (Chomton and Valayer 1972, van Dijk 1975, van Dijk, Visser 1977, Pronk and Hopman 1990, Tayebali et al. 1992) have utilized an energy approach and shown that the total (or cumulative) dissipated energy to failure is related to fatigue life as illustrated in equation 1.4,

$$W_{FAT} = A(N_{FAT})^Z. \quad (1.4)$$

In the SHRP project A-003, Tayebali et al. (1994) proposed two surrogate fatigue models, namely, strain-dependent and energy-dependent models:

$$\text{Strain-dependent: } N_f = A \cdot \exp(B \cdot VFB) \cdot (\epsilon_0)^C \cdot (S_0'')^D \text{ and}$$

$$\text{Energy-dependent: } N_f = A \cdot \exp(B \cdot VFB) \cdot (w_0)^C, \quad (1.5)$$

where N_f = fatigue life,

ϵ_0 = initial strain,

S_0'' = initial loss stiffness, psi,

w_0 = initial dissipated energy per cycle, psi,

VFB = percent voids filled with bitumen, and

A , B , C , and D are experimentally determined coefficients.

Generally, none of the above mentioned approaches recognizes how fatigue damage to the mix actually develops as loading proceeds while the mix is subjected to specific testing conditions. In this chapter, the Weibull function used widely in mechanical engineering, will be introduced as a tool to describe the fatigue damage; subsequently, a Weibull Proportional Hazards model (Weibull PH model) used in survival analysis will assist in developing the fatigue model to include not only mix properties but also environmental and traffic variables. The details of the Weibull PH model will be discussed in Chapter 5.

4.1.2 Interpretation of Weibull Curves

The stiffness ratio (SR) at repetition n , which is defined as the ratio of stiffness at repetition n over the initial stiffness (taken at about 50 repetitions), will be utilized as an index in characterizing the phenomenon of fatigue damage process throughout this study. The use of SR has several advantages over other indices such as dissipated energy. Some of these advantages are: (1) stiffness is easy to measure both in the laboratory and in the field, and (2) stiffness is often utilized as an input for linear layered-elastic programs for pavement analysis, thus making it useful for programming fatigue performance prediction; this will be discussed in detail subsequently.

To present the stiffness deterioration process, the Weibull Curve, a curve following the Weibull survivor function with the form: $y = \exp(-\lambda x^\gamma)$, will serve as a tool to identify the damage process in asphalt concrete. The parameter γ is known as the shape parameter, while the parameter λ is the scale parameter. The Weibull function can also be represented as

$$\ln(-\ln(y)) = \ln \lambda + \gamma \ln x . \quad (4.1)$$

That is to say, by identifying y as the SR, where the term $\ln(-\ln(\textit{stiffness ratio}))$, or $\ln(-\ln(SR))$, represents the y -axis and $\ln(\textit{repetition})$ or $\ln(n)$ the x -axis, then the Weibull survivor function is a straight line. In other words, if the Weibull assumption imposed on the fatigue damage process is tenable, then a plot of $\ln(-\ln(\hat{SR}))$ against $\ln(n)$ would give an approximately straight line (the \hat{SR} being the observed stiffness ratio). Note that the x in equation 4.1 can be mathematically replaced by $\ln x$ or \sqrt{x} . Hereafter, the stiffness deterioration curve in terms of $\ln(-\ln(\hat{SR}))$ versus $\ln(\ln(n))$ or $\ln(n)$ will be referred to as the “*Weibull curve*”.

The feasibility of using Weibull curves to define the fatigue damage process can be schematically demonstrated with data obtained from fatigue tests on WesTrack mixes. Figure 4.1 shows a typical example of the Weibull fitting to flexural fatigue test data. As seen in Figure 4.2, the plot of $\ln(-\ln(\hat{SR}))$ versus $\ln(\ln(n))$ better fits the fatigue damage process than the plot of $\ln(-\ln(\hat{SR}))$ versus $\ln(n)$.

An explanation of the relationship between the fatigue damage process and the slopes and intercepts of Weibull curves is shown schematically in Figures 4.3 and 4.4. In the fourth quadrant of the Cartesian coordinate system of both figures the y -axis is labeled with $\ln(-\ln(SR))$ and x -axis marked as $\ln(\ln(n))$ or $\ln(n)$ respectively. The n_0 is the initial repetition that causes either the term $\ln(\ln(n))$ or the term $\ln(n)$ to vanish.

The following is an explanation of how to interpret the slope and intercept of Weibull curves. As shown in Figure 4.3, two Weibull curves have the same slope, i.e., the same fatigue damage rate, but have different intercepts. After n repetitions curve 1 shows more fatigue damage than does curve 2. In other words, curve 2 has a higher initial fatigue-resistant capacity than curve 1 from the point of view of material strength. In Figure 4.4, two Weibull curves have the same intercepts, i.e., the same initial fatigue-resistant capacity, but have various fatigue damage rates. In this case after n repetitions curve 1 has a more severe fatigue damage rate than does curve 2. Therefore, after n repetitions, material represented by curve 1 with a steep slope will accumulate more fatigue damage. Of great importance is what factors really affect the intercept and slope—initial fatigue-resistant capacity and fatigue damage rate—of Weibull curves. The following sections are devoted to exploring and identifying those significant factors that affect initial fatigue-resistant capacity and fatigue damage rate, particularly with regard to the various types of fatigue tests.

4.1.3 Crack Initiation and Weibull Curves

This study is mainly focused on the initiation of the bottom-up type of cracking, which was the type observed in the WesTrack pavement sections. Figure 4.5 illustrates a series of test results of fatigue tests that were conducted beyond 50 % stiffness reduction. Two observations can be made: (1) the curves have a reversed-S shape, and (2) at $SR = 0.5$, the conventional definition of fatigue failure, is the position where the curve starts to curl up. It is at this point, at the repetition where the curve starts to curl up, where it may be that the macrocrack initiates and starts to propagate.

To study the slope and intercept of the fatigue damage process in the Weibull curve, it is necessary to define the valid data range for the laboratory fatigue test to be utilized as input to the regression analysis. The stiffness deterioration curve should consist of three phases, as defined in Figure 4.6. The three phases are (1) Phase I: heating and arrived at temperature equilibrium, (2) Phase II: crack initiation developing, and (3) Phase III: crack propagating. The data points located in Phase II were used in this study as the valid data that provides the Weibull curve for crack initiation. It has been observed that sometimes no obvious difference exists between Phase I and Phase II. In such cases, the data associated with Phase I were also included.

In this chapter, a large number of fatigue analyses will be represented as $\ln(-\ln(SR))$ versus $\ln(n)$ or $\ln(\ln(n))$, where SR is the stiffness ratio, n the repetitions, and \ln the natural logarithm. In Chapter 5 both the theoretical derivation and application of these Weibull curves are provided. In this chapter, these plots are primarily used to explain the fatigue damage process and to identify significant factors that affect this process. Analyses of some test types in the following sections will be conducted with Splus¹. Their corresponding Splus codes, if any, will be listed in Appendix C.

4.2 Fatigue Tests at 20°C

This data set consists of 151 fatigue beam tests using specimens cut from the 26 WesTrack test sections; 13 of them were from the top lift of the asphalt concrete layer, the other 138 beams were from the bottom lift. These tests were conducted by the author and other UCB staff as part of the WesTrack project, and are in addition to the tests described in the experiment plan developed for this thesis (Table 3.2). All of the beam

specimens used were field-mixed and field-compacted. Table A.4.1 in Appendix A shows the details of mix information, test results, and regression analysis for each beam test. The independent variables investigated are listed in Table 4.1. The av used here is based on the UCB method of air-void measurement. The other independent variables here are adopted from Hand's dissertation (1998) of Table 123 for ac , Tables 136 through 141 for $m200$, sa , and $rs4s50$, and Tables 147 through 152 for the vma and vfa . Six dependent variables $lnnf$, $lnstif$, aa , bb , cc , and dd will be inspected herein. The variables $lnnf$ and $lnstif$, as usual, represent the natural logarithms of fatigue life and stiffness respectively. The aa and bb are the regression coefficients obtained from the relationship $\ln(-\ln(SR)) = aa + bb \cdot \ln(n)$, where SR is the stiffness ratio and n is the repetitions; likewise, the cc and dd are the regression coefficients determined from the equation $\ln(-\ln(SR)) = cc + dd \cdot \ln(\ln(n))$. The ranges of the covariates and six response variables presented in this exploration are described in Appendix A, Table A.4.16.

These laboratory fatigue tests were conducted in the conventional flexural controlled-strain fatigue test setup with a loading frequency of 10 Hz, a test temperature of 20 ± 1 °C, and two test strain levels, 200 and 400 microstrains.

The reader should keep in mind that the identification of significant factors that affect fatigue behavior is the primary goal of this section as well as in the following sections for different types of fatigue tests. To delineate the important factors, a sequence of observations and statistical analyses were conducted in the manner described in the following paragraphs:

¹ Splus is a statistical software package that is from the StatSci division of MathSoft.

- Pairs Diagram and Correlation Matrix

Figures 4.7 and 4.8 are pairs diagrams that quickly explore the relationships among variables. The information presented in Figure 4.7 for fatigue life and stiffness clearly demonstrates that the stn , av , ac , and also vfa which is a function of av and ac , have obvious effects on fatigue life and that av has a significant effect on stiffness.

The correlation matrix shown in Table A.4.6 measures the strength of linear relationships between the pairs of variables. Figure 4.9 presents a series of scatterplots of 500 independent pairs of bivariate normal random variables with several various correlation coefficients so as to give the reader an indication of how the scatterplots look if two normal random variables exist with a certain correlation coefficient. The corresponding algorithm regarding the generation of correlated random numbers is listed in Appendix C. Notice that the clouds of points are roughly elliptical in shape. From Figure 4.9, it seems that the marginally visually recognizable pattern could be set at a correlation coefficient value of 0.4; in other words, it is a subjective judgment.

Based on such subjective criterion, several findings from the scatter plots and correlation matrices can be addressed as follows:

1. The test strain level is highly negative when correlated with fatigue life; that is to say, a higher strain level will tremendously reduce the fatigue life.
2. The test strain level is highly positive when correlated with the coefficients bb and dd , which are the slopes in $\ln(-\ln(SR))$ versus $\ln(n)$ and $\ln(\ln(n))$ charts respectively; in other words, the fatigue damage rate is particularly affected by test strain level.

3. The air-void content counteracts the stiffness with a negative and high correlation coefficient, i.e., a higher air-void content will definitely bring down the value of stiffness.
4. No apparent correlations exist between the coefficients of *aa* and *cc* and the covariates.
5. As for the covariates *grad*, *rs4s50*, *m200*, *sa*, *vma*, and *vfa*, they are all mutually correlative. Note that these covariates are actually gradation-related. This reveals that the multicollinearity problem will be a concern in future regression analyses conducted if these covariates are to be included simultaneously.

- Design Plots, Factor Plots, and ANOVA results

According to the stem-and-leaf diagrams and histograms of each covariate, the covariate was categorized into three factor levels: low, medium, and high. Exceptions were the factor *stn*, which was separated into two factor levels of low and high, and the factor *grad*, which was classified by three factor levels, namely fine-plus, fine, and coarse. Thus, excepting *stn* and *grad*, two delineatory points were determined for each covariate. The *av* was marked “low” if less than 5 percent, “medium” if between 5 and 8 percent, and “high” if greater than 8 percent. For *av* then, the set of points was (5, 8). The same procedures were applied to the other covariates: *ac*, *rs4s50*, *m200*, *sa*, *vma*, and *vfa*, with corresponding sets of points (5, 6), (3, 3.5), (5, 6), (5, 6), (12.5, 13.5), and (65, 80).

A series of design plots based on the category criteria described above are presented in Figures 4.10 through 4.15. In these figures, the horizontal line represents the grand mean of the response variable, the vertical line marked with short ticks indicates the means of factor levels for a specific factor. Therefore, the farther apart the marked factor levels in the vertical line are, the more significant the effect of the factor on the response variable. Accordingly, several findings are remarked upon below:

1. In Figure 4.10, the *lnstif* is primarily affected by the *av* and relatively insensitive to *stn*.
2. As seen in Figure 4.11, *stn* has a significantly greater effect on the fatigue life than it does on stiffness. The *av* and *ac* also affect the fatigue life; it should also be noted that the low *av* content and high *ac* content result in high fatigue life. The same conclusions can be found on the work done by Epps (1968) and Harvey (1992), although their results were for different gradations and controlled-stress testing. Interestingly, although in a marginal sense, the fatigue performance of the coarse gradation is higher than that of either the fine-plus or fine gradations. No evident difference of fatigue performance exists between the fine-plus and fine gradations.
3. The coefficient *aa*, which is the intercept of equation $\ln(-\ln(SR)) = aa + bb \cdot \ln(n)$, is mostly affected by *sa* and to a lesser degree by its relations to *av* and *vma*, as shown in Figure 4.12.
4. The coefficient *bb*, which is the slope of equation $\ln(-\ln(SR)) = aa + bb \cdot \ln(n)$, is primarily affected by *stn* and to a lesser extent by *ac* and *av*, as shown in Figure 4.13. These findings are in keeping with

current ideas regarding the fatigue of asphalt concrete, i.e., higher strain, higher air-void content, and a lower asphalt content will lead to increased fatigue damage.

5. From Figures 4.14 and 4.15, similar conclusions as in (3) and (4) can be drawn for coefficients cc and dd , which are the intercept and slope of equation $\ln(-\ln(SR)) = cc + dd \cdot \ln(\ln(n))$.

In addition to the design plots, Figures 4.16 through 4.24 present the so-called “factor plots” to show the box-and-whisker plots, or simply boxplots, for inspecting the effect of factors on the response variables. Examining the analysis of variance (ANOVA) results also provides a quantitative way to identify significant factors that affect the response variables. The main effects on response variables listed below are based on the ANOVA results at a 5 % significance level:

- *stif*: *grad*, *av*, *ac*, *stn*, *sa*, *vma*, and *vfa*.
 - *nf*: *grad*, *av*, *stn*, and *rs4s50*.
 - coefficient *aa*: *av*, *stn*, *sa*, and *vma*.
 - coefficient *bb*: *av*, *stn*, and *sa*.
 - coefficient *cc*: *av* and *sa*.
 - coefficient *dd*: *grad*, *av*, *stn*, and *sa*.
-
- Test for Parallelism for groups of 200 and 400 microstrain

From the previous discussion, it has been noted that the test strain level has a significant effect on the slopes of the Weibull curves. Thus, we can separate the data by

test strain level and conduct an F-test to test the null hypothesis that the slopes of two groups are equal. The F-statistic is 25896 on 1 and 15944 degrees of freedom, resulting in a p-value of 0, that is to say, the hypothesis of parallelism is strongly rejected. In other words, the tensile strain level affects the fatigue damage process in a significant way. In Figure 4.25, the test results of 151 beams are separated into 200 and 400 microstrain groups and are presented as Weibull curves. The solid regression line is for the 200 microstrain group, the dotted line for the 400 microstrain group. The slopes fitted are 3.649 for the 200 microstrain group and 4.162 for the 400 microstrain group.

In Chapter 4.3 through Chapter 4.7, similar procedures of analysis will be followed, including figures and tables; however, only the topics of interest will be presented and summarized. The associated tables and figures will be included in Appendix A and Appendix B respectively. The factor plots for the other fatigue test types are not included.

In accordance with the identification procedure discussed above, a summary table (Table 4.2) was prepared for various types of fatigue tests. The criteria to mark the significant factors consist of two qualitative methods, design plots and factor plots, and two quantitative ways, a correlation matrix and ANOVA results. The threshold of identifying a significant factor from correlation coefficients is 0.4. A 5 % significance level is set for the ANOVA results. If all these four criteria are check-marked in one independent variable, then this independent variable is considered a "very important" factor. If three criteria are check-marked, the factor is considered as being "important". At lastly, if only one or two criteria are matched, it is deemed as being "less important".

Using the above mentioned criteria, for this data set of fatigue tests at 20°C, several findings can be addressed in the following:

1. The *av* is a very important factor to the *Instif* and is also important to the other independent variables: *lnnf*, *aa*, *bb*, *cc*, and *dd*.
2. The *grad* is important to both *Instif* and *lnnf*. The *grad* shows no effect on the coefficients *aa*, *bb*, *cc*, and *dd*.
3. The *stn* is very important to *lnnf*, *bb*, and *dd*.
4. The *sa* is important to *Instif*, *aa*, *cc*, and *dd*, but less important to *bb*.

4.3 Temperature Susceptibility Fatigue Test (Field)

This data set includes the results of 35 fatigue beam tests on specimens cut from the top lifts of 10 WesTrack sections. The specimens are therefore field-mixed and field-compacted. Table A.4.2 summarizes the mix information, testing conditions, and the test results as well. The covariates and response variables considered are the same as those for the fatigue tests at 20°C but with the addition of a temperature variable, *temp*. The air-void contents were measured using the UCB air-voiding method. The variables *rs4s50*, *m200*, *sa*, *vma*, and *vfa* are according to the tables listed in Hand's dissertation (1998) as mentioned earlier. The ranges of covariates and six response variables (*Instif*, *lnnf*, *aa*, *bb*, *cc*, and *dd*) were listed in Table A.4.16. Figures B.4.1 through B.4.6 illustrate the associated design plots.

Fatigue test data were collected utilizing the conventional fatigue setup with a loading frequency of 10 Hz, various testing temperatures (5°C, 20°C, and 30°C), and

strain levels including 200, 300, 400, and 800 microstrain. Through the identification procedure, the findings can be addressed from the summary Table 4.2 are:

1. The *temp* factor meets the criteria deeming it very important to most of the response variables, but only qualifies as important to *aa* and less important to *lnnf*.
2. The *stn* factor, as usual, is deemed very important to fatigue life *lnnf* but has no effect on the stiffness term *lnstif*. The coefficients *aa*, *bb*, *cc*, and *dd* are affected by *stn* factor in a less important or important degree.
3. The *av* factor is less important to *lnstif*, *lnnf*, and *cc*.
4. The variables associated with the gradation type have little or no effect on the response variables.

4.4 Temperature Susceptibility Fatigue Test (Laboratory)

The purpose of this test was to add to the database of the temperature susceptibility fatigue behavior of WesTrack mixes. The data set for this fatigue test consisted of 24 beams with two gradation types (CM and FM), two asphalt contents (5.7 % and 5.4 %), three temperatures (5 °C, 20 °C, and 30 °C), and two strain levels (200 and 400 microstrain). The "M" in the designations of CM and FM stands for the target gradation compared with the high "H" (slightly finer than target) and "L" (slightly coarser than target) types of gradations mentioned in Chapter 3. The CM is the coarse medium gradation of the WesTrack test sections. The FM is the fine medium gradation and is equivalent to the fine gradation of the WesTrack test sections. It should be noted that the covariates associated with the gradation type, such as *rs4s50*, *m200*, *sa*, *vma*, and *vfa*, for

this specific experiment design, are completely dependent on the gradation variable, which is why the means of the factor levels of these covariates are the same. The associated design plots are listed in Figures B.4.7 through B.4.12. The detailed test results are summarized in Table A.4.3.

From Table 4.2, several findings can be summarized as follows,

1. The *temp* variable is very important to all the response variables and important to the *lnnf* term.
2. It has been widely recognized that the fatigue life *lnnf* is totally influenced by the *stn* term.
3. The effect of *av* term does not show its importance in this fatigue test, because the air-void contents of the beams are very close to each other. Therefore, conclusions related to the *av* term should not be drawn from this data set.
4. The *grad* term has no effect on any of the response variables except that the *grad* is a less important factor of the *lnnf*.

4.5 High Temperature Flexural Controlled-Strain Fatigue Test

In contrast to the literature of studies of high temperature fatigue for mechanical components, little data are available for the high temperature fatigue behavior of asphalt concrete.

The high temperature fatigue test is designed as a full factorial experiment with four factors, with each factor having two levels. The four factors are air-void content with two levels, high (11 ± 1 %) and low (6.6 ± 1 %); aggregate gradation with coarse medium (CM) and fine medium (FM) levels; tensile strain containing the two levels of

200 and 400 microstrains; and test temperature with a 30°C and a 40°C level. Hence, the experiment design will contain $2^4 = 16$ runs. The percent asphalt content is fixed at 5.7%. For this specific experiment design, the variables *rs4s50*, *m200*, *sa*, *vma*, and *vfa*, all of which are associated with gradation type (*grad*), are statistically redundant in that they provide no more information than does *grad*.

According to previous experience in analyzing the WesTrack fatigue data, it was found that the obtained traditional fatigue equations of fine and fine-plus gradations exhibit no obvious difference. Thus, for the high temperature fatigue, only the CM and FM gradations were selected. The selection of the air-void contents was based on the statistical summary from previous tests of the mean air-void content. The temperature of 30°C was chosen to provide a replication of fatigue results for the two fatigue setups (conventional test setup versus modified test setup). Instead of choosing 45°C, which is reached in field pavements on a hot summer day, or 35°C, or including more temperatures, the main concern was the limited amount of available WesTrack material. As for the choosing of the two test strain levels, the main reasons lie in the compatibility to simulation results from a layered-elastic program and the completeness of the existing database.

Instead of using conventional measurements of deflection for a flexural beam test, i.e., LVDT readings, this test utilizes strain gages, which are attached on the top and bottom of both the asphalt concrete and the aluminum support, to conduct a real “controlled-strain” fatigue test. The main advantages of utilizing strain gages are to (1) verify the feasibility of applying linear elastic theory to an asphalt concrete beam, especially while subjected to high temperatures, (2) validate if asphalt concrete exhibits a

nonlinear or bilinear stress-strain relationship at high temperatures, and (3) perform a genuine controlled-strain flexural beam test. However, the LVDT was monitored during the test.

Figures 4.26 and 4.27 illustrate the test results for high temperature fatigue tests for the CM and FM mixes respectively. The Weibull curves for tests conducted at 40°C resemble a falling letter C in shape, especially for the FM mixes. The falling C shape implies that the fatigue damage rate is slowed down and flattens out and thus causes no further fatigue damage after a certain number of repetitions. It is conjectured that the FM mix is flexible at high temperature, thus making it hard to initiate and propagate cracks.

The test results are listed in Table A.4.4. The allied design plots are displayed in Figures B.4.13 through B.4.18. Table A.4.9 shows the correlation matrix. The ANOVA results are not shown here. According to these figures and tables, the appropriate check marks were put in the cell of significance in Table 4.2. Several observations from this table can be abstracted in the following:

1. The *lnstif* term is clearly affected by *temp* term. Temperature has no effect on the *lnnf* term. The *temp* term is less important to the coefficients *aa*, *bb*, *cc*, and *dd*.
2. The *stn* effect on the *lnnf* term is important in this high temperature fatigue test.
3. The *av* term is also important to the response variables *lnstif*, *aa*, *cc*, and *dd*.
4. The *grad* variable is less important to the response variables *lnnf*, *cc*, and *dd*.

The only clear fact emerging from this high temperature fatigue test is that the stiffness is definitely affected by temperature; however, for the WesTrack mixes, the fatigue life is insensitive to the temperature change. It should also be noted that at high temperatures the fatigue life of the FM is greater than that of the CM, whereas in previous experiments (fatigue tests at 20°C) the fatigue life of the FM was less than that of the CM. Reasons for these contradictory results at different temperatures are unclear at this time. Further experiments are recommended.

4.6 Fatigue Test with Various Gradation Types

The purpose of this test was to verify the effect of construction type variability of gradation (as occurs in the asphalt mix plant) on the fatigue performance. The gradation types utilized in this test were three types of coarse gradations: coarse medium (CM), coarse high (CH), and coarse low (CL), and three types of fine gradation: fine medium (FM), fine high (FH), and fine low (FL). The variables $rs4s50$, $m200$, sa , and vma , associated with gradation type ($grad$), are statistically redundant in that they provide no more information than does $grad$ for this experimental design. For the corresponding gradation curve information, please refer to Figures 3.10 to 3.13 and to Table 3.1. The test results are listed in Table A.4.5. The associated designs are displayed in Figures B.4.19 through B.4.24. Table A.4.10 presents the correlation matrix. The ANOVA results are not shown here. According to these figures and tables, the appropriate check marks were put in the cell of significance in Table 4.2. Several observations from this table can be abstracted in the following:

1. The *grad* term is important to the terms *lnstif*, *lnnf aa*, and *bb*, but is less important to the coefficients *cc* and *dd*.
2. The *stn* term is very important to the terms *lnnf* and *bb*.
3. There is no *ac* effect on any of the response variables because the asphalt contents are 5.7 % for CL, CM, and CH and 5.4 % for FL, FM, and FH.
4. The *av* term is less important to the response variables *lnstif*, *lnnf*, *aa*, and *dd*.
5. Most of the gradation-associated variables, *rs4s50*, *m200*, *sa*, and *vma*, are important to the coefficients of *aa*, *bb*, *cc*, and *dd*. This indicates that the gradation is significant to the fatigue damage process.
6. The stiffness of the coarse gradation is more sensitive to gradation variation. Fatigue life has a similar sensitivity to change for both gradations.

4.7 Pooled Fatigue Tests

The pooled fatigue test results include the data sets of the fatigue tests at 20°C, the field-mixed and field-compacted temperature susceptibility fatigue tests, the laboratory-mixed and laboratory-compacted temperature susceptibility fatigue tests, and the high temperature fatigue tests. The fatigue tests with various gradation types were excluded. The associated design plots and factor plots are displayed in Figures B.4.25 through B.4.30. Table A.4.11 presents the correlation matrix. The ANOVA results are not shown here. The data range of this pooled fatigue test is listed in Table A.4.16.

Through the same identification procedure as before, the conclusions are summarized in the following:

1. The *temp* term is very important to the terms *Instif*, *aa*, *bb*, *cc*, and *dd* and important to the *Innf* term.
2. The *stn* term is very important to the *Innf* and *bb* terms and is less important to the other response variables.
3. Compared with the effects of *stn* and *temp* terms, the effects caused by the other covariates seem to be negligible. It can be concluded that the effect of environmental factors on the pavement performance is more significant than the effect of material variables.

4.8 Conventional Fatigue Analysis for WesTrack Project

4.8.1 Model Selection

The conventional fatigue analysis is mainly the model selection of the initial stiffness and the fatigue life. The term “conventional” is applied here to stress the subtle differences that result from using the Weibull proportional hazards model. The purpose in conducting the conventional fatigue analysis is that the stiffness equation plays an important role in calculating the tensile strain in the Weibull dynamic approach. The model selection of fatigue life and stiffness is a trade-off procedure between engineering judgment and theoretical considerations. Therefore, the following sections use the same procedure to choose the most appropriate model to reflect the WesTrack data. Instead of utilizing the backward/forward selection procedure, the model selection discussed here will include the following steps:

- pairs plot to inspect the possible relationship amongst various variables,

- design plot and factor plot,
- correlation matrix of the covariates and response variables,
- ANOVA table to identify the significant terms,
- Mallows' C_p (Seber 1977) to choose the best subset of the covariates,
- regression analysis,
- residual plot, and
- engineering judgment.

Because the model selection involved mountains of figure communications and judgments, only the final results and anything deemed important are presented in the associated sections.

4.8.2 Mallows' C_p statistic

For the detailed derivation of Mallows' C_p statistic of model selection, please refer to the Seber's book (1977): *Linear Regression Analysis*. For comparing models, we use the mean square error criterion. Let's denote $X_{q \times 1} = (x_1, \dots, x_q)$, $X^{(p)} = (x_1, \dots, x_p)$, then for the regression analysis, we have $\hat{Y}_p = X^{(p)'} \hat{\beta}_{sub}$ and $E[Y(X)] = X\beta$. Therefore, a meaningful quantity to minimize could be $E\left[\left(\hat{Y}_p(X^{(p)}) - E[Y(X)]\right)^2\right]$. That is to say, search for the best sub-model such that the above quantity is a minimum; however, this depends on X and might produce for every different X a different optimal p-parameter sub-model. Mallows suggested to minimize a scaled averaged mean square errors,

$\Delta_p = \frac{1}{\sigma^2} \sum_{i=1}^n E[(\hat{y}_{p,i} - E[y_i])^2]$. Through statistical manipulation, the estimate of Δ_p ,

namely C_p , can be expressed as $C_p = \frac{SS_{res,p}}{\hat{\sigma}^2} + 2p - n$, where $SS_{res,p}$ is the residual sum

of the squares of the p-parameter sub-model, $\hat{\sigma}^2$ is the estimate of σ^2 , and n is the sample size. How to interpret and apply this equation is of great importance to model selection. The following presents some guidelines to interpreting the Mallows' C_p

statistic:

- if no large systematic error exists, then $C_p \approx p$.
- if $C_p \gg p$, then it indicates a sub-model with large bias (usually $C_p > p$ or $C_p \approx p$); $C_p < p$ can happen due to variability.
- Consider a sub-model with small C_p and $C_p \approx p$.

Based on these guidelines and the `leaps()` command in Splus, which computes the C_p values for all possible subsets of independent variables, the C_p plot, which is a plot of C_p statistic versus p , can be utilized to decide on the best sub-model.

4.8.3 Data Description

It is important to note that the conventional initial stiffness regression analysis will be utilized as one of the inputs to the Weibull dynamic approach when simulating the fatigue performance prediction for the WesTrack project mixes. Thus, the data include all the fatigue test data except the data from the fatigue tests with variations within a gradation (i.e., FH, FL, CL, and CH described in Chapter 4.6). All the data will be

categorized by gradation type to comply with the mix characteristics of the 26 original constructed sections of WesTrack. The sample size, as well as the data range of the covariates and response variables of each category is listed in Table A.4.16. It is important to emphasize that examination should be limited by the parameters of the data range, as extrapolation can be misleading.

4.8.4 A Regression Example: Coarse Gradation

The conventional fatigue analysis using the laboratory fatigue data for WesTrack mixes categorizes the data into four groups based on the gradation types. It includes coarse, fine, fine-plus, and the combination of fine and fine-plus. Previous experience found no obvious difference between the fine and fine-plus gradations' fatigue performance, therefore, the combined gradations group of fine and fine-plus is discussed as well. A detailed discussion of how to use regression analysis on the coarse gradation is given as an example in the following paragraphs.

- Initial Stiffness

From the correlation matrix of Table A.4.12, the *Instif* has a strong negative correlation with the *temp* term and marginally negatively-correlated with the *av* term. In other words, a higher temperature or air-void content will result in a decrease in initial stiffness. The design plot (Figure B.4.31) shows that the *temp* and *stn* terms have a significant effect on the stiffness. However, based on engineering judgment, the *stn* term was not included. As can be seen in the factor plot of *stn* in Figure B.4.40, it shows that the sample sizes of the 300 and 800 microstrain level tests are too small, and that no

evident difference exists between 200 and 400 microstrain levels. In other words, the visible difference in the design plot is due to data variation. Hence, the strain term will not be included in the formula.

The Mallows' C_p method picks ac , av , $temp$, $lnstn$, and vma as being the best set of covariates. As shown in Figure B.4.46, the selected set with size 6 (including the intercept term) has $C_p = 6.058$, which fits the best. The ANOVA inspection shows that the significant terms include ac , av , $temp$, stn , $rs4s50$, sa , and vma . No interaction terms are regarded as being important.

Through the previous discussion and investigation of regression fitting, the final model chosen for initial stiffness is,

$$E(\ln stif) = 10.6586 - \underset{(0.7081)}{0.2211} ac - \underset{(0.0927)}{0.0607} av - \underset{(0.0095)}{0.0633} temp + \underset{(0.0029)}{0.0703} vma$$

$$R^2 = 0.88.$$

where the $stif$ has the unit MPa and the remainder of the covariates have the same units as listed in Table 4.1.

Notice that the $E(\ln stif)$ term is the expected value of $\ln stif$ and the number in parentheses is the standard error of the parameter estimate. The residual standard error is 0.1824 on 73 degrees of freedom, $R^2 = 0.88$ and the F-statistic pertaining to the test of the hypothesis that all parameters equal zeros is 129.7 on 4 and 73 degrees of freedom, resulting in a p-value of 0. Accordingly, that hypothesis can be rejected.

A graphical representation of the residual analysis of the fit is summarized in Figure B.4.47. Figure B.4.47a shows a plot of estimated residuals versus fitted values.

No evident pattern is observed in this figure indicating that the model is adequately specified for this data set. Figure B.4.47b plots the squared residuals against the fitted responses and exhibits a slightly upward positive dependence of estimated squared residuals on fitted responses, as shown by the lowess²-smoothed line. The assumption of homoskedasticity appears reasonable. Figures B.4.47c and B.4.47d show a normal probability plot and a histogram of the estimated residuals. The figures exhibit nominal skewness and short tails of the distribution. Roughly speaking, the distribution of estimated residuals is close to a normal distribution; in other words, the Gauss-Markov assumption of a normal distribution of the estimated residuals is borne out.

- Fatigue Life

The correlation coefficients shown in the Table A.4.12 indicate the *lnnf* is negatively correlated with the *lnstn* term; however, the *temp* term is slightly positively-correlated with an indistinct correlation coefficient of 0.177. It is suspected that the fatigue life of the coarse gradation is temperature-insensitive. As expected, the higher the strain level the lower the fatigue life. The design plot in Figure B.4.32 indicates that the *stn* term has the most significant effect on fatigue life, while the factors *av*, *temp*, *m200*, *vma*, and *vfa* have only a marginal effect on fatigue life. The factor plot in Figure B.4.39 shows the upward trend of *lnnf* as the temperature increases.

As shown in Figure B.4.48, the best subset chosen based on the Mallows' C_p criterion was the set of *av*, *temp*, *lnstn*, *sa*, and *vfa*, along with a C_p value of 6.220,

² lowess is a Splus command that gives a robust, local smooth of scatterplot data.

which is close to the size 6. The ANOVA results identify *av*, *temp*, *stn*, and *m200* as terms having significant effect, as well as the interaction terms *av*temp* and *temp*stn*.

A compromise based on the previous discussions and regression fitting, the final model determined of fatigue life is:

$$E(\ln nf) = -25.0198 - 0.3716 av + 0.4661 temp - 6.1467 \ln stn - 0.7010 sa - 0.4623 vma \\ + 0.0123 av \cdot temp + 0.0646 temp \cdot \ln stn$$

(5.4150) (0.1372) (0.2110) (0.6148) (0.1771) (0.1168)
(0.0065) (0.0262)

$$R^2 = 0.92 .$$

where the covariates have the same definitions and units as described in Table 4.1.

The residual standard error of the fit is 0.5729 on 69 degrees of freedom, $R^2 = 0.92$ and the F-statistic associated with the test of the hypothesis that all the parameters equal zeros is 114.4 on 7 and 69 degrees of freedom, resulting in a p-value of 0, which refutes that hypothesis.

Figure B.4.49 plots the residual analysis of the fatigue life fit. No strong pattern is perceived in Figure B.4.49a indicating the model specification is correct. In Figure B.4.49b, the squared residuals seems to maintain a constant trend as seen by the lowess-smoothed line. Both the quantile-quantile (Q-Q) plot in Figure 4.49c and the histogram in Figure 4.49d comply with the Gauss-Markov assumptions.

- Coefficients of Weibull Curves

The coefficients of Weibull curves shown in both design and factor plots (Figures B.4.33 through B.4.36 and Figures B.4.37 through B.4.45, respectively) indicate the

significant effect of temperature on this coarse gradation mix. The intercepts, aa and cc , show a convex downward parabolic relation as the temperature increases and seem to have their maximum value around 30°C . The slopes, bb and dd , seem to display an upward parabolic relation as the temperature increase and have their minimum values occurring around 30°C .

When discussing the effect of strain levels on the coefficients of Weibull curves, the 300 and 800 microstrain tests will not be included as their sample size was limited. From the design plots and factor plots (Figures B.4.33 through B.4.36 and Figures B.4.37 through B.4.45, respectively), it seems that no difference is discernible in the effect of tensile strain to the intercept coefficients aa and cc when not considering the 300 and 800 microstrains. However, a slightly upward trend can be perceived, meaning the higher the strain level the larger the fatigue damage.

This same analysis procedure was applied to the fine, fine-plus, and the combination of the fine and the fine-plus gradations. The details of the regression analysis are not presented. Instead, only relevant observations and topics of interest are discussed.

Table 4.3 summarizes the model selection results for each gradation type. The final models of initial stiffness and fatigue life for each gradation are summarized in Table 4.4. In Table 4.3 five statistical measures are utilized as tools to identify the significant factors in model selection. The five statistical measures consist of a correlation matrix designated as C, a design plot (D), a factor plot (F), ANOVA results (A), and Mallow's C_p method (M). If a covariate is identified as significant by one of

the statistical analysis, a check is marked in the box that applies. If five checks are marked for a covariate, then the covariate will be identified as “very important”. If three to four boxes are checked, then the covariate will be regarded as “important”. If only one or two boxes are checked, we will consider it as being a “less important” covariate. The criterion of correlation coefficient to identify the significant factor is set at 0.4. Rather than a quantitative measurement, the criteria for using design and factor plots is subjective and qualitative. Table 4.5 lists the summary statistics of the Weibull coefficients based on gradation types. It uses the same identification procedure as in Table 4.2 to verify the important factors that affect the fatigue damage process.

4.8.5 Regression Analysis Results

Using the same procedure of model selection and regression analysis as shown in Chapter 4.8.4, the identification of significant factors for model selection and the final regression models of initial stiffness and fatigue life are listed in Tables 4.2 and Table 4.4, respectively. The identification of significant factors relating to the fatigue damage process (Weibull equation) is shown in Table 4.5. Table 4.6 presents the associated figures and tables used in the factor identification, model selection, and regression analysis. Notice that the factor plots are listed only for coarse gradation.

From the model selection procedure, as tabulated in Table 4.4, several findings may be addressed as follows:

1. It is obvious that the significance of the temperature’s effect on initial stiffness is similar to that of the strain’s effect on fatigue life. Both factors are very important.

2. The av is an important factor when considering the initial stiffness of fine-plus and the combination of fine and fine-plus gradations.
3. No interaction terms are required when conducting the model selection of initial stiffness, except that the interaction term of ac and av ($ac*av$) is needed for the combination of fine and fine-plus.
4. The temperature factor is important to the gradations of coarse, fine, and the combination of fine and fine-plus, when considering the model of fatigue life.
5. The ac and av are two important factors of the fine-plus gradation in considering the model of fatigue life.
6. The model selection of fatigue life involves various interaction terms, except the fine gradation, for which no interaction term is needed as it is insignificant to the results.

The final regression models of initial stiffness and fatigue life are shown in Table

4.4. Several findings can be summarized as follows:

1. In the stiffness models, ac , av , and $temp$ are the basic covariates constructing the model, in addition, all the coefficients for these three covariates are negative, i.e., the higher the amount of these covariates the lower the stiffness.
2. As for the models of fatigue life, notice that a squared term of temperature is added in the model of the fine gradation whereas no temperature term is presented in the model of the fine-plus gradation; that is to say, statistically, the fine-plus mixes are temperature-insensitive.

The regression models of initial stiffness in the coarse and in the combination of fine and fine-plus are going to be used in the Weibull simulation in Chapter 7.

Table 4.5 lists the results of identifying the significant factors of fatigue damage process. Several findings can be addressed here:

1. Even for various gradation types, the temperature term profoundly affects not only the slopes of the Weibull curves but also the intercepts of the Weibull curves.
2. The strain effect mostly affects the slopes of the Weibull curves for all gradation types.
3. The *ac* effect is much more important to the fine-plus gradation than to any other gradation.

4.9 Flexural Frequency Sweep Test

4.9.1 Test Results

There are two objectives for the flexural frequency sweep test as put forth in the test plan in Chapter 3: (1) determining the compatibility between a modified and a conventional flexural beam setup, and (2) obtaining the flexural stiffness response of asphalt concrete at high temperatures with various loading frequencies. Only four beams were tested, two were coarse medium (CM) mixes and two were fine medium (FM) mixes. The frequency sweep test with the 40C-30C-20C sequence was conducted with a modified fatigue setup and the results were analyzed using the measurements obtained from the strain gage. A piece of Splus code shown in Appendix C was written to

complete the analysis. The frequency sweep test with the 30C-20C-5C sequence was conducted with the conventional fatigue setup and analyzed using LVDT measurements. Table A.4.18 summarizes the test results. Figures 4.28 and 4.29 present the test results for the FM and CM mixes, respectively.

Analysis of the frequency test data suggests the following:

1. In general, the FM mix has a higher value of complex modulus than that of the CM mix with respect to the temperature and loading frequency.
2. For the CM mix, the results of the modified and conventional fatigue setups are highly compatible above a 1 Hz loading frequency at 20°C and 30°C.
3. For the FM mix, the results of the two fatigue setups present a consistent trend but with a tolerable vertical shift above a 0.5 Hz loading frequency at 20°C and 30°C. It is the modified fatigue setup, however, that has a higher estimation.
4. For both mixes, the discrepancies at low loading frequencies, namely from 0.01 Hz to 0.1 Hz, are considerable. Fortunately, the loading frequencies located in this range are out of our interest in terms of the vehicle speeds associated with highways.
5. The test method and the algorithm utilized in calculating the complex modulus of asphalt concrete in the modified fatigue setup are acceptable.

The frequency sweep test results provide information about the complex moduli at various temperatures and various loading frequencies. More importantly, according to the results a mathematical function can be used to describe the phenomenon, thus making

it possible to include the function into the recursive pavement analysis program for the interaction effect of different vehicle speeds and temperatures on the complex moduli of asphalt concrete. The following paragraphs will illustrate one of the possible mathematical functions that can fit the frequency sweep test results.

4.9.2 Fitting with Gamma Distribution Function

The WLF function (Ferry 1980) is widely utilized to find the Master Curve for some reference temperatures. Since the frequencies of interest for a normal highway loading conditions are not found in the extreme values, defining the master curve becomes unnecessary in practice. The main purpose in conducting the nonlinear fitting of the data of frequency sweep tests is to find a suitable mathematical function that can systematically represent the relationship of the complex modulus and loading frequency at various temperatures. The following is a discussion of one of the alternatives. The ability to define a mathematical form for this relationship carries with it the advantage that it can be easily coded for fatigue performance simulations. However, this relationship will not be included in the Weibull dynamic approach at this moment. It is only a conceptual presentation of the possibility of numerically expressing this relationship so that it can be programmed in the simulation approach.

The distribution function of the gamma distribution with shape parameter n (a positive number) and scale parameter β is expressed in the following form (Stone 1996):

$$F(y) = \begin{cases} 1 - e^{-y/\beta} \cdot \sum_{m=0}^{n-1} \frac{y^m}{\beta^m m!} & , y \geq 0 \\ 0 & , y < 0 \end{cases}$$

Figures 4.30 and 4.31 display how the shape and scale parameters interpret the family curves of gamma distribution function. As the same scale parameters are extended from 0.1 to 2 for the shape parameters $n = 2$ and $n = 5$, the difference between these two sets of family curves is readily perceived. It should be noted that the characteristics of the distribution function are (1) the values of y ranged from 0 to 1, (2) the x value starts from zero, and (3) the y value is asymptotic to one as x increases. These aspects of a distribution function are employed in constructing the nonlinear fitting.

The procedure for nonlinear fitting of frequency sweep test data is as follows:

1. Take the natural logarithm for both frequency and complex modulus, i.e., $\ln(\omega)$ and $\ln(S)$.
2. Shift the frequency sweep curve in both x and y directions based on the lowest frequency and the complex modulus at the lowest frequency so that the frequency and complex modulus will start the value from zero, i.e., $\ln(\omega)^* = \ln(\omega) - \ln(\omega_0)$ and $\ln(S)^* = \ln(S) - \ln(S_0)$.
3. Conduct nonlinear fitting on the following formula:

$$\ln(S)^* \sim A \cdot (1 - e^{-\ln(\omega)^*/\beta}) \cdot \sum_{m=0}^{n-1} \frac{(\ln(\omega)^*)^m}{\beta^m m!}.$$

(It is better to fix the n value and estimate the amplitude A and scale parameter β only.)

4. Once satisfactory fitting results are obtained, shift back to the original coordinate system, i.e., the fitting pairs of points are of the form:

$$\left(\ln(\omega), \ln(S_0) + \hat{A} \cdot (1 - e^{-\ln(\omega)^* / \hat{\beta}} \cdot \sum_m^{\hat{n}-1} \frac{(\ln(\omega)^*)^m}{\hat{\beta}^m m!}) \right).$$

Figures 4.32 and 4.33 demonstrate the appropriate nonlinear fit utilizing the Gamma distribution function for tests conducted with the modified and conventional fatigue test setups respectively. The shape parameter $n = 2$ was used for the modified test setup; $n = 3$ was used for the conventional test setup. It was found that the $\hat{A}s$ and $\hat{\beta}s$ are increased as the temperature increases.

4.10 Varied-Strain Fatigue Test

4.10.1 The Strain Effect on Weibull Curves

In the summary Table 4.2, it was found that the strain effect of the fatigue test at 20°C is significant for coefficients bb and dd , which are the slopes of the Weibull curves. Notice that there are only two strain levels of 200 and 400 microstrains. In the hypothesis testing of parallelism (Weibull curves of the same slopes) for these two strain groups (as discussed in Chapter 4.2), it was indicated that different strains cause various fatigue damage rates. At the same test temperature (20°C), no significant strain effect was perceived for the coefficients of aa and cc , which are the intercepts of Weibull curves.

From the temperature susceptibility fatigue test, three fine-plus fatigue test results, designated as WT12FT, WT12DT, and WT21BT, are plotted together in terms of $\ln(-\ln(SR))$ versus $\ln(\ln(n))$, as illustrated in Figure 4.34. The detailed mix information of these three beams is listed in Table A.4.2. They were conducted at 20°C and at three strain levels of 200, 300, and 400 microstrains. The three Weibull curves are straight and mutually parallel, indicating that the Weibull assumption is tenable. As visualized in Figure 4.34, it displays a contradictory result as compared with the strain effect summarized in Table 4.2, i.e, the strain effect should reflect on the change of slopes of the Weibull curves. The distance between the 200 and 300 microstrain curves is distinctly greater than the distance between the 300 and 400 microstrain curves. It would seem that, for fine-plus mixes, the strain effect affects the intercept of the Weibull curves rather than the slopes. It is suspected that this phenomenon is mix-dependent. The plot of stiffness ratio versus repetition and the plot of stiffness versus repetition are shown in Figures 4.35 and 4.36, respectively.

4.10.2 A Hypothesis of Strain-Caused Fatigue Damage

Whether the strain's effect is upon the slopes or the intercepts of the Weibull curves, it is acknowledged that when the strain level changes the fatigue damage process must be changed accordingly. The question then is how to model or describe the fatigue damage process.

Also, it should be noted that, for a simple fatigue test, the test beam is subjected to a constant strain level throughout the test. If the material experiences various strain levels rather than a constant strain level during its service life, how then will the fatigue

damage process behave? To answer this question, a hypothesis is postulated and several sequential fatigue tests are performed to confirm the hypothesis. The hypothesis put forth is:

Hypothesis 1: *If the tensile strain level changes from one level to the other at a given instant (repetition), whereas all other variables remain unchanged, the stiffness deterioration rate will follow the rate of the new level, starting immediately at that specific instant (repetition).*

4.10.3 Test Results and Analysis

According to the test plan of Chapter 3, two 200-400-200 tests, two 400-200-400 tests, one 400-200 test, and one 200-400 test were conducted at a temperature of 20° C, with a loading frequency of 10 Hz, and with a conventional fatigue test setup. Two pre-existing fatigue tests with similar mix properties are utilized as comparison tests. The change (in strain) points for the sequential fatigue tests were carefully selected so as to avoid the following dilemma: the lower strain level will introduce more variance but will have a longer time span; whereas the higher strain level will have less variance but a shorter time span. Accordingly, the change points chosen were at 20,000 and 100,000 repetitions for the 200-400-200 and 400-200-400 tests. For the 400-200 and 200-400 tests, the change point was set at 20,000 repetitions. The air-void content and the asphalt content were about the same for all mixes with coarse gradation in this test series (as shown in Table 4.7).

Recognizing that common engineering sense dictates that the strain level should not affect the initial stiffness, the stiffness ratios calculated for the sequential varied-strain fatigue test were directly divided by the initial stiffness. Figure 4.37 plots the 200-400-200 test results in terms of SR versus repetition (in logarithmic scale). As seen from the figure, several observations can be made:

1. At the beginning, i.e., the 200 microstrain phase, the stiffness deterioration rate is close to the simple 200 microstrain fatigue test.
2. In the second phase, i.e., the 400 microstrain phase, the stiffness deterioration rate sharply drops down and then gradually comes into compliance with the rate of the simple 400 microstrain fatigue test.
3. In the last phase, i.e., back to the 200 microstrain, the stiffness ratio immediately jumps up to approximately 10 % more than, and then slowly deteriorates until matching up with, the deterioration rate of the simple 200 microstrain fatigue curve.

As seen in Figure 4.38, which plots the test results of a 400-200-400 sequential fatigue test, the following observations can be made:

1. In the first phase, that of 400 microstrain, the stiffness deterioration rates are following the same rate as that of a simple 400 microstrain fatigue test.
2. In the second phase, that of 200 microstrain, the SRs have been raised up about 5 % and display no obvious stiffness deterioration, in fact, one even shows a slightly upward trend.

3. In the final phase of 400 microstrain, the deterioration rate accelerated and finally complied with the curve of the simple 400 microstrain fatigue test.

For the 400-200 test, shown in Figure 4.39, the stiffness deterioration rate agrees with the simple 400 microstrain fatigue test at the beginning; thereafter, the stiffness ratio raises up about 5-10 % and then gradually comes to match the deterioration rate of a simple 200 microstrain fatigue test when the strain level switches to 200 microstrains.

In the 200-400 test (Figure 4.40), which switches from a situation of less damage to one of higher damage, the trend of the deterioration curve is in harmony with the simple 200 microstrain test at the beginning, then the stiffness ratio drops down and finally comes to match that of a simple 400 microstrain test.

One thing common to these fatigue tests is that the deterioration rate eventually follows the simple fatigue test curve of the final stage. Initially, the stiffness deterioration rate of each fatigue test complies consistently with the rate of its related simple fatigue test. However, the transition period, here defined as the time needed for the asphalt concrete to adjust itself to a change of strain level, is different for the case of less damage to higher damage (e.g., 200 to 400 microstrains) and in the case of higher damage to less damage (e.g., 400 to 200 microstrains). It shows that the transition period of the case from a higher to a lesser damage level is shorter than that of less to higher. It also illustrates that the stiffness ratio always increases when the strain level switches from a case of high damage to one of less damage.

It is this transition period that makes the test results seemingly incompatible with the hypothesis, especially the part that states, “the stiffness deterioration rate will follow

the rate of the new level, starting immediately at that specific instant (repetition).” Although the test results are “real”, let’s think of an “ideal” material, i.e., a material that can adjust itself in no time when the environmental factor are changed. With this “ideal” material, then, no transition period is called for, and the hypothesis then fits perfectly. Therefore, it is concluded that the hypothesis will hold true if, and only if, the material is an “ideal” material.

Figure 4.41 present the test results of all the fatigue tests. The same information is also illustrated in Figure 4.42 but in terms of stiffness versus repetition. In Figure 4.42, the values of initial stiffness of the fatigue tests are scattered from 6,000 MPa to 9,000 MPa. One of the advantages to utilizing the stiffness ratio instead of stiffness is to eliminate the variation of the data as seen in this figure.

An alternative way to verify the fatigue damage process caused by the strain effect among various sequential fatigue tests is to plot the cumulative dissipated energy versus repetitions as demonstrated in Figure 4.43. Several findings utilizing the dissipated energy to identify the strain pattern can be summarized as follows:

1. The rates of change of cumulative dissipated energy are the same for both the 200 and 400 microstrain levels, as shown by two parallel straight lines on the logarithmic scale of repetition. At a given repetition, the 400 microstrain fatigue test possesses higher cumulative dissipated energy than that of a 200 microstrain fatigue test.
2. The rate of change of cumulative dissipated energy initially follows a straight line (on a logarithmic scale of repetition) and eventually becomes flat. It is believed that observed macrocracks start to propagate when the rate flattens.

3. When the strain level switches from low to high, the rate starts to increase and then slow down until it matches the rate of the higher level; conversely, when switching from high to low the rate starts to decrease until slowly complying with the rate of the lower level.
4. The variation of the cumulative dissipated energy curve is relatively negligible as compared to that of the stiffness ratio plot. Although the energy approach demonstrates its advantages over the stiffness ratio approach, it is still hard to replace the stiffness ratio with the cumulative dissipated energy because it is hard to measure and define the magnitude of energy in real pavement.

4.11 Varied-Temperature Fatigue Test

4.11.1 The Temperature Effect on Weibull Curves

In the temperature susceptibility fatigue tests shown in Table 4.2, it is clear that the temperature effect significantly affects not only the initial stiffness but also the slopes and intercepts of the Weibull curves. Several fatigue tests of coarse mixes were extracted from the temperature susceptibility fatigue tests and the high temperature fatigue tests and were plotted together in terms of $\ln(-\ln(SR))$ versus $\ln(\ln(n))$ as shown in Figure 4.44. Figures 4.45 and 4.46 also present the same information but with different axes. The slopes of the Weibull curves are obviously affected by the temperature. The 5 °C curve has a sharper inclination than do other temperatures, the 40 °C curve has the flattest slope, and the test at 40 °C seems to introduce much temperature variation. The pattern of gradually changed slopes is quite clear among the 5 °C, 20 °C, and 30 °C tests; the

curve of 40 °C, however, does not jibe with this pattern. This figure also shows that the fatigue test results from the modified fatigue test setup are very consistent with the fatigue test results obtained from the conventional fatigue test setup at 30 °C.

4.11.2 A Hypothesis of Temperature-Caused Fatigue Damage

The effect of temperature on the fatigue damage process is evident provided that the asphalt concrete encounters the same temperature throughout its life. This is definitely too simple to reflect the real world; asphalt pavement in the field is subjected to daily and seasonal variations of temperature, a far cry from a lifetime exposure to a constant temperature. Subsequently, the question raised is how the fatigue damage process behaves when subjected to temperature variation. A hypothesis similar to the hypothesis of strain-caused fatigue damage is proposed and several varied-temperature sequential fatigue tests will be conducted to verify this hypothesis. The hypothesis put forth here is:

Hypothesis 2: *If the temperature changes from one level to the other at a given instant (repetition), whereas all other variables remain unchanged, the stiffness deterioration rate will follow the rate of the new level, starting immediately at that specific instant (repetition).*

In other words, when the temperature varies from one level to a higher level, the stiffness deterioration will continue as though it has been deteriorating at the higher temperature level; conversely, when the temperature changes from one level to a lower

level, the stiffness deterioration will continue as though it has been deteriorating at the lower temperature level.

4.11.3 Test Results and Analysis

According to the test plan of Chapter 3, this hypothesis will be confirmed using four varied-temperature fatigue tests, consisting of two 30-20-30 tests, two 20-30-20 tests, one 30-20 test, and one 20-30 test. All tests were conducted at the 400 microstrain level with a loading frequency of 10 Hz and a conventional fatigue test setup. Two pre-existing fatigue tests with similar mix properties were utilized as comparison tests. The change points for the sequential varied-temperature fatigue tests were carefully selected so as to allow enough time for the temperature inside the asphalt concrete beam to stabilize when the temperature has been changed from one level to another level. In addition, another concern was that the fatigue life should cover the phase change of temperature. Figure 4.47 demonstrates the time needed for an asphalt concrete beam to stabilize its temperature from 30°C to 20°C and vice versa. As seen in the figure, the time needed to stabilize the temperature is about one and half hours either from 30°C to 20°C or from 20°C to 30°C. To obtain the data shown in Figure 4.47, a hole, roughly the same diameter as the temperature sensor, was drilled in one end of the beam to a depth of about 10 cm, the sensor plug was inserted, the temperature switched, and the temperature change inside the beam was recorded. Accordingly, the change (in temperature) points chosen were at 3,000 and 57,000 repetitions for the 30-20-30 and 20-30-20 tests. For the 30-20 and 20-30 tests, the change point was set at 3,000 repetitions. The major mix properties of these specimens are listed in Table 4.8.

As stated previously, the initial stiffness is profoundly affected by temperature variation. The stiffness at 30°C is less than the stiffness at 20°C. Henceforth, if presented in terms of SR, the stiffness needs to be divided by appropriate initial stiffness at various temperatures. In doing so, a regression equation of initial stiffness and a temperature variation curve of the beam are necessary to interpolate the initial stiffness in between 20°C and 30°C. No two beams are given the same initial stiffness, even those with the same mix. Thus, for a 20-30-20 and a 30-20-30, or a 30-20 and a 20-30 tests, the awkward situation encountered is that we might easily obtain the initial stiffness at the first temperature of each test but be unable to obtain the initial stiffness at the second temperature. Therefore, utilizing the original stiffness to characterize the property of the fatigue damage process due to the temperature variation is recommended.

Figure 4.48 shows the test results of a 20-30-20 test and two simple fatigue tests at 20°C and 30°C respectively. The two 20-30-20 test curves agree exactly, except in the tail part. Before repetition 3,000, the deterioration rates of the two 20-30-20 tests and a simple fatigue test at 20°C test are almost identical. Notice that, after repetition 111,000, the stiffness deterioration rates of the two 20-30-20 tests are again in compliance with the rate of a simple fatigue test at 20°C.

Two 30-20-30 tests as well as one simple fatigue test at 20°C and one at 30°C are presented in Figure 4.49. The two 30-20-30 test curves resemble the dorsal fin of a killer whale in shape. The stiffness varies proportionally with the temperature. The stiffness stabilizes and then starts to deteriorate once a steady temperature is reached. As seen in the figure, when the temperature raises back up to 30°C, the deterioration rates of these two tests are again compatible with that of the simple fatigue test at 30°C.

Figures 4.50 and 4.51 give an even clearer picture of how the stiffness deteriorates while the temperature changes. As seen in these two figures, the deterioration rate immediately follows the single temperature rate at the time when the temperature of the beam stabilizes at a new level.

Figure 4.52 summarizes all the temperature-varied fatigue tests to show the corresponding relationships among various tests.

For the controlled-strain fatigue tests with the same test strain, the temperature effect on the cumulative dissipated energy is difficult to perceive, as is illustrated in Figure 4.53. Hence, it is not possible to identify the temperature effect on the fatigue damage process utilizing only the cumulative dissipated energy as a tool. Practically, either the stiffness or the SR is a more accessible and useful tool in identifying not only the strain effect but also the temperature effect.

As in the discussion of the varied-strain fatigue test, let's refer again to an "ideal" material, a material which can adjust itself in no time when the environmental factors are changed. Therefore, the transition period will approach zero if the material is an ideal material. It is also concluded that the hypothesis holds true if, and only if, the material is an "ideal" material. The hypothesis of temperature change as contributing to the fatigue damage process is hereby verified without any further proof.

Given that the tests conducted in this study are not enough to include all the possible covariates, the test results simply reveal possible trends that provide clues as to what asphalt concrete encounters during a temperature change.

4.12 Findings and Discussions

4.12.1 Findings in Fatigue Test Results and Regression Analysis

In summarizing the fatigue test results, it was found that the temperature effect on the stiffness and the strain effect on the fatigue life are two effects that are more prominent than those caused by the other material variables. The test results also show that the effect of various gradation types on either the stiffness or the fatigue life is evident. In general, the coarse gradation has better fatigue performance than the fine gradation. However, this finding is at odds with the condition survey data of WesTrack. It might be conjectured that the conventional fatigue analysis, which is based on the assumption of crack initiation at 50 % stiffness reduction, cannot describe the crack propagation phenomenon as it occurs in cold weather.

Upon inspection of the regression results of this study, it was also found that determining the effect of temperature on stiffness and the strain effect on fatigue life provides two primary means of assessing the stiffness and fatigue performance, respectively, of an asphalt concrete material. In this study, no matter what types of fatigue tests were conducted, or gradation types tested, it is clear that this is true.

The conventional regression analysis for fatigue life cannot fully describe the fatigue damage process because instead of taking into account all the points that in combination make-up the fatigue damage process, it only considers the fatigue life at a prescribed failure level, such as a 50 % stiffness reduction. Thus, a conventional fatigue curve, which is plotted in terms of fatigue life versus strain level, contains the fatigue lives as tested at various strain levels with the same mix. A large body of information

pertaining to the fatigue damage process is not collected, thus making it ineffective to apply such an analysis to the prediction of fatigue performance.

4.12.2 Fatigue Life versus Temperature versus Strain Level

Two environmental factors, temperature and strain, greatly affect the magnitude of fatigue life, as seen in Figures 4.54 and 4.55, respectively. The boxplots of Figure 4.54 show a relatively flat and then slightly upward curving relationship of fatigue life versus temperature as the temperature increases. Notice that in Figure 4.54 the data variation for each test temperature was contributed to by all other variables including those of mix properties: *grad*, *ac*, *av*, *rs4s50*, *m200*, *sa*, *vma*, *vfa*, as well as an environmental factor, *stn*. Regardless, these contributors do not obscure the apparent effect of temperature. Likewise, the boxplots of Figure 4.55 demonstrate an even stronger deleterious relationship of fatigue life versus strain level despite the data variation introduced to them by all other variables except the strain level. This signifies not only that temperature and strain level are important factors in determining the magnitude of fatigue life, but also that the strain level is a stronger determinant in regards to fatigue life than is temperature.

In actuality, the strain level and the temperature are two factors that are interrelated in a real pavement. It is known that a temperature change causes the stiffness to change and thus results in a change of strain levels in a pavement while still subjected to the same traffic load. Insofar as determining what the magnitude of this interaction effect is, further study is warranted.

4.12.3 Crack Initiation and Crack Propagation

It has come to be widely thought that the crack development within an asphalt concrete material should consist of two obvious stages, namely crack initiation and crack propagation. Although a phenomenological-and-statistical definition has been proposed in this study as illustrated in Figure 4.6, a greater understanding of crack initiation and propagation from the mechanistic point of view could be achieved by further exploration with a more refined test setup and a more strict definition.

4.12.4 Weibull Curves at Extreme Test Temperatures

Normally, there are three types of Weibull curves encountered when analyzing fatigue tests: the “reversed-S”, the “falling-C”, and the straight-line type. The reversed-S type of Weibull curves always occurs at low to intermediate temperatures, whereas the falling-C type of Weibull curves occur at high temperatures, as seen in Figure 4.56. The reversed-S shape of a Weibull curve implies that the fatigue failure (or macrocrack) after the initiation and early development stages starts to accelerate and results in a quick drop-down of stiffness ratio, likely as a result of the asphalt-aggregate mix’s tendency to be brittle at low to intermediate temperatures. As for the falling-C shaped curves, these indicate that the stiffness deterioration is slowing down after passing the crack initiation phase. It is conjectured that the asphalt-aggregate mixes at high temperatures tend to be soft and flexible, possibly relieving some tension on micro-cracks developed in the crack initiation phase, thus slowing the propagation of the crack. Another observation, discernible in Figure 4.5, is that the conventional failure criterion of fatigue life of a 50 %

stiffness reduction seems to be an appropriate criterion in defining the end of the crack initiation stage.

4.12.5 Coefficients of Weibull Curves

Recall that the coefficients *aa*, *bb*, *cc*, and *dd* of the Weibull curves were obtained in such a way that, for each fatigue test, only the data located inside the crack initiation stage were chosen. As listed in Tables A.4.1 through A.4.5 for various types of fatigue tests, it shows that the R-squared values of the fitting of a Weibull survivor function are consistently high. Therefore, it is concluded that a Weibull survivor function is well-suited to describe the fatigue damage process in crack initiation. Generally, the fitting in terms of $\ln(-\ln(SR))$ against $\ln(\ln(n))$ has a better fit in the warm-up stage (phase I) as compared with the fitting in terms of $\ln(-\ln(SR))$ against $\ln(n)$.

4.12.6 Problems of the High Temperature Fatigue Test

Two main problems were encountered with the high temperature fatigue testing as conducted in this study. First, by inspecting the data variations of the stiffness deterioration curves, the temperature seems to have not been fully controlled. Secondly, prior to testing it was unclear whether to utilize strain gage control or to adopt LVDT control. It was found that, under strain gage control, the asphalt-aggregate mix might relax itself under the repetitive loading; as a result, in order to maintain the desired strain level, the vertical actuator gradually moves up and eventually hits the limit. However, if run under LVDT control, the strain recorded from the strain gage shows that the strain will be gradually decreased as time goes on.

Therefore, test results obtained with either control method are contaminated by a certain degree of error. Further refinement of the test setup and data acquisition system is necessary so as to obtain fully controlled and accurate test results. Additionally, the flexural fatigue beam machine should be equipped with a better environmental control unit for improved control over testing temperatures.

4.12.7 A General Hypothesis of Fatigue Damage

It has been recognized in this data analysis that the tensile strain level and temperature are two extremely important factors affecting the fatigue damage process. However, the interaction effect of temperature and strain level has not been earmarked for inspection in this study. In the verification procedure of hypotheses 1 and 2, we assume the beams to have the same (or similar) mix properties and vary only one factor, either temperature or strain level, each time. However, variations of the design material variables or testing conditions makes a noticeable difference on the stiffness deterioration curves even with the same mix and at the same temperature. Thus, we conclude another important feature observed in these tests is that each stiffness deterioration curve is unique among its peers within the corresponding testing condition. Accordingly, a hypothesis can be stated as follows:

Hypothesis 3: *For every testing situation containing many variables, there exists one and only one associated stiffness deterioration curve in the SR-N space. If the testing situation changes from one state to the other at a given*

instant (repetition), the stiffness deterioration rate will follow the rate of the new state, starting immediately at that specific instant (repetition).

It is expensive in terms of both time and cost to conduct such hypothesis testing, not to mention that there was only a limited amount of material available from the WesTrack project. In the next chapter, it is taken for granted that hypothesis 3 holds true without any further validation.

4.12.8 Time Hardening and Strain Hardening

Monismith et. al. (1975), utilized “Time Hardening” and “Strain Hardening” procedures to obtain the cumulative permanent strain from the results of simple loading tests. Unfortunately, neither method was very successful in quantitatively describing the experiment data. These two methods are summarized in Figure 1.6.

Revisiting the ideas of the “Time Hardening” and the “Strain Hardening” procedures, Figures 4.57 through Figure 4.60 schematically illustrate the application of these procedures to the fatigue damage process as expressed by stiffness ratio versus time (or repetition). The plot applying the time hardening procedure from low damage level to high damage level is shown in Figure 4.57a. The trajectory of the final stiffness deterioration curve combined from the simple fatigue tests presents an unconventional curve, as seen in Figure 4.57b, one which is not very smooth. As for the damage level being switched from high to low, as viewed in Figure 4.58a, a problem arises in that there is no available curve that can be intersected to continue the procedure. The compound stiffness deterioration curve is shown in Figure 4.58b.

Figures 4.59 and 4.60, respectively, display the application of the strain hardening procedure to the fatigue damage process from low damage level to a high damage level and vice versa.

As verified by the varied-strain and varied-temperature fatigue tests conducted, the appropriately corresponding hypotheses are actually in favor of the strain hardening procedure. Based on the limited number of fatigue tests run, no strong evidence for rejection of the hypotheses was presented. By the same token, there was no proof evident that can strongly support the hypotheses either. Therefore, it is worthwhile to continue the study of the fatigue damage process especially as subjected to varied strains and temperatures.

Table 4.1. Covariates investigated in Chapter 4.

Covariate	Description	Units
<i>grad</i>	Gradation type	NA
<i>ac</i>	Percent asphalt content	%
<i>av</i>	Percent air-void content	%
<i>stn</i>	Test strain level	Microstrain
<i>rs4s50</i>	Ratio of the percent passing the 4.75 mm (#4) and 0.3 mm (#50) sieves	NA
<i>m200</i>	Percent passing the 0.075 mm (#200) sieve	%
<i>sa</i>	Blended aggregate surface area	m ² /kg
<i>vma</i>	Percent voids in mineral aggregate	%
<i>vfa</i>	Percent voids filled with asphalt	%
<i>temp</i>	Test temperature	°C

Note:

1. NA: not available

2. $vma = \left[\frac{V_T - V_{agg}}{V_T} \right] \times 100\%$, where V_T = total volume of mix, V_{agg} = volume of aggregate.

3. $vfa = \left[\frac{V_{asp}}{V_T - V_{agg}} \right] \times 100\%$, where V_{asp} = volume of asphalt.

Table 4.3. Model selection of stiffness and fatigue life of the WesTrack project.

Type of Gradation model	Coarse					Fine					Fine-plus					Fine + Fine-plus					
	C	D	F	A	M	C	D	F	A	M	C	D	F	A	M	C	D	F	A	M	
<i>Instif</i>	covariate																				
	<i>grad</i>				√				√						√						√
	<i>ac</i>				√				√						√						√
	<i>av</i>				√				√						√						√
	<i>temp</i>	√	√	√	√	√	√	√	√	√	√	√	√	√	√	√	√	√	√	√	√
	<i>stn</i>				√				√						√						√
	<i>rs4s50</i>				√				√						√						√
	<i>m200</i>				√				√						√						√
	<i>sa</i>				√				√						√						√
	<i>vma</i>				√				√						√						√
<i>yfa</i>															√					√	
Interaction term from ANOVA	none										none					<i>ac*av</i>					
<i>lmf</i>	<i>grad</i>																				
	<i>ac</i>																				
	<i>av</i>				√				√						√						√
	<i>temp</i>			√	√	√	√	√	√	√	√	√	√	√	√	√	√	√	√	√	√
	<i>stn</i>	√	√	√	√	√	√	√	√	√	√	√	√	√	√	√	√	√	√	√	√
	<i>rs4s50</i>																				
	<i>m200</i>				√				√						√						√
	<i>sa</i>																				
	<i>vma</i>																				
	<i>yfa</i>																				
Interaction term from ANOVA	<i>av*temp, temp*stn</i>										none					<i>av*stn, av*rs4s50, av*m200</i>					

Note: 1. C: correlation matrix; D: design plot; F: factor plot; A: ANOVA result; M: Mallows' Cp.
 2. The five-in-a-row diagonal shaded area means the covariate is "very important" to the corresponding response variable.

Table 4.4. Final regression models of stiffness and fatigue life of the WesTrack project.

Regression Model for Stiffness			R^2
Type of Gradation	Model Specification		
Coarse	$E(\ln stif) = 10.6586 - 0.2211 ac - 0.0607 av - 0.0633 temp + 0.0703 vma$ (0.7081) (0.0927) (0.0095) (0.0029) (0.0306)		0.88
Fine	$E(\ln stif) = 9.9468 - 0.1752 ac - 0.0846 av - 0.0570 temp + 0.3898 rs4s50$ (0.5593) (0.0480) (0.0092) (0.0026) (0.1238)		0.89
Fine plus	$E(\ln stif) = 12.1807 - 0.3409 ac - 0.0980 av - 0.0595 temp$ (0.3075) (0.0455) (0.0087) (0.0036)		0.86
Fine + Fine plus	$E(\ln stif) = 11.3220 - 0.2133 ac - 0.0808 av - 0.0548 temp$ (0.1941) (0.0304) (0.0055) (0.0021)		0.87
Regression Model for Fatigue Life			R^2
Type of Gradation	Model Specification		
Coarse	$E(\ln nf) = -25.0198 - 0.3716 av + 0.4661 temp - 6.1467 \ln stn - 0.7010 sa - 0.4623 vma$ (5.4150) (0.1372) (0.2110) (0.6148) (0.1771) (0.1168) $+ 0.0123 av \cdot temp + 0.0646 temp \cdot \ln stn$ (0.0065) (0.0262)		0.92
Fine	$E(\ln nf) = -22.9544 - 0.2030 av - 0.1805 temp + 0.0071 temp^2 - 4.6276 \ln stn$ (2.3022) (0.0394) (0.0422) (0.0010) (0.2708)		0.85
Fine plus	$E(\ln nf) = -25.1391 + 0.3354 av - 0.2175 av - 4.7373 \ln stn - 0.2484 m200$ (1.9349) (0.1747) (0.0338) (0.1771) (0.1391)		0.93
Fine + Fine plus	$E(\ln nf) = -33.4822 - 0.1206 av + 0.4443 temp - 4.6667 \ln stn + 1.0204 m200 + 0.0342 vfa$ (2.1271) (0.0319) (0.0655) (0.1823) (0.3033) (0.0074) $- 0.0779 m200 \cdot temp$ (0.0136)		0.86

Note: 1. The "E" in model specification stands for "Expected".

2. The number inside the parentheses is the standard error of regression coefficient.

Table 4.6. Associated figures and tables for regression analysis.

Gradation Type	Figures				Tables
	Design Plot	Factor Plot	Mallow's Cp Plot	Residual Plot	Correlation Matrix
Coarse	B.4.31-B.4.36	B.4.37-B.4.45	B.4.46, B.4.48	B.4.47, B.4.49	A.4.12
Fine	B.4.50-B.4.55	NA	B.4.56, B.4.58	B.4.57, B.4.59	A.4.13
Fine-Plus	B.4.60-B.4.65	NA	B.4.66, B.4.68	B.4.67, B.4.69	A.4.14
Fien and Fine-Plus	B.4.70-B.4.75	NA	B.4.76, B.4.78	B.4.77, B.4.79	A.4.15

Table 4.7. Mix properties for the varied-strain fatigue test.

Specimen	Strain sequence	Gradation	AC	AV
WTCM57-2CA	200-400-200	CM	5.7	7.1
WTCM57-20CB	200-400-200	CM	5.7	7.6
WTCM57-26CA	400-200-400	CM	5.7	7.3
WTCM57-18CA	400-200-400	CM	5.7	7.3
WTCM57-28CA	400-200	CM	5.7	5.6
WTCM57-28CB	200-400	CM	5.7	5.6
WT23AT	400	CM	5.78	5.5
WT23DT	200	CM	5.78	7.1

Table 4.8. Mix properties for the varied-temperature fatigue test.

Specimen	Strain sequence	Gradation	AC	AV
WTCM57-4CB	20-30-20	CM	5.7	7.3
WTCM57-6CB	20-30-20	CM	5.7	7.0
WTCM57-6CA	30-20-30	CM	5.7	7.5
WTCM57-16CB	30-20-30	CM	5.7	7.6
WTCM57-24CB	30-20	CM	5.7	6.8
WTCM57-10CA	20-30	CM	5.7	7.6
WT23FT	30	CM	5.78	6.0
WT23AT	20	CM	5.78	5.5

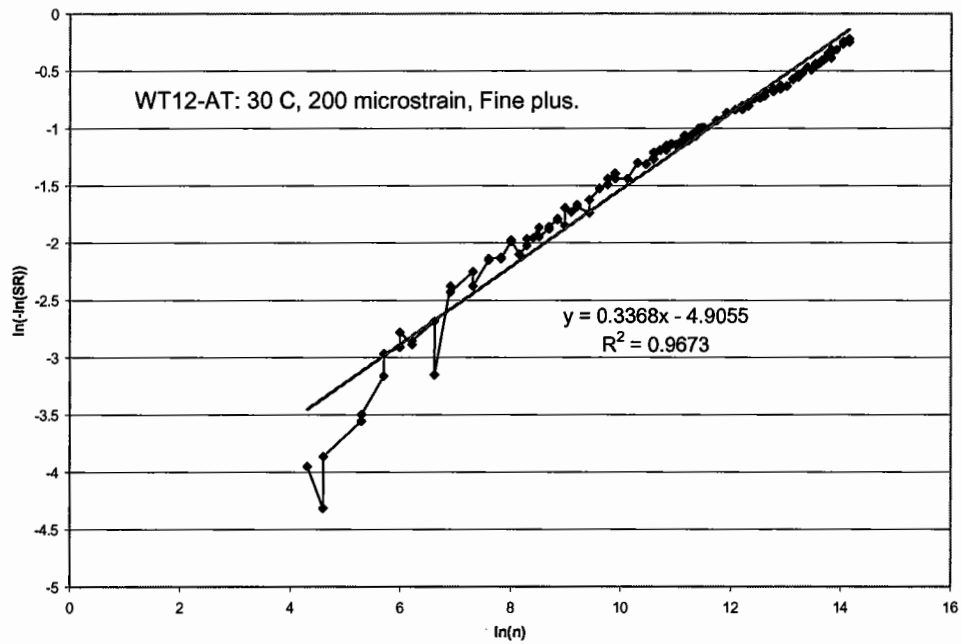


Figure 4.1. An example of fitting the Weibull survivor function to a fatigue test result in terms of $\ln(-\ln(SR))$ versus $\ln(n)$.

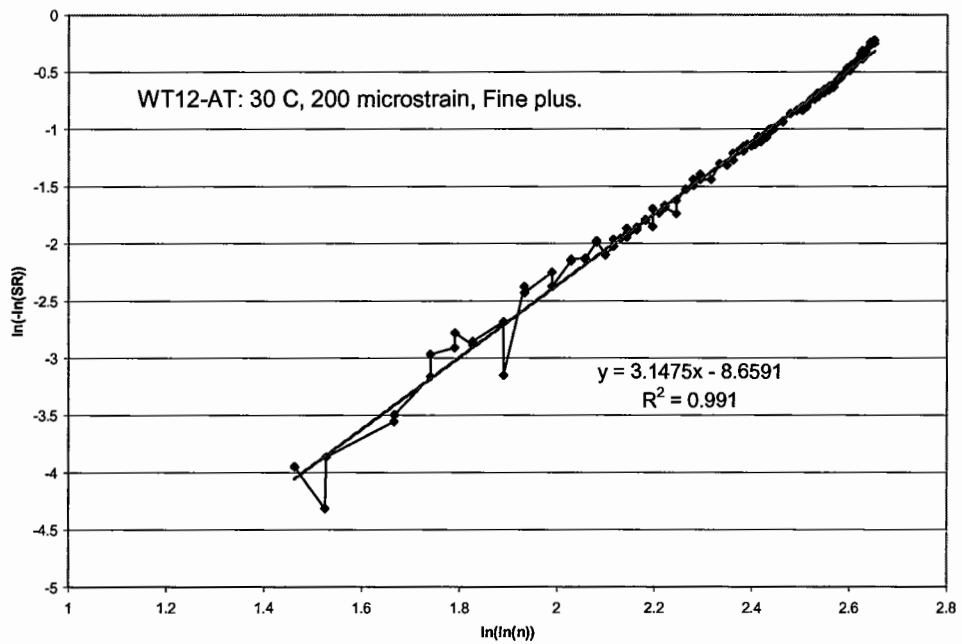


Figure 4.2. An example of fitting the Weibull survivor function to a fatigue test result in terms of $\ln(-\ln(SR))$ versus $\ln(\ln(n))$.

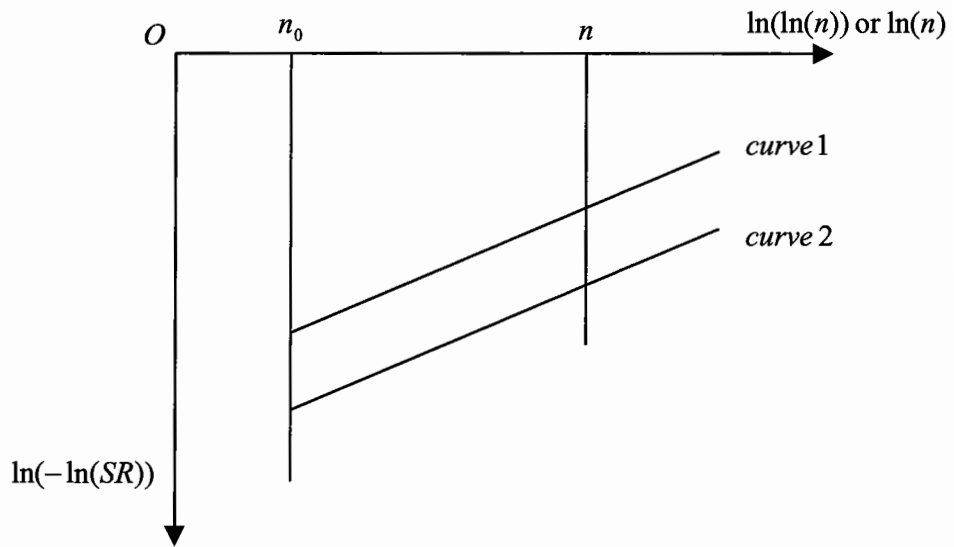


Figure 4.3. Two parallel Weibull curves.

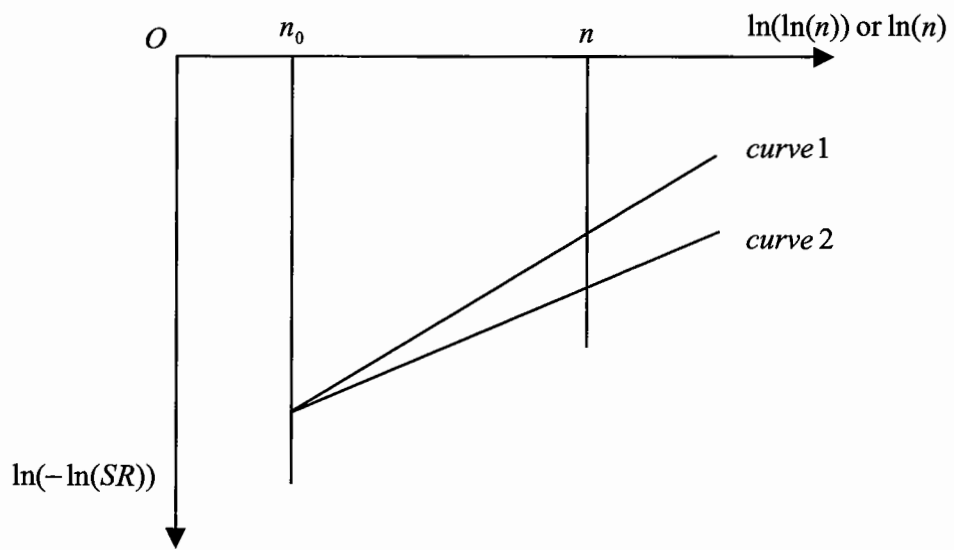


Figure 4.4. Two concurrent Weibull curves.

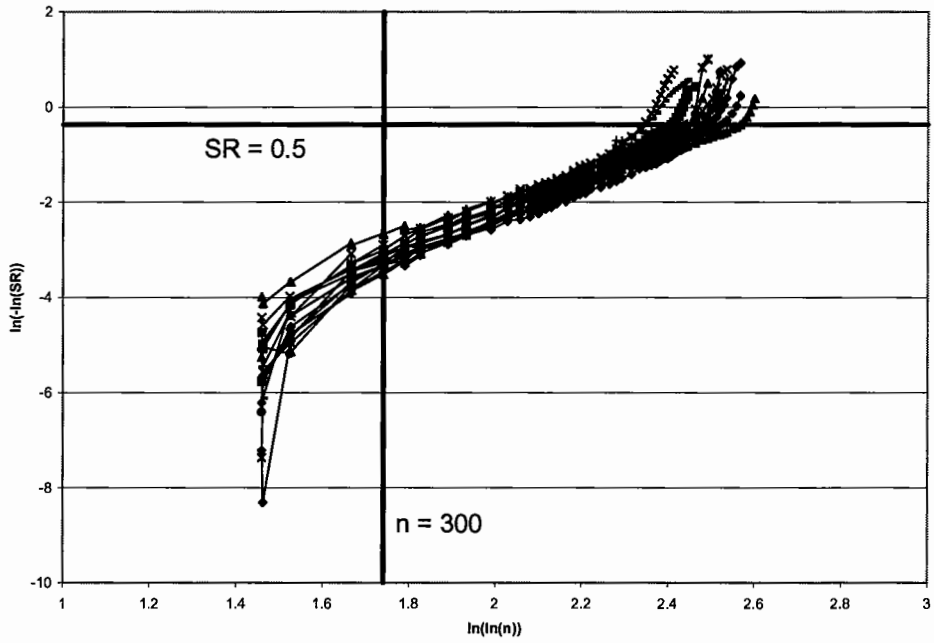


Figure 4.5. Weibull curves in reversed S shape.

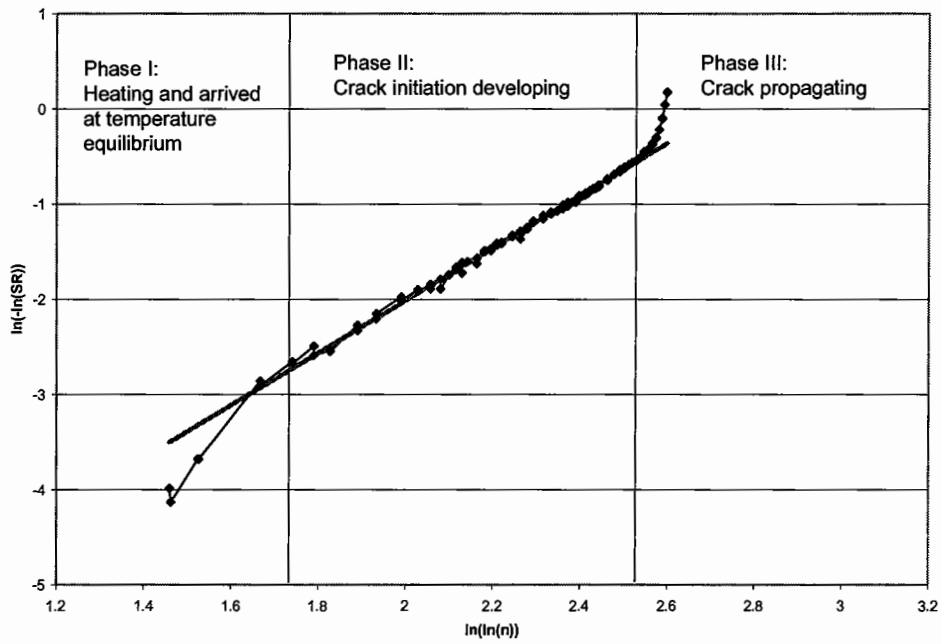


Figure 4.6. Weibull curve in three phases: (1) Phase I: Heating and arrived at temperature equilibrium, (2) Phase II: Crack initiation developing, and (3) Phase III: Crack propagating.

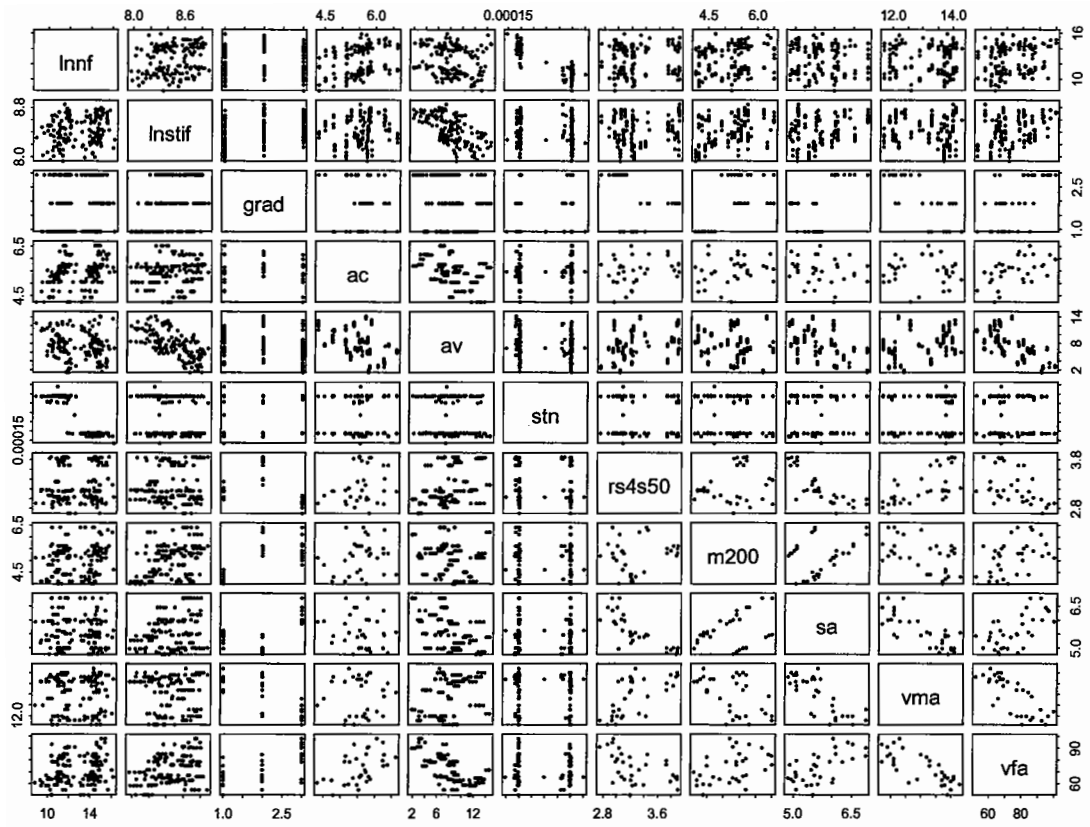


Figure 4.7. Pairs diagram for *instif* and *lnnf* (fatigue tests at 20°C).

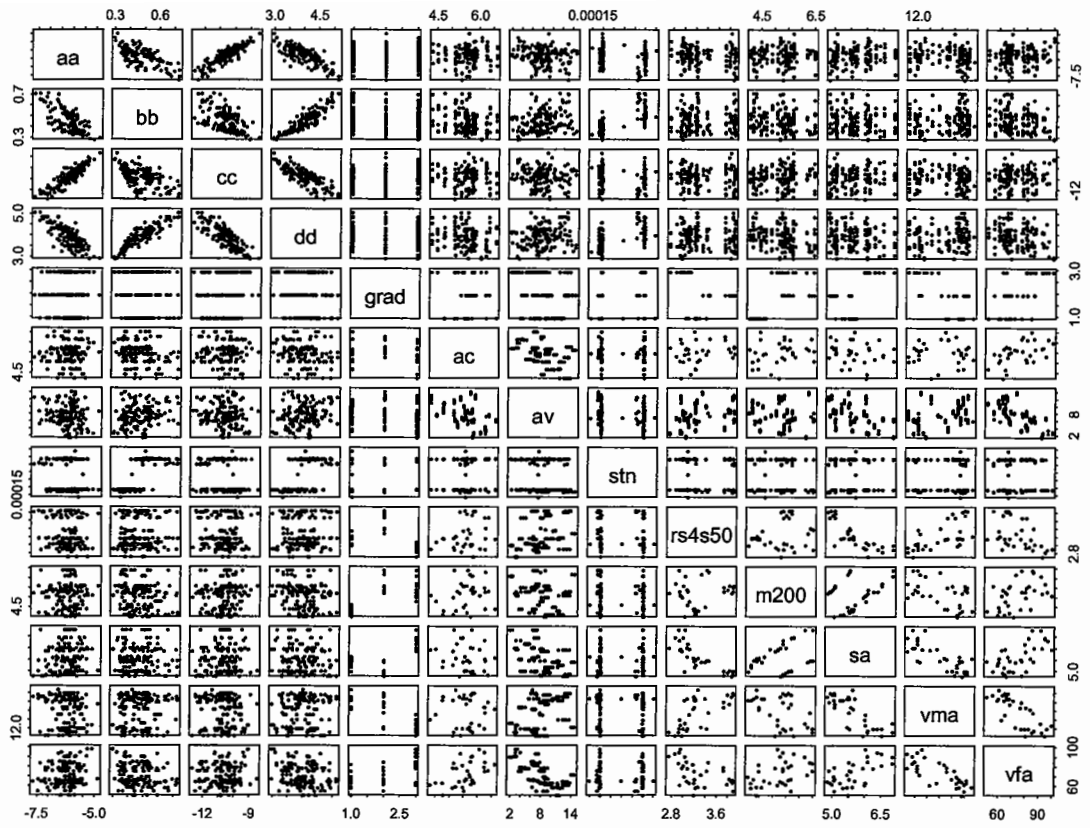


Figure 4.8. Pairs diagram for the regression coefficients aa , bb , cc , and dd of the Weibull curves (fatigue tests at 20°C).

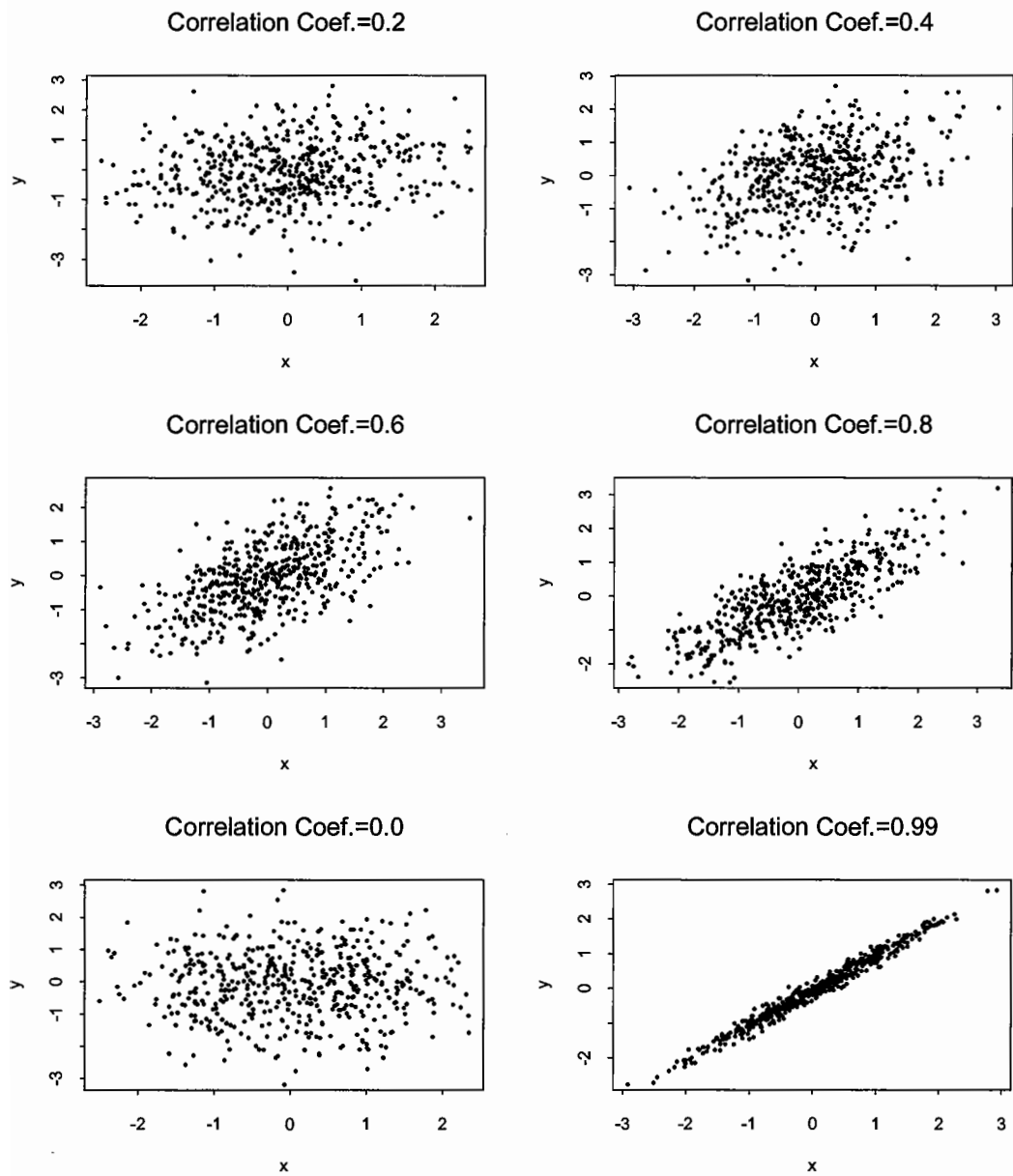


Figure 4.9. Scatterplots of 500 independent pairs of bivariate normal random variables with correlation coefficient $\rho = 0.2$, $\rho = 0.4$, $\rho = 0.6$, $\rho = 0.8$, $\rho = 0.0$, and $\rho = 0.99$.

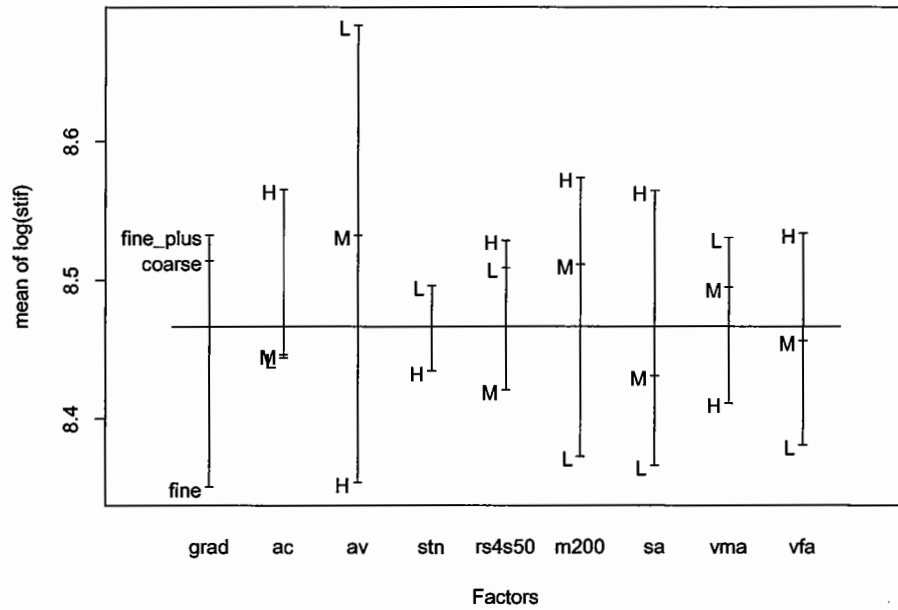


Figure 4.10. Design plot of *lnstif* (fatigue tests at 20°C).

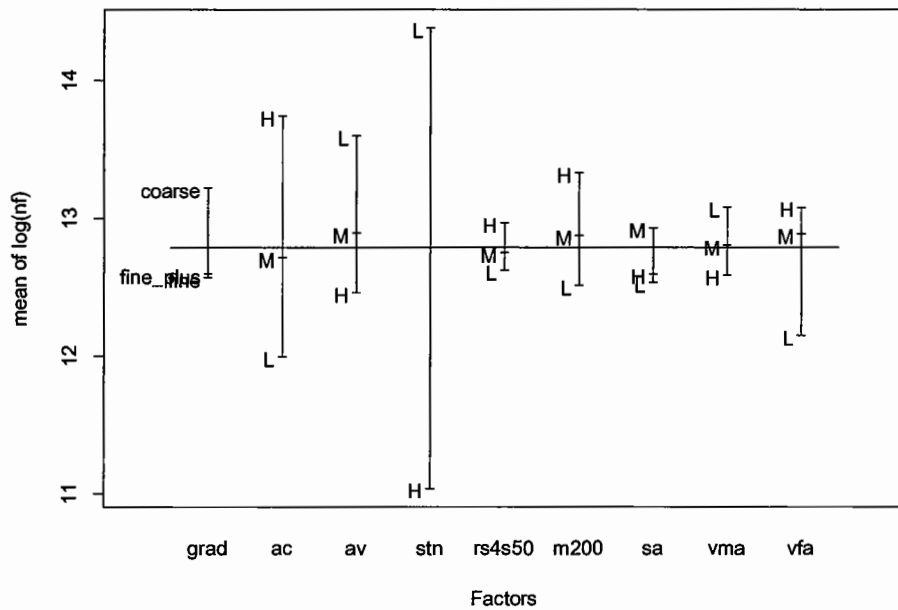


Figure 4.11. Design plot of *lnnf* (fatigue tests at 20°C).

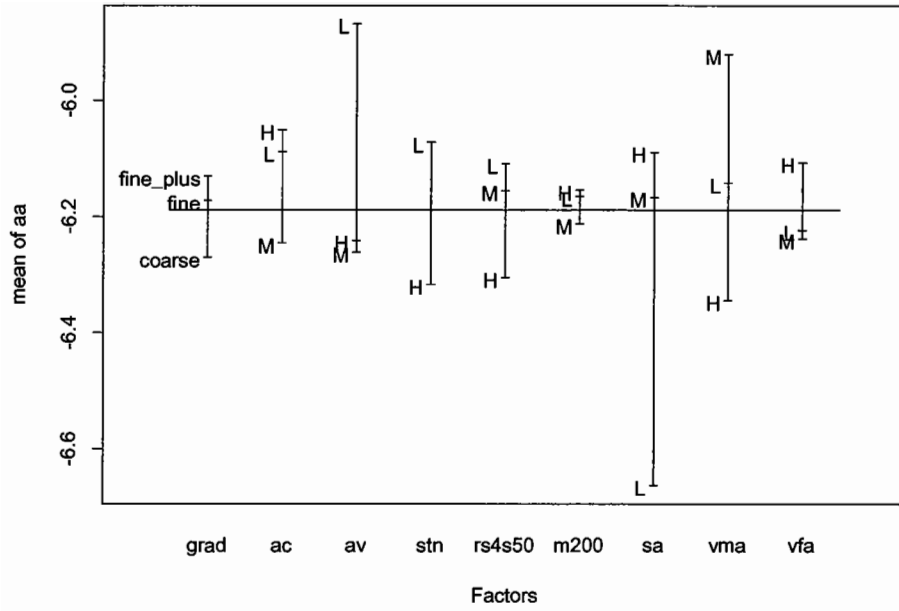


Figure 4.12. Design plot of *aa* (fatigue tests at 20°C).

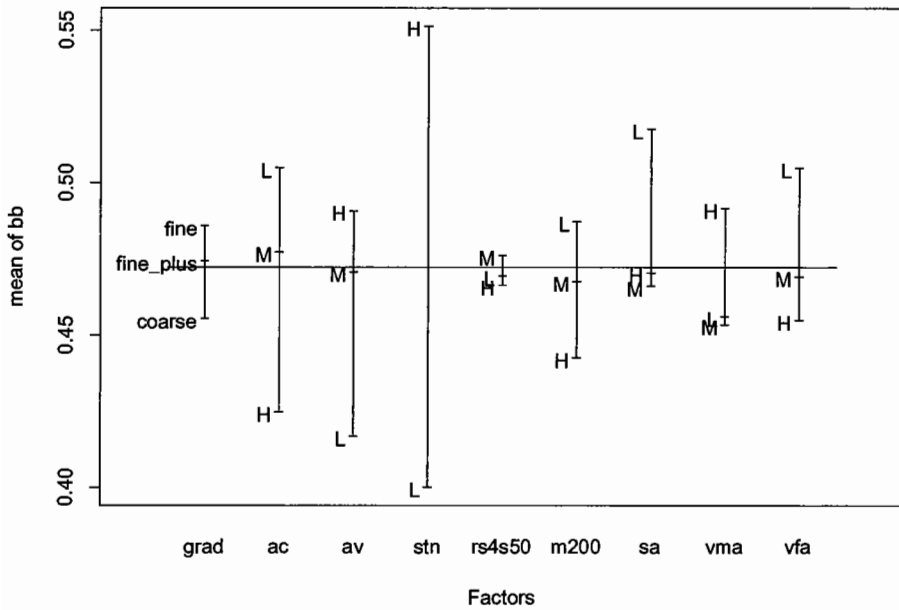


Figure 4.13. Design plot of *bb* (fatigue tests at 20°C).

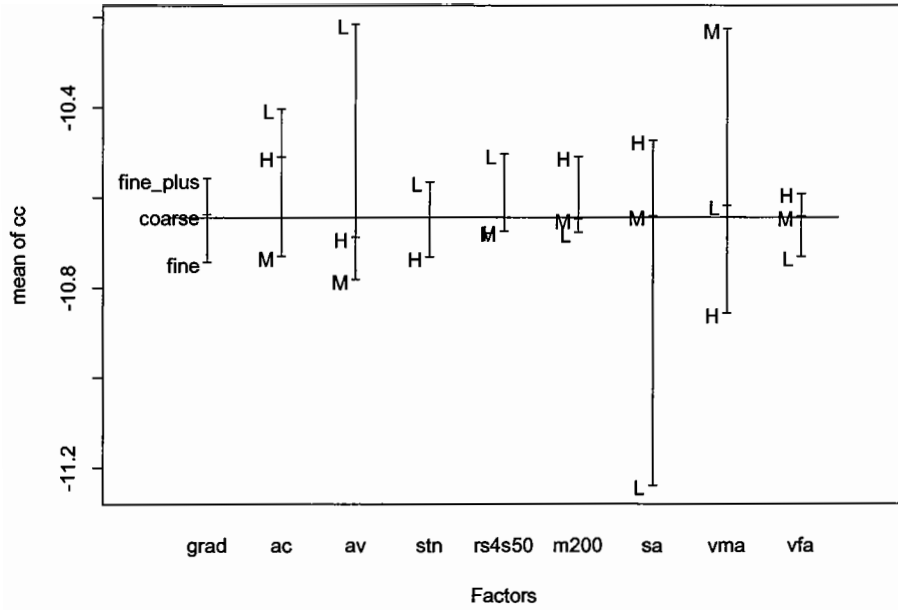


Figure 4.14. Design plot of *cc* (fatigue tests at 20°C).

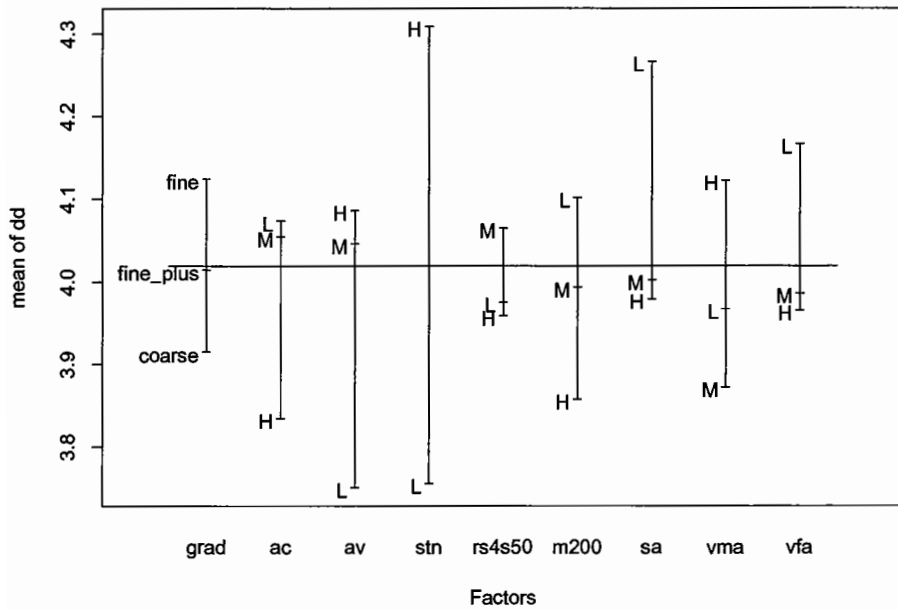


Figure 4.15. Design plot of *dd* (fatigue tests at 20°C).

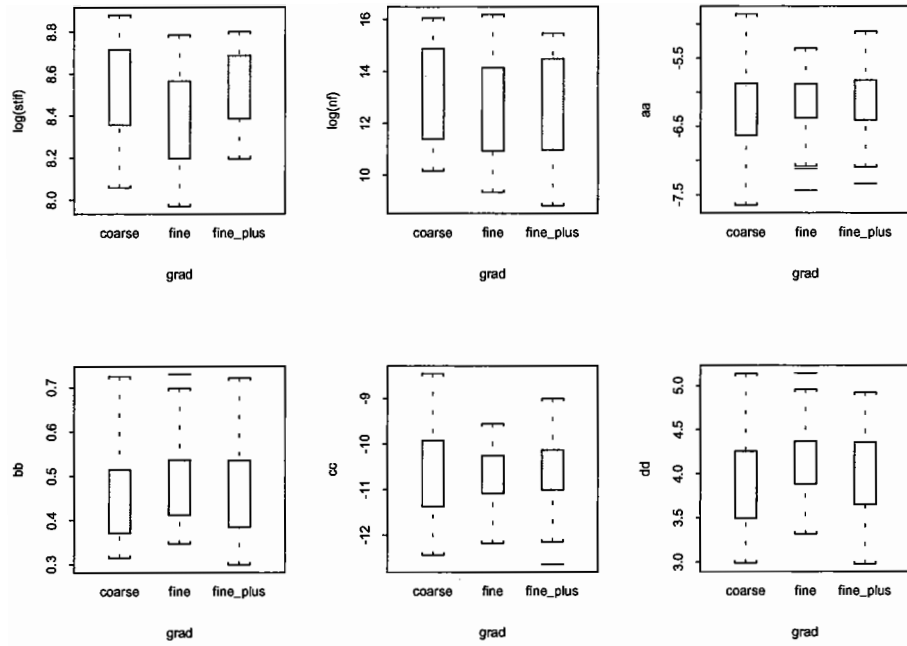


Figure 4.16. Boxplots for factor *grad* (fatigue tests at 20 °C).

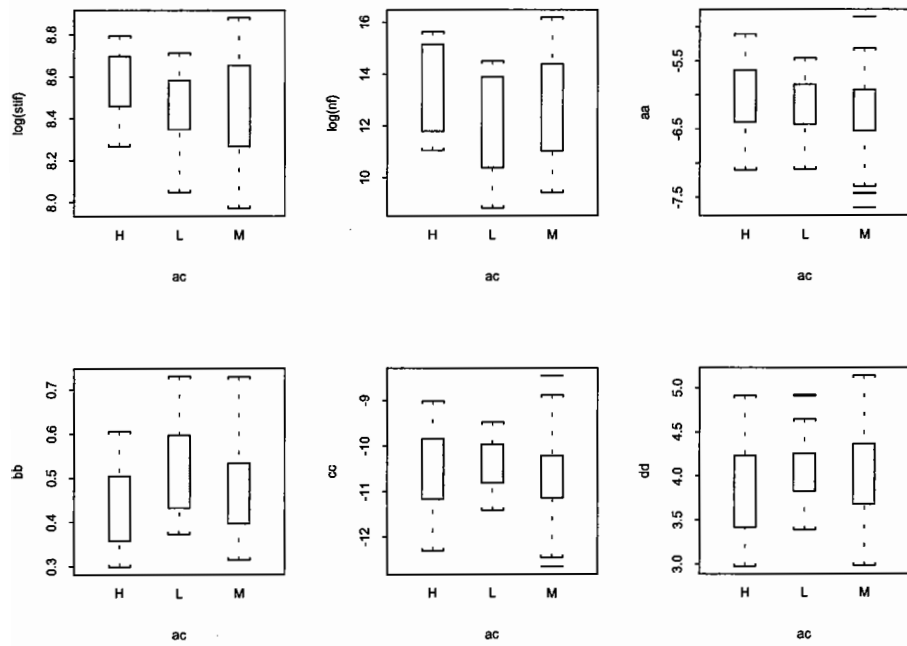


Figure 4.17. Boxplots for factor *ac* (fatigue tests at 20 °C).

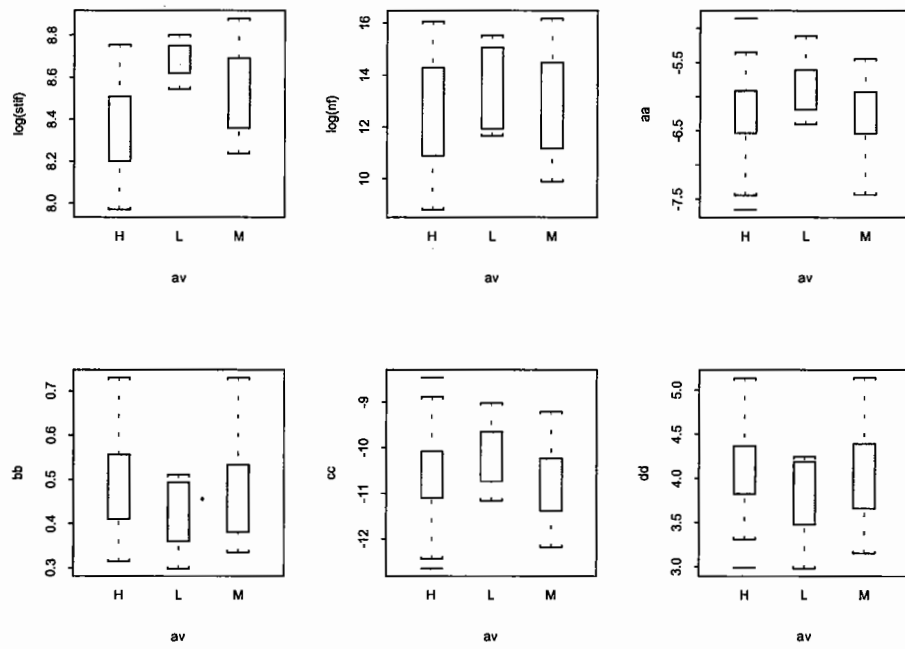


Figure 4.18. Boxplots for factor *av* (fatigue tests at 20°C).

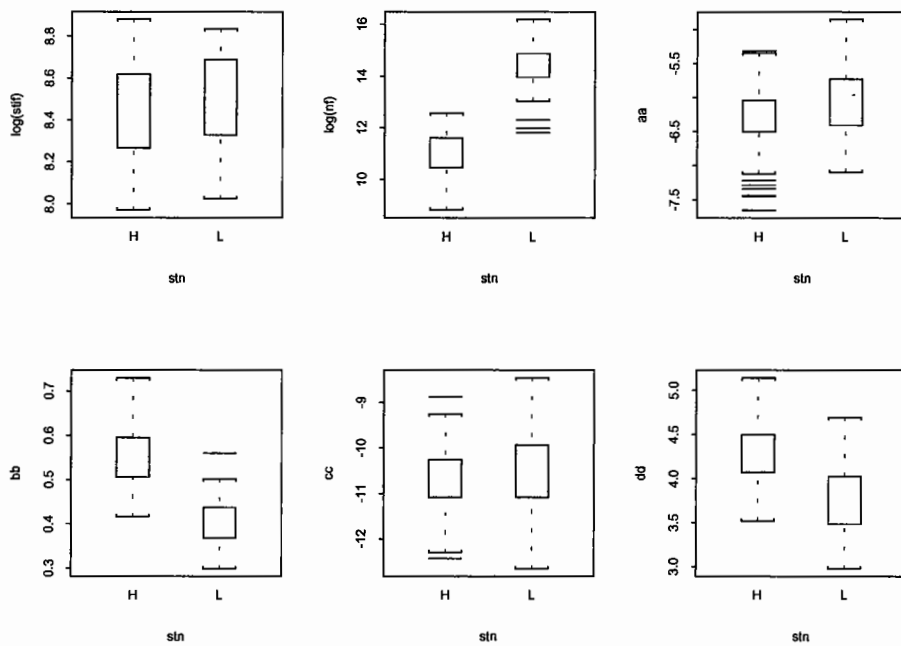


Figure 4.19. Boxplots for factor *stn* (fatigue tests at 20°C).

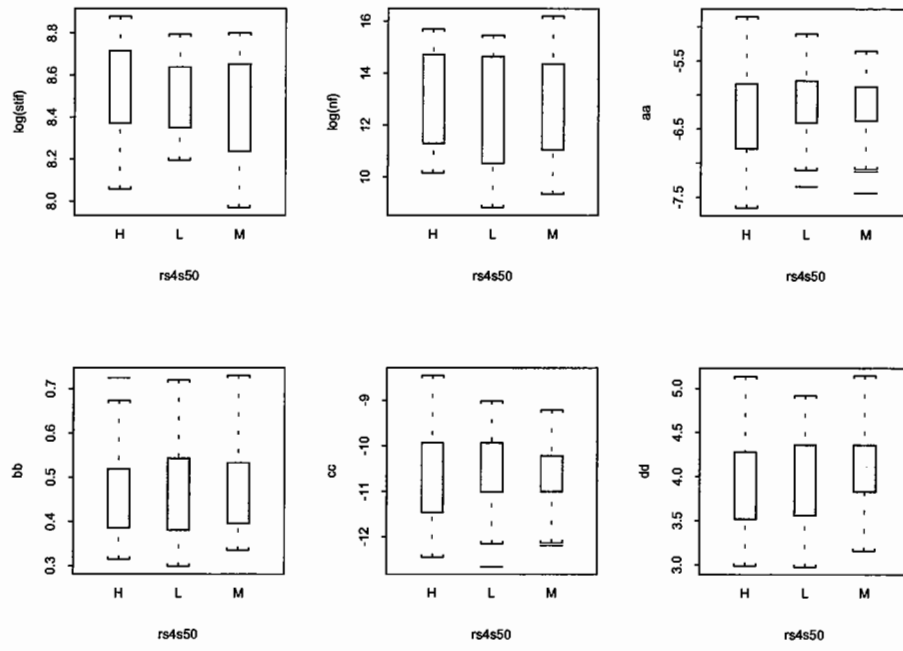


Figure 4.20. Boxplots for factor *rs4s50* (fatigue tests at 20 °C).

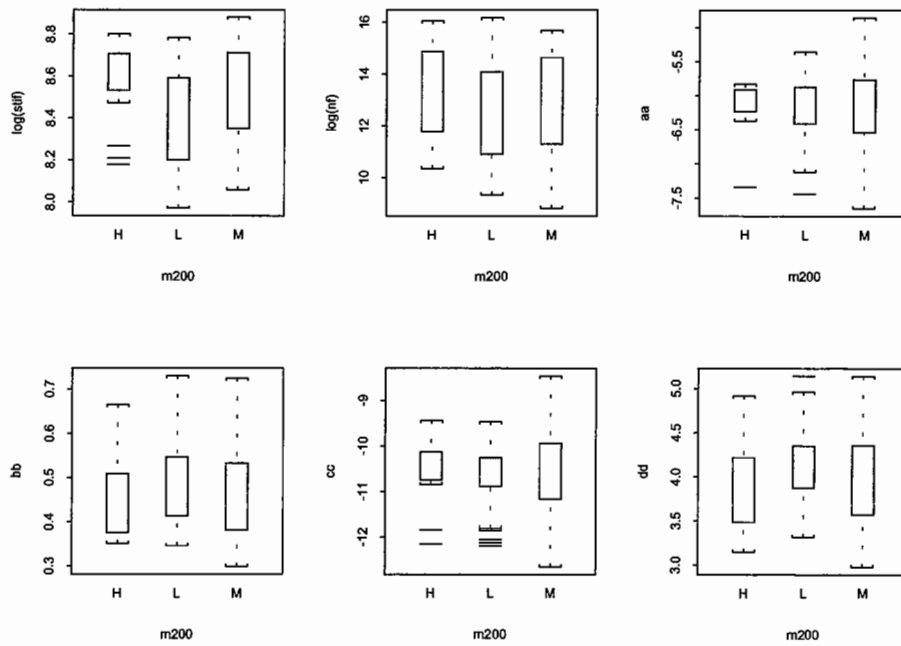


Figure 4.21. Boxplots for factor *m200* (fatigue tests at 20 °C).

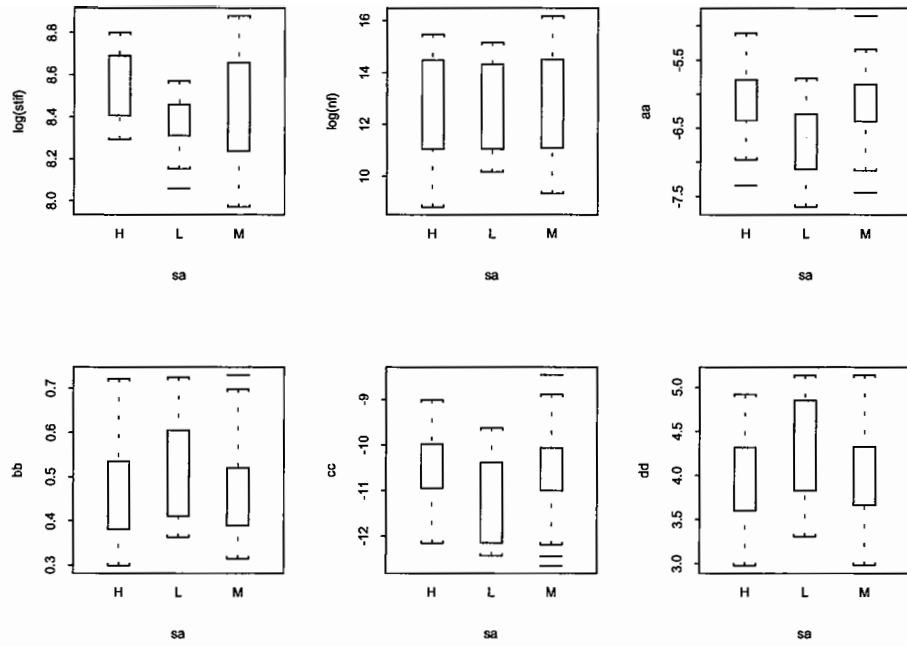


Figure 4.22. Boxplots for factor *sa* (fatigue tests at 20 °C).

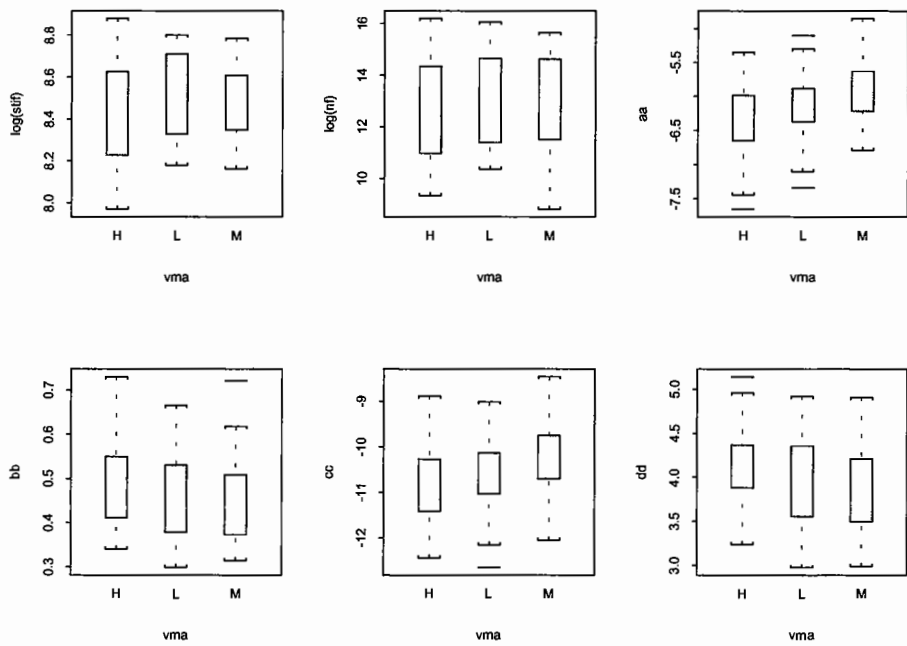


Figure 4.23. Boxplots for factor *vma* (fatigue tests at 20 °C).

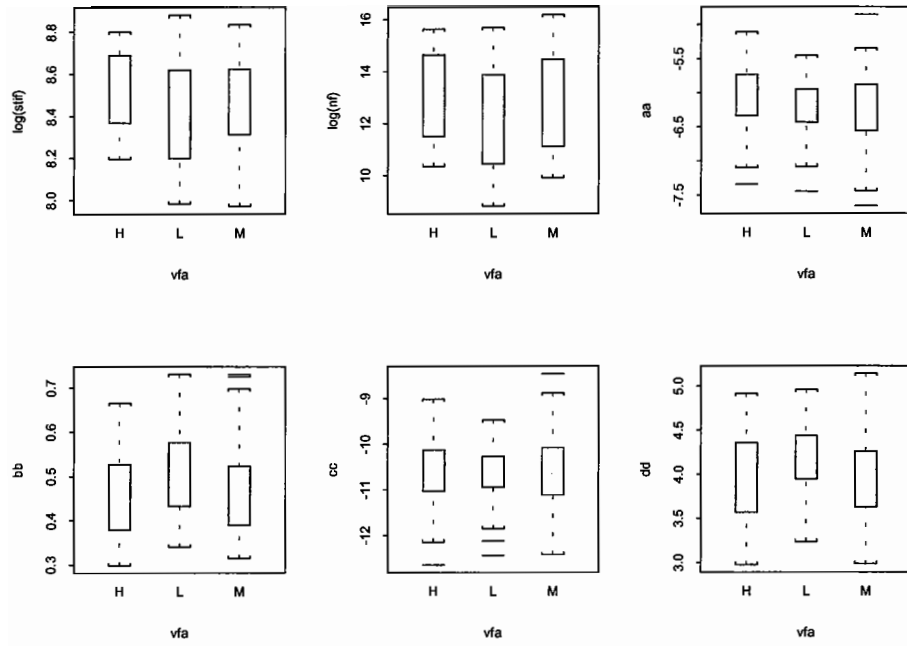


Figure 4.24. Boxplots for factor *vfa* (fatigue tests at 20°C).

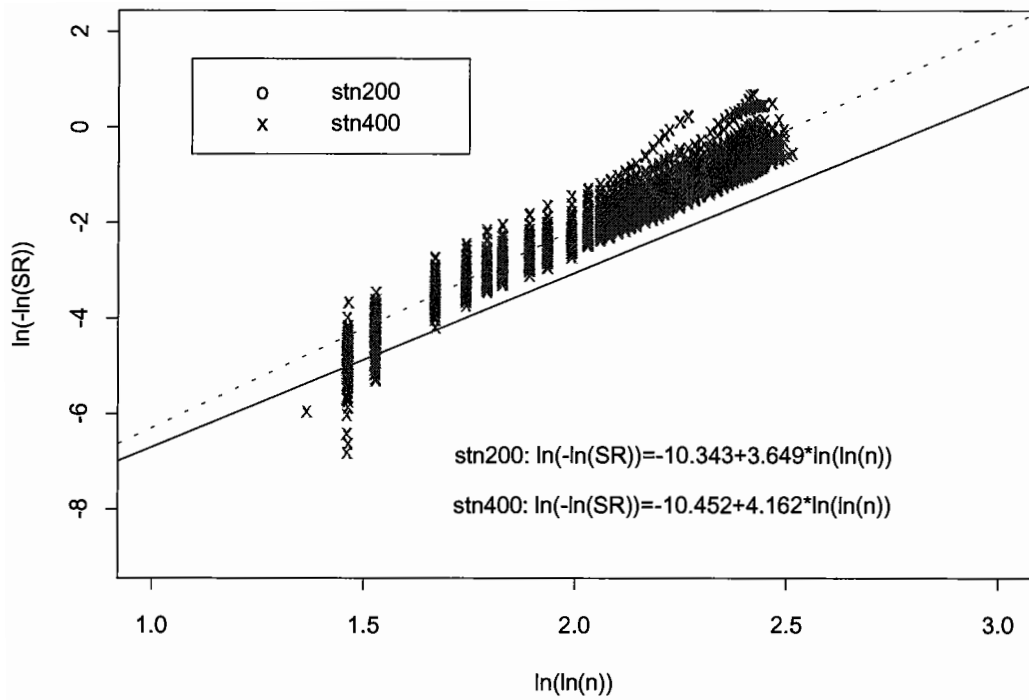


Figure 4.25. Weibull curves in two strain groups (fatigue tests at 20° C).

WesTrack Coarse Medium Mixes (CM)

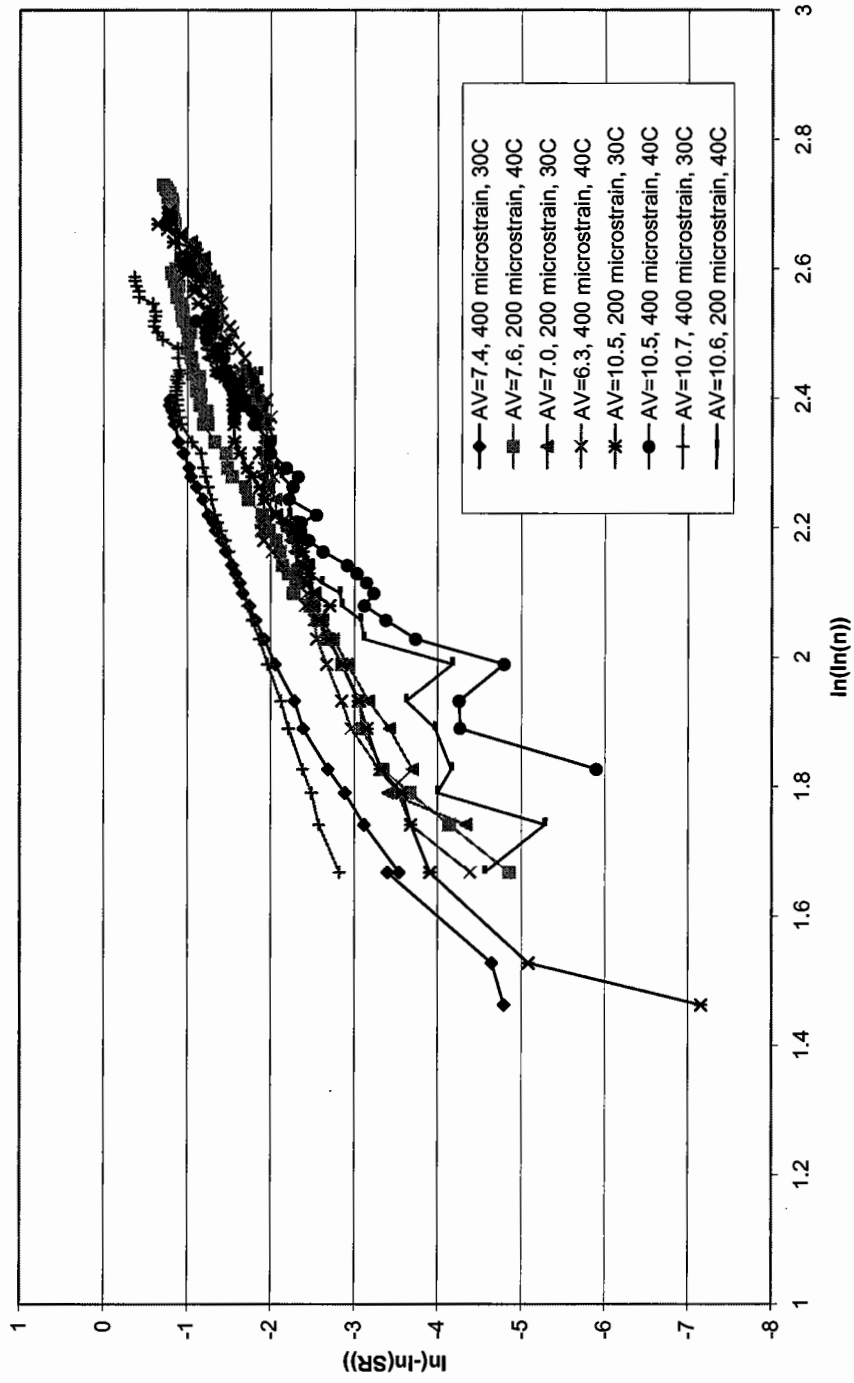


Figure 4.26. Test results of high temperature fatigue test for CM mixes.

WesTrack Fine Medium Mixes (FM)

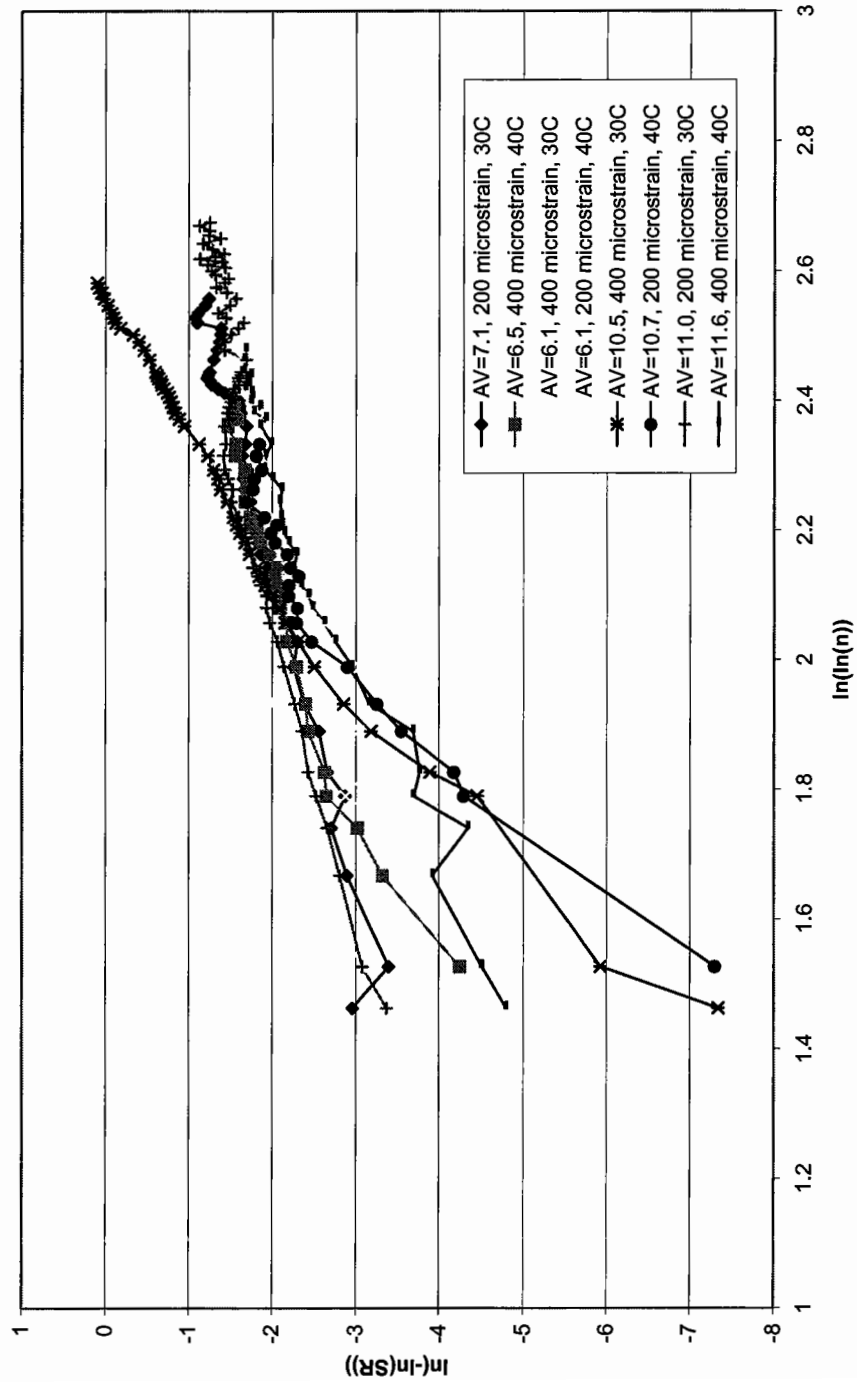


Figure 4.27. Test results of high temperature fatigue test for FM mixes.

Frequency Sweep Test for FM mixes (300 microstrain)

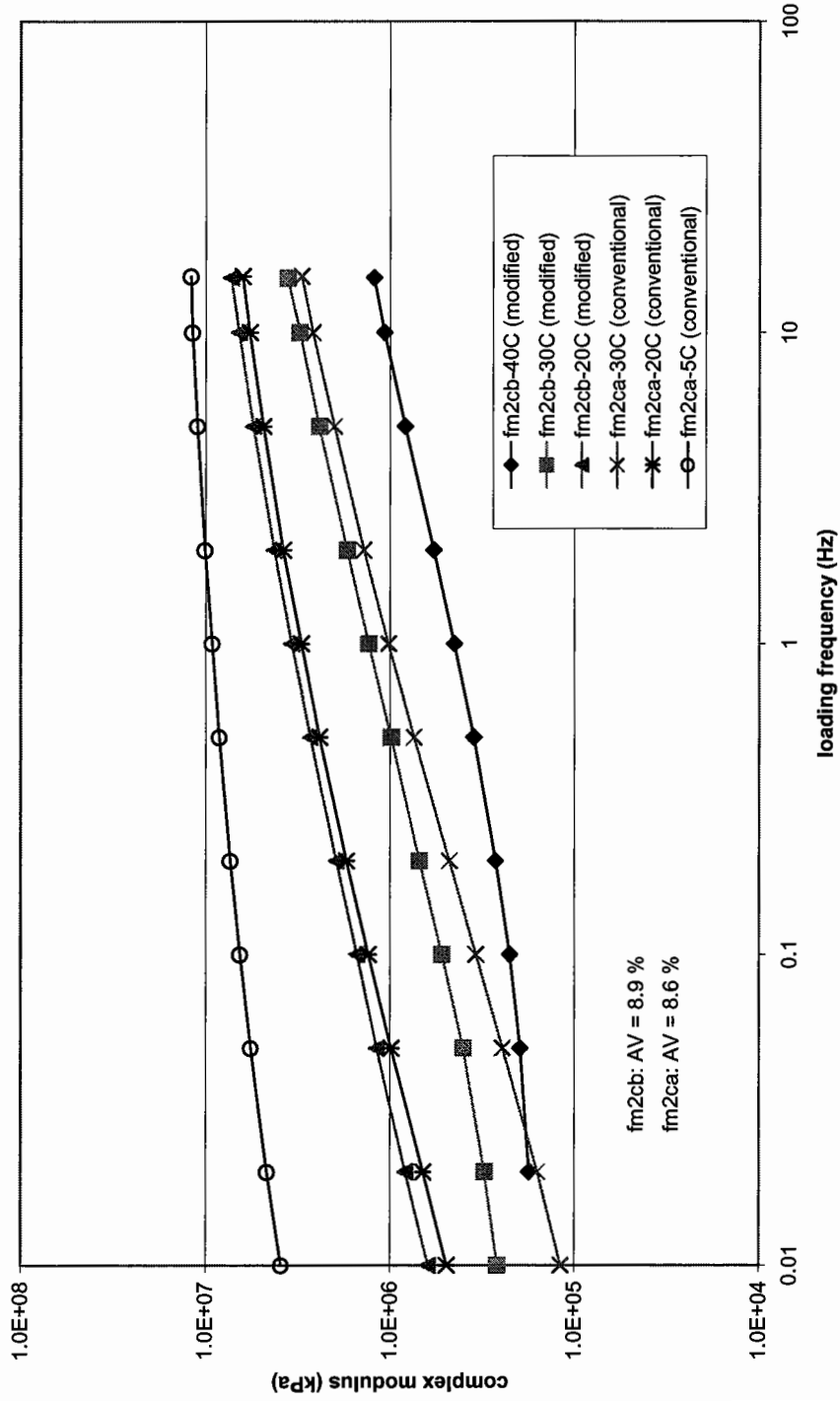


Figure 4.28. Flexural frequency sweep test results for FM mixes at 300 microstrain.

Frequency Sweep Test for CM mixes (300 microstrain)

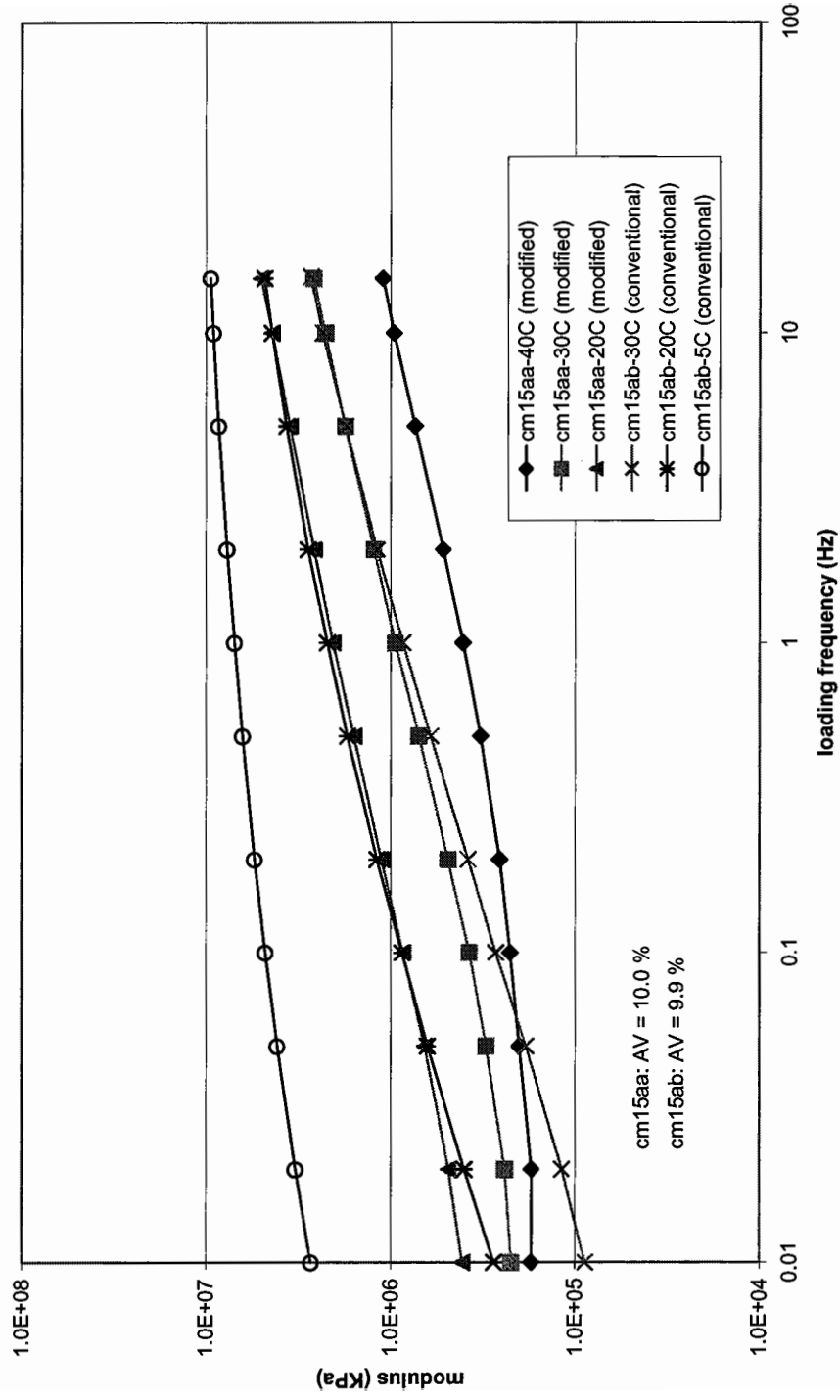


Figure 4.29. Flexural frequency sweep test results for CM mixes at 300 microstrain.

shape parameter: $n=2$; scale parameter: β =varied

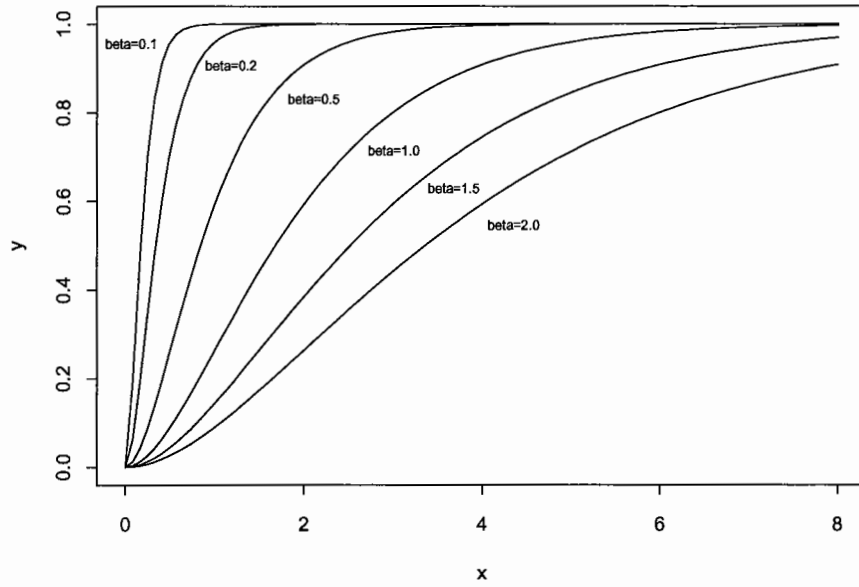


Figure 4.30. Gamma distribution curves with shape parameter $n = 2$ and scale parameters $\beta = 0.1, 0.2, 0.5, 1, 1.5,$ and 2 .

shape parameter: $n=5$; scale parameter: β =varied

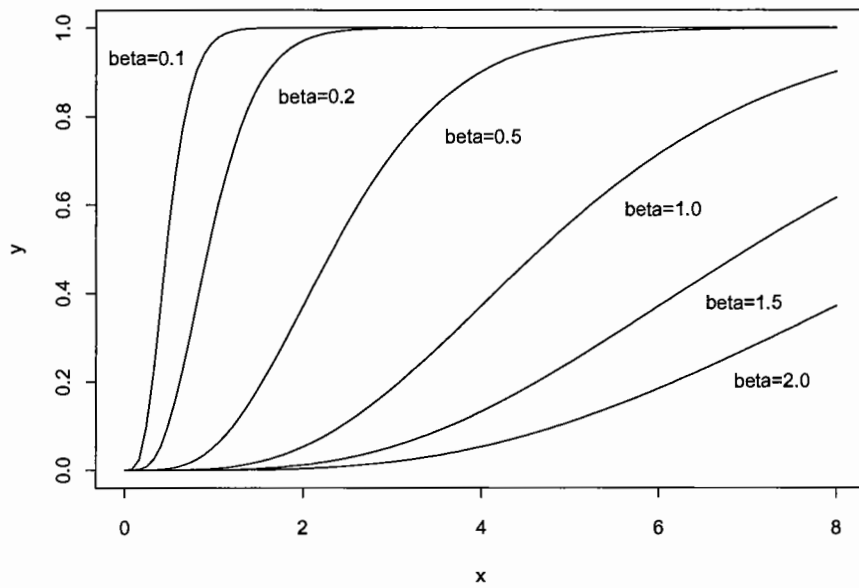


Figure 4.31. Gamma distribution curves with shape parameter $n = 5$ and scale parameters $\beta = 0.1, 0.2, 0.5, 1, 1.5,$ and 2 .

Gamma Distribution Function-Nonlinear Fitting

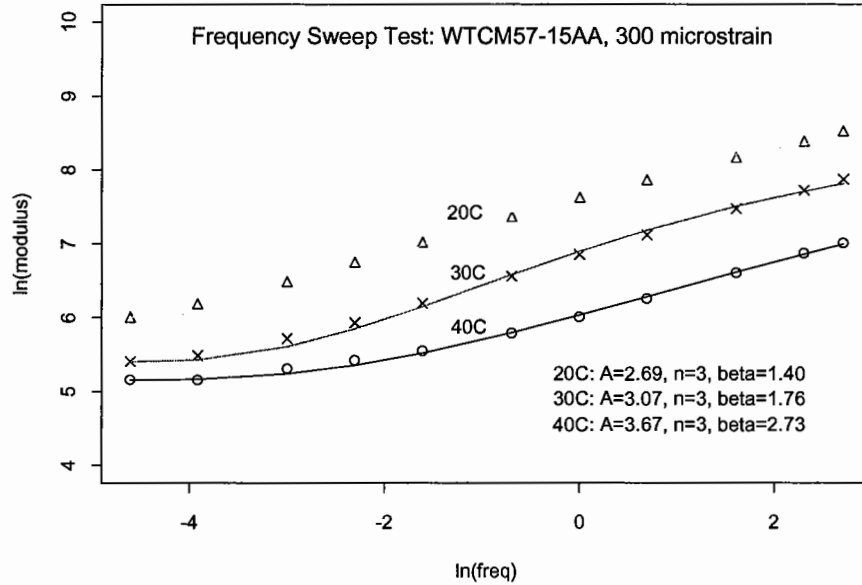


Figure 4.32. Nonlinear fitting of flexural frequency sweep test using Gamma distribution function (modified fatigue test setup).

Gamma Distribution Function-Nonlinear Fitting

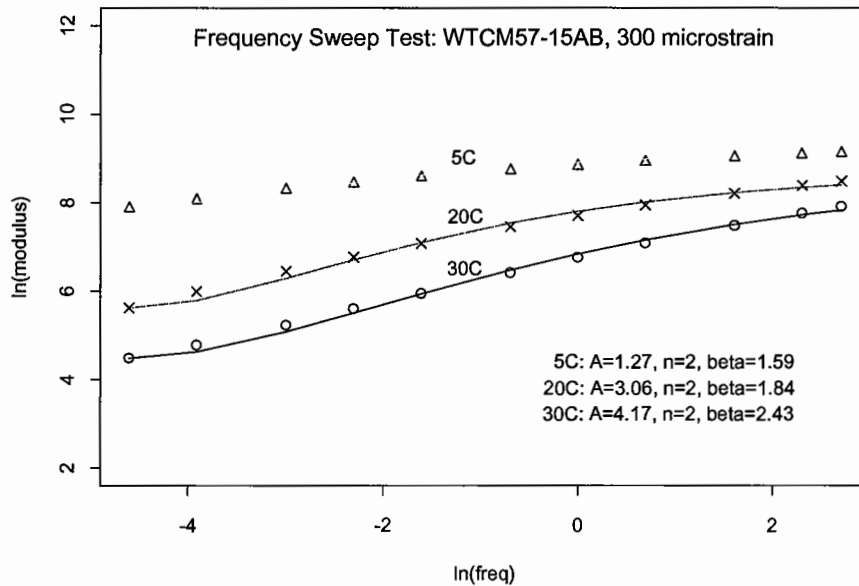


Figure 4.33. Nonlinear fitting of flexural frequency sweep test using Gamma distribution function (conventional fatigue test setup).

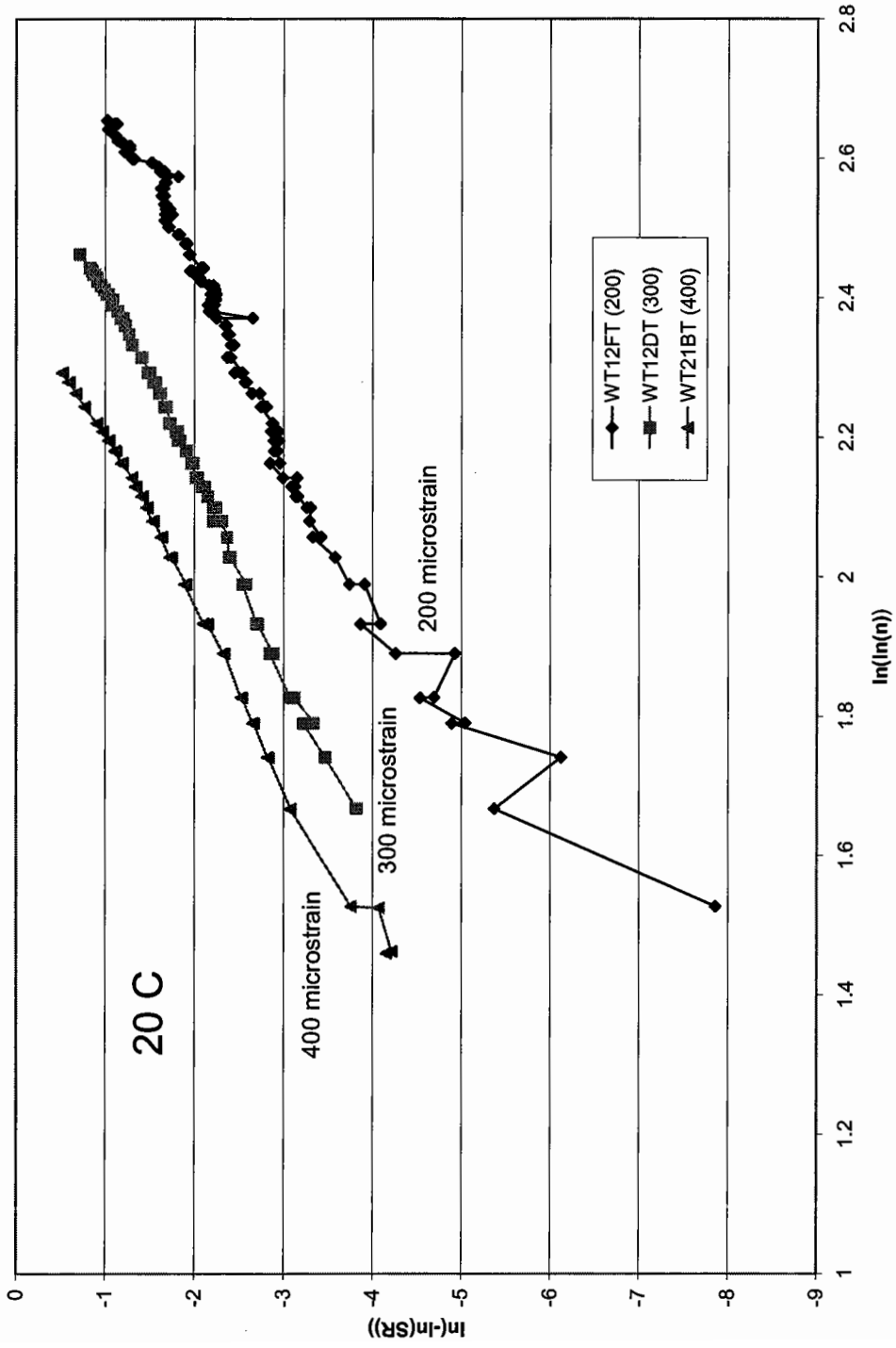


Figure 4.34. Weibull curves at various strain levels.

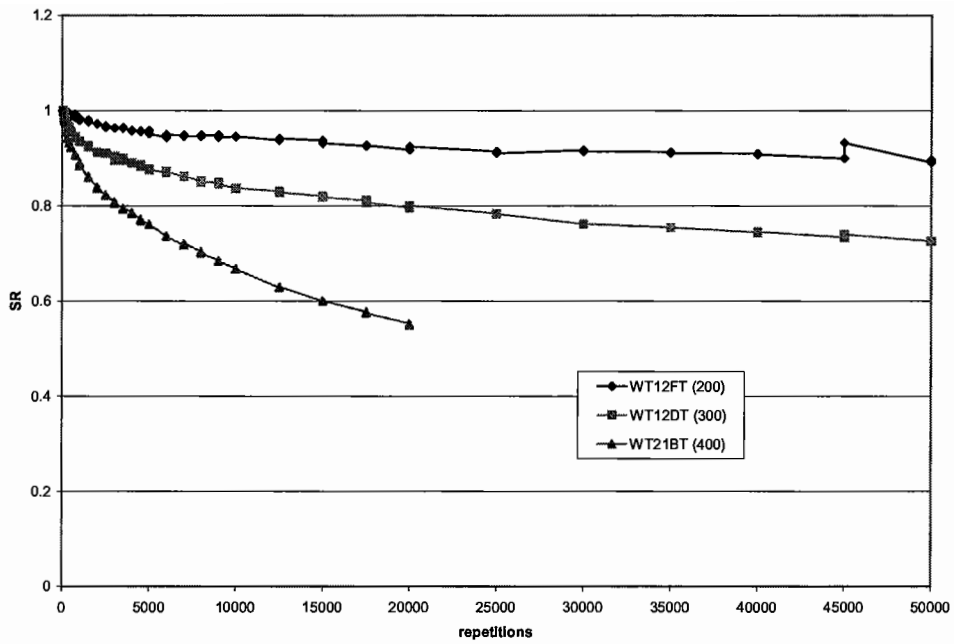


Figure 4.35. Stiffness deterioration curves at various strains in terms of SR versus repetition.

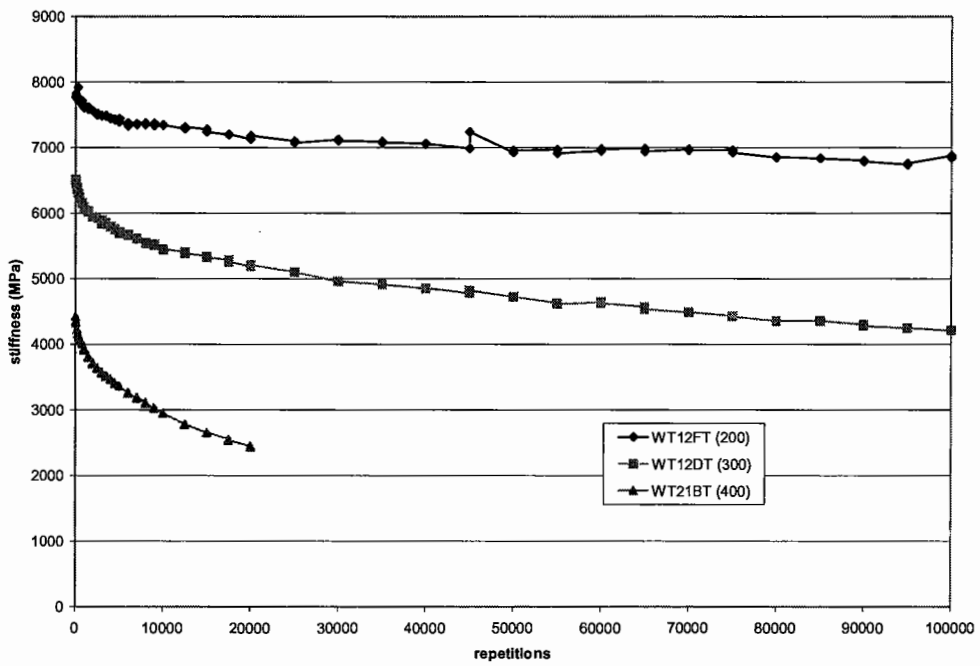


Figure 4.36. Stiffness deterioration curves at various strains in terms of stiffness versus repetition.

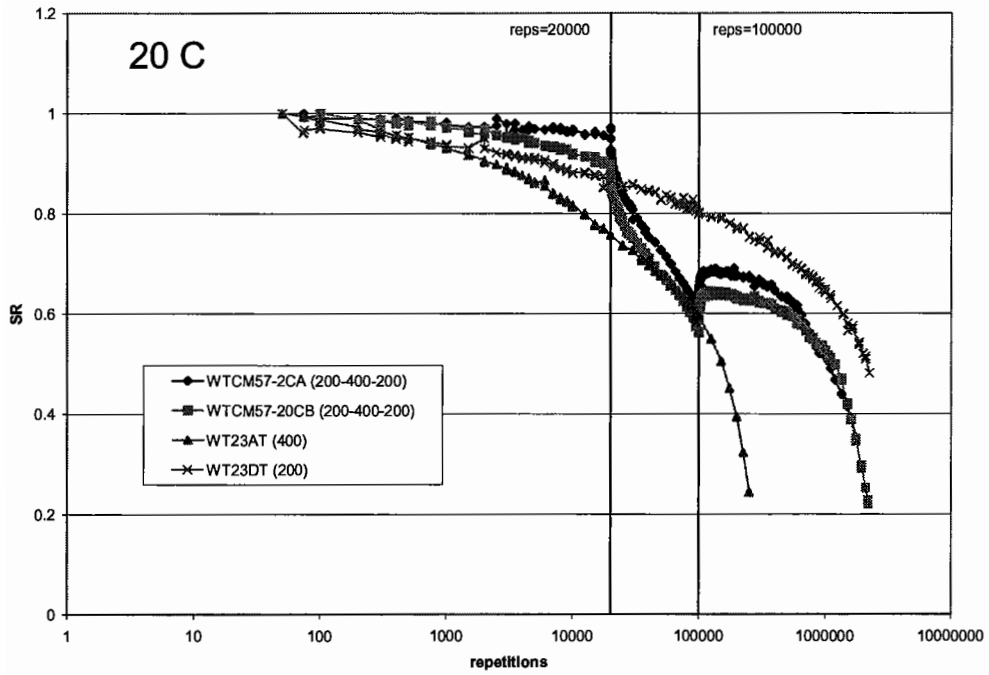


Figure 4.37. A 200-400-200 sequential fatigue test.

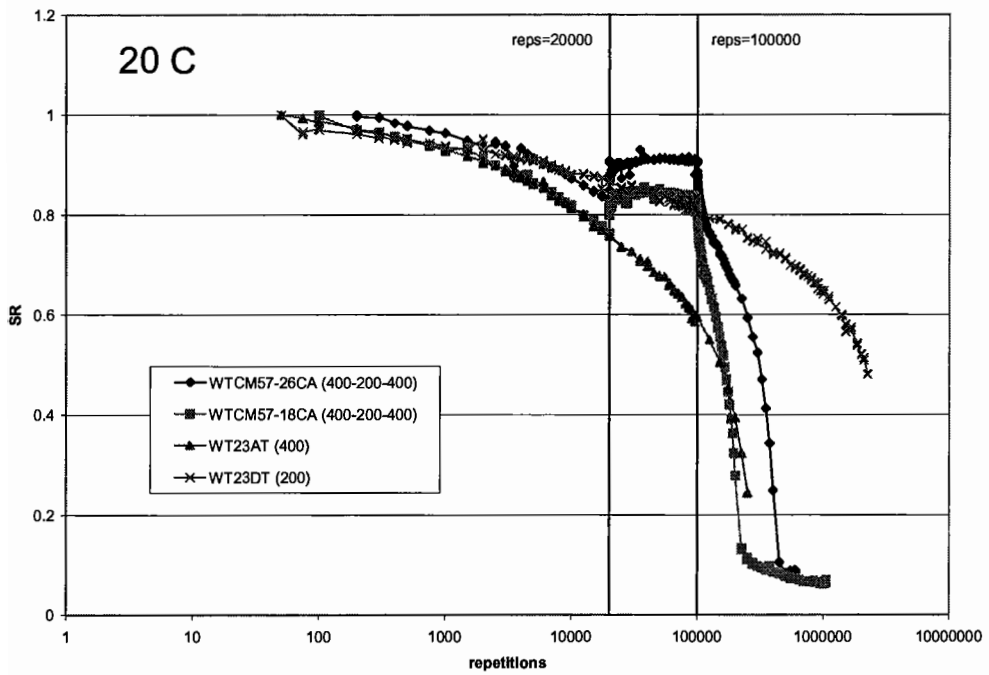


Figure 4.38. A 400-200-400 sequential fatigue test.

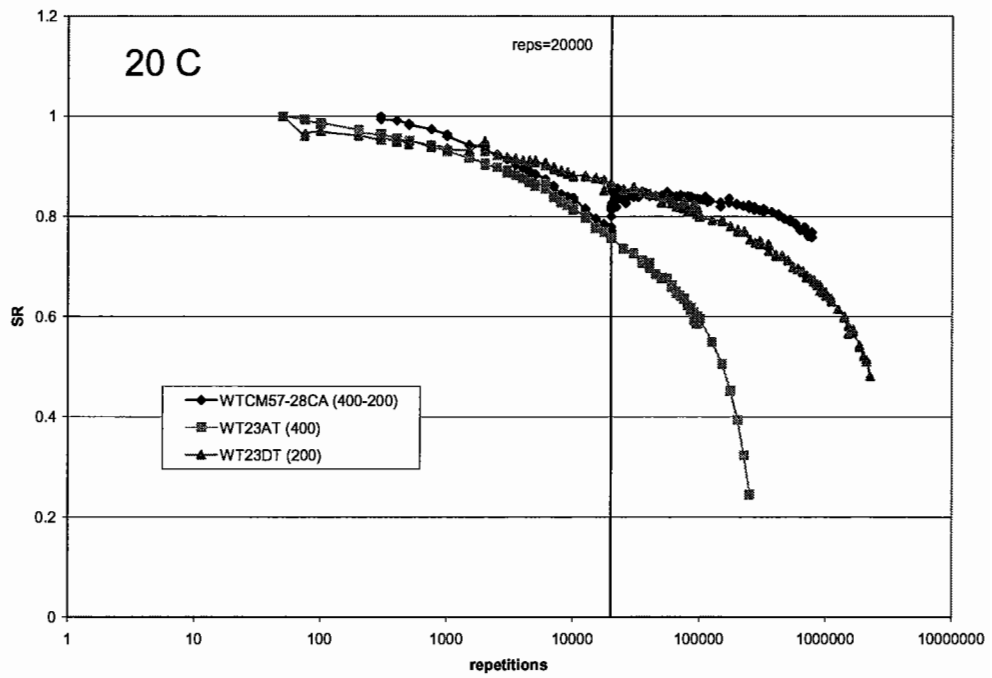


Figure 4.39. A 400-200 sequential fatigue test.

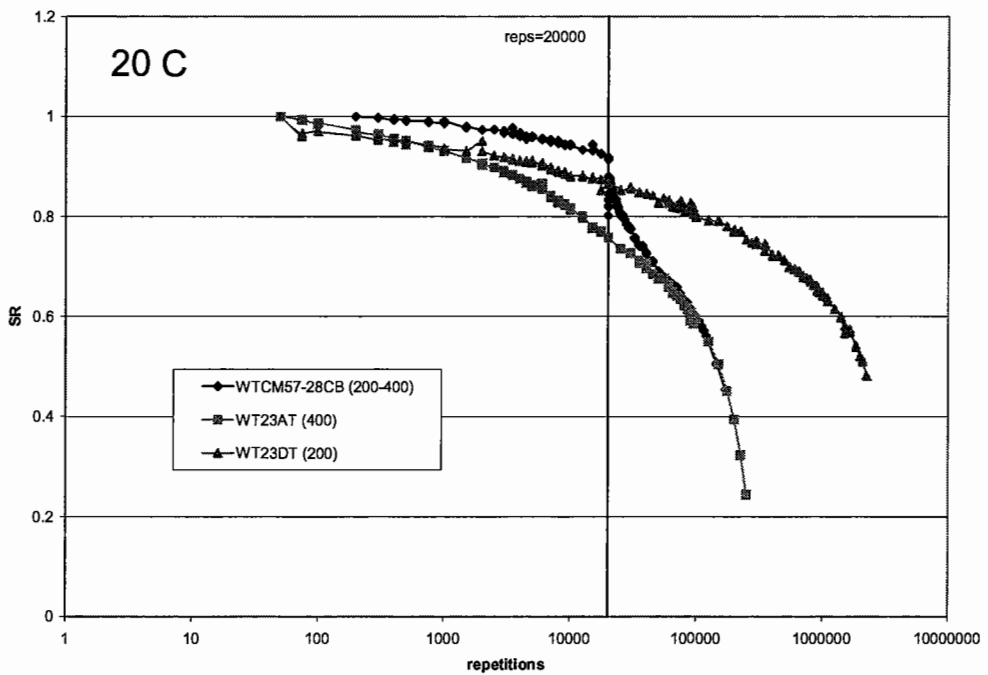


Figure 4.40. A 200-400 sequential fatigue test.

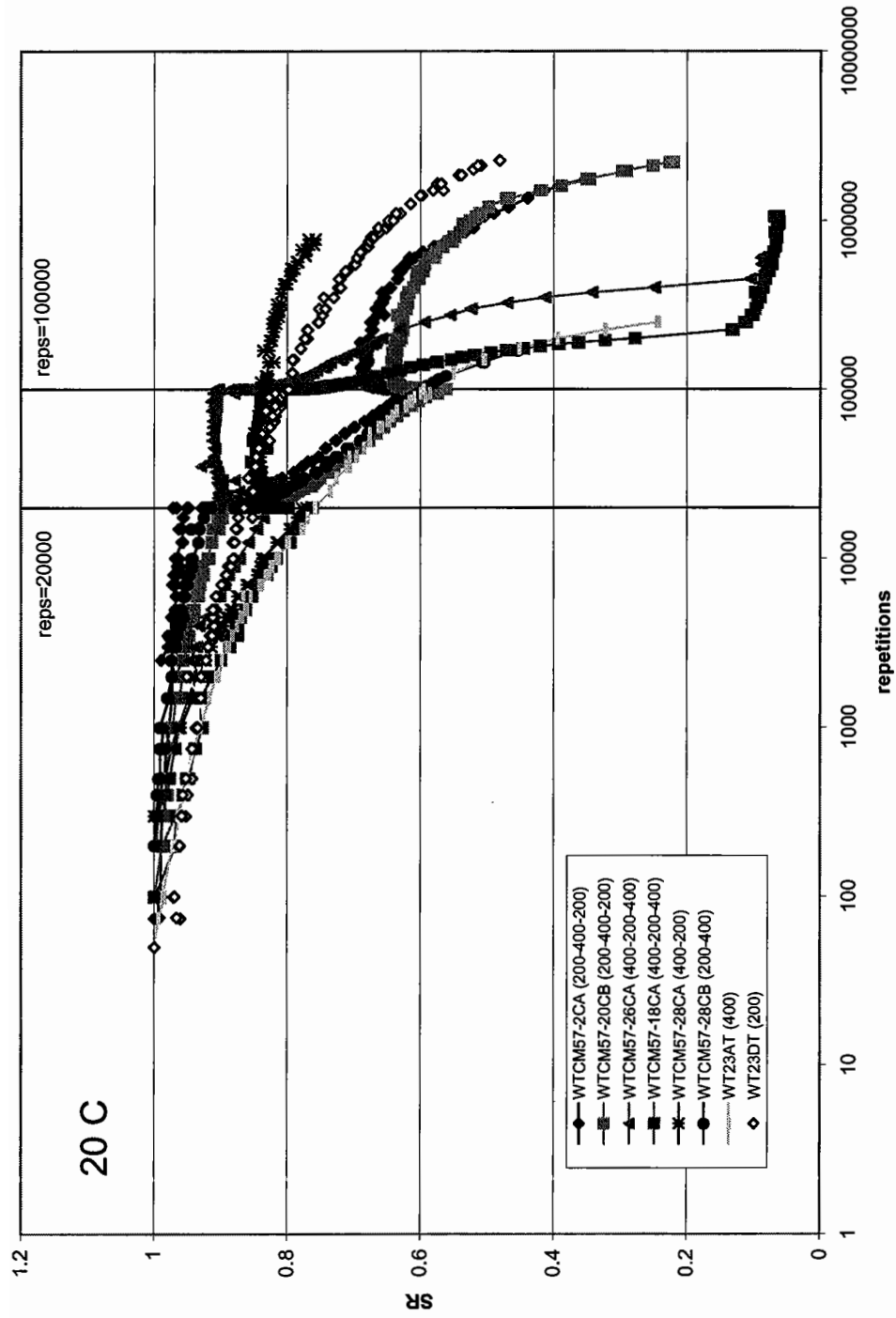


Figure 4.41. A summary of varied-strain fatigue tests in terms of SR versus repetition.

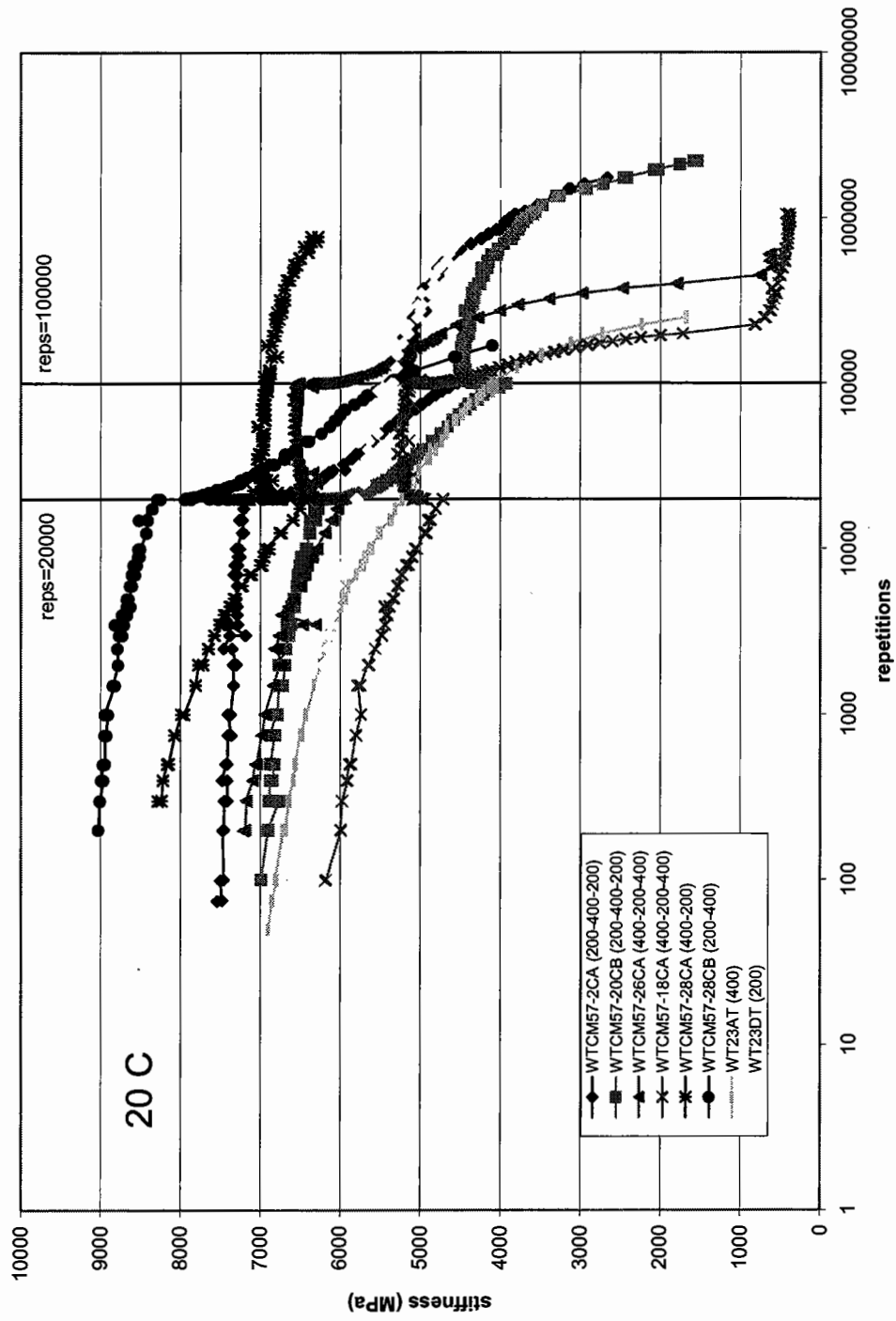


Figure 4.42. A summary of varied-strain fatigue tests in terms of stiffness versus repetition.

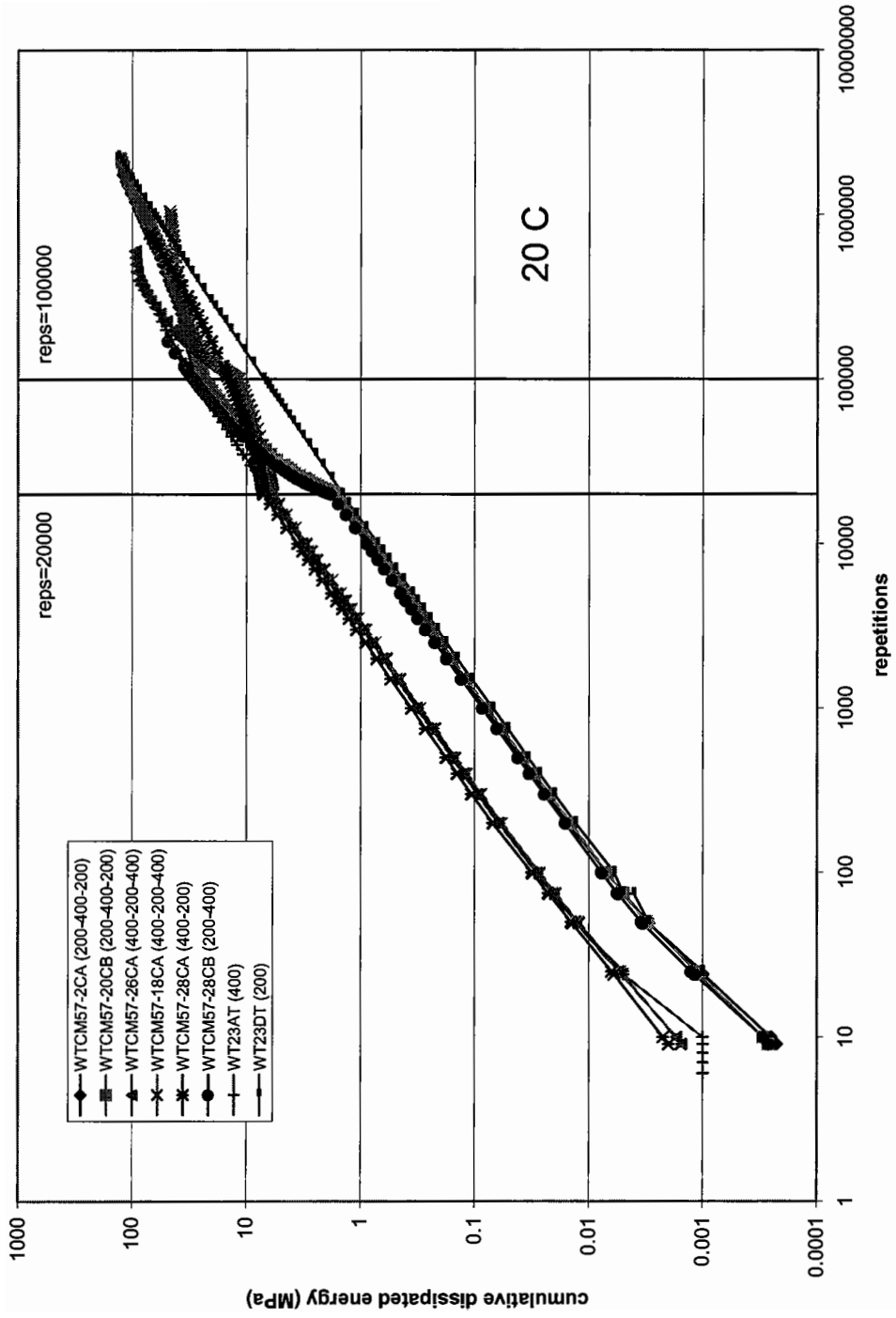


Figure 4.43. Cumulative dissipated energy plot for varied-strain fatigue tests.

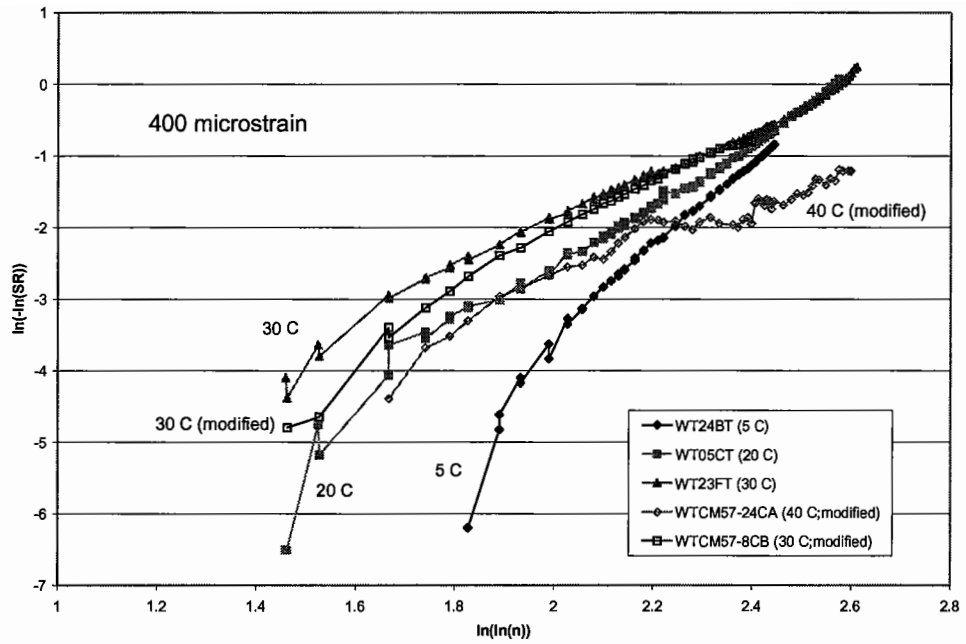


Figure 4.44. Weibull curves at various temperatures.

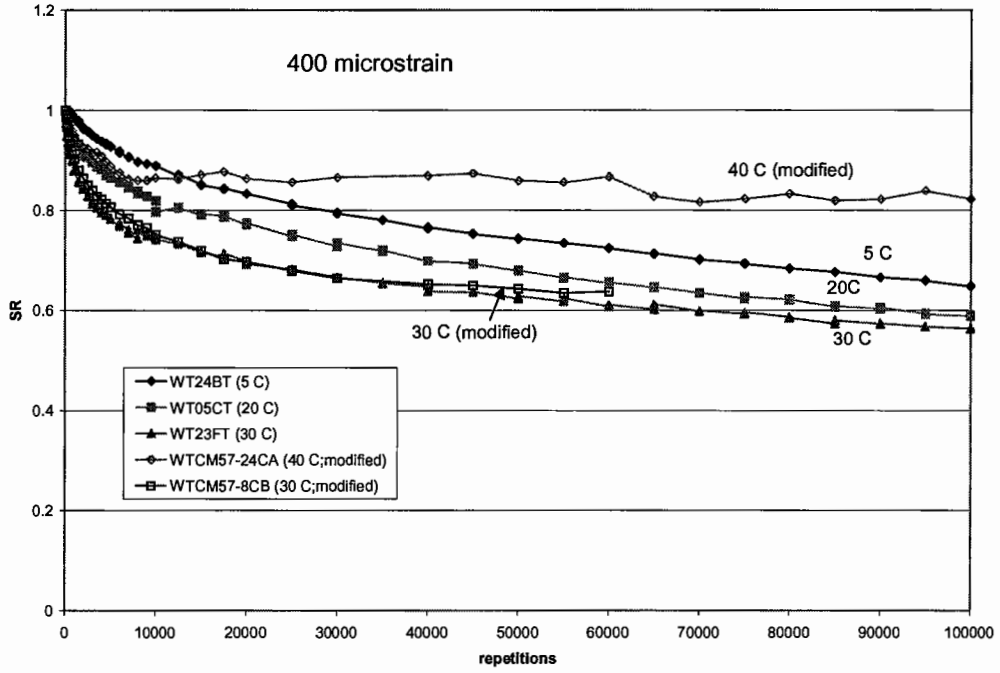


Figure 4.45. Stiffness deterioration curves at various temperatures in terms of SR versus repetition.

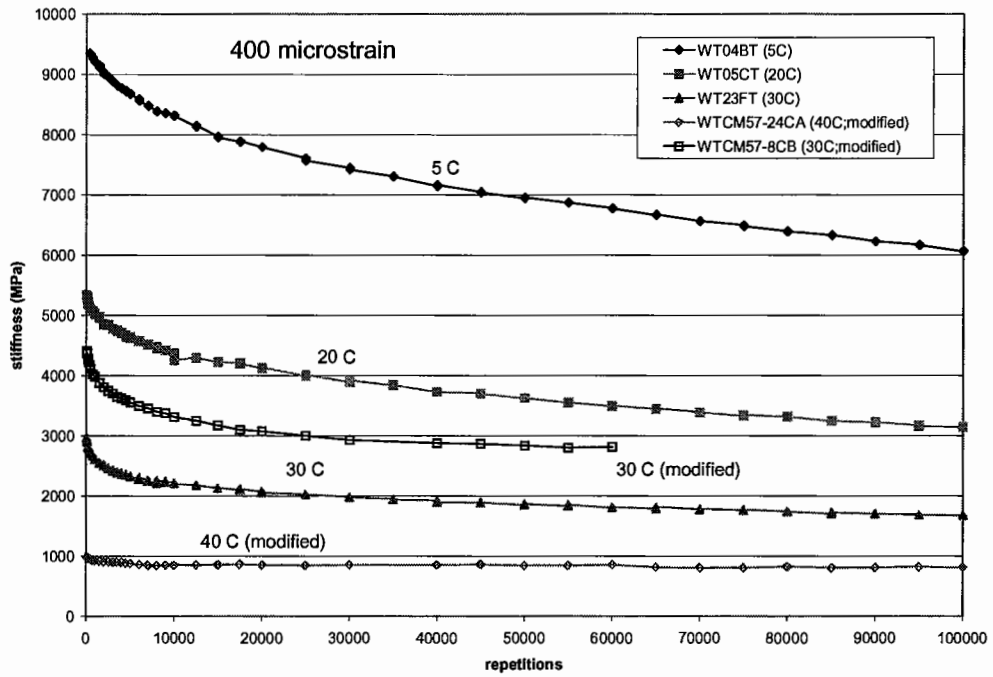


Figure 4.46. Stiffness deterioration curves at various temperatures in terms of stiffness versus repetition.

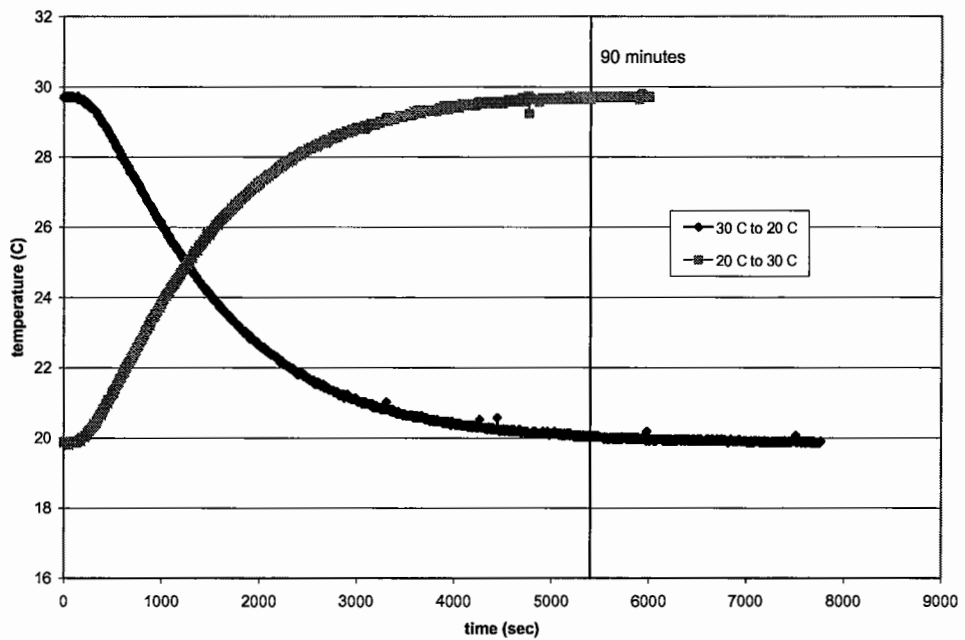


Figure 4.47. Time needed for internal temperature stabilization of a beam.

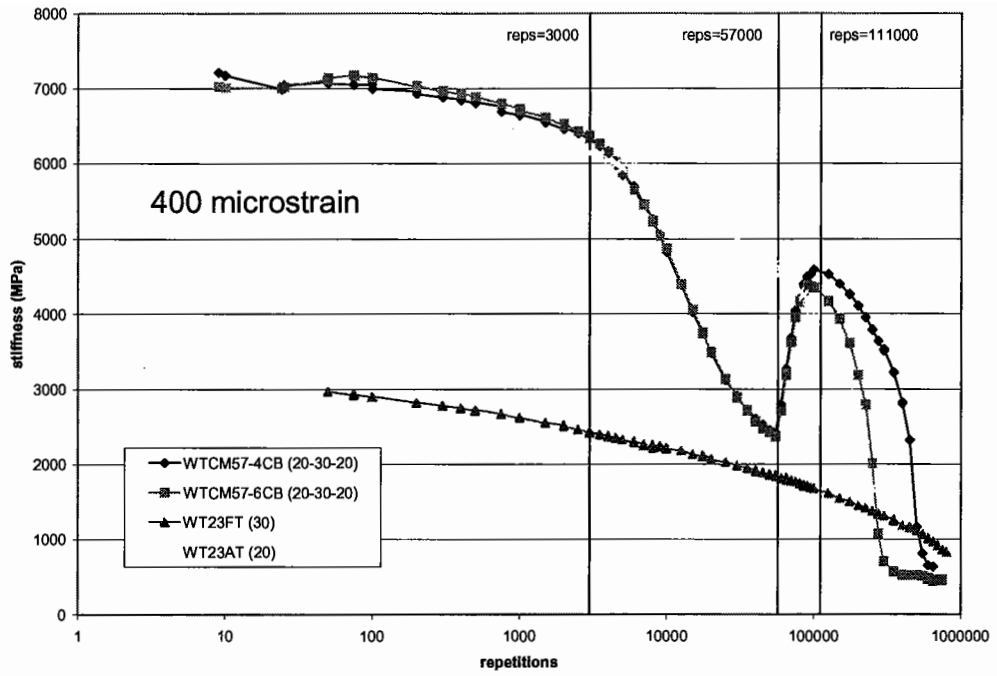


Figure 4.48. A 20-30-20 sequential fatigue test.

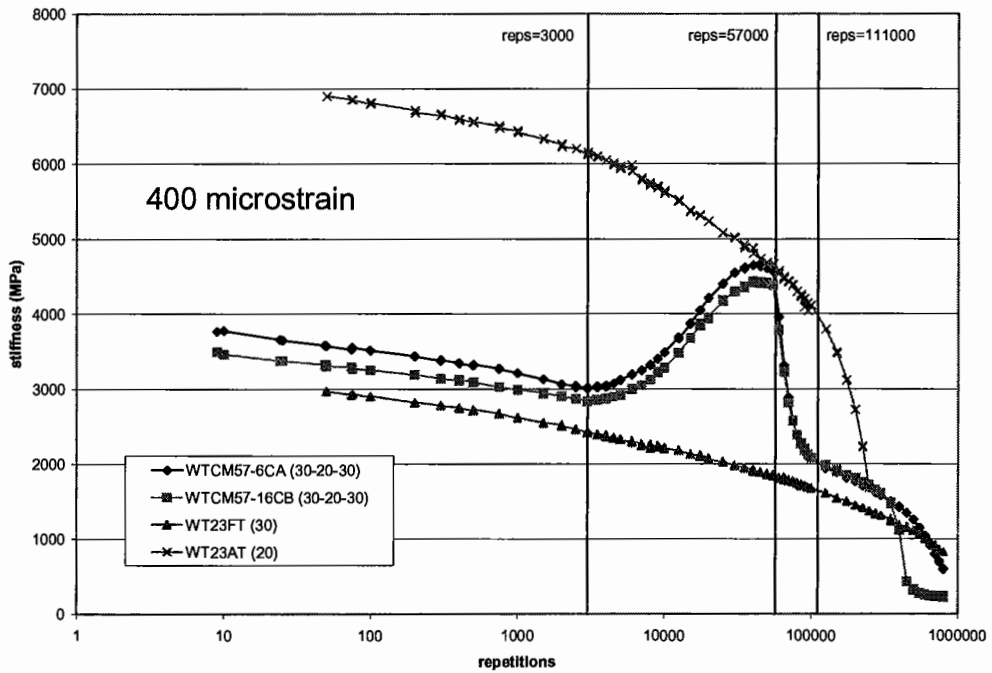


Figure 4.49. A 30-20-30 sequential fatigue test.

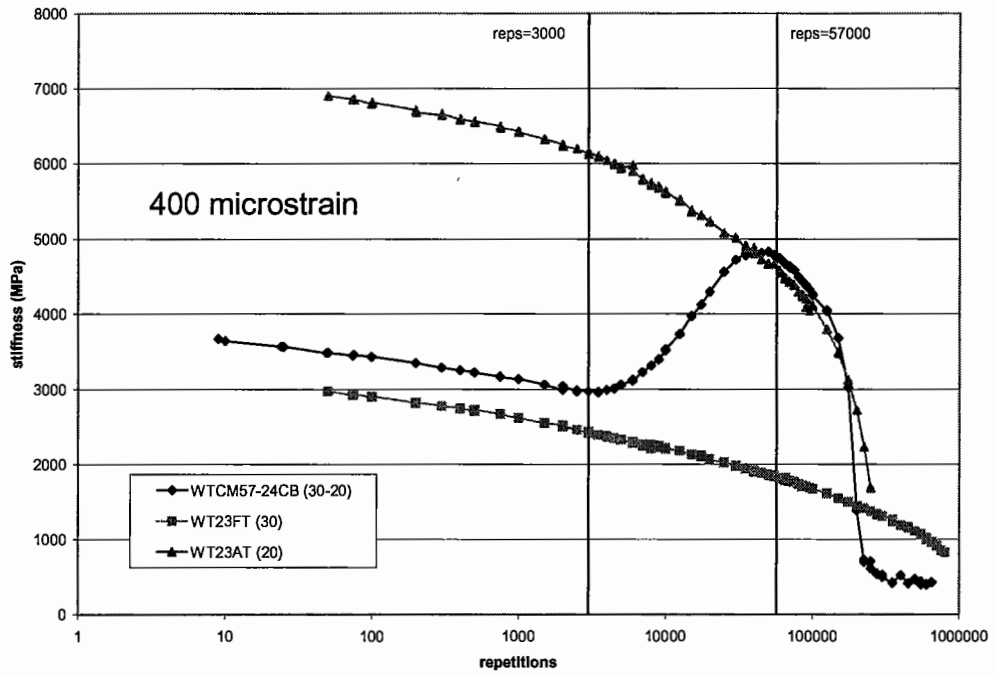


Figure 4.50. A 30-20 sequential fatigue test.

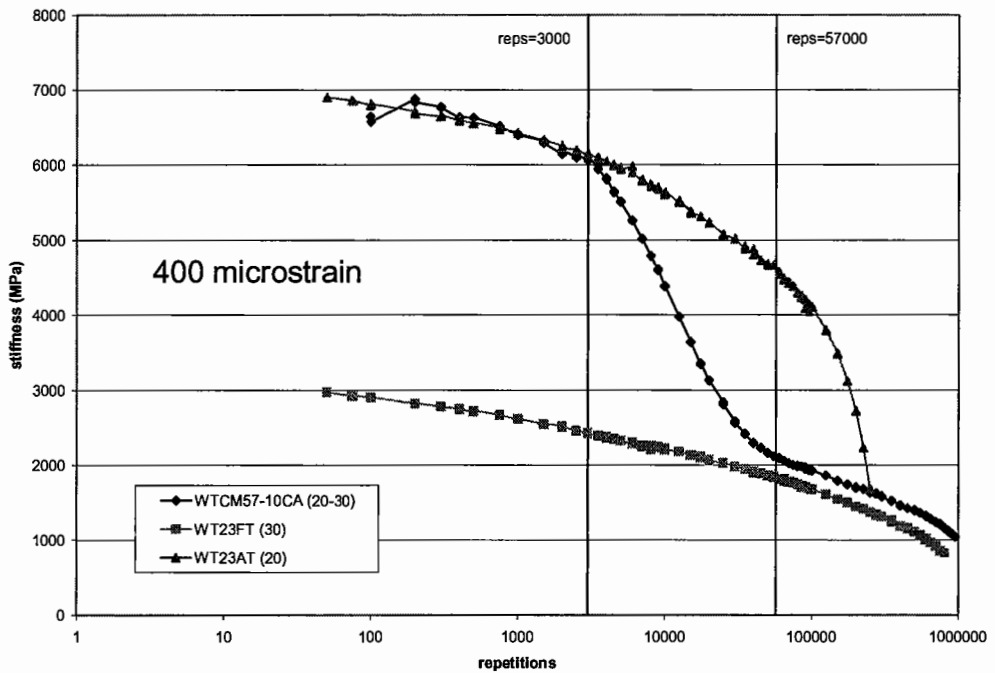


Figure 4.51. A 20-30 sequential fatigue test.

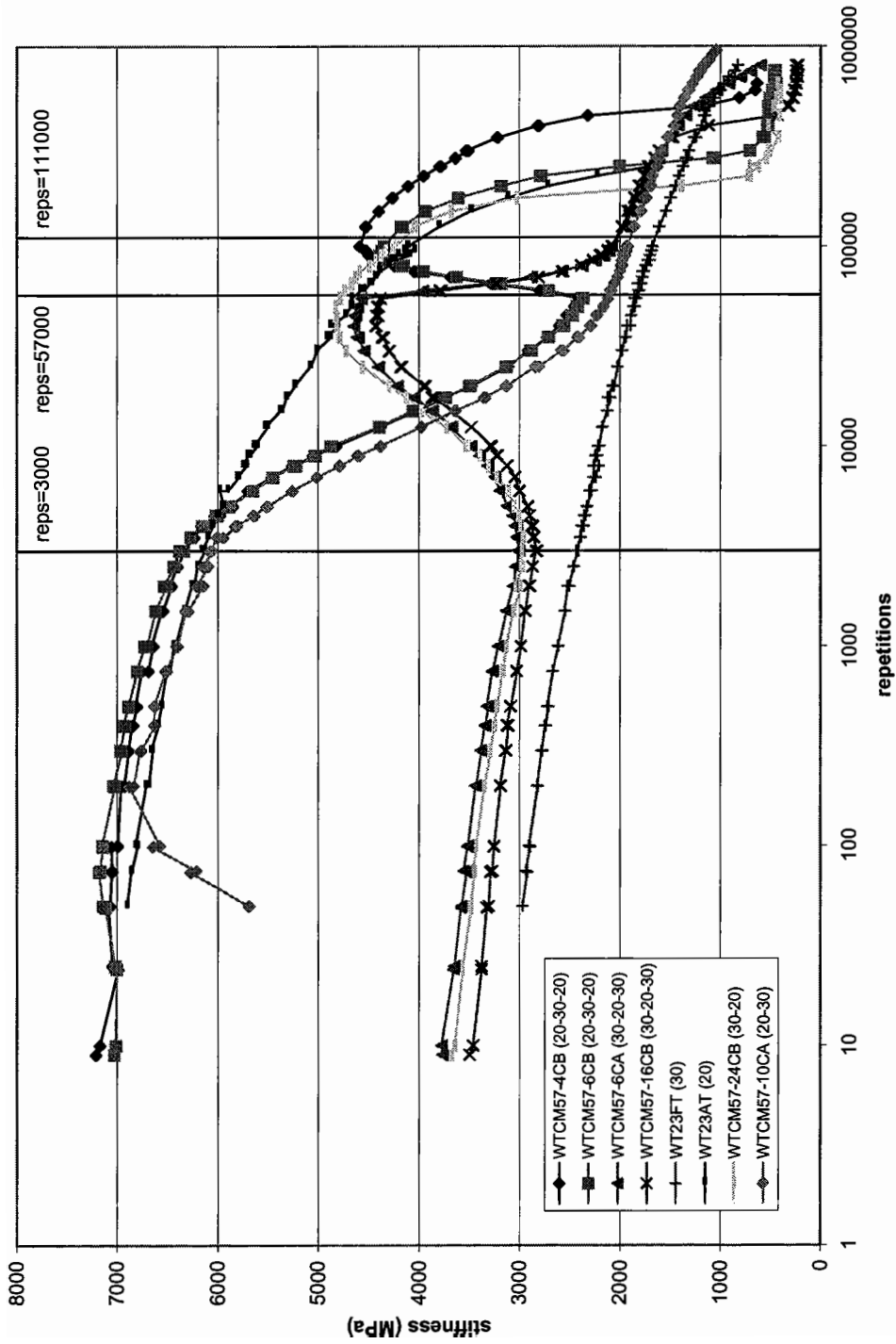


Figure 4.52. A summary of varied-temperature fatigue tests in terms of stiffness versus repetition.

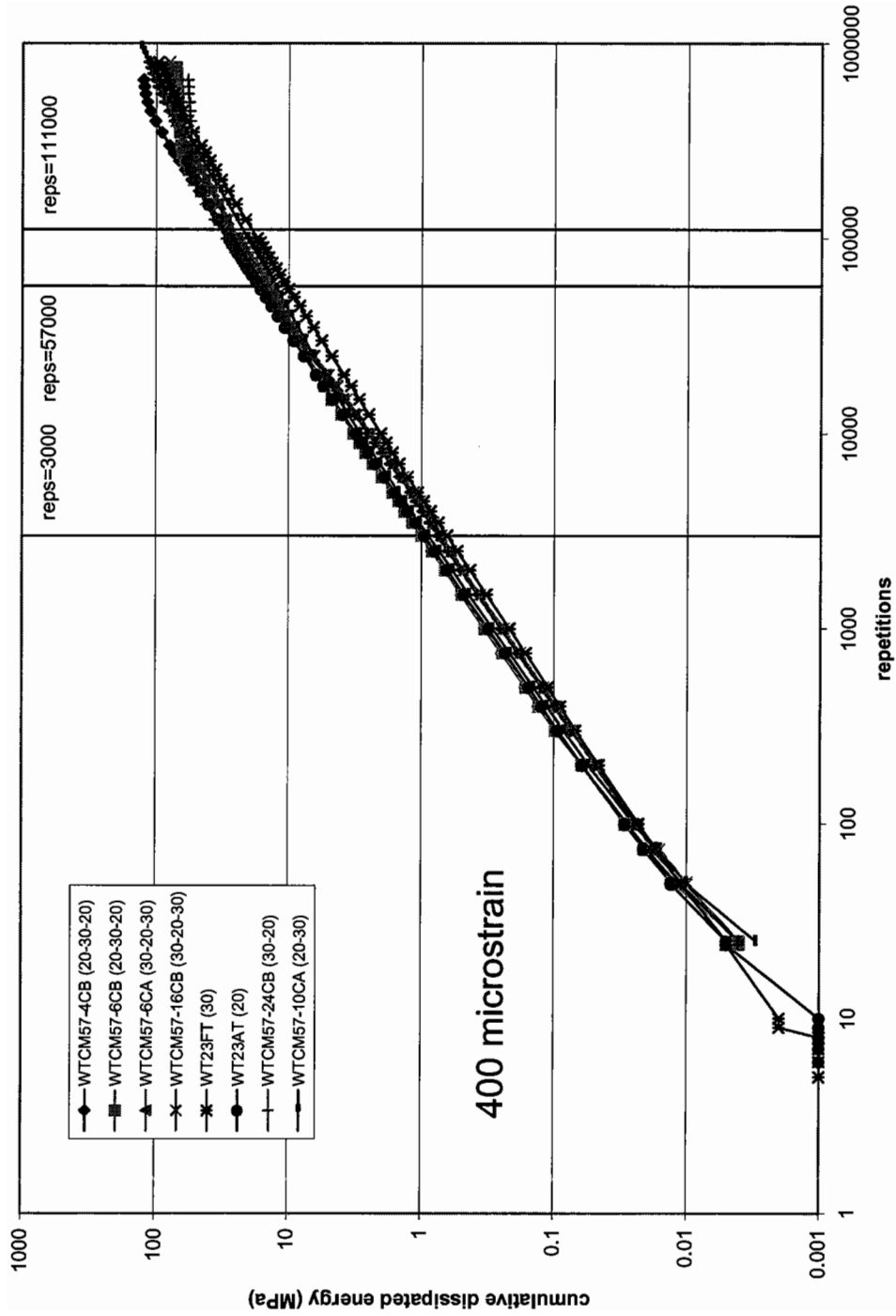


Figure 4.53. Cumulative dissipated energy plot for varied-temperature fatigue tests.

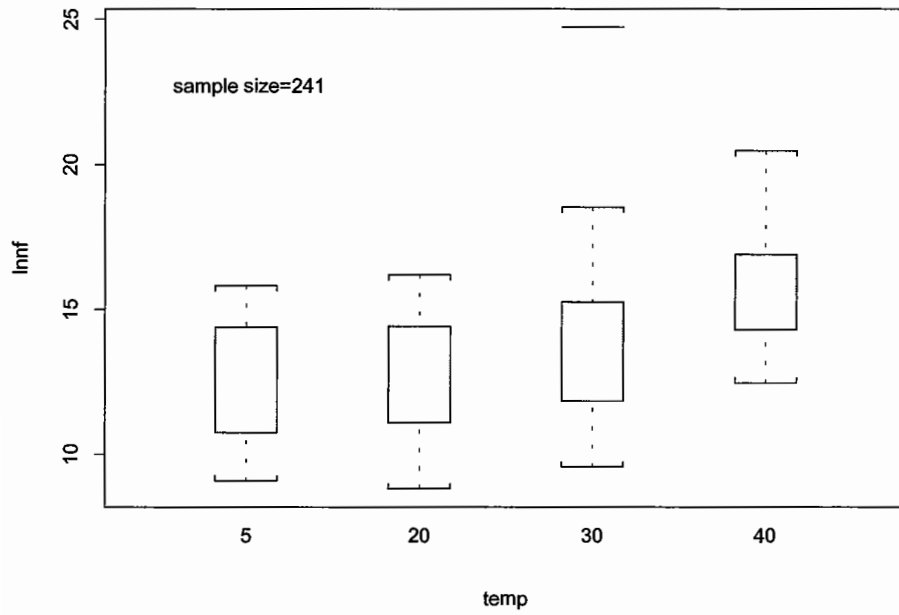


Figure 4.54. Boxplot of fatigue life versus temperature ($^{\circ}$ C).

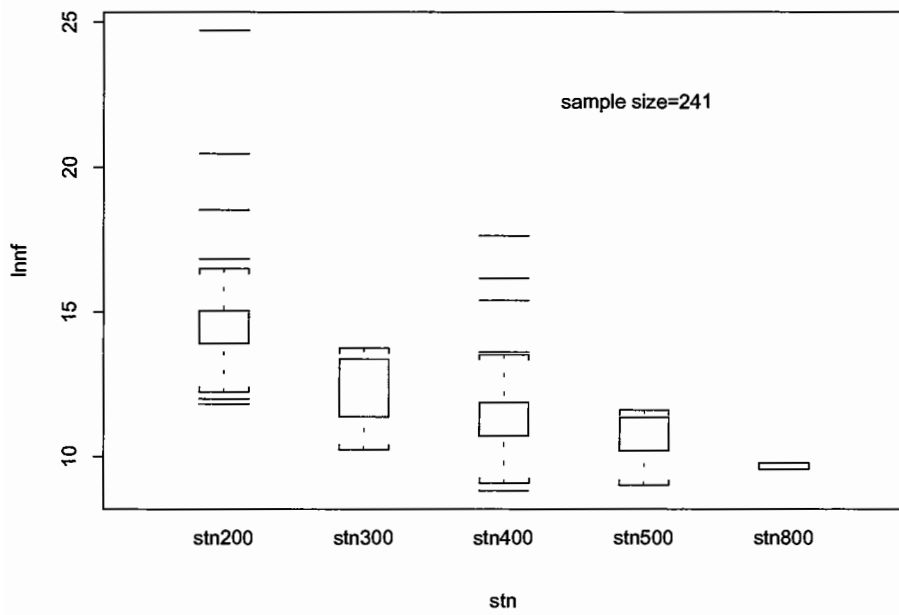


Figure 4.55. Boxplot of fatigue life versus strain.

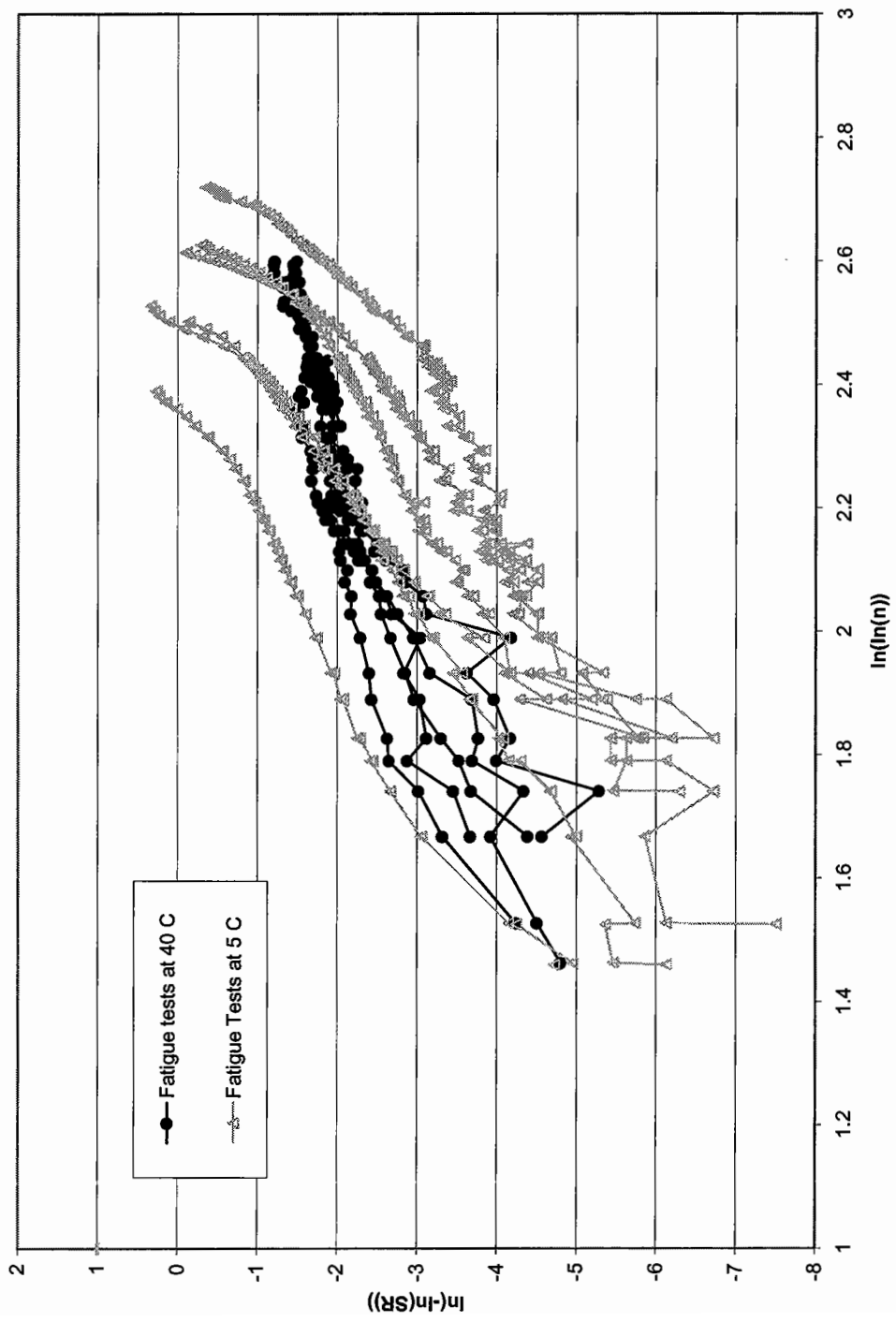
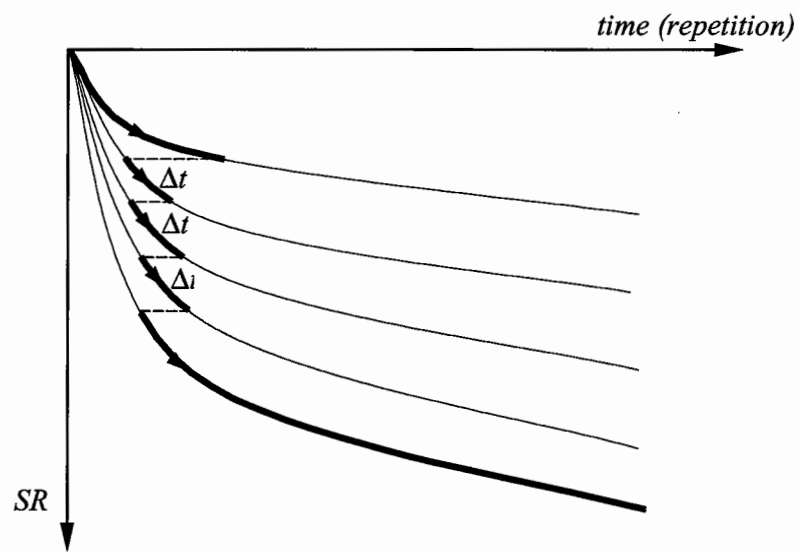
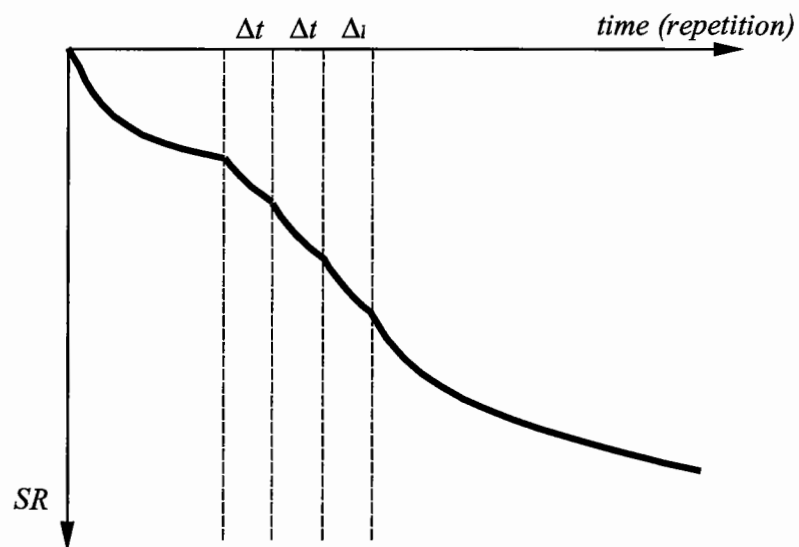


Figure 4.56. Weibull curves at extreme temperatures.

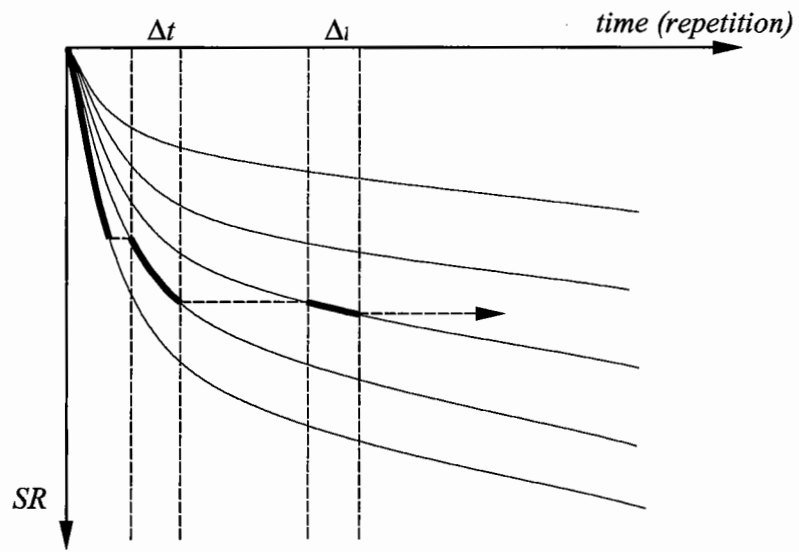


(a) construction procedure

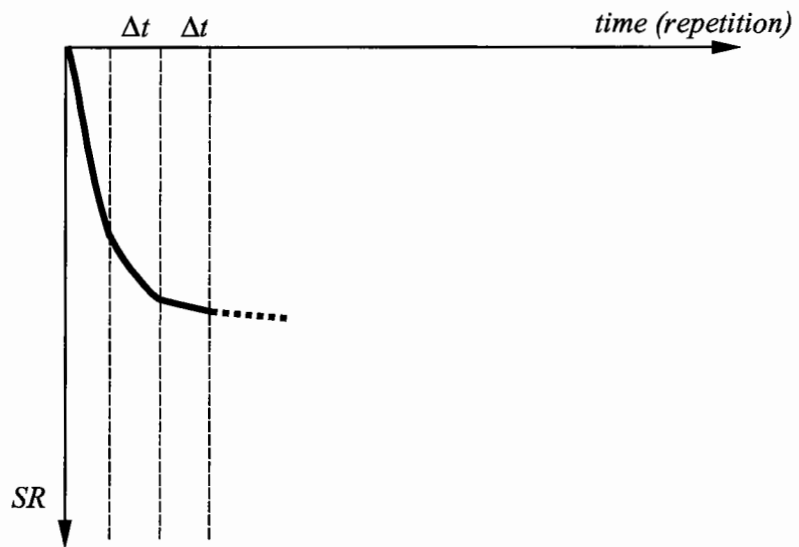


(b) compound stiffness deterioration curve

Figure 4.57. Application of time hardening procedure from a low damage state to a high damage state in terms of SR .

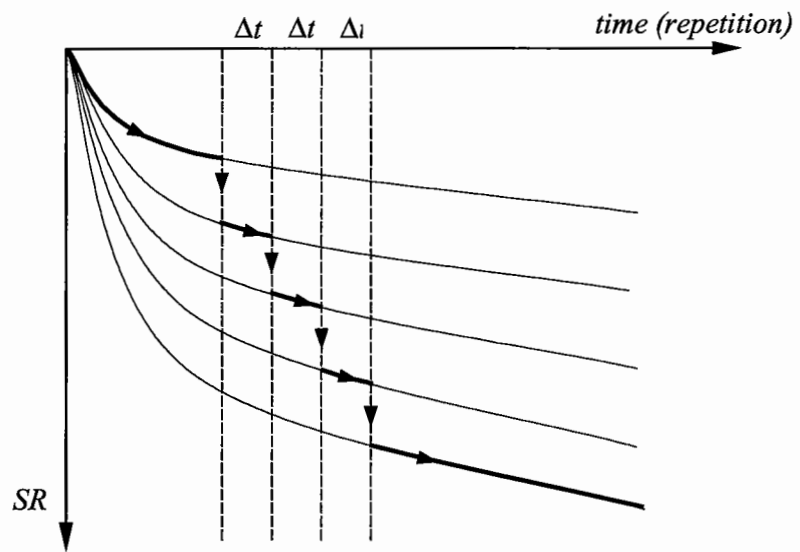


(a) construction procedure

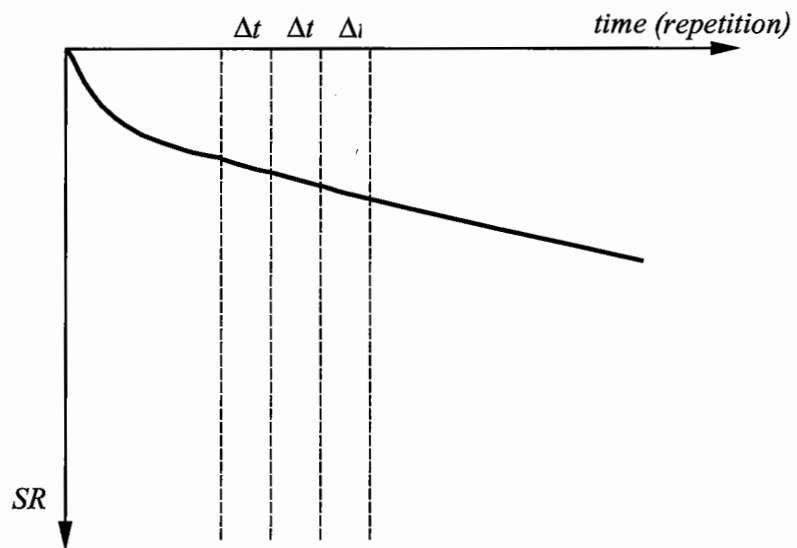


(b) compound stiffness deterioration curve

Figure 4.58. Application of time hardening procedure from a high damage state to a low damage state in terms of SR .

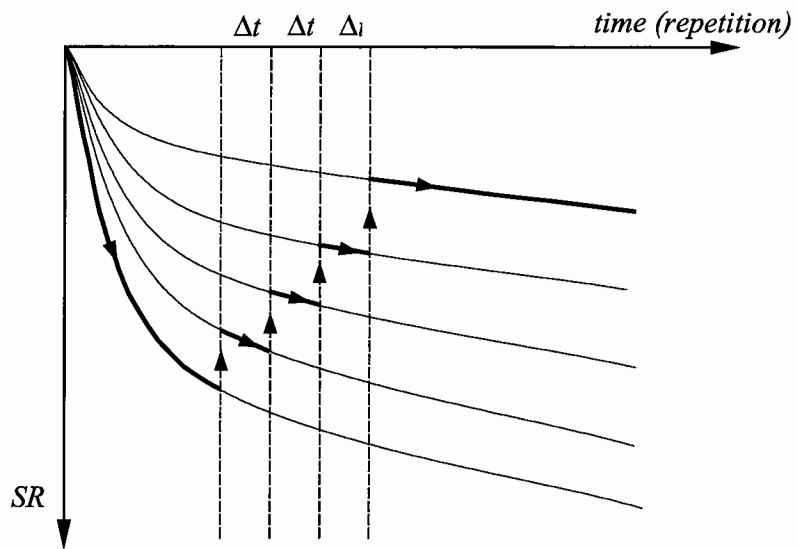


(a) construction procedure

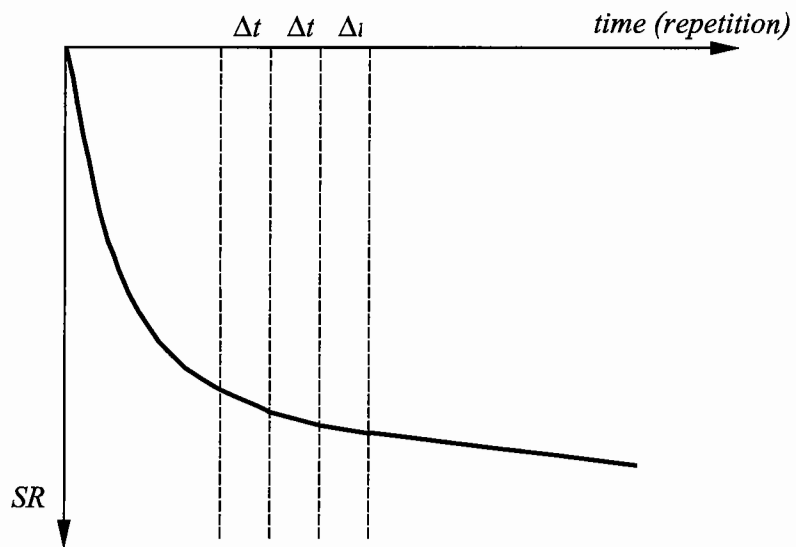


(b) compound stiffness deterioration curve

Figure 4.59. Application of strain hardening procedure from a low damage state to a high damage state in terms of SR .



(a) construction procedure



(b) compound stiffness deterioration curve

Figure 4.60. Application of strain hardening procedure from a high damage state to a low damage state in terms of SR .

5.0 WEIBULL THEORY

5.1 Introduction

The applicability of using the Weibull curves to describe the fatigue damage (crack initiation) of asphalt concrete has been successfully demonstrated from the statistical study in Chapter 4. The question that follows will be how to apply the Weibull curves obtained from the laboratory to predict in situ pavement fatigue performance. Therefore, the goal of this chapter is to present an approach to simulate the in situ pavement fatigue damage process using the Weibull proportional hazards model (Weibull PH model). The advantage of the Weibull PH model is that it can estimate the baseline function and thus make it possible to estimate the parameters of the model with linear regression.

The fatigue damage process is a stiffness deterioration process caused by the combined effects of material, traffic, and environmental variables. Some of the material variables include air-void content, asphalt content, fines content, aggregate type and gradation, and asphalt type; some traffic variables are traffic load composition, traffic wander, and vehicle speed; and finally, environmental variables mainly include temperature, moisture content, and precipitation. As a result, the fatigue damage process should be a function of all these variables. Stiffness ratios from laboratory fatigue tests is studied herein, to develop a function that reflects the effects of both material and environment variables on the fatigue damage process.

Following the definition given by Bogdanoff (1985): “a stochastic process is a mathematical model of any dynamic process whose evolution with time is governed by

probabilistic laws,” it was found that the fatigue failure of a laboratory prepared asphalt concrete beam can be appropriately described by the survivor function with a Weibull density function.

In the following sections, the theoretical background of the Weibull PH model will be briefly described. A set of data from the laboratory temperature sensitivity tests of WesTrack samples is used as an example to illustrate the application of the Weibull PH model. A comparison of predicted regression results and real data is also included. The approach, namely the Weibull dynamic approach, to applying the Weibull PH model to real pavement is also discussed. The use of Miner’s Law to explain stiffness ratio change and fatigue life is examined. To bridge the gap caused by the difference of boundary conditions between laboratory test results and in situ performance, a model, the Weibull accelerated failure time model, is proposed in this chapter. Additionally, an example utilizing the MDD data of CAL/APT Goal 1 Section 503RF is given to verify the feasibility of this failure time model. It should be mentioned that the derivation process of the Weibull theory and the Weibull accelerated failure time model generally follows Collett’s famous book on survival analysis (Collett 1994).

5.2 Survival Analysis

Collett offers the following definition of survival analysis: “Survival analysis is the phrase used to describe the analysis of data that correspond to the time from a well-defined time origin until the occurrence of some particular event or end-point.” In brief, survival time is the time until an event occurs. In the category of asphalt concrete, the survival time could be defined as the load, stress or strain repetitions, which is the

survival time, until the stiffness reaches its 50 % reduction, which is the event. In the laboratory tests time and repetition are interchangeable because the loading frequency in this study is fixed at 10 Hz. It should be noted that the survival time is heavily dependent on how the event is defined.

5.2.1 Survivor and Hazard Functions

Two important functions, namely the survivor and hazard functions, are crucial to the survival analysis. The actual survival time of an individual beam, t , can be regarded as the value of a variable T , which is the random variable of survival time. Thus, the different values that T can take have a probability distribution function, called $f(t)$. The distribution function of T is then given by

$$F(t) = P(T < t) = \int_0^t f(u) du .$$

The survivor function $S(t)$ is defined as the probability that the survival time is greater than or equal to t , that is,

$$S(t) = P(T \geq t) = 1 - F(t) .$$

In this study, the stiffness ratio as a function of repetition (or time) is regarded as the survivor function in survival analysis.

The hazard function is defined as the probability that, for example, the beam will reach its failure criteria, say a stiffness reduction of 50 %, at time t , conditional on the beam's having survived to that time. Thus, for an asphalt concrete beam, the hazard function is the instantaneous damage rate for a beam surviving to time t . Hence,

$$h(t) = \lim_{\delta t \rightarrow 0} \left\{ \frac{P(t \leq T < t + \delta t \mid T \geq t)}{\delta t} \right\}.$$

According to the probability theory, for two events A and B with $P(B) \neq 0$, the conditional probability of A given B can be expressed as

$$P(A \mid B) = \frac{P(A \cap B)}{P(B)}.$$

Therefore,

$$P(t \leq T < t + \delta t \mid T \geq t) = \frac{P(t \leq T < t + \delta t)}{P(T \geq t)} = \frac{F(t + \delta t) - F(t)}{S(t)}.$$

Hence,

$$h(t) = \lim_{\delta t \rightarrow 0} \left\{ \frac{P(t \leq T < t + \delta t \mid T \geq t)}{\delta t} \right\} = \lim_{\delta t \rightarrow 0} \left\{ \frac{F(t + \delta t) - F(t)}{\delta t} \cdot \frac{1}{S(t)} \right\} = \frac{F'(t)}{S(t)}.$$

The derivative of $F(t)$ with respect to t is $f(t)$. Hence, the hazard function $h(t)$ used in survival analysis is defined as

$$h(t) = \frac{f(t)}{S(t)} = -\frac{d}{dt}(\ln S(t)).$$

5.2.2 Fatigue Damage Process and Survivor Function

The fatigue damage process is regarded as a process of stiffness deterioration caused by repetitive loading. Stiffness ratio is a normalized quantity that normalizes the stiffness value relative to its initial stiffness, which is defined as the stiffness at the 50th repetition, for a given testing condition. For incorporation with the survivor probability function, henceforth in this thesis the fatigue damage process is represented in terms of stiffness ratio, starting from 1.0 and decreasing along with time (repetitions) until, if possible, 0.0.

To begin with, the survival time is defined as the time until an event occurs; so it is important to recognize that the survival time is dependent on how the event is defined. To explain the fatigue damage process utilizing the concept of survival analysis, it is necessary to extend the definition of event.

For example, let's randomly pick a finite set of points from a uniform distribution ranging from 0 to 1. This set will be designated as the S set. For our purposes, the S set is the set of stiffness ratios. Then, it is declared that the survival time is the repetition when one of the elements in S set is reached. The event will be the specified stiffness ratio in S set. If the elements in S set are sorted with a descending order, then the

survival times found correspondingly will construct the fatigue damage process (survivor function).

Thus, the interpretation of an SR-N curve (fatigue damage curve or stiffness deterioration curve) is that, for a given SR and its corresponding N, a testing beam has a probability, SR times 100 %, to survive after the Nth repetition. Alternatively, it can be stated that a testing beam will have SR times 100 % fatigue life remaining after the Nth repetition.

5.3 Weibull Proportional Hazards Model

5.3.1 Weibull Density Function

The stiffness deterioration in terms of stiffness ratio is utilized as an index of fatigue damage in this Weibull dynamic approach. As presented in Chapter 4, the fit of the stiffness deterioration curve following a two-parameter Weibull function was clearly evident. Figure 5.1 illustrates an example of a fatigue damage process in terms of stiffness ratio versus repetition. As seen in this figure, the stiffness deterioration can be fit very well with the function $\exp(-\lambda t^\gamma)$ with $\lambda = 0.002$ and $\gamma = 0.412$. The corresponding Weibull density function with these two parameters was drawn in a semi-logarithm plot as visualized in Figure 5.2. Henceforth, it is assumed that the probability density function of T will follow a two-parameter Weibull density function.

The Weibull density function has the following form

$$f(t) = \lambda \gamma t^{\gamma-1} \exp(-\lambda t^\gamma), \quad 0 \leq t \leq \infty.$$

where λ is the scale parameter and γ is the shape parameter.

Therefore, the survivor function can be expressed as

$$S(t) = 1 - \int_0^t f(u) du = 1 - \int_0^t \lambda \gamma u^{\gamma-1} \exp(-\lambda u^\gamma) du = 1 - \int_0^t \frac{d(\exp(-\lambda u^\gamma))}{du},$$

$$= \exp(-\lambda t^\gamma)$$

which results in

$$\ln(-\ln(S(t))) = \ln \lambda + \gamma \ln t.$$

That is to say, if the Weibull assumption is tenable, where $\hat{S}(t)$ is the observed stiffness ratio, then a plot of $\ln(-\ln(\hat{S}(t)))$ against $\ln t$ should give an approximately straight line.

5.3.2 Weibull Proportional Hazards Model

To understand the Weibull proportional hazards model, it is necessary to comprehend the nature and significance of the Cox proportional hazards model (Cox 1972). The formula for the Cox PH model is:

$$h(t, X) = h_0(t) \exp\left(\sum_{i=1}^p \beta_i X_i\right)$$

where $h_0(t)$ = baseline hazard function,

$X = (X_1, X_2, \dots, X_p)$, the covariates.

Another important definition pertinent to the derivation of the Weibull PH model is the hazard ratio (HR), which is defined as the hazard for one individual (or beam) divided by the hazard for a different individual (or beam). Two individuals can be distinguished by the set of different covariates, i.e., the X 's. The Cox PH model assumption requires that the HR stays constant over time.

$$HR = \frac{h(t, X^*)}{h(t, X)} = \text{constant} .$$

It should be noted that in the Cox PH model the baseline hazard ($h_0(t)$) is an unspecified function.

Recall that the survivor function and the hazard function with a Weibull density function can be expressed as follows:

$$S(t) = \exp(-\lambda t^\gamma), \text{ and}$$

$$h(t) = \frac{d(-\ln S(t))}{dt} = \lambda \gamma t^{\gamma-1} .$$

For any laboratory fatigue test, imagine that there exists a baseline function such that

$$\frac{h_i(t)}{h_0(t)} = \frac{\lambda_i \gamma t^{\gamma-1}}{\lambda_0 \gamma t^{\gamma-1}} = \frac{\lambda_i}{\lambda_0} = \varphi,$$

that is,

$$h_i(t) = \varphi h_0(t).$$

The Weibull PH model has the same formula as the Cox PH model, except that in the Weibull PH model the baseline function can be specified and expressed as

$$h_0(t) = \lambda \gamma t^{\gamma-1}.$$

The φ cannot be negative as it is a function of test conditions and material variables. One way to express and ensure the positiveness for any variable values is to use the exponential function.

Thus, if the survival time has a Weibull distribution, then the hazard function can be in the following form,

$$h(t, X) = \lambda \gamma t^{\gamma-1} \exp\left(\sum_{i=1}^p \beta_i X_i\right).$$

After performing substitution and integration, the general Weibull survivor function for various fatigue tests can be obtained as:

$$S(t, X) = \exp \left\{ - \exp \left(\sum_{i=1}^p \beta_i X_i \right) \lambda t^\gamma \right\}, \text{ or}$$

$$\ln(-\ln(S(t, X))) = \sum_{i=1}^p \beta_i X_i + \ln \lambda + \gamma \ln t. \quad (5.1)$$

Thus, the Weibull PH model then transforms into a linear regression model. Hereafter, this linear regression model will be termed the Weibull equation. With the observations of the survivor function (stiffness ratio function in our case) and the relevant covariates (material variables, temperature and test strain level), the parameters, namely β_i , λ , and γ , can then be estimated.

5.4 Weibull Equations of WesTrack Project

5.4.1 An Example: Fitting the Weibull PH Model

The data to which the Weibull PH model is applied is the temperature sensitivity fatigue test data for WesTrack fine-plus gradation. Table 5.1 lists the material variables, testing strain levels, and the testing temperatures. Due to the large amount of stiffness ratio data from the duration of each test, they are not itemized here.

As seen from Figure 5.3 through Figure 5.5, the temperature and strain level have significant effects. In addition to this, three important observations can be made:

1. All slopes are almost the same.
2. The intercept ($\ln \lambda + \sum_{i=1}^p \beta_i X_i$) of equation 5.1 is definitely affected by the material variables and test conditions.
3. All the intercepts are negative.

The data lines in the plots of $\ln(-\ln(SR))$ against $\ln(n)$ of Figures 5.3 through 5.5 are reasonably straight, indicating that the Weibull assumption is adequate for dealing with the fatigue damage process of laboratory testing. It can be easily seen that in these figures, for the same test temperature, the lines are almost parallel in the order of test strain levels. The higher the test strain level, the bigger the numerical value of the intercept. Also, the effect of strain level on the space among the Weibull curves decreases as the test temperature increases. It indicates that there is interaction effect between the temperature and strain level.

The following shows you the Splus result of regression equation.

```
Call: lm(formula = log(-log(sr)) ~ av + m200 + r.s4s50 + log(strain) + temp + t
emp *
log(strain) + log(n))
Residuals:
    Min       1Q   Median       3Q      Max
-4.525 -0.2541  0.03081  0.3204  1.245
Coefficients:
              Value Std. Error t value Pr(>|t|)
(Intercept)  31.1304   1.2732   24.4508  0.0000
          av    0.1027   0.0099   10.4026  0.0000
          m200 -1.3976   0.1131  -12.3546  0.0000
          rs4s50 -2.7272   0.3066   -8.8964  0.0000
    log(strain)  2.8252   0.1238   22.8140  0.0000
          temp  -0.2448   0.0451   -5.4254  0.0000
          log(n)  0.4935   0.0058   84.8145  0.0000
temp:log(strain) -0.0355   0.0054   -6.6206  0.0000
```

Residual standard error: 0.5183 on 1369 degrees of freedom
 Multiple R-Squared: 0.8674
 F-statistic: 1279 on 7 and 1369 degrees of freedom, the p-value is 0

Notice that each term in this application model is significant and the multiple R-squared is 0.8674. The *rs4s50* term appearing as a significant item in this equation could be due to the data variation; otherwise, for the same mix the *rs4s50* should be the same.

The final Weibull PH model then is

$$E(\ln(-\ln(SR))) = 31.1304 + 0.1027 av - 0.2448 temp - 2.7272 rs4s50 - 1.3976 m200 \\
+ 2.8252 \ln(stn) + 0.4935 \ln(n) - 0.0355 temp \cdot \ln(stn)$$

(1.2732) (0.0099) (0.0451) (0.3066) (0.1131)
(0.1238) (0.0058) (0.0054)

where *SR* = stiffness ratio,

av = percent air-void content,

m200 = percent passing #200 (0.075 mm) sieve,

rs4s50 = ratio of percent passing #4 (4.75 mm) and #50 (0.3 mm) sieves,

ln = natural logarithm,

stn = microstrain,

temp = test temperature (°C), and

n = repetition.

The number embraced by the parentheses is the standard error of the regression coefficient. The “E” at beginning of the equation stands for the “expected” and the present style is really a strict statistical model specification, otherwise an error term should be specified in the equation. It should be noted that the *av*, *lnstn* and *lnn* have

positive coefficients, whereas the $m200$, $rs4s50$, $temp$, and the interaction term $temp \cdot \ln(stn)$ have negative coefficients. To interpret the physical meaning of these coefficients, let's make a simple example of the change of percent air-void content to the effect of stiffness ratio, based on the obtained regression equation.

Example:

Two mixes, A and B, have the same material and environmental variables except one has 8 % av , the other has 5 % av , respectively. Thus, to reach the same stiffness ratio, say sr_t ,

$$\text{For mix A: } \ln(-\ln(sr_t)) = C + 0.1027 \times 8 + 0.4935 \ln n_A$$

$$\text{For mix B: } \ln(-\ln(sr_t)) = C + 0.1027 \times 5 + 0.4935 \ln n_B$$

Subtracting formula B from formula A, we have,

$$0.1027 \times (8 - 5) + 0.4935 \left(\ln \frac{n_A}{n_B} \right) = 0 \Rightarrow \ln \frac{n_A}{n_B} = -0.6243 \Rightarrow n_A = 0.536 n_B.$$

That is to say that mix B (with 5 % av) needs almost twice the repetitions to reach the same stiffness ratio as mix A does. In other words, mix A fails faster than mix B. Since the av , $\ln(stn)$ and $\ln(n)$ have the positive coefficients in the model, their effects to the stiffness reduction are negatively correlated: the higher the values, the quicker the failure.

The temperature has a negative coefficient in the model; therefore, the higher the temperature, the slower the failure. The temperature range of this application model is from 5 °C to 30 °C.

Figure 5.6 displays the comparison of the application model (solid line in plots) and real data in the plots of $\ln(-\ln(SR))$ against $\ln(n)$ for each specimen. In this experiment, the fitting is quite promising and satisfactory. The model replicates the main trend of each specimen. Of great importance for the Weibull dynamic approach is that a single equation derived from the Weibull PH model can reflect all of the individual tests performed in the laboratory.

5.4.2 Weibull Equation of Coarse Gradation

The intent of estimating the Weibull equation is to try to incorporate this equation, along with other inputs, to conduct a computer-based simulation of the Weibull dynamic approach for predicting fatigue performance of WesTrack project sections. Before discussing the algorithm of the Weibull dynamic approach, a more thorough evaluation of the corresponding Weibull equations for all of the WesTrack gradations is discussed.

The procedure for model selection is the same procedure described as in Chapter 4. Henceforth, the details will be hidden, and only the final model is listed and discussed. The data utilized to estimate the Weibull equation is the same data set used to obtain the conventional coarse stiffness equation in Chapter 4. For the coarse gradation, the final model chosen is listed below.

$$\begin{aligned}
E(\ln(-\ln(SR))) = & 105.8248 - 1.8679 av + 17.4844 \ln stn + 1.1902 temp - 10.3682 rs4s50 \\
& \quad (8.6671) \quad (0.0793) \quad (0.8926) \quad (0.1702) \quad (1.2809) \\
& - 8.8144 m200 + 4.8639 \ln(\ln(n)) - 0.1674 av \cdot \ln stn - 0.0110 av \cdot temp \\
& \quad (0.6664) \quad (0.1027) \quad (0.0075) \quad (0.0009) \\
& + 0.2041 av \cdot rs4s50 - 0.0237 av \cdot \ln(\ln(n)) - 0.0786 \ln stn \cdot temp \\
& \quad (0.0097) \quad (0.0076) \quad (0.0030) \\
& - 1.5698 \ln stn \cdot rs4s50 - 1.3200 \ln stn \cdot m200 - 0.2416 temp \cdot rs4s50 \\
& \quad (0.1303) \quad (0.0701) \quad (0.0262) \\
& - 0.1082 temp \cdot m200 - 0.0534 temp \cdot \ln(\ln(n)) \\
& \quad (0.0129) \quad (0.0036)
\end{aligned}$$

$$R^2 = 0.83.$$

The covariates have the same definition and unit as described in Chapter 4. The corresponding Splus output of the regression equation is as follows:

```
Call: lm(formula = llsr ~ av + lnstn + temp + rs4s50 + m200 + lln + av * lnstn +
av * temp + av * rs4s50 + av * lln + lnstn * temp + lnstn * rs4s50 + lnstn * m200 + temp
* rs4s50 + temp * m200 + temp * lln)
```

Residuals:

```
      Min       1Q   Median       3Q      Max
-3.506 -0.257  0.03644  0.3304  1.519
```

Coefficients:

	Value	Std. Error	t value	Pr(> t)
(Intercept)	105.8248	8.6671	12.2100	0.0000
av	-1.8679	0.0793	-23.5662	0.0000
lnstn	17.4844	0.8926	19.5877	0.0000
temp	1.1902	0.1702	6.9910	0.0000
rs4s50	-10.3682	1.2809	-8.0942	0.0000
m200	-8.8144	0.6664	-13.2276	0.0000
lln	4.8639	0.1027	47.3504	0.0000
av:lnstn	-0.1674	0.0075	-22.2370	0.0000
av:temp	-0.0110	0.0009	-12.8006	0.0000
av:rs4s50	0.2041	0.0097	21.1038	0.0000
av:lln	-0.0237	0.0076	-3.1378	0.0017
lnstn:temp	-0.0786	0.0030	-26.0603	0.0000
lnstn:rs4s50	-1.5698	0.1303	-12.0453	0.0000
lnstn:m200	-1.3200	0.0701	-18.8390	0.0000
temp:rs4s50	-0.2416	0.0262	-9.2205	0.0000
temp:m200	-0.1082	0.0129	-8.4121	0.0000
temp:lln	-0.0534	0.0036	-14.9808	0.0000

Residual standard error: 0.4827 on 8238 degrees of freedom

Multiple R-Squared: 0.8254

F-statistic: 2434 on 16 and 8238 degrees of freedom, the p-value is 0

Figure 5.7 displays the residual plots for this regression model. Figure 5.7a illustrates the residual versus the fitted values. Keep in mind that, for a given testing

condition, the applied Weibull equation represents a stiffness deterioration curve; hence, in the residual plot it will be close to a line. Looking at the residual plot, the pattern is generally acceptable. Notice, however, that there is a group of points with fitted values greater than 0. It is conjectured that some tests included in this set proceeded to the crack propagation stage. Figure 5.7b indicates the assumption of constant variance (homoscedasticity) is valid, except for some potential outliers. Figures 5.7c and 5.7d show that the distribution of residual values is very close to normal; however, some outliers make it skew to the left.

5.4.3 Weibull Equation of Fine and Fine-Plus Gradations

The data utilized to estimate the Weibull equation is the same data set used to obtain the conventional fine and fine-plus stiffness equations in Chapter 4. For the fine and fine-plus gradations, the final model selected is presented here:

$$\begin{aligned}
 E(\ln(-\ln(SR))) = & -55.4911 + 7.0102 ac + 0.6083 av + 0.4755 temp - 1.3899 \ln stn \\
 & + 7.0609 rs4s50 + 0.9143 m200 + 8.0053 \ln(\ln(n)) - 0.0528 ac \cdot av \\
 & - 0.0753 ac \cdot temp + 0.1186 ac \cdot \ln stn - 1.0103 ac \cdot rs4s50 \\
 & - 0.2657 ac \cdot m200 + 0.0908 ac \cdot \ln(\ln(n)) - 0.0045 av \cdot temp \\
 & + 0.0177 av \cdot \ln stn - 0.0266 av \cdot rs4s50 - 0.0057 av \cdot m200 \\
 & + 0.0340 av \cdot \ln(\ln(n)) - 0.0776 temp \cdot \ln stn - 0.1069 temp \cdot rs4s50 \\
 & - 0.0296 temp \cdot m200 - 0.0661 temp \cdot \ln(\ln(n)) + 0.4191 \ln stn \cdot rs4s50 \\
 & + 0.1871 \ln stn \cdot m200 + 0.5835 \ln stn \cdot \ln(\ln(n)) + 0.8220 rs4s50 \cdot m200 \\
 & + 0.2449 rs4s50 \cdot \ln(\ln(n)) + 0.1018 m200 \cdot \ln(\ln(n))
 \end{aligned}$$

$$R^2 = 0.91.$$

The following lists the relevant Splus results of the regression equation.

```
Call: lm(formula = llsr ~ ac + av + temp + lnstn + rs4s50 + m200 + lln + ac * av
+ ac * temp + ac * lnstn + ac * rs4s50 + ac * m200 + ac * lln + av * temp + av * lnstn +
av * rs4s50 + av * m200 + av * lln + temp * lnstn + temp * rs4s50 + temp * m200 + temp *
lln + lnstn * rs4s50 + lnstn * m200 + lnstn * lln + rs4s50 * m200 + rs4s50 * lln + m200 *
lln)
```

```
Residuals:
    Min       1Q   Median       3Q      Max
-3.643 -0.1289  0.01508  0.1742  1.408
```

```
Coefficients:
              Value Std. Error t value Pr(>|t|)
(Intercept) -55.4911   4.2948  -12.9204  0.0000
          ac    7.0102   0.5779   12.1298  0.0000
          av    0.6083   0.0558   10.8974  0.0000
          temp  0.4755   0.0922    5.1562  0.0000
         lnstn -1.3899   0.3329   -4.1744  0.0000
        rs4s50  7.0609   1.0012    7.0526  0.0000
          m200  0.9143   0.2540    3.5997  0.0003
          lln   8.0053   0.4530   17.6705  0.0000
        ac:av  -0.0528   0.0027  -19.6552  0.0000
        ac:temp -0.0753   0.0035  -21.7018  0.0000
        ac:lnstn  0.1186   0.0214    5.5394  0.0000
        ac:rs4s50 -1.0103   0.1395   -7.2427  0.0000
        ac:m200  -0.2657   0.0292   -9.0998  0.0000
        ac:lln   0.0908   0.0241    3.7746  0.0002
        av:temp  -0.0045   0.0003  -14.8512  0.0000
        av:lnstn  0.0177   0.0040    4.4628  0.0000
        av:rs4s50 -0.0266   0.0111   -2.3969  0.0165
        av:m200  -0.0057   0.0026   -2.2078  0.0273
        av:lln   0.0340   0.0045    7.5070  0.0000
        temp:lnstn -0.0776   0.0017  -46.3067  0.0000
        temp:rs4s50 -0.1069   0.0169   -6.3401  0.0000
        temp:m200  -0.0296   0.0054   -5.5093  0.0000
        temp:lln  -0.0661   0.0019  -34.0057  0.0000
lnstn:rs4s50  0.4191   0.0705    5.9465  0.0000
lnstn:m200    0.1871   0.0192    9.7235  0.0000
lnstn:lln     0.5835   0.0307   19.0056  0.0000
rs4s50:m200   0.8220   0.0329   24.9925  0.0000
rs4s50:lln    0.2449   0.0879    2.7857  0.0053
m200:lln     0.1018   0.0230    4.4289  0.0000
```

```
Residual standard error: 0.3304 on 14720 degrees of freedom
Multiple R-Squared: 0.9132
F-statistic: 5529 on 28 and 14720 degrees of freedom, the p-value is 0
```

Figure 5.8 presents the residual plots for this regression model. The same conclusions as for the coarse regression are pertinent to the residual plots of this fine and fine-plus regression, except that the R-squared of this regression is higher. These two obtained Weibull equations, coarse and fine and fine-plus, will be utilized as the input of the *Weibull* program in Chapter 7.

5.5 Prediction of Fatigue Performance Using Weibull Theory

Now it is time to explore how the Weibull theory can be applied to prediction of the in situ fatigue performance. Recall that both the general hypothesis of fatigue damage postulated in Chapter 4, as well as the other significant assumption made to complete the procedure: that the fatigue damage is irrecoverable in whatever situation. The assumptions that center the algorithm of the fatigue performance prediction are summarized as follows,

- 1. For every testing situation containing many variables, there exists one and only one associated stiffness deterioration curve in the SR-N space. If the testing situation changes from one state to the other at a given instant (repetition), the stiffness deterioration rate will follow the rate of the new state, starting immediately at that specific instant (repetition).*
- 2. The SR cannot be increased.*

Figure 5.9 is a schematic illustration of the general hypothesis of fatigue damage. Two stiffness deterioration curves, representing situations 1 and 2, are shown on this figure. At time (or repetition) $t - \Delta t$, the material begins to deteriorate along the situation 1 curve for Δt time (or repetitions) of traffic loading. During this period, the stiffness of the material was reduced by the amount $\Delta SR_{t-\Delta t \rightarrow t}^{(1)}$, which is the difference of stiffness ratio from $t - \Delta t$ to t at situation 1. Suddenly, the situation changes from 1 to 2 at time t . According to the general hypothesis of fatigue damage, the stiffness deterioration rate will follow the rate of the situation 2, starting immediately at time t .

After Δt passing, the total stiffness deterioration will be $\Delta SR_{t \rightarrow t+\Delta t}^{(2)}$, which means the difference of stiffness ratio from t to $t + \Delta t$ at situation 2.

Figure 5.10 demonstrates how the irrecoverable assumption of fatigue damage (assumption 2) can be applied to the Weibull dynamic approach to find the material's true stiffness deterioration curve. Assume the stiffness ratio at time $t - \Delta t$ is $SR_{t-\Delta t}^{(0)}$. Then, the stiffness ratio at time t is going to be $SR_t^{(1)} = SR_{t-\Delta t}^{(0)} + \Delta SR_{t-\Delta t \rightarrow t}^{(1)}$; likewise, the stiffness ratio at time $t + \Delta t$ will be $SR_{t+\Delta t}^{(2)} = SR_t^{(1)} + \Delta SR_{t \rightarrow t+\Delta t}^{(2)}$.

By repeating this procedure, the fatigue damage caused by the situation change is then clearly and dynamically described. This iteration procedure is the essence of the *Weibull* program included in Appendix E. The Weibull equation is an equation that can include all the situations, making it very easy to calculate the ΔSR after each time step Δt .

5.6 Miner's Law and Weibull Theory

In 1945, Miner proposed a hypothesis of cumulative damage to explain the fatigue life of aluminum alloys of aircraft. The hypothesis was simply expressed as,

$$\sum \frac{n_i}{N_i} = 1, \quad (5.2)$$

where n_i = number of repetitions applied at i th stress,

N_i = number of repetitions to failure at i th stress.

The equation states that the failure of a material subjected to a series of stresses, will, due to the cumulative damage, occur at a time when the $\sum \frac{n_i}{N_i}$ is equal to unity. It should be noted that the emphasis was on different stress levels and not on various strain levels. Not until 1960 did Saal and Pell suggest that, instead of stress, strain would seem to be the appropriate criterion when applying Miner's Law to asphalt concrete.

In 1961, Monismith et al. related Miner's Law to asphalt pavement design in such a way that a satisfactory design should fulfill the criterion $\sum \frac{n_i}{N_i} \leq 1$. Notice that during this stage Miner's Law was related to not only the strain but to the combination of fatigue life and various strain levels. This increases the applicability of the controlled-strain flexural fatigue test, for strain-versus-fatigue-life is the typical test result. As illustrated in Figure 5.11, if $\sum \frac{n_i}{N_i}$ equals unity, cracking will develop at the end of design life; if $\sum \frac{n_i}{N_i}$ is greater than unity, cracking will develop before the end of design life. In the latter case, the thickness of the pavement or the properties of mix should be modified to reduce the maximum tensile strain occurring at the asphalt concrete layer so that Miner's Law result is kept below unity for the desired number of repetitions.

5.6.1 Miner's Law in Explanation with Stiffness Ratio

Conventionally, the fatigue life is defined as the fatigue-resistant capacity to withstand repetitive flexural bending without cracking; however, in a controlled-strain fatigue test, the fatigue life is defined as when the mix stiffness reaches a 50 % reduction

from the initial stiffness. From the standpoint of stiffness ratio, such a definition requires and predicts only two points in the plot of repetitions versus stiffness ratio, the first point being—repetition 0, stiffness ratio 1, and the second point—fatigue life, stiffness ratio 0.5. This will construct a straight line in the repetitions versus stiffness ratio plot.

Now, let's view Miner's Law from the standpoint of stiffness deterioration. Before starting this argument, let's first explore Miner's Law in a little more depth.

Take, for example, the Miner's Law $\sum_{i=1}^p \frac{n_i}{N_i} = 1$. It is assumed that there are p situations

in conducting controlled-strain fatigue tests and each single test represents a specified situation. From the point of view of linear algebra, the reciprocal set of N_i , i.e.,

$\left\{ \frac{1}{N_1}, \frac{1}{N_2}, \dots, \frac{1}{N_p} \right\}$, will form a base for the equation $\sum_{i=1}^p \frac{n_i}{N_i} = 1$, which is also a linearly

independent set. More important, this base will construct a linear space (or vector space) and thus inherit the properties of addition and scalar multiplication. These properties infer that the cumulative fatigue damage is additive and thus cannot be recovered. Notice

that in the reciprocal set of N_i , i.e., $\left\{ \frac{1}{N_1}, \frac{1}{N_2}, \dots, \frac{1}{N_p} \right\}$, each element in this set

represents the fatigue damage rate, that is, the $1/N_i$ portion of total available fatigue life lost when one loading repetition is applied on the i th situation. Figure 5.12 plots the linear relationship of repetitions versus stiffness ratio according to conventional controlled-strain fatigue test results. As illustrated in Figure 5.12, we have

$$\frac{n_i}{N_i} = \frac{\Delta SR_i}{SR_{0.5}}, \quad (5.3)$$

where ΔSR_i = the loss of stiffness ratio due to apply n_i repetitions at i th situation,
 $SR_{0.5}$ = the stiffness ratio at which stiffness is 50 % reduction of its initial
value.

Therefore, Miner's Law can be expressed as

$$\sum \frac{n_i}{N_i} = \sum \frac{\Delta SR_i}{SR_{0.5}} = 1,$$

and results in

$$\sum \Delta SR_i = SR_{0.5}. \quad (5.4)$$

Notice that,

$$\Delta SR_i = \frac{1}{N_i} \times n_i \times SR_{0.5}.$$

$\frac{1}{N_i}$ and $SR_{0.5}$ are constants. It shows that the ΔSR_i is linearly proportional to n_i ;

in other words, ΔSR_i is a linear function of n_i with a slope $\frac{SR_{0.5}}{N_i}$. If we regard the

stiffness deterioration as an index of fatigue damage, then Miner's Law implicitly

indicates that the fatigue damage cannot be recovered. The cumulative fatigue damage is then the sum of stiffness loss contributed by each single application of loading.

5.6.2 Generalized Miner's Law

Generally speaking, Miner's Law does not explicitly indicate the linearity of the relationship n_i/N_i , if viewed in terms of stiffness ratio. Obviously, in equation 5.3, the linearity of n_i/N_i depends on the linearity of ΔSR_i .

In Figure 5.12, based on the conventional fatigue life definition, ΔSR_i is in proportion to n_i during the whole stiffness deterioration process; however, this is not necessarily the case. If the stiffness deterioration process can be suitably described by a Weibull function, then $\Delta SR_i = W_i(n_{i-1} + \Delta n_i) - W_i(n_{i-1})$, where W_i is the Weibull function at the i th situation, and n_{i-1} is the cumulative loading repetitions before applying Δn_i loading repetitions. Since the Weibull function is nonlinear, ΔSR_i is no longer in proportion to n_i and exhibits nonlinear aspects. However, the equation 5.4 will still hold for predicting cumulative fatigue damage. Remember that this equation is actually the same approach utilized in the Weibull fatigue damage prediction algorithm. Therefore, the Weibull theory extends the interpretation of Miner's Law into a nonlinear domain.

In sum, Miner's Law can be applied either to the linear domain or to a nonlinear domain. It should be noted that the Weibull theory is just an instance of the generalized Miner's Law, for it is probable that functions other than the Weibull function can efficiently describe the fatigue damage process.

Regarding the Weibull approach as a special instance of the generalized Miner's Law, several points can be addressed to further extend and interpret the hypothesis of Miner's Law.

1. The linearity of Miner's Law depends on how you choose and define the second dimension space, in our case, the stiffness ratio.
2. No matter what linear or nonlinear functions are used to describe the fatigue damage process, the loading sequence will decide the time to reach the fatigue failure and therefore the loading sequence cannot be exchanged in equation 5.2.
3. The fatigue damage cannot be increased regardless of the linear or nonlinear functions utilized.
4. Once the failure criteria are determined, the linear function, conventional controlled-strain fatigue test result, or a nonlinear function such as the Weibull function, will have the same fatigue lives.
5. As shown in Figure 5.13, the time to reach pre-defined failure is eventually the same for both linear and nonlinear functions. The linear approach actually utilizes the average fatigue damage rate as opposed to the sharp to flat damage rate of the Weibull function. The fatigue damage process is thus path-independent; that is to say, either a linear approach or Weibull's nonlinear approach will reach the same failure time. However, the Weibull approach preserves the intermediate information of the fatigue damage process.

It seems that Miner's Law, using its linear methodology, will provide quite satisfactory prediction in fatigue life prediction for compound loading cases. As might be expected, the prediction results from both linear or nonlinear approaches should have a certain degree of consistency. Chapter 6 will present the results of simulation of the WesTrack experiment using the linear Miner's Law. Chapter 7 will illustrate the simulation results using the Weibull approach.

5.7 Weibull Accelerated Failure Time Model

5.7.1 Introduction

Laboratory testing is extremely valuable and irreplaceable in pavement design, for it is the most economical and efficient way to evaluate the mix properties before the pavement is built. The information obtained from the laboratory must be applied to prediction of the performance of a proposed pavement. However, it is inefficient and very difficult to make the boundary conditions of laboratory tests exactly match those of field pavements; as a consequence, a correction factor is needed to correct the gap caused by different boundary conditions. It has been recognized that the correction factor to translate laboratory fatigue test results into the real pavement performance should not be taken for granted as a number from the pocket of Merlin; instead, to predict the in situ fatigue performance, it is important to understand every aspect of the correction factor. The following discussion will explain how the Weibull accelerated failure time model can be used to correct for the boundary condition effect.

The Weibull accelerated failure time model is discussed here to evaluate how the stiffness deterioration curve is deviated from the Weibull curve obtained in laboratory due to the difference of boundary conditions. It should be noted that the comparison between field curves and laboratory curves needs to be made under the same test conditions, i.e., temperature, loading frequency, etc. These conditions, if not the same, should be as similar as possible to eliminate a potential variance or bias.

The data source used in this discussion is from the test results of Section 503RF performed as part of Goal 1 of the CAL/APT Strategic Plan (California Department of Transportation 1995). Section 503RF was a full-scale pavement constructed at the Richmond Field Station that was designed and constructed according to Caltrans procedures and contains an asphalt concrete layer on untreated aggregate base and subbase. In addition to these field performance data, several laboratory fatigue tests with the same mixes (field-mixed and field-compacted) are utilized to verify the feasibility of the Weibull accelerated failure time model. One major reason for having chosen Section 503RF is its well-controlled test temperature, which was maintained at $20 \pm 3^\circ\text{C}$.

Without the aid of the back-calculated layer moduli, this discussion of the Weibull accelerated failure time model cannot be performed. The methodology of back-calculation utilized here is based on an Microsoft EXCEL spreadsheet developed by Per Ullidtz (1999). The layer moduli were calculated using the collected multi-depth deflectometer (MDD) data and a five-layer pavement system.

A demonstration example combining the laboratory fatigue test results and the back-calculated moduli of asphalt concrete is presented so as to certify the feasibility of the Weibull accelerated failure time model. In addition to this, the mode factor,

controlled-strain fatigue tests, and controlled-stress fatigue tests are discussed in a general way.

5.7.2 Accelerated Failure Time Model

The following paragraph will focus on a general discussion of the accelerated failure time model. The independent variable, stiffness or stiffness ratio of asphalt concrete, as measured in the field is assumed to act multiplicatively on the time scale relative to the stiffness observed in the laboratory. Intuitively, the model can be utilized as a comparison measurement in terms of the speed of the stiffness deterioration process between the fatigue tests conducted in the laboratory and fatigue performance in the field. It is postulated that the stiffness deterioration process in the field pavement follows a Weibull function.

Under an accelerated failure time model, the survival time of a beam tested in the laboratory is taken to be a multiple of the survival time obtained from back-calculation in the field. Thus the effect owing to different boundary conditions is to increase or decrease the damage caused by each load application. Under this assumption, the probability that a beam tested in the laboratory survives beyond time t is the probability that a pavement in the field survives beyond time ϕt , where ϕ is an unknown, positive constant. The ϕ term is also identified as the shift factor, a correction factor to be multiplied by the laboratory fatigue life to obtain the corresponding fatigue life in the field, and is for the most part caused by the differences of boundary conditions between laboratory and field. The ϕ term will be verified by comparing the back-calculation moduli from MDD data of Section 503RF to the fatigue test results from the laboratory.

Now let $S_{Lab}(t)$ and $S_{Field}(\phi t)$ be the survivor functions for laboratory and field respectively. Then, the accelerated failure time model specifies that

$$S_{Lab}(t) = S_{Field}(\phi t)$$

for any value of the survival time t .

Following the relationship between the survivor function $S(t)$, probability density function $f(t)$ and hazard function $h(t)$, the relationship between the density and hazard functions can be derived as follows.

Let's take the derivative with respect to time of the equation above,

$$\frac{dS_{Lab}(t)}{dt} = \frac{dS_{Field}(\phi t)}{dt}.$$

Then we have

$$f_{Lab}(t) = \phi f_{Field}(\phi t).$$

According to the definition of the hazard function

$$\frac{f_{Lab}(t)}{S_{Lab}(t)} = \frac{\phi f_{Field}(\phi t)}{S_{Field}(\phi t)},$$

we obtain

$$h_{Lab}(t) = \phi h_{Field}(\phi t),$$

that is,

$$h_{Field}(t) = \phi^{-1} h_{Lab}(\phi^{-1} t).$$

The parameter ϕ must be non-negative; therefore, it is convenient to set ϕ as an exponential function e^β , if the Weibull proportional hazards model is utilized. This Weibull function is not to be confused with a Weibull distribution, for the fatigue damage process is a consecutive process with time, which should not be considered as the survival time value arrived at by following a Weibull distribution. The stiffness deterioration process, namely the survivor function or the fatigue damage process, of laboratory fatigue tests is assumed to follow a Weibull function and its baseline hazard function is supposed to have the form

$$h_{Lab}(t) = \lambda \gamma t^{\gamma-1}.$$

Under the assumption that the stiffness deterioration process of laboratory fatigue tests is a Weibull function with scale parameter λ and shape parameter γ , the hazard function of the accelerated failure time model for the field performance can be represented as the following:

$$h_{Field}(t) = \phi^{-1} h_{Lab}(\phi^{-1}t) = \phi^{-1} \lambda \gamma (\phi^{-1}t)^{\gamma-1} = \phi^{-\gamma} \lambda \gamma t^{\gamma-1},$$

and its survivor function can be represented as

$$S_{Field}(t) = \exp\left(-\int_0^t h_{Field}(u) du\right) = \exp\left(-\int_0^t \phi^{-\gamma} \lambda \gamma u^{\gamma-1} du\right) = \exp(-\lambda \phi^{-\gamma} t^{\gamma}),$$

which is a Weibull function with scale parameter $\lambda \phi^{-\gamma}$ and shape parameter γ .

Therefore, if the stiffness deterioration processes of asphalt concrete both in the field and in the laboratory are following the Weibull function when subjected to the same test conditions (excluding test setup), then according to the Weibull accelerated failure time model, $\phi > 1$ will slow down the deterioration process while $0 < \phi < 1$ will accelerate it.

Figure 5.14 illustrates why $0 < \phi < 1$ speeds up the deterioration process and $\phi > 1$ slows it. If we take $\phi = 1$ as a standard curve and term it as “standard ϕ curve”, then for the $\phi = 2$ curve, at any given SR value, the survival time is twice that of the standard ϕ curve; namely, if $\phi = 2$, the fatigue life will be twice that of standard ϕ curve.

What the value of ϕ will be for one field section is going to be verified in the next paragraphs using the back-calculation moduli from MDD data of Section 503RF and the fatigue test results of 503RF (field-mixed and field-compacted).

5.7.3 Demonstration Example

Herein is an example to demonstrate how the ϕ is assessed and a discussion of the associated details will follow. The step-by-step procedures to assess ϕ are shown below:

1. Back-calculate moduli using MDD data,
2. Fit a Weibull function,
3. Find the laboratory Weibull function, and
4. Assess the ϕ value.

5.7.3.1 Back-Calculation of Layer Moduli for Section 503RF

This demonstration example will illustrate a procedure to find the shift factor ϕ caused by the different boundary conditions. Figure 5.15 represents the back-calculation results of Section 503RF of the CAL/APT project trafficked using a Heavy Vehicle Simulator (HVS), the section was subjected to a dual wheel load of 40 kN for the first 150,000 repetitions to prevent excessive deformation of the newly constructed asphalt concrete. The repetitions from 150,000 to 200,000 were applied with an 80 kN dual wheel load. After 200,000 repetitions, the trafficking load was increased to and maintained at 100 kN. It should be noted that the equivalent loading frequency obtained is about 0.075 Hz, which is far less than the loading frequency of 10 Hz utilized in laboratory testing. For more information about the test program of Section 503RF, please refer to the "CAL/APT Program: Test Results from Accelerated Pavement Testing on Pavement Structure Containing Aggregate Base-Section 503RF" (Harvey et al. 1997).

The first 200,000 repetitions yielded very little damage; thus, this demonstration example will consider the 200,000 repetition mark as its starting point. To know the stiffness deterioration in the field, the MDD data was collected and analyzed. The

methodology of back-calculation used here is based on an Microsoft EXCEL spreadsheet developed by Per Ullidtz (1999). The essence of this spreadsheet is mainly based on Odemark's method (Ullidtz 1987) and the minimization of the residual sum of squares, i.e., the sum of squares of the difference between observed deformation and calculated deformation.

It should be noted that after 200,000 repetitions the trafficking load was maintained at 100 kN, however, a 40 kN and a 100 kN wheel load were used to measure deflections during data acquisition.

In Figure 5.15, two stiffness deterioration curves are calculated, one using deflections under the 40 kN wheel load, and the other using deflections under a 100 kN wheel load. Clearly, the 100 kN curve shows less stiffness deterioration than that of the 40 kN curve. It is conjectured that the 100 kN wheel load may have caused a higher confining pressure in the base and thus increased the stiffness of the asphalt concrete. However, as an example, the stiffness deterioration curve measured with 40 kN wheel load deflections will be adapted here for the following discussion.

It should be noted that the strain level occurring at the bottom of the asphalt concrete in Section 503RF varies during fatigue loading as stiffness decreases. In other words, according to the Weibull theory, the stiffness deterioration curve in Section 503RF is a fatigue damage curve consisting of several simple Weibull curves, resulting from laboratory controlled-strain tests at different strain levels but all at the same test temperature. Namely, it is not the laboratory controlled-strain fatigue test curve at 20 °C. However, for simplicity, we will assume the stiffness deterioration curve in the field

follows a Weibull function under constant strain. The fitted Weibull function thus obtained is illustrated in Figure 5.16 and has the equation:

$$\ln(-\ln(SR_{Field})) = -7.7391 + 0.6563 \ln(rep).$$

where rep = the repetitions of traffic loading.

5.7.3.2 Correction Factor and Laboratory Fatigue Test Results for Section 503RF

A field-mixed and field-compacted beam with a 3.4 % air-void content tested at 20 °C at a 200 microstrain level with a loading frequency of 10 Hz will be utilized as the comparison laboratory Weibull curve. The laboratory Weibull function obtained is

$$\ln(-\ln(SR_{Lab})) = -8.3312 + 0.6178 \ln(rep).$$

From the Weibull accelerated failure time model, we know that

$$S_{Lab}(t) = \exp(-\lambda t^\gamma) \text{ and}$$

$$S_{Field}(t) = \exp(-\lambda \phi^{-\gamma} t^\gamma),$$

Taking the logarithm, multiplying by -1, and taking the logarithm again, we have

$$\ln(-\ln(SR_{Lab})) = \ln \lambda + \gamma \ln t \text{ and}$$

$$\ln(-\ln(SR_{Field})) = \ln \lambda - \gamma \ln \phi + \gamma \ln t .$$

It should be noted that the shape parameter γ in this Weibull accelerated failure time model is kept the same for both laboratory and field Weibull functions.

Taking the average value of shape parameters, we then have $\gamma = 0.6371$. According to the Weibull accelerated failure time model, we have,

$$-8.3312 - 0.6371 \ln \phi = -7.7391 \quad \Rightarrow \quad \phi = 0.395$$

The ϕ , which is less than one, indicates that the fatigue damage rate for the HVS site is far quicker than that of the laboratory fatigue test.

5.7.4 Mode Factor and Controlled-Strain Fatigue Test

Monismith and Deacon (1969) proposed a definition of mode of loading to describe the phenomenon. "Damaging fatigue loading has been found to gradually alter the strength and stiffness properties of asphalt paving mixes. ..., in which stress and strain levels are permitted to vary during fatigue loading, that is, the mode of loading." The form is defined as follows:

$$MF = \frac{|A| - |B|}{|A| + |B|} \quad (5.5)$$

where MF = mode factor,

A = percentage change in stress due to a stiffness decrease of C,

B = percentage change in strain due to a stiffness decrease of C, and

C = an arbitrary but fixed percentage reduction in mix stiffness.

Apparently, MF equals -1 for controlled-stress tests and 1 for controlled-strain tests. Any values lying between -1 and 1 represent the intermediate modes. And, most of the time, asphalt concrete pavements in the field will behave like the intermediate mode to different degrees depending upon support conditions, thickness of the asphalt concrete, temperature, and other factors.

An alternative form of the definition of mode of loading can be represented in terms of MF as shown in the following:

$$\frac{|A|}{|B|} = \frac{1+MF}{1-MF}$$

The ratio of $|A|/|B|$ indicates the ratio of percentage change in stress to the percentage change in strain due to a fixed percentage reduction in stiffness. If the ratio is greater than 1 , then, for a fixed percentage decrease in stiffness, the percentage change in stress is higher than the percentage change in strain. In other words, the mode of loading is close to the strain-controlled test. Figure 5.17 plots the $|A|/|B|$ ratios versus the values of MF. As illustrated, $\frac{|A|}{|B|} > 1$, if $0 < MF \leq 1$; $0 < \frac{|A|}{|B|} < 1$, if $-1 \leq MF < 0$. The ratio is sharply increased when the MF is greater than 0.5 . This indicates that the

percentage change in strain can be neglected as compared with the percentage change in stress.

To further explore the mode factor, the fitted Weibull function obtained from back-calculating the results of MDD data for Section 503RF was utilized to run the Circly program. In this simulation, the fixed percentage stiffness change was set to be 5 %, which is the C in equation 5.5. Thus, for every 5 % change in stiffness, the stress and strain calculated from the Circly program will be utilized to compute the mode factor. The initial stiffness of asphalt concrete was set as 5,467 MPa. The pavement structure used in the simulation is listed in Table 5.2.

The top and bottom lifts of one two-lift asphalt concrete layer in Section 503RF are treated as one integrated layer here. The stiffness values are based on the fitted Weibull function. Figure 5.18 shows the history of maximum tensile strains at the bottom of the asphalt concrete layer of Section 503RF utilizing the Circly program; the tensile strain increases as the stiffness decreases and behaves like an exponential function. The tensile strains ranges from 100 to 300 microstrains. The average tensile strain is about 180 microstrain, which is close to the 200 microstrain laboratory fatigue test utilized in finding the correction factor for boundary condition effect as demonstrated in Chapter 5.7.3.2.

The mode factors calculated for this simulation are plotted in Figure 5.19. Note that the starting point of this figure is moved to the repetition at which the 100 kN test wheel load starts to traffic because the damage caused by loads less than 100 kN is fairly limited. It shows that the MF is a little less than zero at the beginning and grows linearly as the stiffness decreases. Hence, in the sense of mode of loading, at first it is between a

controlled-strain and a controlled-stress type, but most of time it exhibits a gradual tendency towards the controlled-strain type.

Two observations can be made from Figure 5.19: (1) when stiffness reaches a 50 % reduction, the MF is about 0.13 and the $|A|/|B|$ ratio is around 1.3; (2) when MF equals 0.5, the stiffness ratio is about 0.2 and $|A|/|B|$ ratio is about 3.0.

It seems that the Weibull proportional hazards model obtained from the controlled-strain fatigue test is quite reasonable and acceptable to apply in explaining real field performance in comparison to the back-calculation results of layer moduli of 503RF data.

5.7.5 Findings and Discussions

From the above Weibull accelerated failure time model and the demonstration example, it seems that the controlled-strain fatigue test is a fair test to explain the phenomenon of the fatigue damage process. However, several restrictions cannot be discounted in this discussion of the Weibull accelerated failure time model. These restrictions are:

1. Using the Circly program, which is a linear layered-elastic program, cannot completely describe the viscoelastic properties of asphalt concrete, especially at high temperatures.
2. Although Section 503RF is well controlled in both environmental and traffic test conditions, this still cannot overcome the intrinsic fact that stiffness deterioration due to fatigue loading will alter the strain levels, therefore

making it problematic to compare laboratory fatigue test data and field performance data, even when both are subjected to the same test conditions.

3. The back-calculation methodology as it now stands is somewhat questionable. The current method seems to introduce considerable variance even if the accuracy of MDD instrumentation is ensured.
4. The wheel speed of the HVS is about 6 miles/hour (mph) and the travel distance of the test wheels is about 6 meters effective length. Thus, the loading frequency is about 0.075 Hz, far slower than that of the laboratory fatigue testing.

Although several unavoidable constraints on the accuracy are inherent in this type of analysis, numerous findings are still worthy of mention, notably

1. The results of the demonstration example indicate that the stiffness deterioration rate of the field ($\phi \cong 0.4$) is about two and a half times faster than that of laboratory tested samples ($\phi = 1.0$). The 200 microstrain level used in laboratory testing is roughly compatible with the 180 average microstrain calculated from the Circly simulation, which has been discussed in Chapter 5.7.4. The test temperature utilized both in the laboratory and at the HVS site is 20°C. The major deviance is in the loading frequency: 10 Hz in laboratory, whereas a very slow frequency 0.075 Hz was used in the field. It is conjectured that the slow loading frequency of the HVS could impart more energy per repetition and thus result in more damage.

2. Instead of maintaining constant tensile strain level, the maximum tensile strain, which occurred at the bottom of the asphalt concrete layer, increases as the load repetitions increase.
3. The deterioration process will increase the tensile strain level at the bottom of the asphalt concrete layer. According to the Weibull theory, the stiffness deterioration process is actually a combined Weibull curve that consists of several simple Weibull curves with different strain levels at the same test temperature. Therefore, it is hard to find out the exact value ϕ in this calculation; in other words, the ϕ should be time-dependent.
4. The inherent properties of the controlled-stress fatigue test will display an infinite strain level if there is no physical limit or constraint of material. This phenomenon contradicts the situation in the field where the asphalt concrete layer is supported by the structure underneath and its deformation is thus partly controlled by it, which restricts the possibility of developing infinite strain. According to the definition of mode factor and the results of simulations, it is certainly reasonable to utilize the results of controlled-strain flexural fatigue tests to predict performance in the field. And, it worked well for a pavement that had an asphalt concrete layer of 150 mm (relatively thick).
5. A better way of assessing the ϕ value is to conduct a trial-and-error iteration method. At first, construct the Weibull proportional hazards model using laboratory fatigue tests with the same mix. Then, assume a ϕ value and use this value to modify the Weibull proportional hazards model. After this, follow the algorithm described before to construct the stiffness deterioration

curve and then compare the curve obtained from back-calculation. If it does not match with the field performance, then change the ϕ value and redo it until they converge. With the aid of an effective modulus back-calculation methodology and the Weibull dynamic approach, the iteration procedure to find the ϕ will be useful for research purposes and provide understanding of shift factors for field real pavement design.

It should be conjectured that it might have given better performance prediction if the finite element program was engaged, for the fatigue damage function is still needed to provide a specified input for finite element program. The accuracy of the finite element method (FEM) to calculate the stress and strain will be eliminated if an inadequate fatigue damage function is utilized. Actually, the change of combination status of the stress and strain is the major property and index to reflect fatigue damage in field pavement. The laboratory controlled-strain fatigue test is adapted for the explanation of fatigue damage because it is easy to control and perform in the laboratory; in other words, neither controlled-stress nor controlled-strain fatigue test can completely describe the fatigue damage behavior of asphalt concrete. As mentioned before, we try to utilize simple and economical tests to identify the fatigue damage behavior and thus bridge the result to fatigue performance in the field. Hence, utilizing the controlled-strain fatigue test to describe the fatigue damage in the field requires, as you might think, some corrections in order to predict the real performance. The debut of the Weibull accelerated failure time model can serve the purpose of determining the correction factor caused by boundary condition effect. However, a more extensive database of real pavement

performance should be created so as to supplement further studies and verify the feasibility of the Weibull accelerated failure time model.

Table 5.1. Temperature susceptibility fatigue test results of WesTrack fine-plus gradation.

specimen	AV	AC	M200	r.s4s50	Temp.	Strain	Nf
WT12ET	5.0	5.35	6.0	2.92	5.1	0.000196	3872422
WT19ET	8.4	5.41	5.8	2.87	5.1	0.000178	923182
WT19FT	9.3	5.41	5.8	2.87	5.1	0.000296	144082
WT21AT	8.1	6.25	5.4	2.94	5.1	0.000400	25615
WT12FT	4.5	5.35	6.0	2.92	19.8	0.000198	3308278
WT11ET	8.8	5.50	5.5	3.10	19.7	0.000178	1191716
WT12DT	5.3	5.35	6.0	2.92	20.2	0.000298	194603
WT21BT	6.5	6.25	5.4	2.94	19.5	0.000401	25559
WT12AT	7.5	5.35	6.0	2.92	30.1	0.000199	925205
WT19CT	9.4	5.41	5.8	2.87	30.2	0.000181	820324
WT12CT	7.6	5.35	6.0	2.92	30.1	0.000300	174999
WT12BT	8.9	5.35	6.0	2.92	30.1	0.000404	49999

Table 5.2. Pavement structure for mode factor simulation.

	Thickness (mm)	Stiffness (MPa)	Poisson ratio
Asphalt concrete	162	Variable	0.35
Aggregate base	274	300	0.35
Aggregate subbase	305	150	0.35
subgrade	Semi-infinite	70	0.45

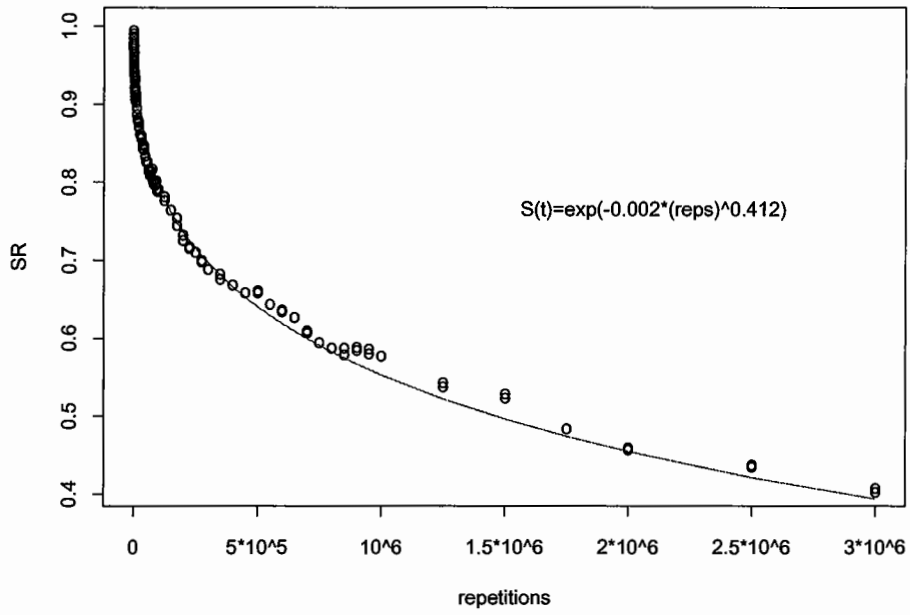


Figure 5.1. Stiffness deterioration curve fitted with a Weibull survivor function with $\lambda = 0.002$ and $\gamma = 0.412$.

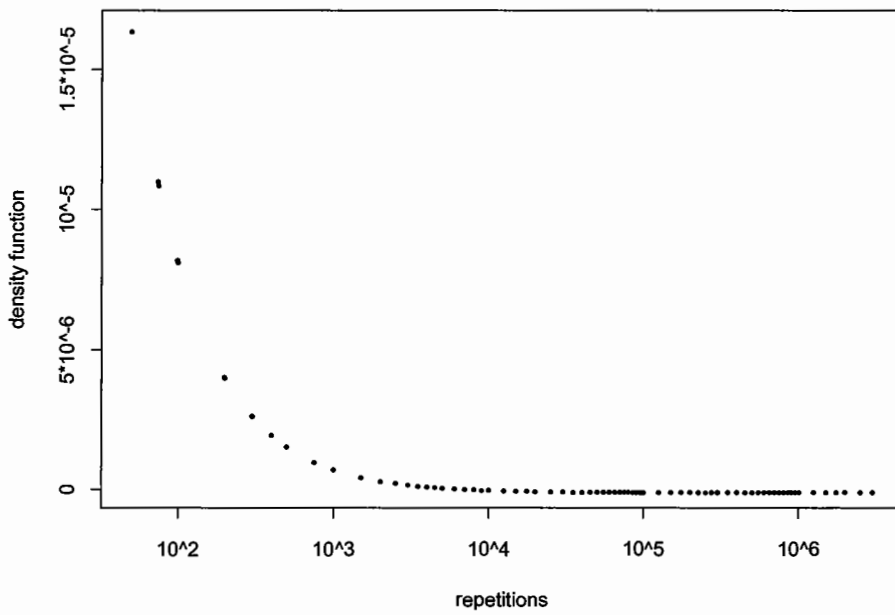


Figure 5.2. Weibull density function with $\lambda = 0.002$ and $\gamma = 0.412$.

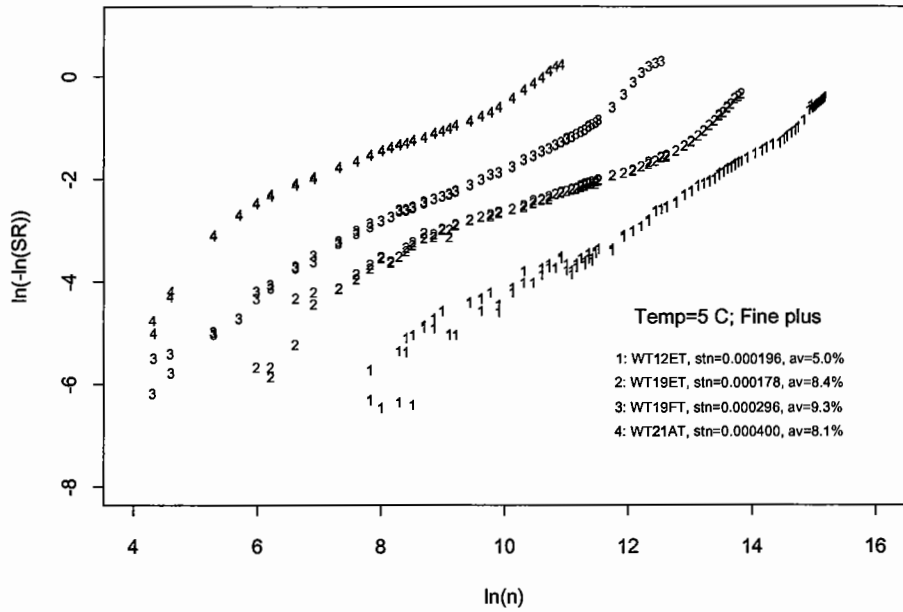


Figure 5.3. Weibull curves for fine-plus gradation at temperature 5 °C.

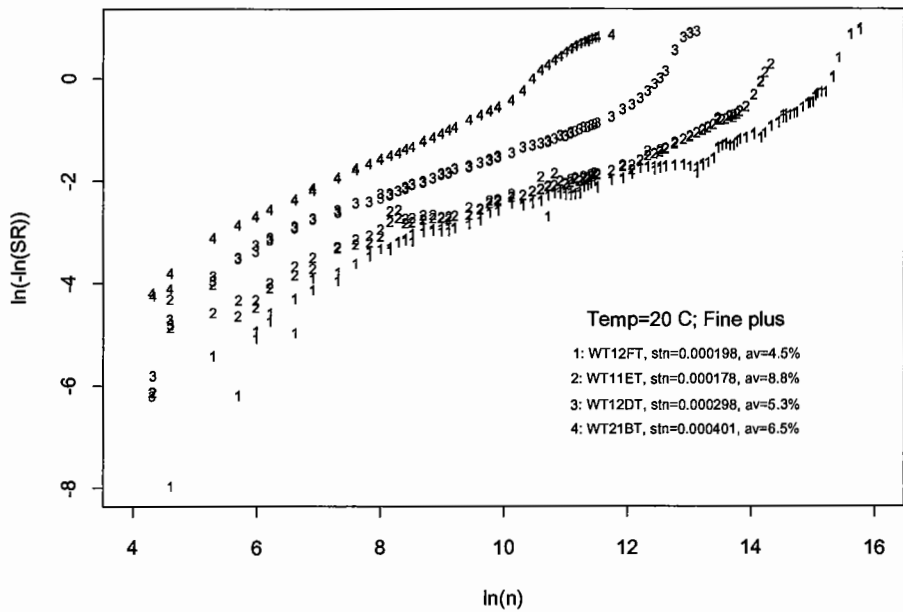


Figure 5.4. Weibull curves for fine-plus gradation at temperature 20 °C.

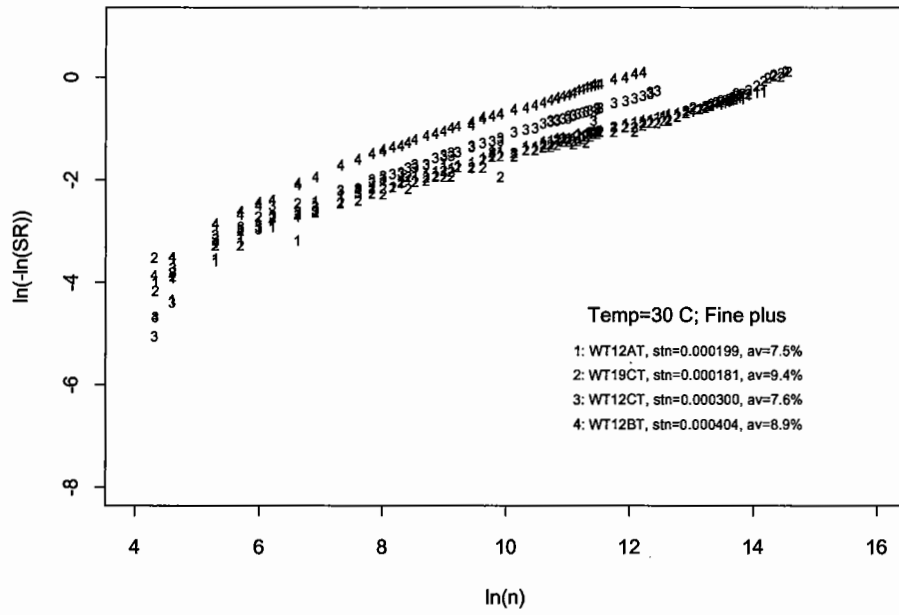


Figure 5.5. Weibull curves for fine-plus gradation at temperature 30°C.

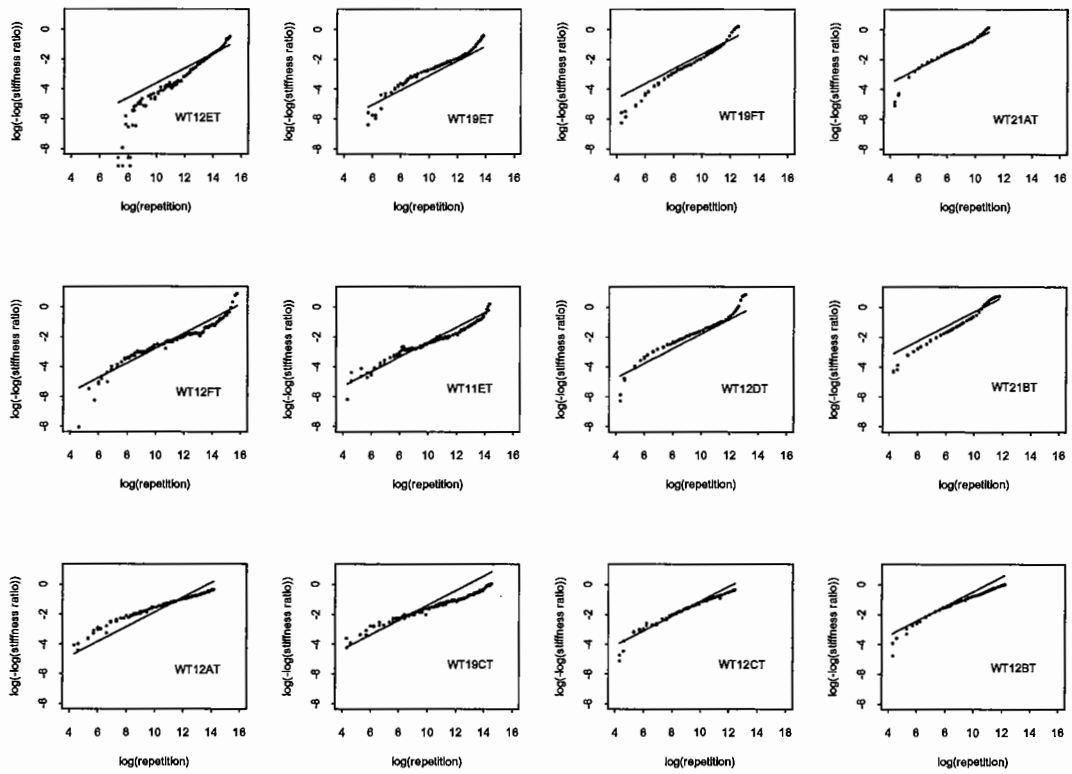


Figure 5.6. Weibull regression fitting and real data for fine-plus gradation.

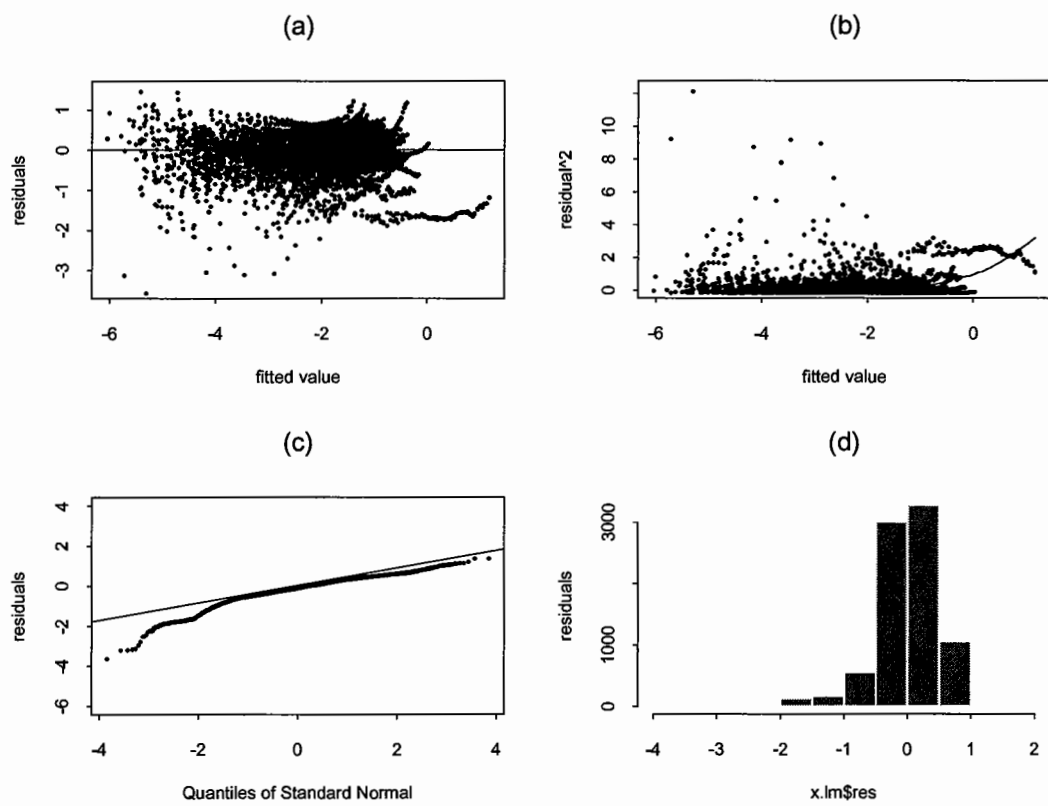


Figure 5.7. Residual plots of Weibull regression equation for coarse gradation.

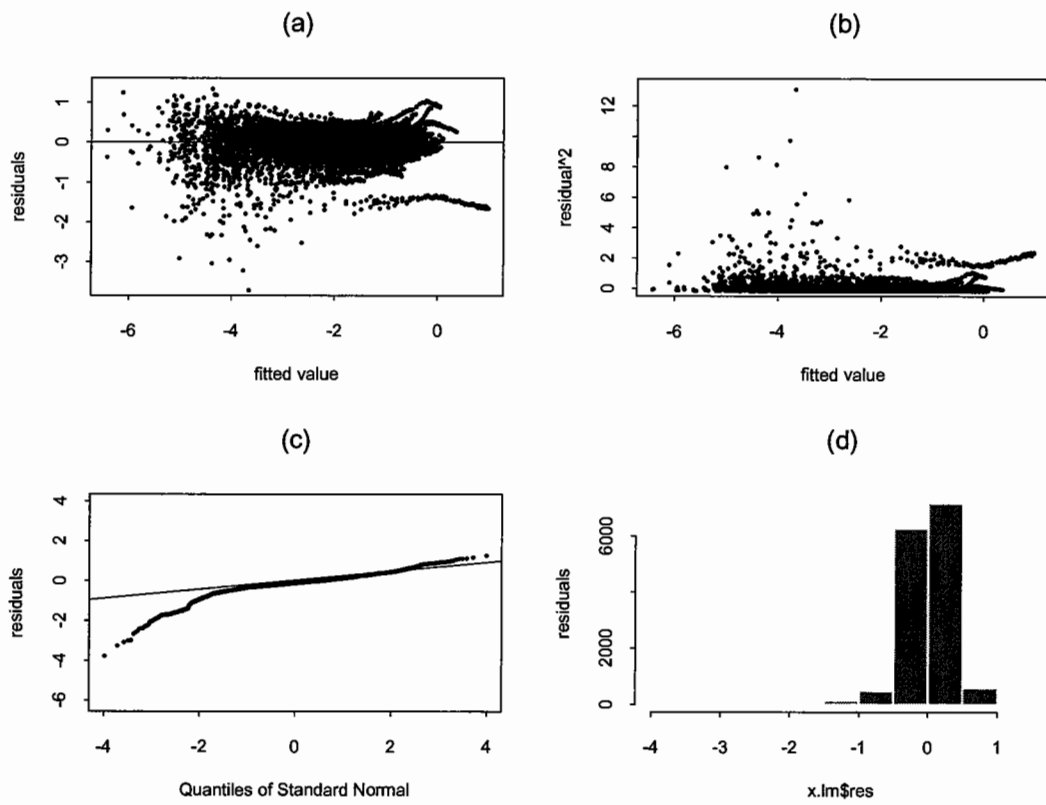


Figure 5.8. Residual plots of Weibull regression equation for fine and fine-plus gradations.

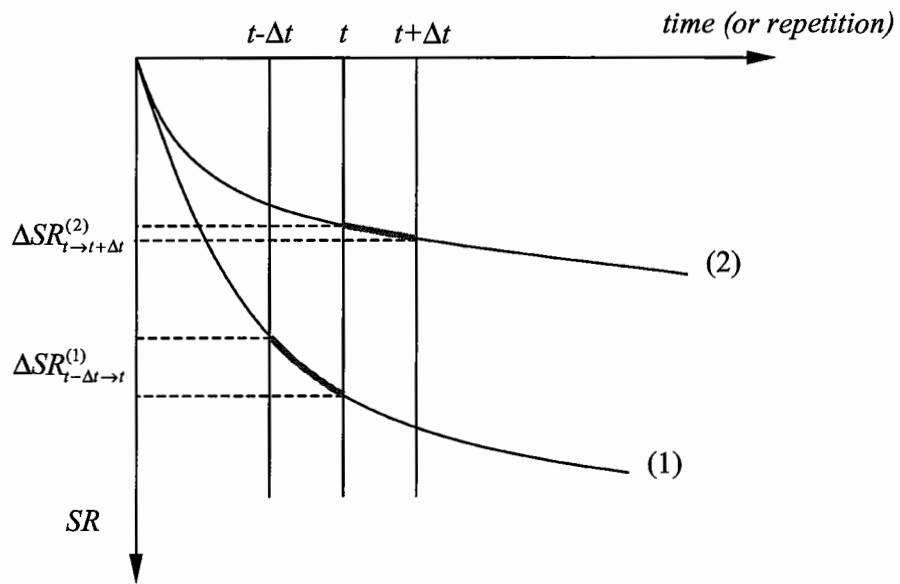


Figure 5.9. Change of stiffness ratios along various stiffness deterioration curves.

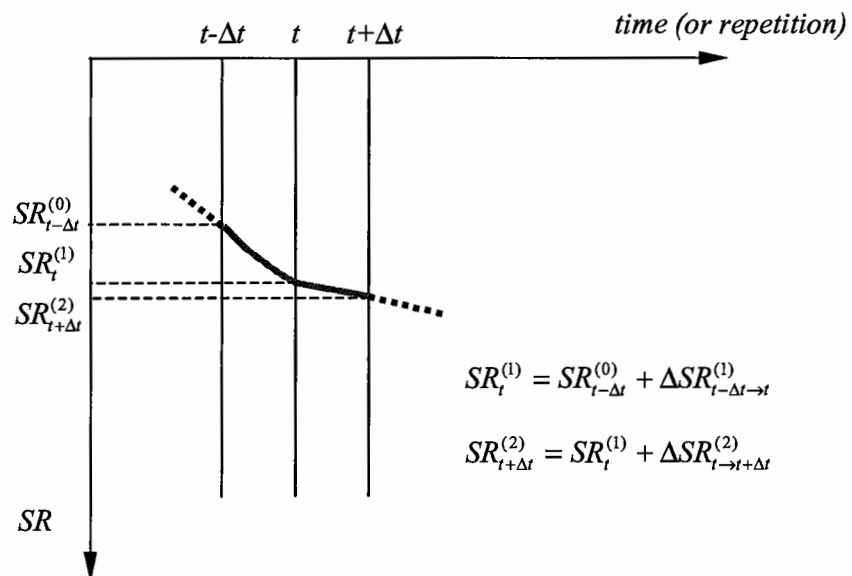


Figure 5.10. Construction of the compound stiffness deterioration curve with Weibull dynamic approach.

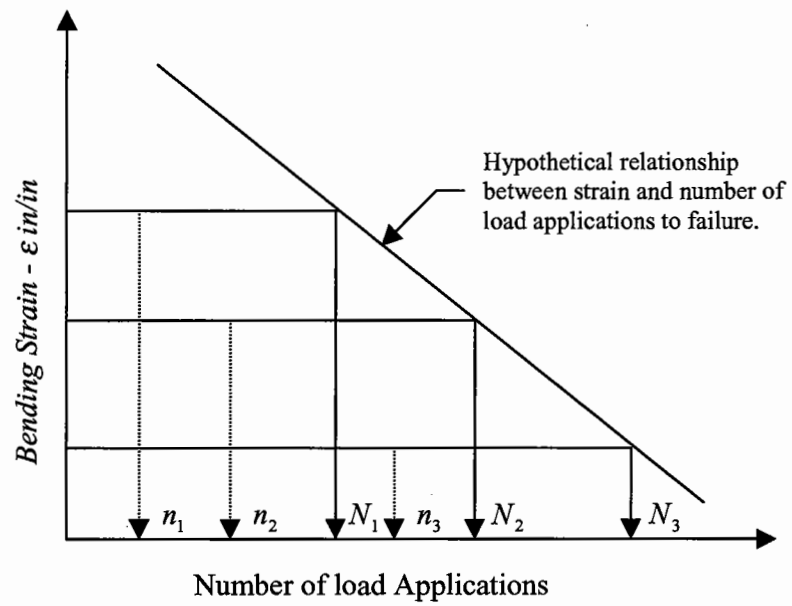


Figure 5.11. Prediction of fatigue life (adapted from Monismith, et al., 1961).

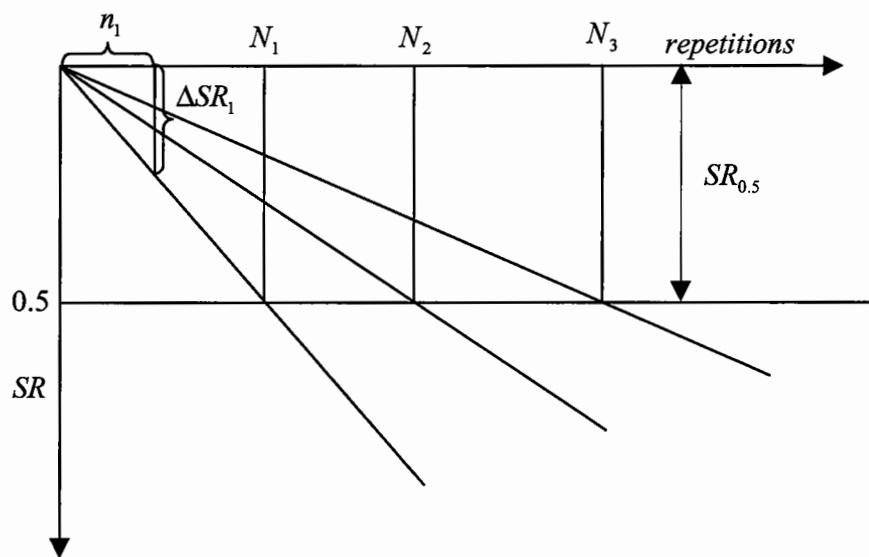


Figure 5.12. Miner's Law in explanation with stiffness ratio and fatigue life.

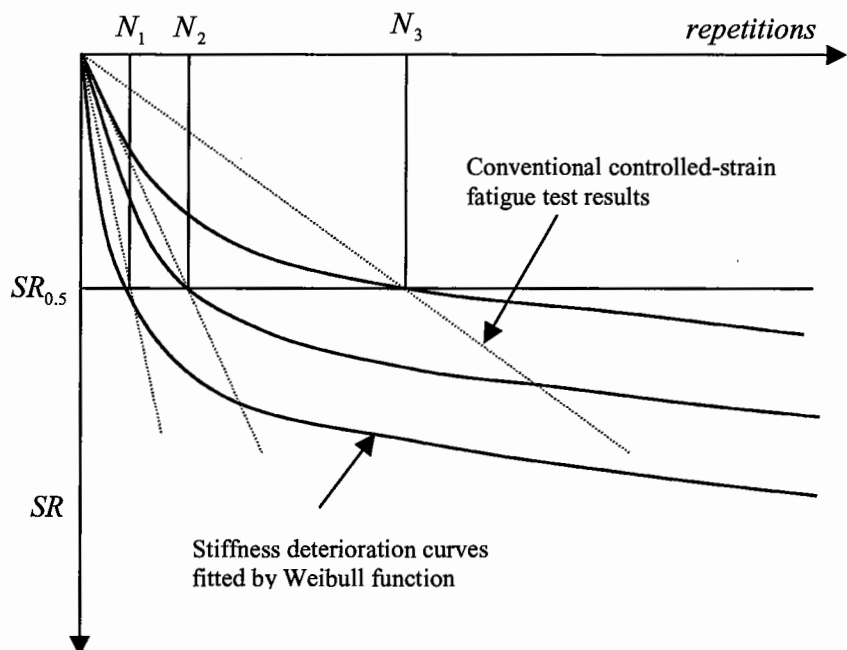


Figure 5.13. Comparison between Miner's Law and Weibull theory.

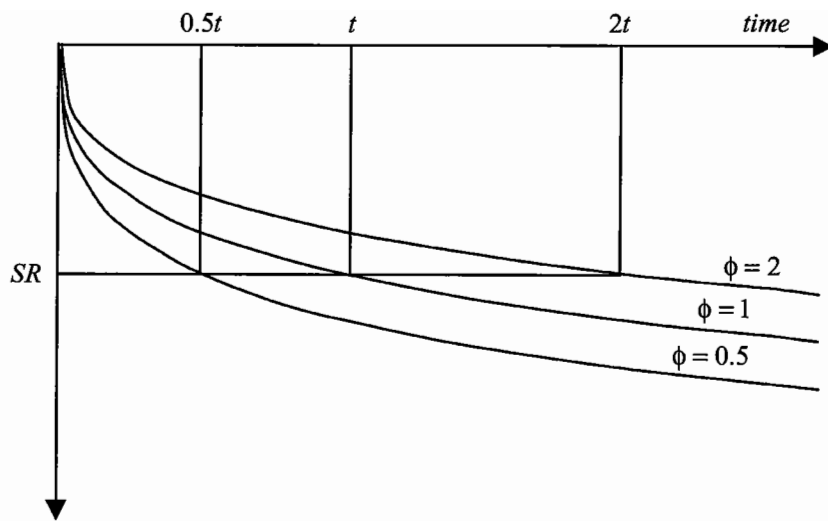
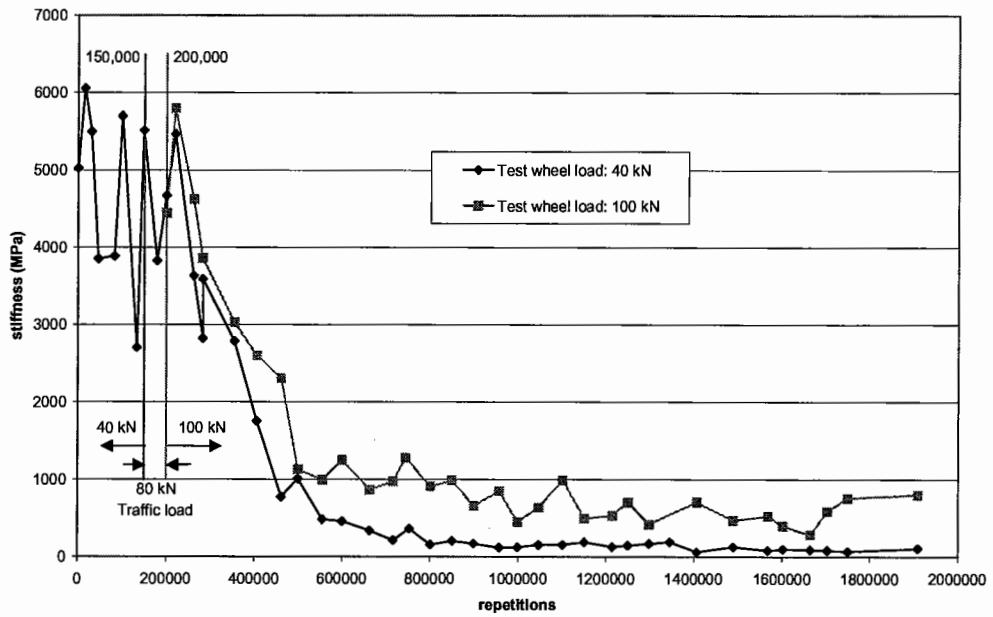
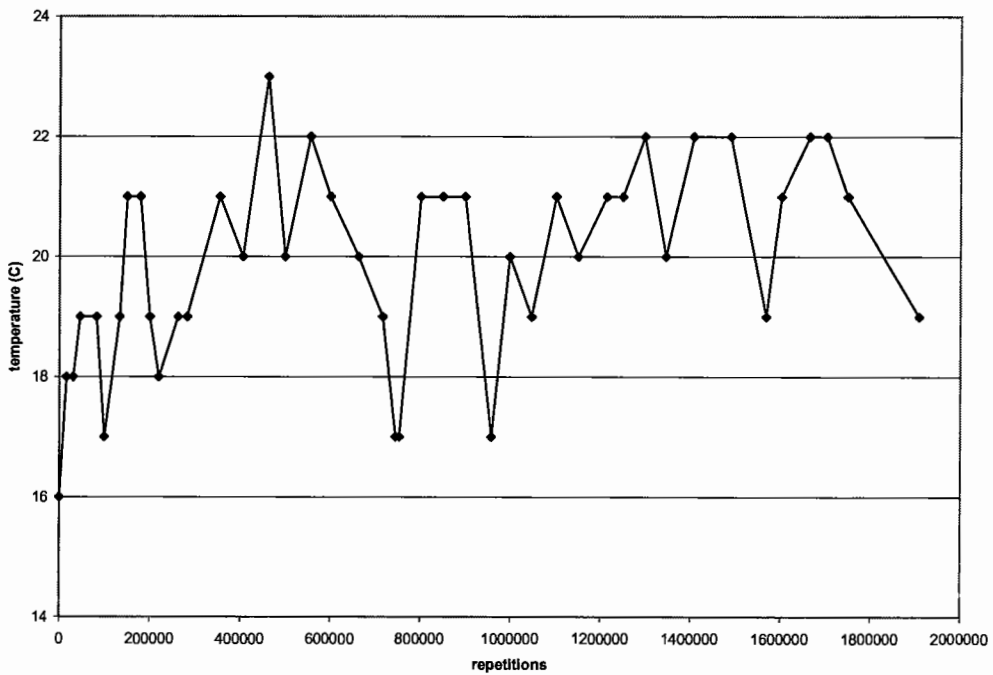


Figure 5.14. Weibull accelerated failure time model with different correction factors.

CAL/APT Goal 1 section 503RF: test wheel load, 40 kN, 100 kN @ MDD4



(a)



(b)

Figure 5.15. Back-calculated moduli of CAL/APT Goal 1 Section 503RF with test wheel loads of 40 kN and 100 kN subjected to a test temperature of $20 \pm 3^\circ\text{C}$.

HVS section: 503RF

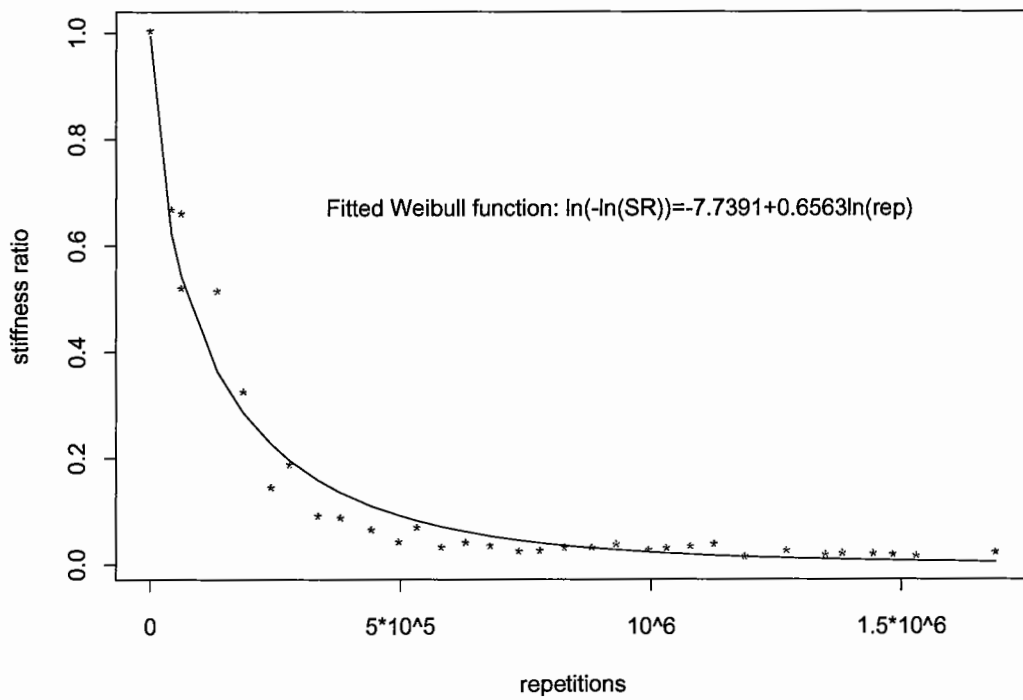


Figure 5.16. Fitted Weibull equation of back-calculated moduli of Section 503RF with a 40 kN test wheel load.

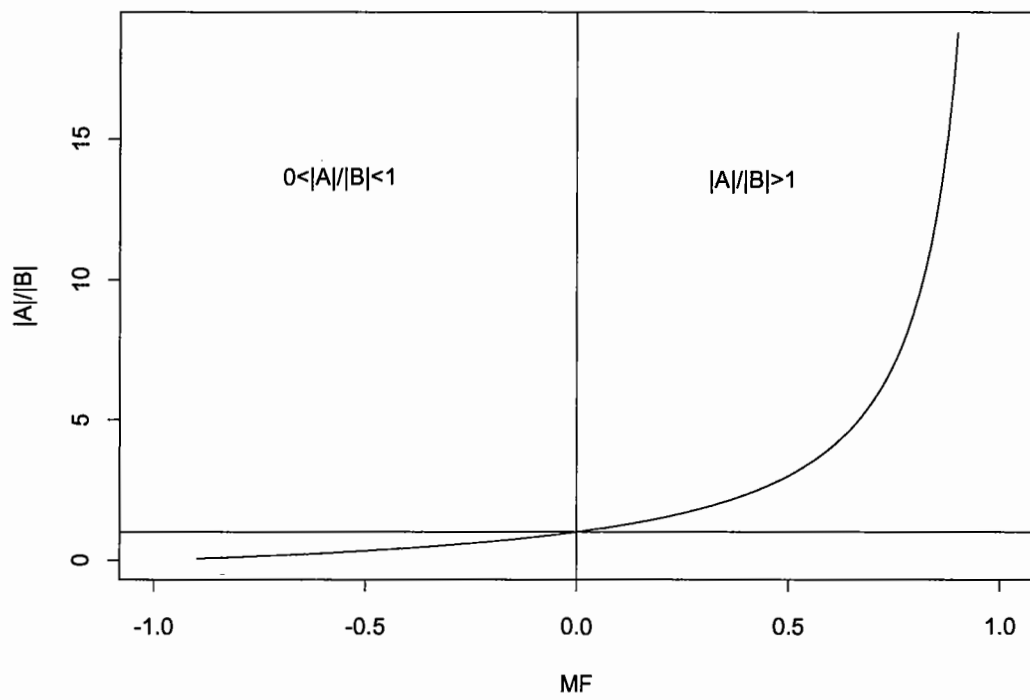


Figure 5.17. Relationship of $|A|/|B|$ ratio versus MF.

Section 503RF: history of maximum tensile strain

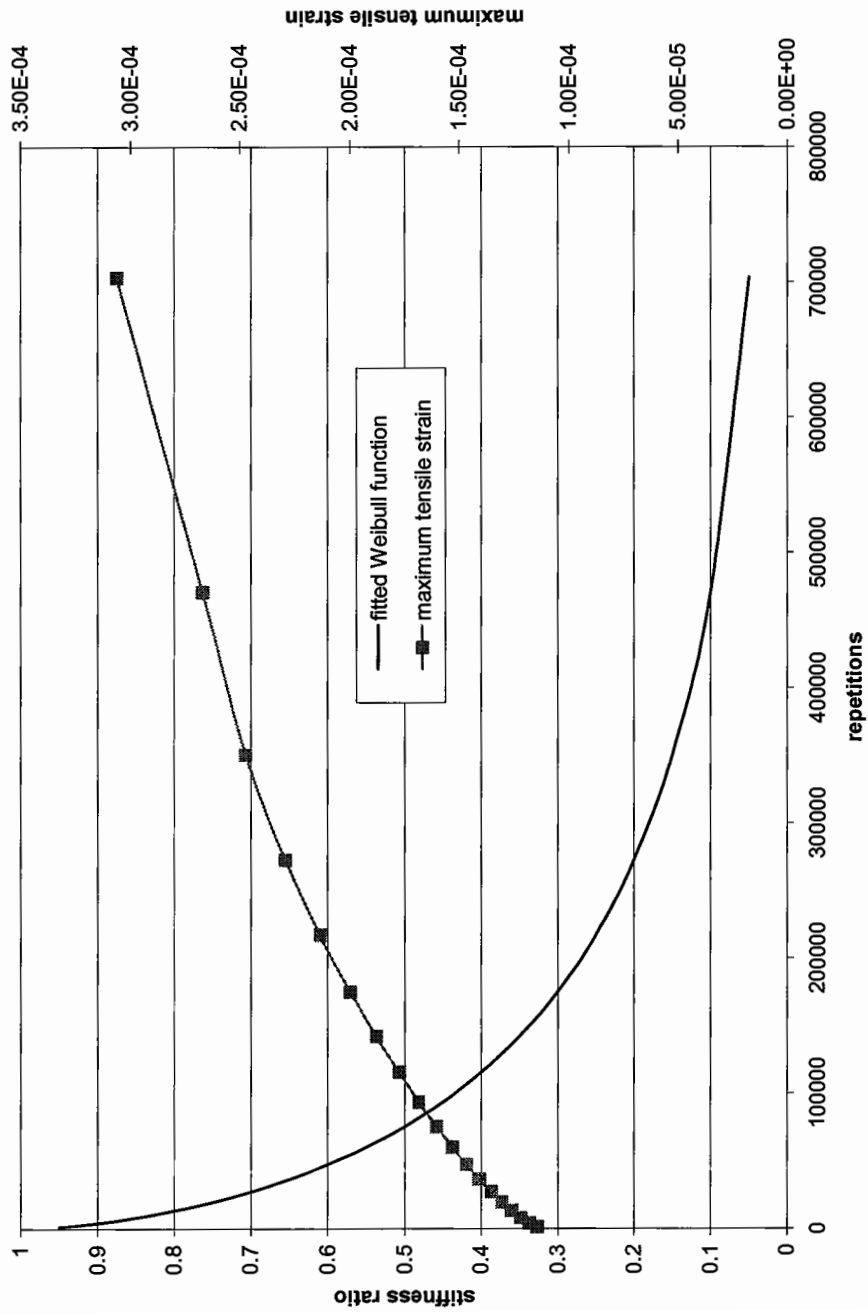


Figure 5.18. History of maximum tensile strain of Section 503RF.

HVS section: 503RF

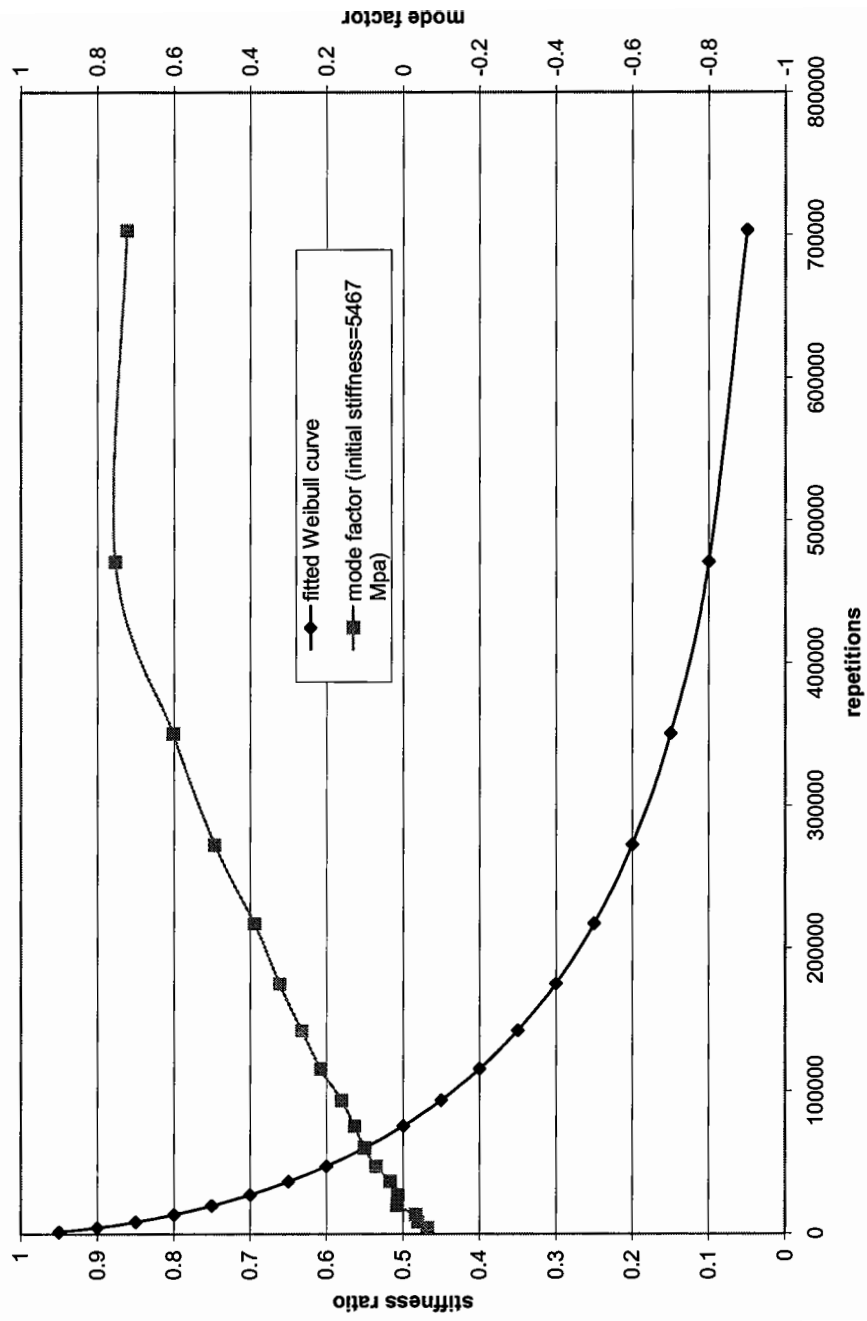


Figure 5.19. History of mode factor of Section 503RF.

6.0 WESTRACK SIMULATION USING MINER'S LAW

6.1 Introduction

The ultimate objective of laboratory tests of asphalt concrete is to economically predict and explain the performance of asphalt concrete in the field. This chapter explains the use of fatigue test results from a laboratory test program to construct a fatigue performance prediction approach using Miner's Law and compares the simulation results with the condition survey data defining fatigue performance in the WesTrack test pavements. The fatigue simulation methodology focuses on the occurrence of crack initiation at the bottom of the asphalt concrete layer, the location at which cracking was observed to start in the WesTrack pavements.

The laboratory fatigue test results to define fatigue failure are based on the 50 % stiffness reduction that is assumed to be approximately representative of crack initiation. To develop a crack propagation model, a deliberate and advanced test method or algorithm is needed to clearly define the crack propagation phenomenon occurring in the asphalt concrete and is beyond the scope of this investigation. A different approach, based on the Weibull model and including the study of high temperature fatigue, will be postulated in the next chapter.

The recording and analysis periods of WesTrack are summarized in Table 6.1. Temperature data were recorded from 3/3/96 to 10/2/98 on an hourly basis. Collection of traffic data started on 2/3/96, but to comply with the first available temperature data, the traffic data used in the simulation starts on 3/3/96. The last application of traffic loading concluded on 9/3/98. These data were also collected on an hourly basis.

Accordingly, the simulation covers the period 3/3/96 to 9/3/98. During the period from 2/3/96 to 3/3/96, traffic loading was negligible as compared with the total applied traffic and thus it is not used in the performance prediction. The temperature analysis period is extended one month past the traffic recording period to incorporate the total available temperature data.

Three basic assumptions are required to apply the procedure herein to the evaluation of pavement fatigue performance. First, it is assumed that the stresses and strains in the real pavement structure can be evaluated by layered-elastic theory. Second, the regression equations for fatigue life obtained from laboratory tests, including temperature as an independent variable, are considered to be valid when the extrapolated bottom temperatures of asphalt concrete are greater than 30°C, which is the upper limit for a conventional fatigue test. Third, when analyzing a dual-tire traffic load such as at WesTrack, the tensile strains calculated by the Circly program can be regarded as a bi-normal function, that is the addition of two overlapping normal density functions. More details of the bi-normal function will be discussed herein.

A general procedure to predict fatigue performance using Miner's Law is outlined below. Some terms will be explained in more detail later in this chapter. The simulation procedure can be summarized as follows:

1. Obtain laboratory mechanistic-empirical models for stiffness and fatigue life.
2. Categorize the observed WesTrack temperature data.
3. Run Circly program to evaluate the maximum principal tensile strain at the underside of the asphalt concrete layer.

4. Conduct regression analysis to represent the tensile strain as a function of the covariates: wander offset, air-void content (av), asphalt content (ac), and the temperature-related group (T_b, g, sg), where T_b is the temperature at the bottom of asphalt layer; g is the temperature gradient; and sg is the subgrade modulus.
5. Run fatigue performance prediction simulation (crack initiation).
 - a. Construct input matrix and find four parameters of strain function
 - b. Compute the tensile strains with offsets
 - c. Determine the fatigue life with offsets
 - d. Construct the repetition matrix
 - e. Evaluate the fatigue damage matrix and apply Miner's Law

Figure 6.1 outlines a flow chart for the simulation procedure. It should be remembered that this simulation methodology is only for the prediction of crack initiation time and not for the prediction of crack propagation time. In sum, the purpose of this simulation procedure is to eliminate the computational effort of layered-elastic programs, especially for calculations on an hourly basis, and replace the determinate solution of tensile strain with one found by a set of statistically analyzed equations. It should be noted that the simulation procedure was conducted using Splus. The simulation program and its corresponding functions written by Splus are listed in Appendix D.

6.2 WesTrack Data Summary

6.2.1 Temperature Distribution

Figure 6.2 is a time series plot of the WesTrack representative temperatures, at a depth of 50 mm in the asphalt concrete layer, from 3/3/96 to 10/2/98, and exhibits the obvious seasonal and daily variations. The daily bandwidths vary as much as 30°C. The histogram in Figure 6.3 plots the temperature density function, also at a depth of 50 mm. It should be noted that since the histogram is scaled as a probability density; the sum of the bar height and bar width equals one. Shown in this figure are two modes located at temperatures 5°C and 30°C. The resulting shape of the density function looks like two overlapping normal distributions.

Figure 6.4 illustrates the temperature distribution function at a depth of 50 mm in the asphalt concrete layer of WesTrack from 3/3/96 to 10/2/98. Note that this figure shows that the probability of the temperature being greater than 30°C is about 0.25.

The time series plot in Figure 6.5 shows a narrower bandwidth of daily temperature variation at a depth of 150 mm than measured at 50 mm. In the histogram shown in Figure 6.6, the temperature density function at a depth of 150 mm, the two modes are even more pronounced and the temperature spread is narrower than the variance of the density function at a depth of 50 mm, shown in Figure 6.3. In Figure 6.7, the portion of temperatures at this depth greater than 30°C and less than 40°C is about 20% of the total recorded time. Therefore, the temperature range of 30°C to 40°C was selected as the key range to study the effect of high temperatures on fatigue in this project.

Figure 6.8 is a time series plot of temperature gradient. Figure 6.9 and Figure 6.10 present the density function and distribution function of temperature gradient of

WesTrack from 3/3/96 to 10/2/98. Recall that the temperature gradient is defined as $(T_{50} - T_{150})/100$, where T_{50} is the temperature at 50 mm and T_{150} is that at 150 mm. Hence, the negative gradient means the temperature at the top of asphalt concrete layer is less than the temperature at the bottom of the asphalt concrete layer. In Figure 6.10, most of the negative gradients range from -0.05 to 0 whereas the positive gradients spread from 0 to 0.15 . Those temperature gradients ranging from -0.05 to 0 represent about 60 % of the total recorded time. Thus the temperature differences of top and bottom range from 0°C to -5°C for 60 % of time.

6.2.2 Traffic Pattern

A time series plot of cumulative ESALs for various wander locations is shown in Figure 6.11. Because the WesTrack traffic pattern was planned, it does not have a randomly distributed wander pattern as in Figure 6.12 which is an example of typical wheel distribution pattern (Allen 1979). For this reason four periods were identified to reflect the specific different traffic patterns of WesTrack. The bar charts of Figure 6.13 list these four periods in a time sequence, (a) 3/3/96 to 7/15/96, a period of no wander or human driver, (b) 7/16/96 to 12/14/96, a period of being trafficked at 5R and 5L wander locations only, (c) 12/15/96 to 2/18/97, a period of being trafficked only 135,249 ESALs (about 2.7 % of total applied ESALs), and (d) 2/19/97 to 9/3/98, a period of varied wander pattern.

Figure 6.14 illustrates a bar chart of the wander distributions throughout the whole simulation period. It is apparent that this bar chart does not match the wander distribution shown in Figure 6.12 which means that traffic wander at WesTrack did not

match that of typical field highway pavements. The wander locations at 5R and 5L represent 32 percent of the total applied ESALs.

Figure 6.15 overlaps the temperature spectrum at depth 150 mm and the total cumulative ESALs. The horizontal part of the cumulative ESAL curve represents a period of no applied traffic; the slope of the curve reflects the cumulative rate of applied ESALs—a sharp slope results from intensive applied trafficking load.

6.3 Mechanistic-Empirical Models for Stiffness and Fatigue Life

Recall that the main purpose of this chapter is to present an alternative method for estimating the cumulative fatigue damage of wander and no-wander traffic loading using Miner's Law. However, Miner's approach has some inherent drawbacks that cannot be mended by any improvements of the statistical regression models. Therefore, instead of using the regression models of initial stiffness and fatigue life obtained in Chapter 4, the mechanistic-empirical models of stiffness and fatigue life originally developed during the WesTrack project were utilized in the simulation. These models were obtained based on the results of two groups of tests, namely, WesTrack temperature sensitivity fatigue tests and WesTrack fatigue tests at 20°C.

The WesTrack temperature sensitivity fatigue tests were conducted at three temperatures, 5°C, 20°C, and 30°C, and subjected to various strain levels, 200, 400, and 800 microstrain. Table A.4.2 summarizes the test results. The WesTrack fatigue tests at 20°C were conducted at 200 and 400 microstrain levels for each section and the results and associated testing conditions are tabulated in Table A.4.1. A summary of the sample sizes tested in these two groups with three gradations is listed in Table 6.2.

Space does not permit the presentation of the regression analyses that resulted in the following stiffness and fatigue life models. Hence, whether linear or nonlinear, all the regression analyses, including model selection, residual plots, or parameter estimations, are not illustrated here.

6.3.1 Stiffness Models

The initial stiffness of asphalt concrete is defined as the ratio of maximum stress and maximum tensile strain at the 50th repetition of the fatigue test. It was found that no significant difference in stiffness models exists between the fine and fine-plus gradations. Hence, the fine and fine-plus data were pooled together to increase the sample size to 121. The sample size for coarse gradation was 65. The regression results are listed below.

Stiffness models:

Fine and Fine-Plus

$$\ln Stif = 11.4677 - \underset{(0.1854)}{0.0827} av - \underset{(0.0051)}{0.2285} ac - \underset{(0.0028)}{0.0579} temp \quad R^2 = 0.85 \quad (6.1)$$

Coarse

$$\ln Stif = 11.4707 - \underset{(0.5362)}{0.0576} av - \underset{(0.0086)}{0.2142} ac - \underset{(0.0049)}{0.0606} temp \quad R^2 = 0.79 \quad (6.2)$$

where $Stif$ = stiffness (MPa),

av = percent air-void content,

ac = percent asphalt content,

$temp$ = temperature at 150 mm ($^{\circ}$ C),

\ln = natural logarithm.

The value inside the parentheses is the standard error of the estimated coefficient. Also, notice that the signs of the regression coefficients of covariates av , ac , and $temp$ are all negative; this means that increases in these covariates will decrease the magnitude of stiffness.

6.3.2 Fatigue Life Models

The fatigue life models utilized the pooled data from the WesTrack temperature sensitivity tests and WesTrack fatigue tests at 20° C. Sample size for the fine gradation was 59, fine-plus was 62, and coarse was 65. Following are the results of linear regression for each gradation.

Fatigue life models:

Fine

$$\ln N_f = -27.0265 - 0.1439 av + 0.4148 ac - 4.6894 \ln stn \quad R^2 = 0.88 \quad (6.3)$$

(1.5343) (0.0230) (0.1245) (0.1632)

Fine-plus

$$\ln N_f = -27.3409 - 0.1431 av + 0.4219 ac + 0.0127 temp - 4.6918 \ln stn \quad (6.4)$$

(1.5658) (0.0231) (0.1247) (0.0126) (0.1632)

$$R^2 = 0.88$$

Coarse

$$\ln Nf = -27.6723 - 0.0941av + 0.6540ac + 0.0331temp - 4.5402 \ln stn \quad (6.5)$$

(2.3308) (0.0299) (0.2853) (0.0174) (0.1878)

$$R^2 = 0.92$$

where Nf = fatigue life,

av = percent air-void content,

ac = percent asphalt content,

$temp$ = temperature at 150 mm ($^{\circ}$ C),

stn = maximum tensile strain, and

\ln = natural logarithm.

Inspecting the signs of regression coefficients of above fatigue life equations, several conclusions can be drawn as follows:

1. The $temp$ term is not included in the fatigue life equation of the fine gradation; that is, fine gradation is not temperature sensitive with respect to fatigue life.
2. The effects of covariates av , ac , $temp$, and stn to fatigue life are the same for all three gradations. Hence, the fatigue life will increase as ac and $temp$ increase; on the contrary, the fatigue life will decrease as av and stn increase.
3. The absolute magnitude of the regression coefficient for av for the coarse gradation is about 35 % less than that for the fine and fine-plus gradation

4. The negative sign of the regression coefficient of strain level shows that the smaller the strain, the greater the fatigue life.

Please note that the effective temperature range to apply the fatigue life equations is from 5 °C to 30 °C . For temperatures outside of this range, extrapolation is needed.

6.4 Stratification of the WesTrack Temperature Data

As mentioned previously, the simulation period started on 3/3/96 and ended on 9/3/98. This period contains a total of 21,943 hours. The environmental and traffic variables, including T_b , g , sg , wander, and trafficking repetitions, are varied hour by hour; that is to say, the stress and strain status at the asphalt concrete layer are varied with time. It can thus be inferred that the fatigue damage is time dependent.

Generally, to assess fatigue damage, one needs to know the maximum tensile strain occurring at the bottom of asphalt concrete layer as well as the trafficking load configuration so as to calculate how much fatigue life will remain after traffick loading at a specified tensile strain level. However, to calculate the maximum tensile strain, most programs, either linear or nonlinear, require input of the layer moduli and loading configuration. The layer moduli are a function of material variables and environmental variables—temperature being the significant one for asphalt bound layers. Since the (T_b, g, sg) embeds the inherent property of seasonal variation, it should be regarded as an integrated unit when conducting any further analysis. Also, note that this (T_b, g, sg) group, in our case, will serve as the layer moduli variable. In sum, the objective is to stratify the observed WesTrack data into (T_b, g, sg) groups to utilize a statistical

approach and reduce computational time to an acceptable level. It would be extremely burdensome to run the Circly program 21,943 times, for each simulation hour.

The idea is to subdivide T_b , g , and sg into some manageable subintervals so as to reduce the 21,943 cases. T_b ($^{\circ}\text{C}$), the temperature at the bottom of the asphalt concrete layer, will be subdivided into the following separated points, -10, 0, 10, 20, 30, 40, and 50. G ($^{\circ}\text{C}/\text{mm}$), the temperature gradient defined as $g = \frac{T_{50} - T_{150}}{100}$, starts at -0.15 and ends at 0.15 with an increase interval of 0.05, i.e., -0.15, -0.1, -0.05, 0, 0.05, 0.1, and 0.15. Sg (MPa), the subgrade modulus, based on Deacon's equation (Deacon 1998),

$$E_{sg} = \exp(9.597089 + 0.118063 \cdot \sin((day - 250.3937) / 365 \cdot 2\pi)), \quad (6.6)$$

will be subdivided into subintervals starting at 90 MPa and ending at 120 MPa with an increase of 5 MPa.

It should be noted that the ranges of these three variables are defined according to the field data. Based on these subintervals of (T_b, g, sg) , a total of 216 ($6 \times 6 \times 6$) combination cases will be formed. In a sense of three-dimensional space, these subintervals will form 216 cubic cells; the 21,943 (T_b, g, sg) cases will fall into cubic cells according to their magnitudes. An Splus code was written to categorize the field data into suitable cubic cells and the stratification result is listed in Appendix D. The mean values of each cell were estimated and will be utilized in the following Circly run

and regression analysis. It should be noted that not every cell contains observed field data and it turns out that only 110 (T_b, g, sg) cubic cells are found in the observed field data.

6.5 Tensile Strain Function Using Circly Program

6.5.1 WesTrack Pavement Structure and Loading Configuration

As illustrated in Figure 1.2, the pavement structure consists of a 0.15 m asphalt concrete layer, following by 0.305 m base, and the assumed infinite thickness of subgrade. The corresponding Poisson ratios are 0.35 for the asphalt concrete layer, 0.40 for the base, and 0.45 for the subgrade. The asphalt concrete layer was divided into three sublayers; the thickness of each sublayer is 0.05 m, so as to reflect the change in stiffness due to the temperature gradient. In this simulation, the moduli of the asphalt concrete and the subgrade are varied with the daily and seasonal temperature variation respectively, but the modulus of base remains the same with a value of 172.4 MPa. The moduli of asphalt concrete are based on equations 6.1 and 6.2; the moduli of the subgrade follow equation 6.6.

6.5.2 Circly Program with 110x3x3 Cases

The possible combination cases of (T_b, g, sg) that were occupied by observed WesTrack data are 110. The values of the air-void content were decided by choosing the low, mean, and high values from the result of a UCB air-void method (Del Valle 1985) applied to the WesTrack field sample. Thus, the three air-void contents chosen for this simulation were two extremes 1.9 % and 13.7 %, and the mean value of 8.0 %. Three

asphalt contents that are identified in Hand's dissertation (Hand 1998) were selected—the two extremes 4.3 % and 6.2 % and the mean of 5.5 %. Hence a total of 110x3x3 cases were conducted using Circly program. For each single case, the principal tensile strains at 51 locations at the bottom of asphalt concrete layer were calculated. It should be noted that there are 990 cases for the coarse mix and another 990 cases for the fine and fine-plus mixes. As compared with the 21,943 Circly runs, the 990 runs substantially reduce the computation effort, not to mention the extra input and output time required while running the Circly program.

6.5.3 Bi-Normal Density Function

After inspecting the results of Circly output, it appears reasonable to represent the tensile strain profile as two overlapping normal density functions. This is hereafter referred as the bi-normal density function and has the following form:

$$\varepsilon(m_1, m_2, \sigma, A, x) = \frac{A}{\sigma\sqrt{2\pi}} \left[\exp\left(-\frac{(x-m_1)^2}{2\sigma^2}\right) + \exp\left(-\frac{(x-m_2)^2}{2\sigma^2}\right) \right] \quad (6.7)$$

where ε is the desired tensile strain,

x is the offset,

m_1 is the mean position of the left-handed normal density function,

m_2 is the mean position of the right-handed normal density function,

σ is the standard deviation for both normal density functions, and

A is the multiplication factor.

The four parameters in the equation above are to be determined by nonlinear regression fit and will be represented as a function of (T_b, g, sg) , av , and ac .

Figure 6.16 plots the nonlinear regression fit and the Circly output results in hot weather conditions. The fitted regression curve is superposed by two normal density functions—one with mean position $m_1 = 0.0010$, the other with mean position $m_2 = 0.3551$, and the common $\sigma = 0.1361$ —with a multiplication factor $A = 0.0001435$. The corresponding simulation case is subjected to $T_b = 41.10^\circ\text{C}$, $g = 0.1091^\circ\text{C}/\text{mm}$, $sg = 95.79\text{ MPa}$, $AV = 14.7\%$, and $AC = 6.2\%$ (coarse gradation).

Figure 6.17 is a typical output of tensile strain in cold weather. The fitted nonlinear regression curve is made by two normal density functions—one with mean position $m_1 = -0.0188$, the other with mean position $m_2 = 0.3751$, and the common $\sigma = 0.1806$ —with a multiplication factor $A = 0.0000286$. The corresponding simulation case is subjected to $T_b = -2.24^\circ\text{C}$, $g = -0.0518^\circ\text{C}/\text{mm}$, $sg = 113.30\text{ MPa}$, $AV = 14.7\%$, and $AC = 6.2\%$ (coarse gradation).

From Figures 6.16 and 6.17, several findings can be summarized:

1. The nonlinear regression fit utilizing bi-normal density functions appears to be satisfactory. Although the tail of the bi-normal density function is deviated from the calculated result, it does not affect the wander application, since fitting to the peaks is more important.
2. It is adequate to represent the tensile strain profile obtained by the Circly program with m_1 , m_2 , σ , and A four parameters.

3. The tensile strain profile is symmetrical to the position of $(m_1 + m_2)/2$.
4. It is weather conditions that cause the difference in pavement performance. In hot weather the tensile profile exhibits two peaks, in cold weather one. The magnitude of tensile strain is small in cold weather as compared to that in hot weather. In other words, fatigue damage will accumulate less in cold weather.

With the recognition that a tensile strain profile can be represented with these four parameters, the next step is to run the nonlinear regression fits based on bi-normal density functions for each single case.

6.5.4 Regression Analysis for Strain Function

Recall that the tensile strain profile can be represented by four parameters m_1 , m_2 , σ , and A ; refer to equation 6.7. After running the Circlly program for 990×2 cases (including coarse, and fine and fine-plus gradations), the maximum principal tensile strains were extracted from the output and were piped in as the input of the nonlinear linear regression. A command named `nls()` of Splus, which is a command that conducts the nonlinear regression fit, was utilized to determine the four parameters $\{m_1, m_2, \sigma, A\}$.

It is necessary to provide the layer moduli while running the Circlly program to obtain the tensile strain profile at the bottom of the asphalt concrete layer. To calculate the layer moduli of the asphalt concrete layer, Equations 6.1 and 6.2 were utilized. Notice that these two equations contain the covariates of air-void content, asphalt content, and temperature. With 110 (T_b, g, sg) cases, three air-void levels, and three asphalt

contents, each combination provides a set of $\{m_1, m_2, \sigma, A\}$ to represent the tensile strain profile at that specified $\{(T_b, g, sg), av, ac\}$ combination. Therefore, for a specific gradation type, a total of 990 sets of $\{m_1, m_2, \sigma, A\}$ were assessed through nonlinear regression analysis. However, these four parameters function as intermediate parameters because they are not of as much interest for interpreting the results as are $\{(T_b, g, sg), av, ac\}$, the five material and environment covariates. Hence, a further regression analysis was conducted to substitute $\{m_1, m_2, \sigma, A\}$ with $\{(T_b, g, sg), av, ac\}$. In other words, the strain function can be transformed into the following equation:

$$\varepsilon(\underline{X}, x) = \frac{A(\underline{X})}{\sigma(\underline{X})\sqrt{2\pi}} \left[\exp\left(-\frac{(x - m_1(\underline{X}))^2}{2\sigma(\underline{X})^2}\right) + \exp\left(-\frac{(x - m_2(\underline{X}))^2}{2\sigma(\underline{X})^2}\right) \right],$$

where the \underline{X} vector stands for the $\{(T_b, g, sg), av, ac\}$ vector.

It was found that the results of regression analyses are improved if the temperature gradients are treated separately in subintervals; namely, in each temperature gradient subinterval, the $\{m_1, m_2, \sigma, A\}$ parameters have their own regression equations.

The general specifications of regression equations for the four parameters $\{m_1, m_2, \sigma, A\}$ are listed below:

$$m_1 = C_0 + C_1 T_b g + C_2 T_b sg + C_3 T_b g^2 + C_4 T_b sg^2 + C_5 G + C_6 Sg + C_7 av + C_8 ac + C_9 T_b g \cdot av + C_{10} T_b sg \cdot av + C_{11} T_b g \cdot ac + C_{12} T_b sg \cdot ac + C_{13} av \cdot ac + \varepsilon,$$

$$m_2 = C_0 + C_1 m_1 + \varepsilon,$$

$$\sigma = C_0 + C_1 m_1 + C_2 m_1^2 + C_3 m_1^3 + C_4 m_1^4 + C_5 m_1^5 + \varepsilon, \text{ and}$$

$$A = C_0 + C_1 T_b g + C_2 T_b s g + C_3 T_b g^2 + C_4 T_b s g^2 + C_5 G + C_6 S g + C_7 a v + C_8 a c \\ + C_9 T_b g \cdot a v + C_{10} T_b s g \cdot a v + C_{11} T_b g \cdot a c + C_{12} T_b s g \cdot a c + C_{13} a v \cdot a c + \varepsilon$$

where C_i is the regression coefficients,

$T_b g$ is a term generated by multiplying T_b and g ,

$T_b s g$ is a term generated by multiplying T_b and $s g$,

$T_b g^2$ is the square of $T_b g$,

$T_b s g^2$ is the square of $T_b s g$,

$T_b g \cdot a v$ is the interaction term of $T_b g$ and $a v$,

$T_b g \cdot a c$ is the interaction term of $T_b g$ and $a c$,

$T_b s g \cdot a v$ is the interaction term of $T_b s g$ and $a v$,

$T_b s g \cdot a c$ is the interaction term of $T_b s g$ and $a c$, and

ε is the error term.

The sample size of each temperature gradient subinterval is listed in the following: 36 for [-0.15, -0.10], 189 for [-0.10, -0.05], 207 for [-0.05, 0.0], 207 for [0.0, 0.05], 207 for [0.05, 0.10], and 144 for [0.10, 0.15].

The details of the regression analysis are not presented here. Tables 6.3a through 6.3d and 6.4a through 6.4d tabulate the regression results for both coarse mix and fine and fine-plus mixes respectively.

6.6 Fatigue Performance Prediction Simulation (Crack Initiation)

6.6.1 Simulation Procedures

For simplicity, Section 8 at WesTrack will serve as a demonstration to explain how the fatigue performance prediction simulation is completed and evaluated. The simulation procedure is manipulated using the Splus software. The simulation tasks included the following:

- Construct input matrix and find four parameters of strain function,
- Compute the tensile strains with offsets,
- Determine the fatigue life with offsets,
- Construct the repetition matrix, and
- Evaluate the fatigue damage matrix and apply Miner's Law.

6.6.1.1 Input Matrix and Four Parameters Strain Function

A basic input matrix, named $tbgs_g_8$ (the subscript 8 representing test section 8), including five columns for T_b , g , sg , av , and ac was constructed on an hourly basis.

That is,

$$tbgs_g_8 = \begin{bmatrix} T_b & g & sg & av & ac \\ \vdots & \vdots & \vdots & \vdots & \vdots \\ \vdots & \vdots & \vdots & \vdots & \vdots \end{bmatrix}_{21943 \times 5} .$$

The number of 21,943 as stated earlier is the total recorded hours of WesTrack from 3/3/96 to 9/3/98. Next, according to the regression coefficients of Tables 6.3a to 6.3d for coarse mix and Tables 6.4a to 6.4d for fine and fine-plus mixes, a matrix, named $tbgs_g.coef_8$, with four parameters m_1 , m_2 , σ , and A , of the strain function can thus be calculated

$$tbgs_g.coef_8 = \begin{bmatrix} m_1 & m_2 & \sigma & A \\ \vdots & \vdots & \vdots & \vdots \\ \vdots & \vdots & \vdots & \vdots \end{bmatrix}_{21943 \times 4} .$$

In sum, for each single hour, there exists a unique set of $\{m_1, m_2, \sigma, A\}$ that forms a specific strain function for that specified set of T_b , g , sg , av , and ac .

6.6.1.2 Tensile Strains with Offsets

Because the four parameters m_1 , m_2 , σ , and A can define a continuous function of maximum tensile strain, it is possible to identify the magnitude of tensile strain caused by wander. While the applied traffic loading is in a no-wander position, the location that incurs most fatigue damage is set at the point of maximum tensile strain. The Newton-Raphson algorithm was utilized to resolve the position of maximum tensile strain. An Splus program called `findsolnr()` (Appendix D) was utilized for this step. Figure 6.18

illustrates the method used to estimate the strain with wander. As can be seen, the maximum tensile strain occurs at position x_m for the no-wander condition. If there is a wander loading at a distance L on the right side of the no-wander position, then the tensile strain occurring at x_m is $\epsilon(x_m - L)$; conversely, if the wander loading is at a distance L on the left side, then the tensile strain occurring at x_m is going to be $\epsilon(x_m + L)$. Therefore, for each hour, the tensile strains at different wander locations can thus be calculated and represented in matrix form as follows:

$$stn_g = \begin{bmatrix} 5L & 4L & 3L & 2L & 1L & Center & 1R & 2R & 3R & 4R & 5R \\ \vdots & \vdots & \vdots & \vdots & \vdots & \vdots & \vdots & \vdots & \vdots & \vdots & \vdots \\ \vdots & \vdots & \vdots & \vdots & \vdots & \vdots & \vdots & \vdots & \vdots & \vdots & \vdots \end{bmatrix}_{21943 \times 11} .$$

The calculations of tensile strains at various wander locations are based on the location of the maximum tensile strain, x_m , obtained from the no-wander situation. It should be noted that the location of maximum tensile strain varies with temperature and therefore changes each hour.

6.6.1.3 Fatigue Life with Offsets

Once the strains have been calculated for each wander position and each hour, the fatigue-resistant capacity at each entry of matrix stn_g can be computed based on the laboratory-obtained fatigue life equations. For instance, the fatigue life matrix of the coarse mix has the following form:

$$Nf_8 = \exp \left(-27.6723 - 0.0941 \cdot \begin{bmatrix} av \\ \vdots \\ \vdots \end{bmatrix} + 0.654 \cdot \begin{bmatrix} ac \\ \vdots \\ \vdots \end{bmatrix} + 0.0331 \cdot \begin{bmatrix} T_b \\ \vdots \\ \vdots \end{bmatrix} - 4.5402 \cdot \log[stn_8] \right).$$

The dimensions of matrices $[av]$, $[ac]$, $[T_b]$, stn_8 , and Nf_8 are all 21943×11 . Note that $[av]$ and $[ac]$ are constant matrices because av and ac were maintained the same during this simulation. The $[T_b]$ matrix is a temperature matrix, which is prepared by a column vector of 21,943 temperatures and then duplicated 11 times. The fatigue life equations utilized in this simulation are varied by gradation types: equation 6.3 for fine gradation, equation 6.4 for fine-plus gradation, and equation 6.5 for coarse gradation.

6.6.1.4 Repetition Matrix

In the Circlly layered-elastic theory simulations the actual loads and their repetitions were used rather than the 40 kN (9,000 lb) wheel load associated with the ESALs. Also, as mentioned in Chapter 2, a multiplication factor of 0.7633 needs to be applied to convert the ESALs (original traffic data format) into repetitions for the specific loading configuration of WesTrack. For the traffic and wander data, a matrix named $REPS_8$, with the same dimension as the stn_8 matrix, can be constructed as follows:

$$REPS_8 = \begin{bmatrix} R_{5L} & R_{4L} & R_{3L} & R_{2L} & R_{1L} & R_{Center} & R_{1R} & R_{2R} & R_{3R} & R_{4R} & R_{5R} \\ \vdots & \vdots & \vdots & \vdots & \vdots & \vdots & \vdots & \vdots & \vdots & \vdots & \vdots \\ \vdots & \vdots & \vdots & \vdots & \vdots & \vdots & \vdots & \vdots & \vdots & \vdots & \vdots \end{bmatrix}_{21943 \times 11}.$$

It should be noted that the repetitions applied to the "OFF" position in the original data set, meaning that the truck was maneuvered by a driver, were evenly distributed to the other 11 positions.

6.6.1.5 Fatigue Damage Matrix and Miner's Law

Accordingly, the failure criterion is set as $\sum \frac{n_i}{N_i} = 1$, where n_i represents the applied repetitions at entries of the matrix $REPS_8$; N_i is the fatigue-resistant capacity as expressed in the entries of matrix Nf_8 . If the cumulative ratio reaches one, then it is said that the crack initiation is triggered at the bottom of the asphalt concrete layer. The fatigue damage matrix is thus defined as

$$\frac{REPS_8}{Nf_8} = \begin{bmatrix} \frac{R_{5L}}{Nf_{5L}} & \frac{R_{4L}}{Nf_{4L}} & \frac{R_{3L}}{Nf_{3L}} & \frac{R_{2L}}{Nf_{2L}} & \frac{R_{1L}}{Nf_{1L}} & \frac{R_{Center}}{Nf_{Center}} & \frac{R_{1R}}{Nf_{1R}} & \frac{R_{2R}}{Nf_{2R}} & \frac{R_{3R}}{Nf_{3R}} & \frac{R_{4R}}{Nf_{4R}} & \frac{R_{5R}}{Nf_{5R}} \\ \vdots & \vdots & \vdots & \vdots & \vdots & \vdots & \vdots & \vdots & \vdots & \vdots & \vdots \\ \vdots & \vdots & \vdots & \vdots & \vdots & \vdots & \vdots & \vdots & \vdots & \vdots & \vdots \end{bmatrix} \quad \text{J21943x11}$$

The summation of ratios in each row in the above matrix indicates the cumulative fatigue damage caused by the trafficking load at that hour. Accordingly, a plot of hourly cumulative fatigue damage versus hourly cumulative repetitions can be drawn, as shown in Figure 6.19. The plot represents the "with wander" cumulative fatigue damage curve. To construct the "without wander" damage curve, we assume that the total hourly repetitions are applied only at the central position (the black arrow position in Figure 6.18). In the laboratory, the controlled-strain flexural fatigue tests are conducted with a

constant strain level. Since, it is recognized that compounding strain history is found in a specific location in the asphalt concrete layer, it is necessary to further evaluate the wander effect if the laboratory fatigue tests are to be applied in the field.

The following is a sample Splus log to exemplify the methodology used to predict crack initiation.

```
> # section 8:coarse,AV=8.5,AC=5.47
> tbgsg.coef<-stnregfunc(tbgsg[,1],tbgsg[,2],tbgsg[,3],8.5,5.47)
> range(tbgsg.coef[,3])
[1] 0.1356376 0.1938631
> tbgsg.coef8<-tbgsg.coef
> rm(tbgsg.coef)
> dim(tbgsg.coef8)
[1] 22627 4
> stn8<-findmatstns(tbgsg.coef8)
> dim(stn8)
[1] 22627 11
> nf8<-exp(-27.6723-0.0941*8.5+0.654*5.47+0.0331*tbgsg[1:21943,1]-
4.5402*log(stn8[1:21943,]))
> dim(nf8)
[1] 21943 11
> ratio8center<-esalcenter/nf8[,6]
> ratio8<-ratiomat(nf8,esal)
> plot(cumsum(esalcenter),cumsum(ratio8center),xlab="cumulative ESALs",ylab="cumulative
ratio of ni/Ni",main="Section 8:coarse,AV=8.5,AC=5.47. 3/3/96~9/3/98")
> points(cumsum(esalcenter),ratio8,col=2)
> abline(h=1)
> text(locator(1),"with no wander")
> text(locator(1),"with WestTrack Wander Pattern",col=2)
> dev.copy(win.printer,file="clipboard",format="metafile")
> dev.off()
>
```

Figure 6.19 shows the output of this methodology. It should be kept in mind that

the crack initiation is defined as when the summation of ratios, $\sum \frac{n_i}{N_i}$, reaches one.

6.6.2 Simulation Results

Following the procedure discussed above, the crack initiation time and its corresponding cumulative repetitions for both wander and no-wander cases, can be evaluated in an efficient way. Figures B.6.1 to B.6.8 present the simulation results for

coarse gradation, Figures B.6.9 to B.6.17 for fine gradation, and Figures B.6.18 to B.6.26 for fine-plus gradation. Table 6.5 summarizes the simulation results and the condition surveys for fatigue performance of the 26 original test sections of WesTrack project. Figure 6.20 illustrates the contents of Table 6.5. The results categorized by gradation type are shown in Figures 6.21 through 6.23. Note that in Figures 6.20 to 6.23 the first diamond (\blacklozenge) in the time axis represents the crack initiation time without wander and the second diamond the crack initiation time with wander. For the condition survey results, the first cross (x) stands for the 10 % surface fatigue cracking and the second cross the 50 % surface fatigue cracking.

As a general observation, in spite of the difference in percent air-voids, percent asphalt content, and gradation, the 26 original test sections display the same type of fatigue damage curves not only in the "with wander" case but also in the "without wander" case. It can be conjectured that this is because all 26 sections were subjected to the same simulation conditions, i.e., the same temperature spectrum, the same pavement structure, and the same traffic pattern. However, the cumulative rate of ratio n_i/N_i is different for the different mixes. Since n_i represents applied traffic and is the same for all 26 sections, the differences in the cumulative rates are due to differences in mix stiffness and fatigue response, which are expressed in the mechanistic-empirical stiffness and fatigue life equations.

In the simulation results shown in Figures B.6.1 to B.6.26, two "plateaus" (horizontal part of the fatigue damage curve representing a slow rate of damage accumulation) occur during two repetition periods, 9.2×10^5 through 2.1×10^6 repetitions and 2.7×10^6 through 3.5×10^6 repetitions. These two periods correspond to the time

periods, 10/13/96 ~ 5/18/97 and 10/24/97 ~ 4/11/98, which are over the winter and spring seasons. This suggests that in cold seasons the cumulative fatigue damage rate is comparably less than that in hot seasons.

6.7 Findings and Discussions

Whether viewed by mechanics analysis, statistical modeling, or understanding of the fatigue damage process, the simulation methodology introduced herein is not a perfect approach that can predict exact fatigue performance but rather an approach that, as a myopic eye, can identify the distant objects but with a blurred image. Although the methodology is not complete at this moment, several disadvantages can be pinpointed.

1. Apparently, this simulation methodology does not take into account the fact that the stiffness of the asphalt concrete layer deteriorates as the fatigue damage gradually accumulates. The effect of stiffness deterioration on the fatigue performance, however, can be assessed by using the Weibull theory to conduct a dynamic analysis, as will be seen in next chapter.
2. In this simulation methodology, the fatigue-resistant capacity of field asphalt concrete pavement was directly substituted by the laboratory-obtained fatigue life equations. However, this neglects the fact that the boundary conditions of a laboratory test setup are different than those of field pavement; a correction factor (or a shift factor) should be introduced to compensate for this difference.
3. In the stratification process, we reduced the total 21,943 cases to 110. Each cubic cell, formed by T_b , g , and sg , contains a different number of

observations, and is “weighted” differently. However, in this chapter, the mean values of each cubic cell were utilized to conduct the regression analysis.

Several findings and conclusions from the simulation results of the WesTrack project are addressed below.

1. Both the simulation results and the condition survey data reinforce the important role of air-void content in fatigue performance. However, the change of air-void content due to trafficking compaction was not included in this simulation methodology; instead, the air-void content was maintained the same during the whole simulation process. It has been found in current laboratory investigations that the air-void contents of WesTrack samples decreased after trafficking and exhibited a trend similar to that of a soil consolidation curve. Thus changes in air-void contents occurring in asphalt concrete pavement cannot be neglected and must be included in the simulation methodology, once the behavior of the change of air-void content is truly understood.
2. For coarse mixes containing air-void contents greater than 10 %, such as that used in test sections 6 and 26, the predicted crack initiation times were ahead of the actual surface cracking that occurred in the first winter. Those sections with medium to low air-void contents had predicted crack initiation times in the second winter, but surface cracks never appeared during the life of the project. It is worthwhile to pay attention to the test sections 5 and 8 where surface cracks developed in the first winter before the predicted crack

initiation time. Implicitly, it might indicate that utilizing the fatigue theory alone will not truly explain the cumulative fatigue damage caused by the combined effects of cold weather and traffic load. In addition, an adequate crack propagation model applied for cold temperatures should be superimposed with the fatigue theory to obtain reasonable estimates.

3. For fine mixes, the test sections containing air-void contents greater than 10 %, had predicted crack initiation times in the very early trafficking stage. The corresponding surface cracks developed in the second winter but the 50 % surface cracking was never observed. For the sections with low to medium air-void contents, the 10 % surface cracks never occurred. Also, since during the period 3/3/96 to 7/15/96 the sections were trafficked in no-wander or human driver situations, no obvious difference exists in the predicted crack initiation times between the “with wander” and “without wander” cases.
4. For fine-plus mixes, the sections with medium to high air-void contents, presented early predicted crack initiation times of around the first summer time. The predicted crack initiation times of sections with low air-void contents were during the first winter and the second summer. However, for all these sections; no actual surface cracking has been perceived. On the whole, from the simulation results and condition survey data, it seems that the fine-plus mixes have better resistance to fatigue damage than do the fine mixes when both mixes have equal air-void contents.

5. Finally, a summary of experience gained applying this simulation methodology of fatigue performance prediction of crack initiation time to pavement design as follows:

With regard to Correction Factor (CF):

a. *Coarse mix:*

Major cracks (10 % to 50 % cracking) will occur at next winter after the predicted crack initiation time.

b. *Fine mix:*

Major cracks will happen at the second winter after the predicted crack initiation time.

c. *Fine-plus mix:*

Major cracks will develop more than two winters later unless the air-void content is greater than 10%; if this is the case, then subtract one winter.

Table 6.1. Recording and analysis periods of WesTrack project.

	from	To
Temperature Recording Period	3/3/96	10/2/98
Traffic Recording Period	2/3/96	9/3/98
Temperature Analysis Period	3/3/96	10/2/98
Simulation Period (both traffic and temperature)	3/3/96	9/3/98

Table 6.2. Sample sizes of fatigue tests for various gradations.

	WesTrack fatigue tests at 20 °C	WesTrack temperature sensitivity fatigue tests	Total
Fine	48	11	59
Fine-plus	50	12	62
Coarse	53	12	65
Sum	151	35	186

Table 6.3 (a). Results of regression coefficients m_1 of coarse mixes at different temperature gradient intervals.

gradient	[-0.15,-0.10]	[-0.10,-0.05]	[-0.05,0.0]	[0.0,0.05]	[0.05,0.10]	[0.10,0.15]
Intercept	-0.08175863	-0.03479309	-0.03411011	-0.0431191	-0.03614109	-0.03233883
Tbg	0.01950062			0.03462285		
Tbsg		6.717861e-6	6.793519e-6		6.942432e-6	7.675834e-6
Tbg^2	0.002959697			-0.009660887		
Tbsg^2		-3.21376e-11	-1.247114e-10		-2.164686e-10	-3.704025e-10
G		0.0845437	0.03453812		0.05250905	0.04367304
Sg	0.0009615674		-0.00002152473	0.00002656082		-0.00003846102
Av	0.001093299	0.0006746544	0.0006666258	0.0006601759	0.0006720647	0.0006863074
Ac	0.003705114	0.00226696	0.002230678	0.002233238	0.002180534	0.002211977
Tbg*av	0.0001268999			-0.0002971607		
Tbsg*av		-5.584353e-8	-6.137919e-8		-7.738638e-8	-8.894092e-8
Tbg*ac	0.0004663344			-0.001021566		
Tbsg*ac		-2.0672e-7	-2.257651e-7		-2.846534e-7	-3.27908e-7
Av*ac	-0.00002792679	-0.00001991557	-0.00002062941	-0.00001568069	-0.00002628364	-0.00002838366
R^2	0.9959	0.9972	0.9971	0.9875	0.9965	0.999

Table 6.3 (b). Results of regression coefficients m_2 of coarse mixes at different temperature gradient intervals.

gradient	[-0.15,-0.10]	[-0.10,-0.05]	[-0.05,0.0]	[0.0,0.05]	[0.05,0.10]	[0.10,0.15]
Intercept	0.3562	0.3562	0.3562	0.3561	0.3562	0.3562
M1	-1.0066	-1.0053	-1.0062	-1.0071	-1.0085	-1.0095
R^2	0.9999	1.0000	1.0000	1.0000	1.0000	1.0000

Table 6.3 (c). Results of regression coefficients σ of coarse mixes at different temperature gradient intervals.

gradient	[-0.15,-0.10]	[-0.10,-0.05]	[-0.05,0.0]	[0.0,0.15]	[0.15,0.10]	[0.10,0.15]
Intercept	0.1431	0.1423	0.1426	0.1445	0.1412	0.1409
M1	-5.5021	-3.5916	-4.9619	-8.6655	-4.0365	-21.2729
M1 ²	-125.6612	-182.4311	-126.0442	-224.8148	-308.7180	-283.9384
M1 ³		-8698.2050	-668.5057		-22427.9359	15039.9723
M1 ⁴		-226481.9409			-873964.3969	
M1 ⁵		-2393516.9861			-13472803.3775	
Sin(m/0.01)	0.0216		0.0166	0.0453		0.172
R ²	0.9999	0.9998	0.9999	0.9958	0.9999	0.9998

Table 6.3 (d). Results of regression coefficients A of coarse mixes at different temperature gradient intervals.

gradient	[-0.15,-0.10]	[-0.10,-0.05]	[-0.05,0.0]	[0.0,0.05]	[0.05,0.10]	[0.10,0.15]
Intercept	-13.39914	-11.58667	-11.12271	-11.49544	-12.01581	-11.10854
Tbg	1.53532			2.294153		
Tbgs		0.0005025015	0.0004804504		0.0004590989	0.0005093146
Tbg ²	0.2220458			-0.5428994		
Tbgs ²		-1.161947e-9	-5.566515e-9		-1.683449e-9	-1.405131e-8
G		6.384203	0.6557571		5.63907	2.487178
Sg	0.05892822		-0.006828288	-0.002321114		-0.007310587
Av	0.06316996	0.04783163	0.04758049	0.04731206	0.04742552	0.04794235
Ac	0.2173902	0.1641741	0.163119	0.1601871	0.1608133	0.1615919
Tbg*av	0.005865289			-0.01427007		
Tbgs*av		-3.361553e-6	-3.468244e-6		-3.921476e-6	-4.321448e-6
Tbg*ac	0.02175577			-0.0527957		
Tbgs*ac		-0.0000124667	-0.00001285962		-0.00001453973	-0.00001601667
Av*ac	-0.00146397	-0.001153217	-0.001164524	-0.001324928	-0.001308766	-0.001402494
R ²	0.9987	0.9923	0.9985	0.9962	0.9917	0.9974

Table 6.4 (a). Results of regression coefficients m_1 of fine and fine-plus mixes at different temperature gradient intervals.

gradient	[-0.15,-0.10]	[-0.10,-0.05]	[-0.05,0.0]	[0.0,0.05]	[0.05,0.10]	[0.10,0.15]
Intercept	-0.07988474	-0.03634856	-0.03691352	-0.04270346	-0.03327317	-0.03607125
Tbg	0.0159674			0.03393941		0.006677723
Tbsg		7.199499e-6	6.842651e-6		7.529676e-6	
Tbg^2	0.002579341			-8.99276e-3		-0.0003165719
Tbsg^2		-1.351548e-10	-1.361373e-10		-3.466108e-10	
G		0.07178455	0.02041707			
Sg	0.0008506537			2.267549e-5		0.00004793386
Av	0.001564374	0.00100384	0.0009612834	0.001012483	0.0009535552	0.0009445551
Ac	0.003935108	0.002520002	0.002413306	0.002475931	0.002344938	0.002294424
Tbg*av	0.0001833901			-0.0004657914		-0.000101136
Tbsg*av		-9.289788e-8	-9.387046e-8		-1.124367e-7	
Tbg*ac	0.0004900334			-0.001215362		-0.0002752519
Tbsg*ac		-2.543658e-7	-2.57598e-7		-3.074625e-7	
Av*ac	-0.000046345	-0.0000360965	-3.451985e-5	-0.0000428518	-0.0000418012	-0.00004531004
R^2	0.9929	0.9971	0.9967	0.9898	0.9943	0.9976

Table 6.4 (b). Results of regression coefficients m_2 of fine and fine-plus mixes at different temperature gradient intervals.

gradient	[-0.15,-0.10]	[-0.10,-0.05]	[-0.05,0.0]	[0.0,0.05]	[0.05,0.10]	[0.10,0.15]
Intercept	0.3562	0.3562	0.3562	0.3560	0.3562	0.3561
M1	-1.0073	-1.0062	-1.0069	-1.0086	-1.0096	-1.0103
R^2	0.9999	1.0000	1.0000	1.0000	1.0000	0.9999

Table 6.4 (c). Results of regression coefficients σ of fine and fine-plus mixes at different temperature gradient intervals.

gradient	[-0.15,-0.10]	[-0.10,-0.05]	[-0.05,0.0]	[0.0,0.15]	[0.15,0.10]	[0.10,0.15]
Intercept	0.1425	0.1423	0.1422	0.1485	0.1411	0.1409
M1	-6.7044	-6.4943	-6.5630	-3.3726	-4.2418	-4.4155
M1 ²	-162.0980	-157.8808	-160.1644	-57.7235	-379.9716	-503.7375
M1 ³					-31839.2312	-58146.4542
M1 ⁴					-1396525.8838	-3559716.1828
M1 ⁵					-23722319.7929	-84038344.7616
Sin(m/0.01)	0.0310	0.0294	0.0304	0.0073		
R ²	0.9999	0.9998	0.9998	0.9968	0.9998	0.9998

Table 6.4 (d). Results of regression coefficients A of fine and fine-plus mixes at different temperature gradient intervals.

gradient	[-0.15,-0.10]	[-0.10,-0.05]	[-0.05,0.0]	[0.0,0.05]	[0.05,0.10]	[0.10,0.15]
Intercept	-13.41943	-11.60635	-11.93162	-11.52406	-11.99708	-11.81081
Tbg	1.319236			2.235742		0.4622427
Tbgs		0.0004821816	0.0004740113		0.0004566367	
Tbg ²	0.1982441			-0.5164648		-0.01628367
Tbgs ²		1.14947e-9	-2.061125e-9		-3.015393e-9	
G		5.958508	-2.517388		5.119211	
Sg	0.05352491			-0.002119558		0.002269168
Av	0.09092601	0.06912625	0.06805976	0.06760431	0.06782119	0.06745517
Ac	0.2349178	0.1777141	0.1748931	0.1720754	0.1727083	0.1707851
Tbg*av	0.008588157			-0.02108253		-0.005128277
Tbgs*av		-5.169588e-6	-5.12326e-6		-5.737562e-6	
Tbg*ac	0.02376517			-0.05790203		-0.01413554
Tbgs*ac		-0.00001428444	-0.00001414514		-0.00001582453	
Av*ac	-0.002397742	-0.001936588	-0.001916482	-0.002129637	-0.002135857	-0.002265763
R ²	0.9975	0.9919	0.9933	0.9967	0.9926	0.9975

Table 6.5. Summary table of fatigue performance prediction and condition survey data of WesTrack.

Section No.	Mix Type	AV (%)	AC (%)	Reps @Center		Reps @Wander		10% fatigue cracking		50% fatigue cracking	
				Reps	Date	Reps	Date	ESAL	Date	ESAL	Date
5	Coarse (Non-Critical)	8.1	5.63	2,255,114	10/24/96	3,698,621	08/11/97	1,757,238	12/30/96	2,311,472	04/08/97
6		10.8	5.71	606,774	08/03/96	1,888,032	09/22/96	1,668,205	12/16/96	1,794,207	02/19/97
7		6.9	6.49	3,786,621	08/11/97	DNO	09/03/98	DNO	09/03/98	DNO	09/03/98
8		8.5	5.47	2,076,977	09/26/96	2,507,188	07/31/97	1,515,380	12/01/96	1,789,150	01/01/97
23		4.9	5.79	DNO	03/09/98	DNO	09/03/98	DNO	09/03/98	DNO	09/03/98
24		7.2	5.94	2,525,817	07/26/97	DNO	04/06/98	DNO	09/03/98	DNO	09/03/98
25		3.7	6.55	DNO	09/03/98	DNO	09/03/98	DNO	09/03/98	DNO	09/03/98
26		11	5.31	550,317	07/30/96	1,358,144	09/02/96	1,487,207	11/29/96	1,626,490	12/10/96
1	Fine (Critical)	8.8	5.55	341,549	06/17/96	387,558	06/21/96	DNO	09/03/98	DNO	09/03/98
2		10.4	4.92	266,730	06/08/96	277,101	06/14/96	2,899,176	07/26/97	DNO	09/03/98
3		12.4	4.97	219,394	05/12/96	231,000	05/14/96	3,585,531	11/05/97	4,340,103	02/18/98
4		6.6	5.12	513,676	07/28/96	833,323	08/23/96	DNO	09/03/98	DNO	09/03/98
14		9	6.05	318,975	06/16/96	354,101	06/18/96	DNO	09/03/98	DNO	09/03/98
15		8.7	5.42	347,832	06/20/96	395,017	06/22/96	DNO	09/03/98	DNO	09/03/98
16		12.2	4.75	229,994	05/14/96	236,768	05/21/96	3,720,800	11/17/97	DNO	09/03/98
17		11	5.74	244,454	06/06/96	259,553	06/07/96	4,227,572	01/18/98	DNO	09/03/98
18	4.3	6.04	2,091,353	09/14/96	2,489,843	08/02/97	DNO	09/03/98	DNO	09/03/98	
9	Fine Plus (Super-Critical)	7.2	5.89	473,673	07/26/96	719,415	08/07/96	DNO	09/03/98	DNO	09/03/98
10		10.9	5.88	255,845	06/06/96	267,610	06/08/96	DNO	09/03/98	DNO	09/03/98
11		4.2	6.75	2,195,380	10/07/96	3,432,750	08/10/97	DNO	09/03/98	DNO	09/03/98
12		8.1	5.23	406,488	07/16/96	521,132	07/28/96	DNO	09/03/98	DNO	09/03/98
13		3.9	6.56	2,322,881	04/23/97	DNO	08/21/97	DNO	09/03/98	DNO	09/03/98
19		11.8	5.28	238,956	05/25/96	247,211	06/03/96	1,750,322	12/29/96	4,215,885	01/17/98
20		7.9	5.99	405,359	07/16/96	528,188	07/28/96	DNO	09/03/98	DNO	09/03/98
21		4.6	5.84	2,205,678	10/07/96	2,662,463	08/08/97	DNO	09/03/98	DNO	09/03/98
22	5.9	6.51	628,477	08/04/96	2,108,536	10/03/96	DNO	09/03/98	DNO	09/03/98	

Note: DNO stands for "did not occur".

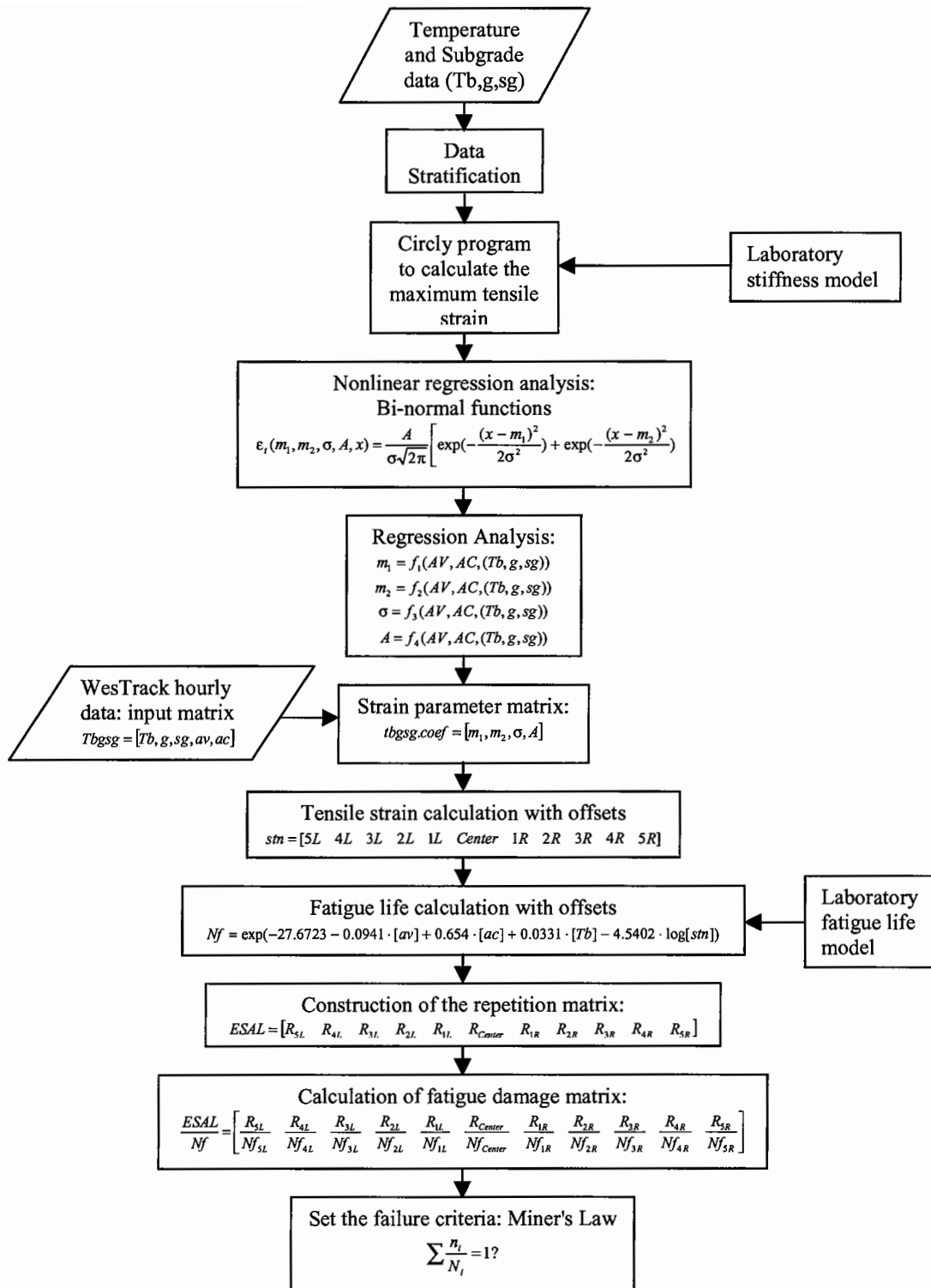


Figure 6.1. Flow chart of the simulation procedure for fatigue performance prediction (crack initiation time).

Secs 12+25: Depth @ 50 mm

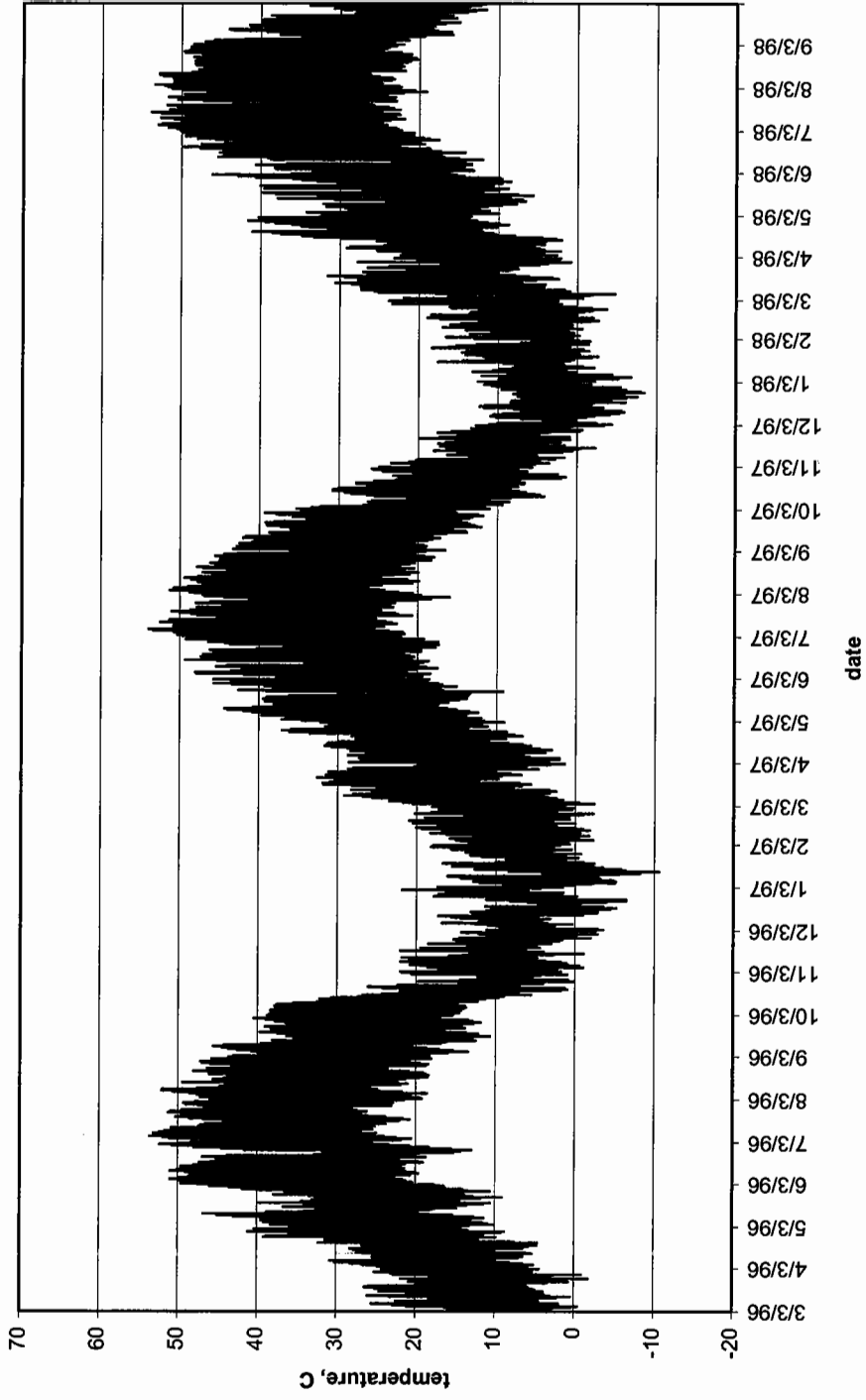


Figure 6.2. Temperature spectrum of WesTrack at a depth of 50 mm from 3/3/96 to 10/2/98.

Temperature Density Function: 50 mm, 3/3/96-10/2/98

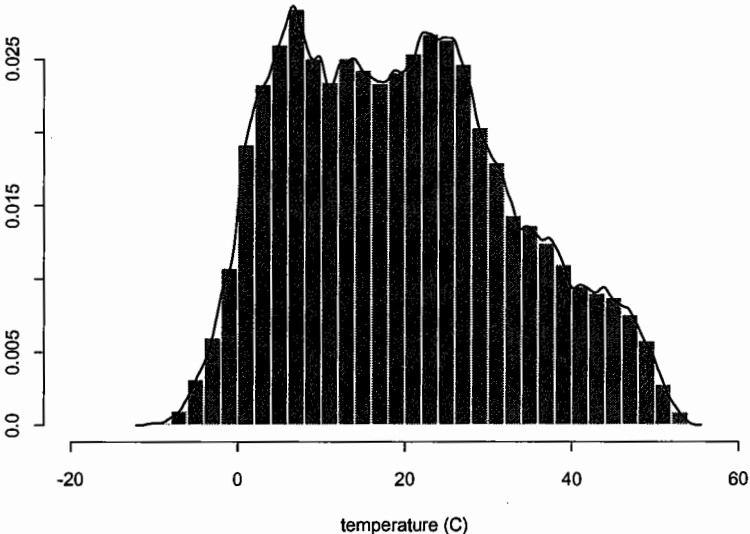


Figure 6.3. Temperature density function of WesTrack at a depth of 50 mm from 3/3/96 to 10/2/98.

Temperature Distribution Function: 50 mm, 3/3/96-10/2/98

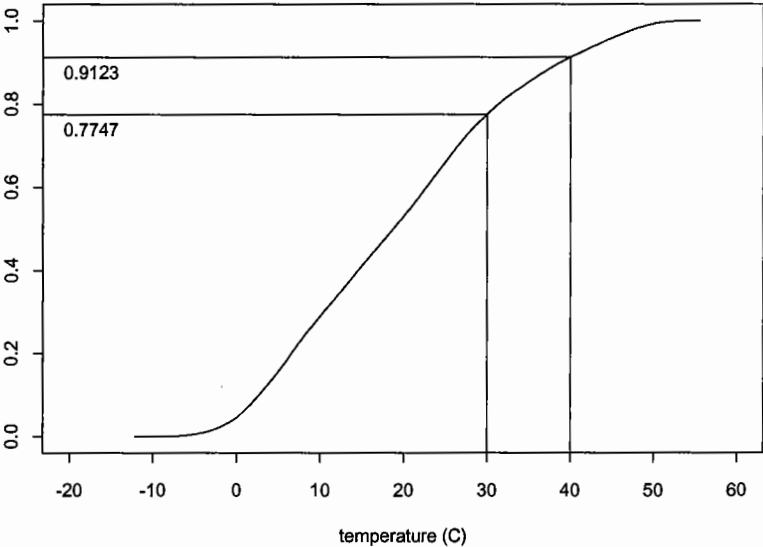


Figure 6.4. Temperature distribution function of WesTrack at a depth of 50 mm from 3/3/96 to 10/2/98.

Secs 12+25: Depth @ 150 mm

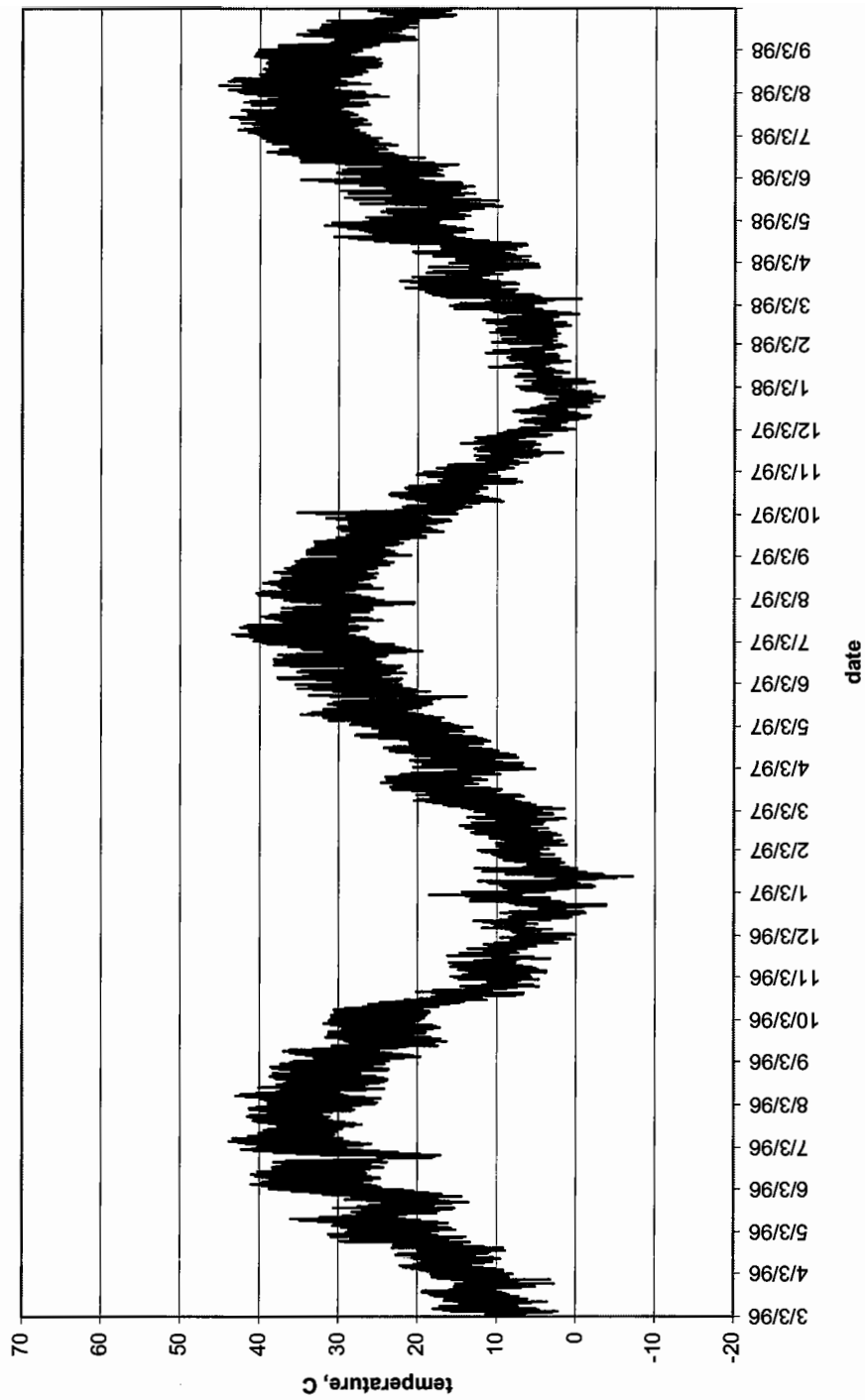


Figure 6.5. Temperature spectrum of WesTrack at a depth of 150 mm from 3/3/96 to 10/2/98.

Temperature Density Function: 150 mm, 3/3/96-10/2/98

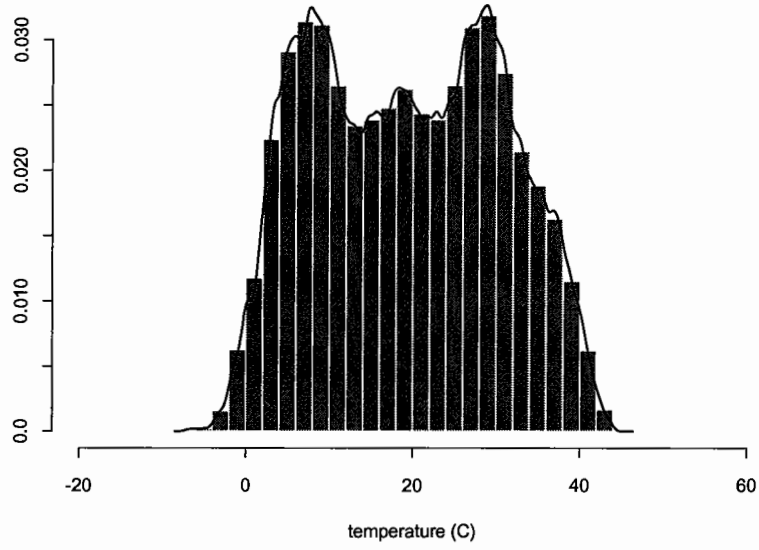


Figure 6.6. Temperature density function of WesTrack at a depth of 150 mm from 3/3/96 to 10/2/98.

Temperature Distribution Function: 150 mm, 3/3/96-10/2/98

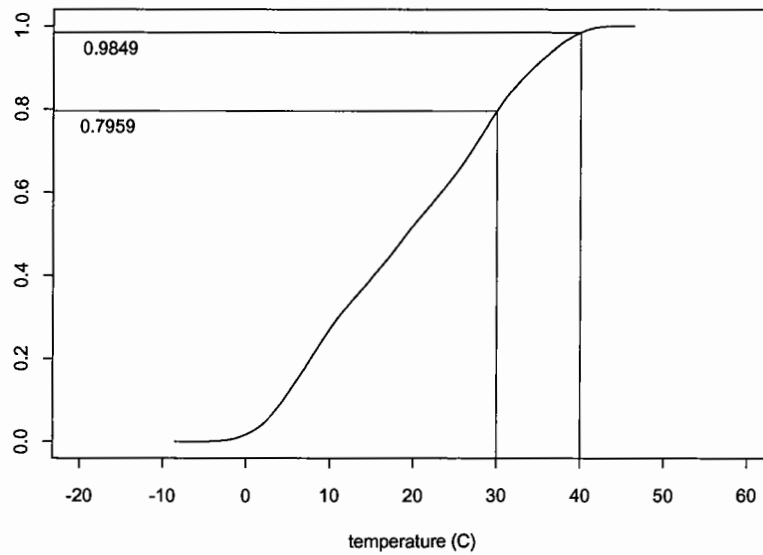


Figure 6.7. Temperature distribution function of WesTrack at a depth of 150 mm from 3/3/96 to 10/2/98.

Secs 12+25: temperature gradient

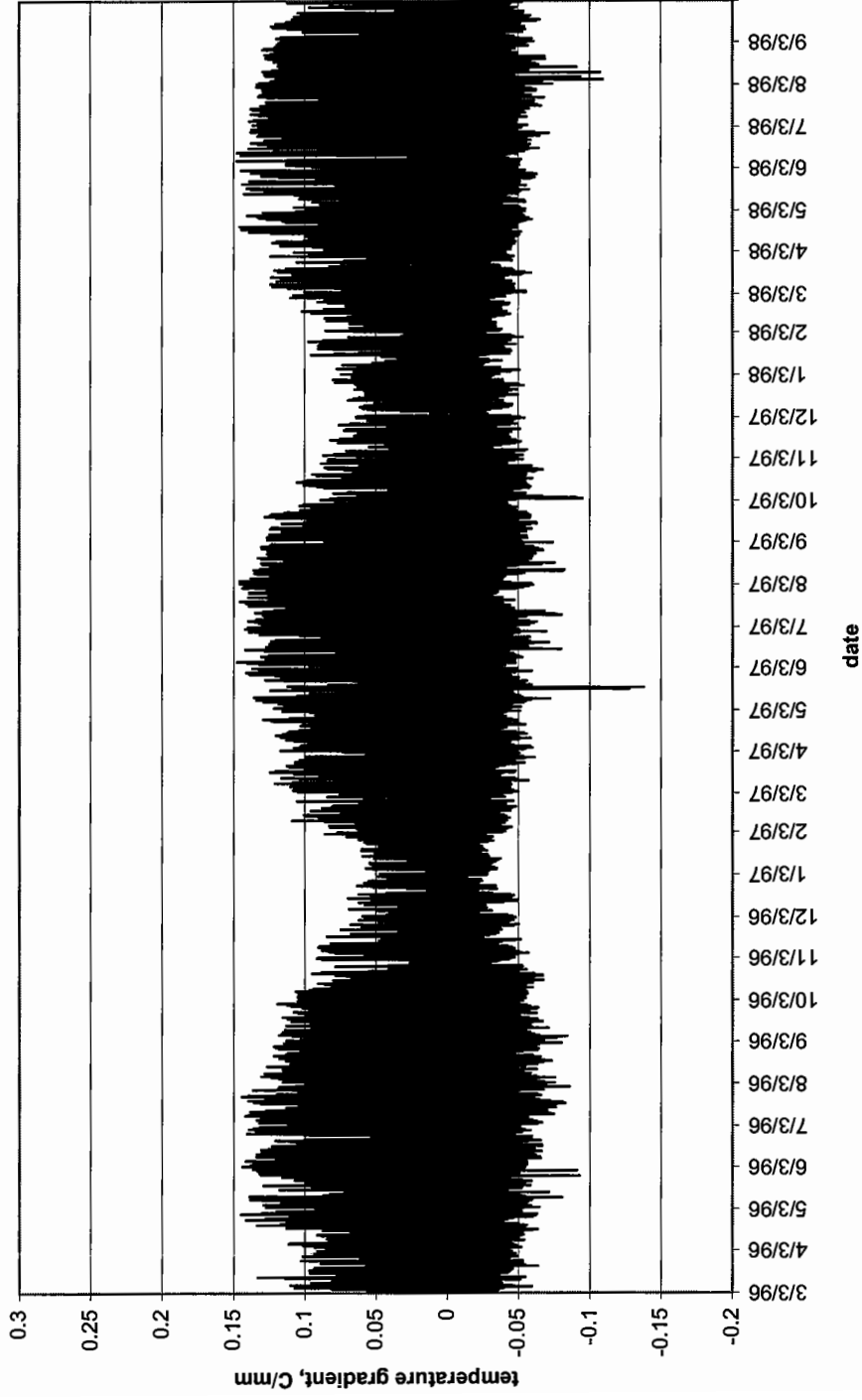


Figure 6.8. Spectrum of temperature gradient at WesTrack from 3/3/96 to 10/2/98.

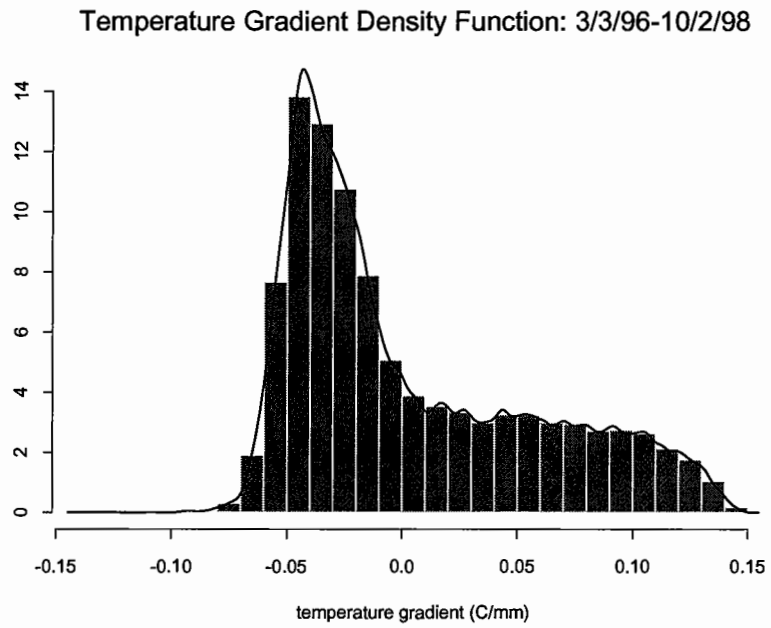


Figure 6.9. Temperature gradient's density function at WesTrack from 3/3/96 to 10/2/98.

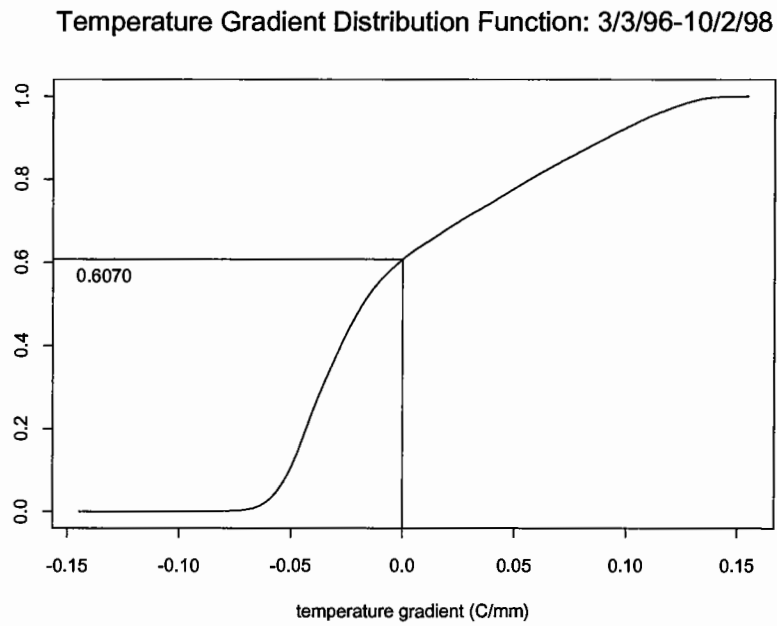


Figure 6.10. Temperature gradient's distribution function at WesTrack from 3/3/96 to 10/2/98.

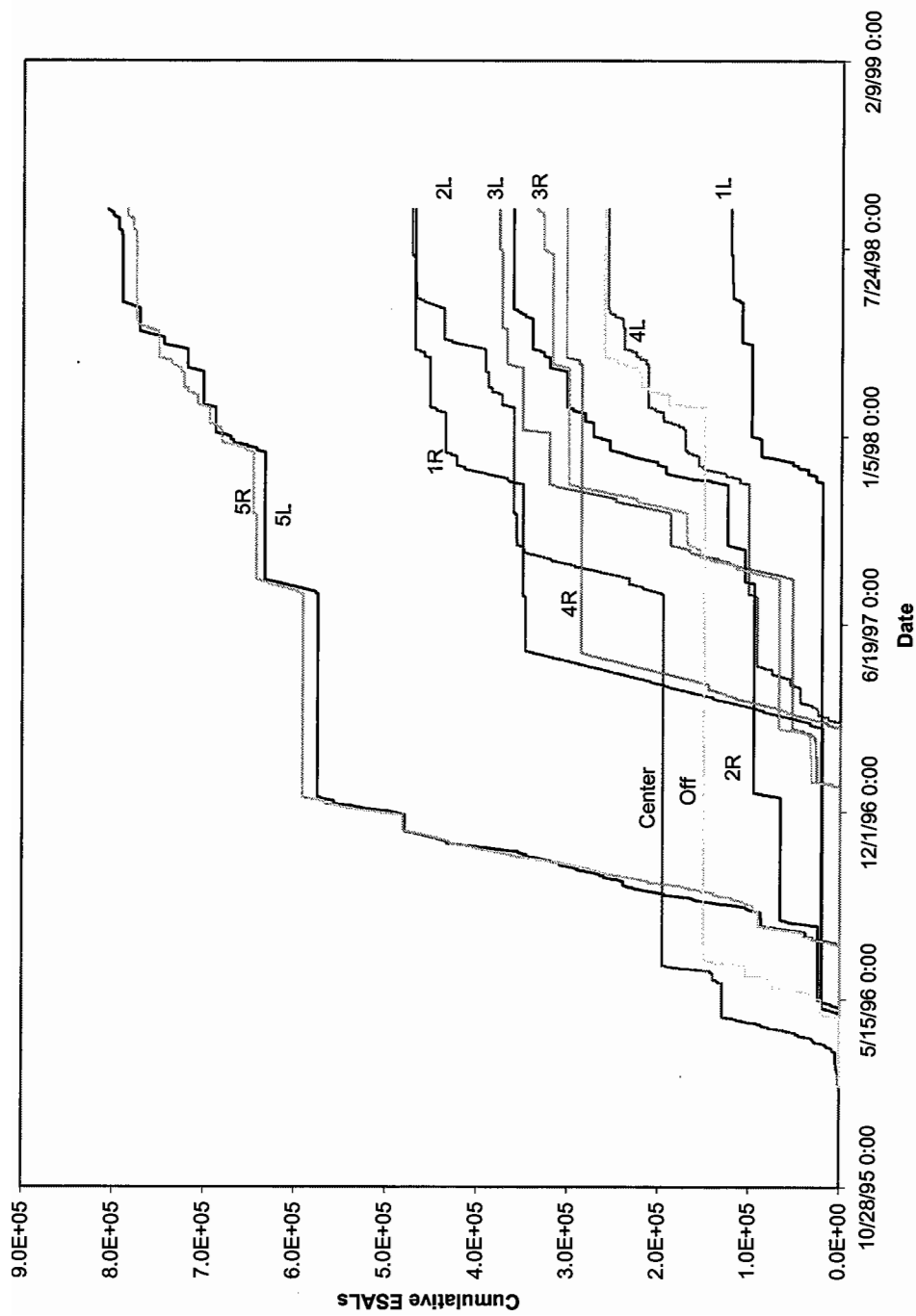


Figure 6.11. Applied traffic at various wander locations of WesTrack.

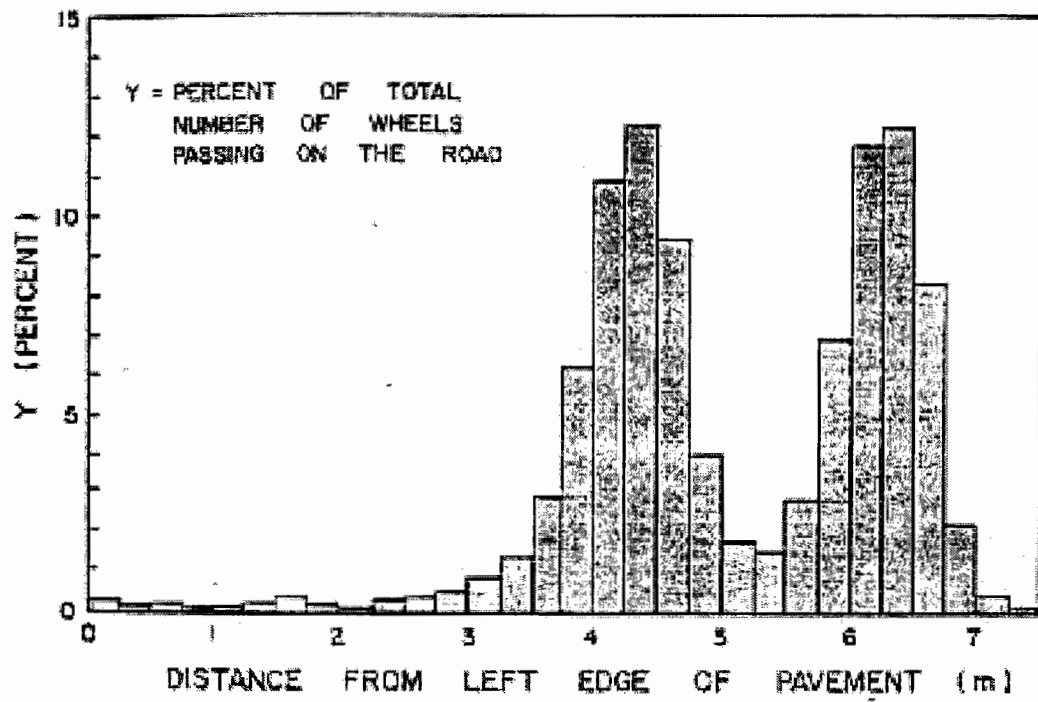


Figure 6.12. Typical highway wander pattern (after Allen).

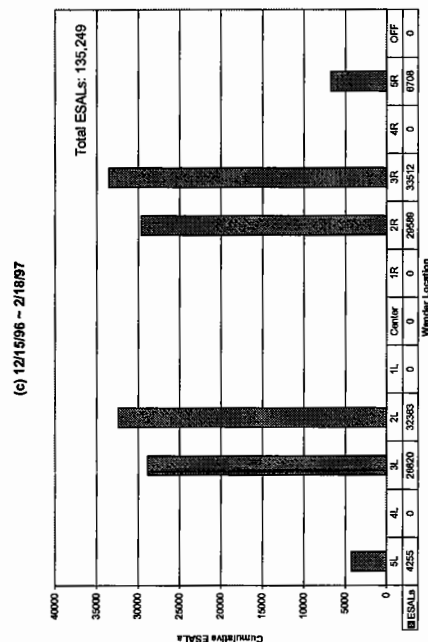
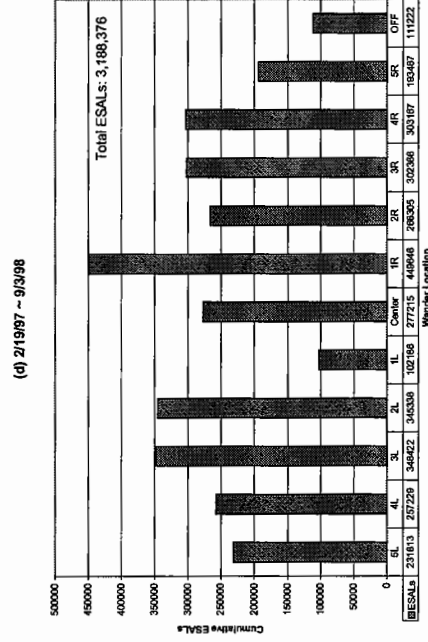
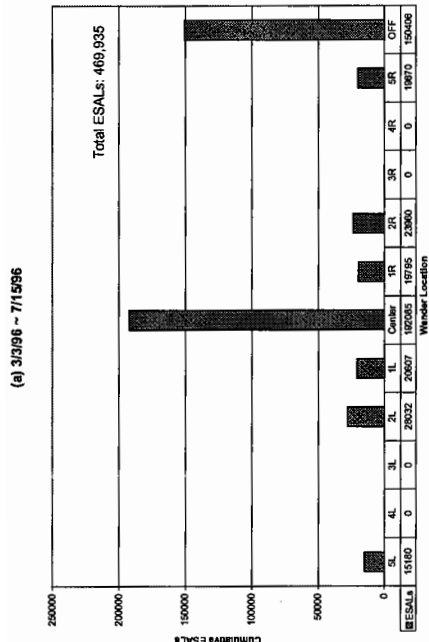
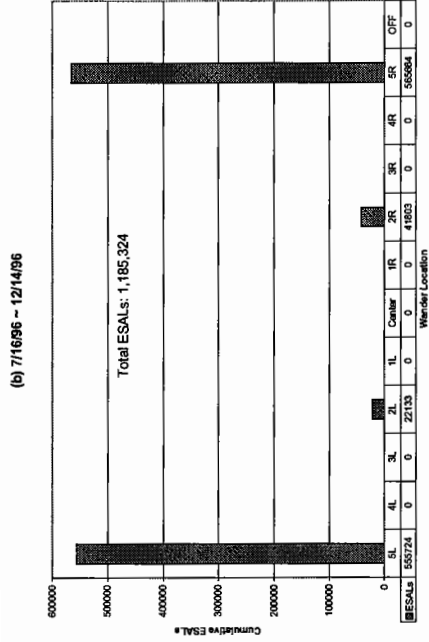


Figure 6.13. Bar charts of applied traffic at various wander locations at different periods of WesTrack: (a) 3/3/96-7/15/96: no wander or antenna off, (b) 7/16/96-12/14/96: traffic only at 5R and 5L, (c) 12/15/96-2/18/97: only 135,249 ESALs applied, and (d) 2/19/97-9/3/98: varied wander pattern.

WesTrack Traffic Pattern: 3/3/96 ~ 9/3/98

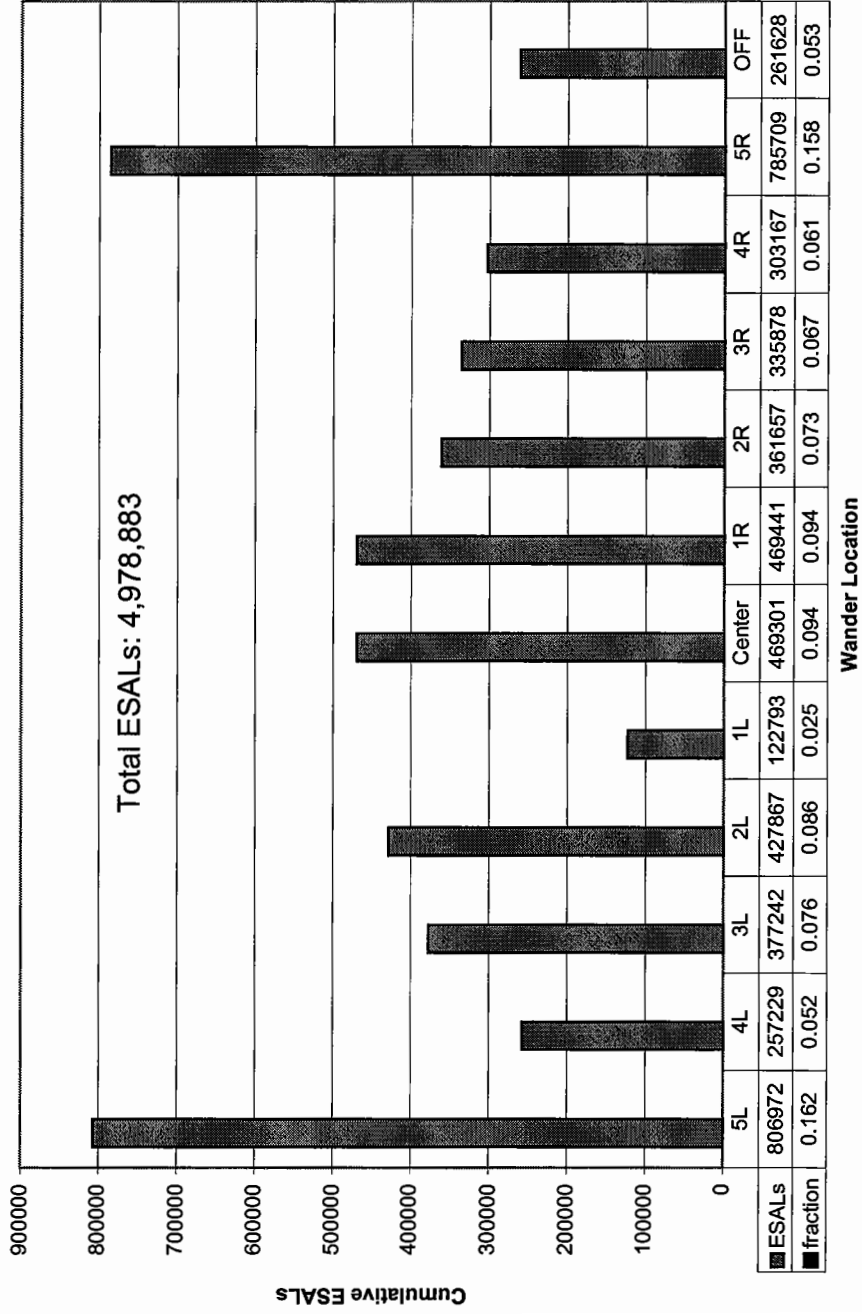


Figure 6.14. Bar chart of applied traffic at various wander locations from 3/3/96-9/3/98.

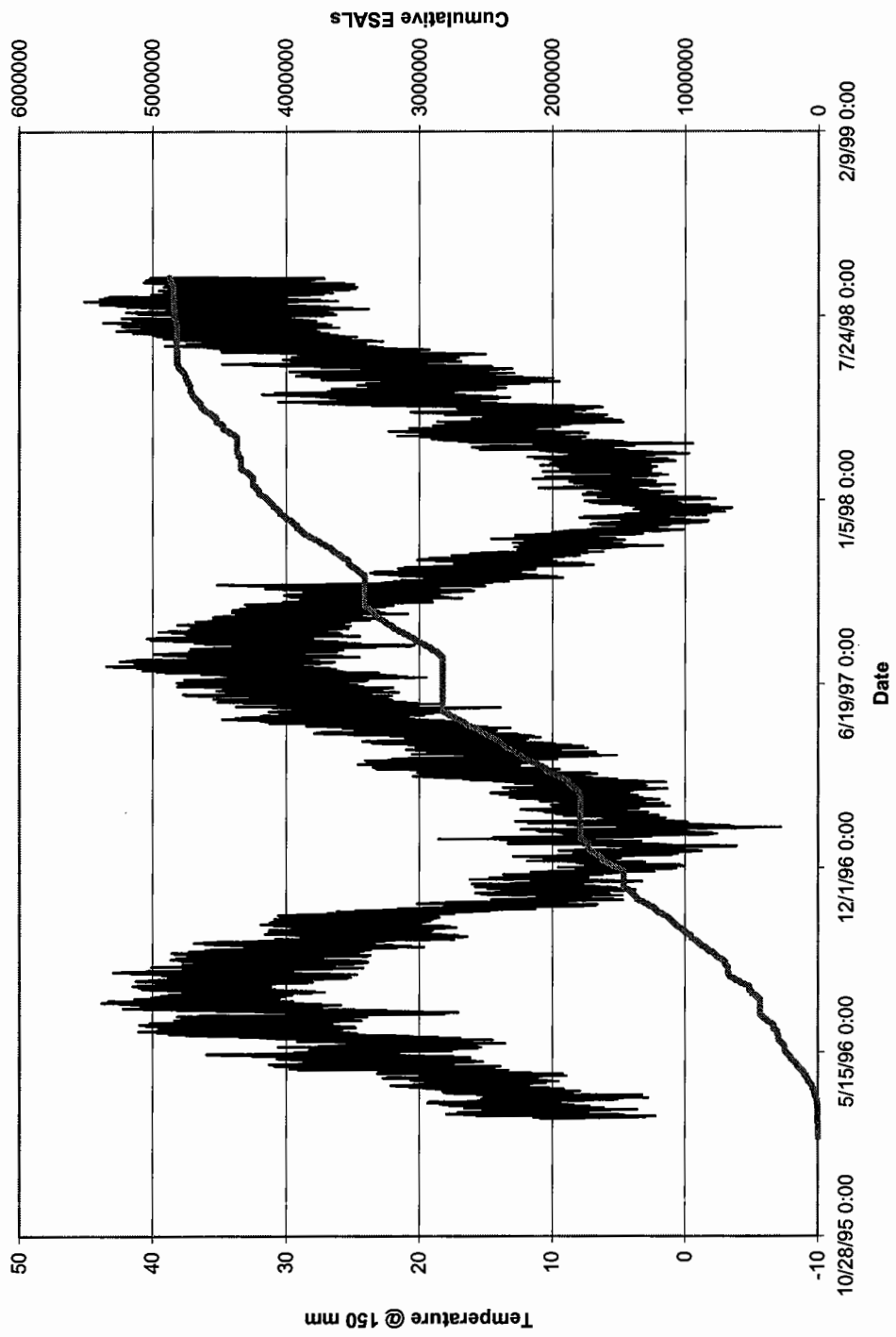


Figure 6.15. Plot of cumulative ESALs and temperature spectrum at a depth of 150 mm.

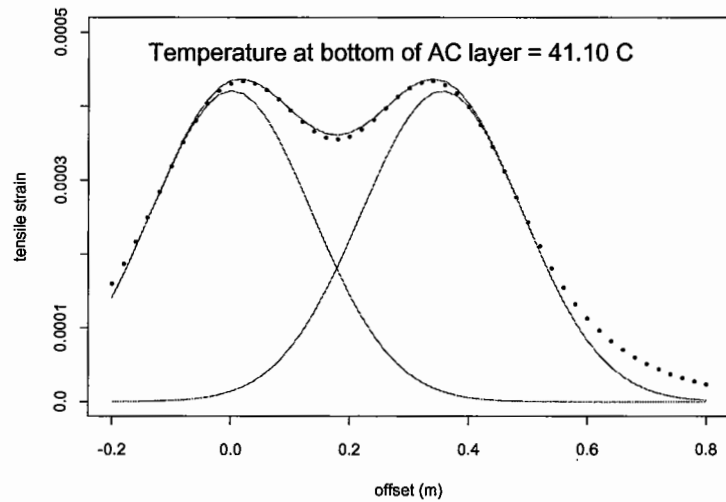


Figure 6.16. Maximum tensile strains fitted with a bi-normal distribution functions, $N(0.0010, 0.1361)$ and $N(0.3551, 0.1361)$, with a multiplication factor of $A = 0.0001435$, subjected to the following simulation case: $T_b = 41.10^\circ\text{C}$, $g = 0.1091$, $sg = 95.79\text{ MPa}$, $av = 13.7\%$, and $ac = 6.22\%$. (Note: the dots represent the tensile strains obtained from the Circlly program).

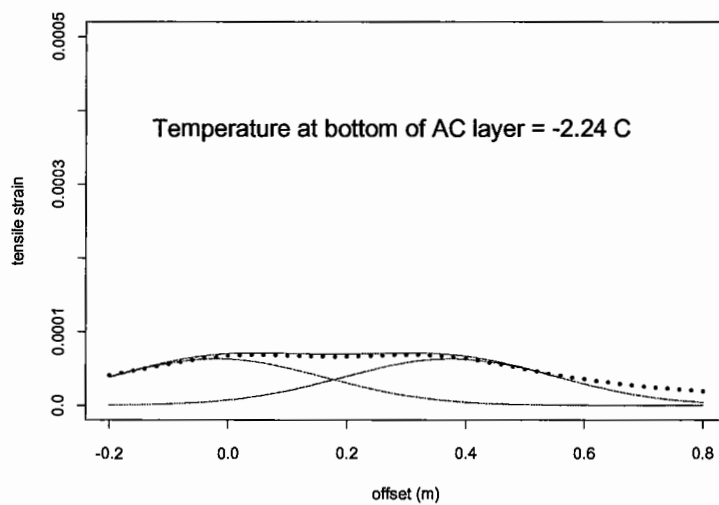
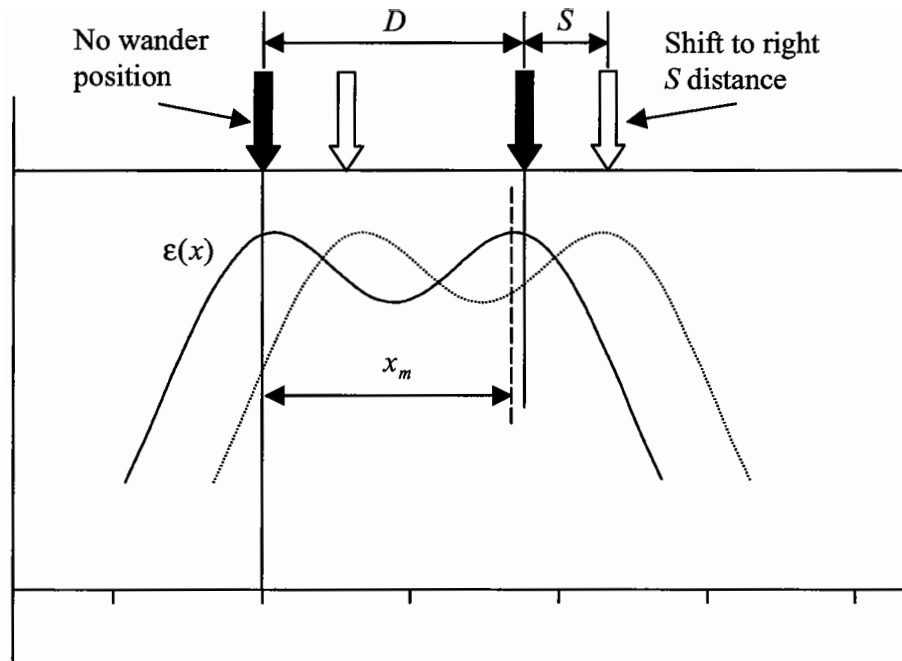


Figure 6.17. Maximum Tensile strains fitted with a bi-normal distribution functions, $N(-0.0188, 0.1806)$ and $N(0.3751, 0.1806)$, with a multiplication factor of $A = 0.0001435$, subjected to the following simulation case: $T_b = -2.24^\circ\text{C}$, $g = -0.0518$, $sg = 113.30\text{ MPa}$, $av = 13.7\%$, and $ac = 6.22\%$. (Note: the dots represent the tensile strains obtained from the Circlly program).



Note: $\epsilon(x_m) = \epsilon(x_m - S)$, if shift to right S distance.
 $\epsilon(x_m) = \epsilon(x_m + S)$, if shift to left S distance.

Figure 6.18. Illustration of tensile strain calculation with wander.

Section 8:coarse,AV=8.5,AC=5.47.(3/3/96~9/3/98)

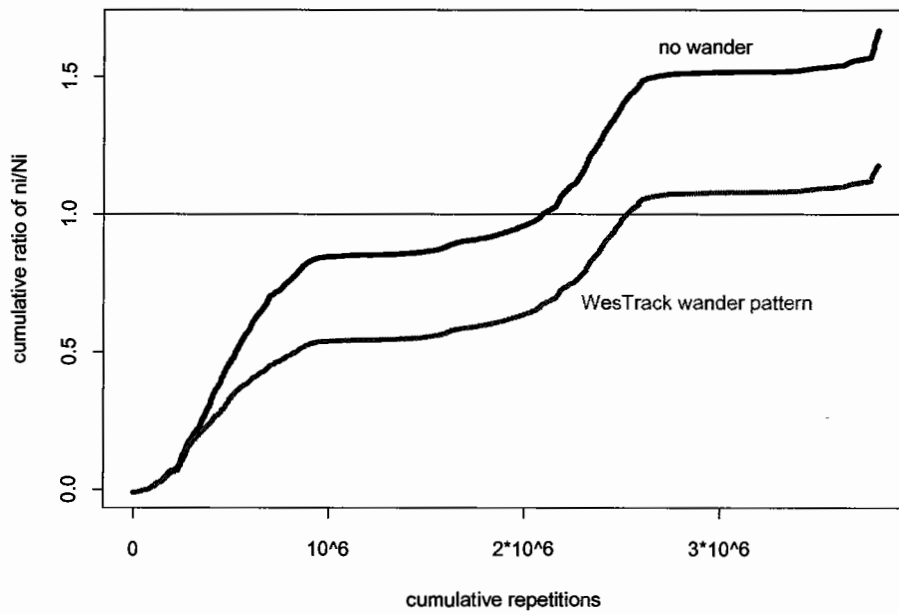


Figure 6.19. Fatigue performance prediction of crack initiation with and without wander for Section 8.

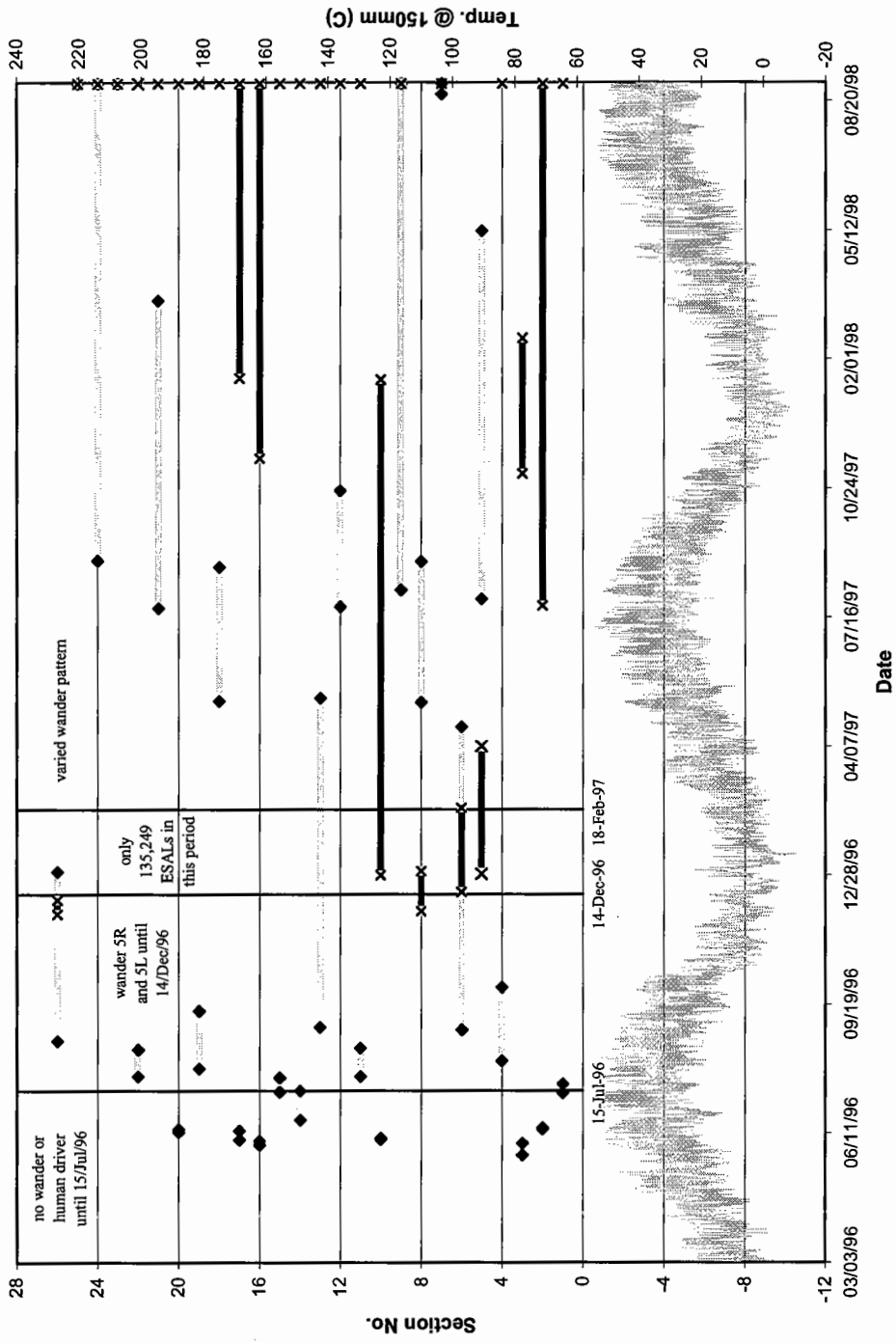


Figure 6.20. Simulation results of fatigue performance prediction and condition survey of 26 original test sections of the WesTrack project. (Note: the left \blacklozenge means the result of no wander; the right \blacklozenge is the result of 10 % fatigue cracking and the right \times is the 50 % fatigue cracking.)

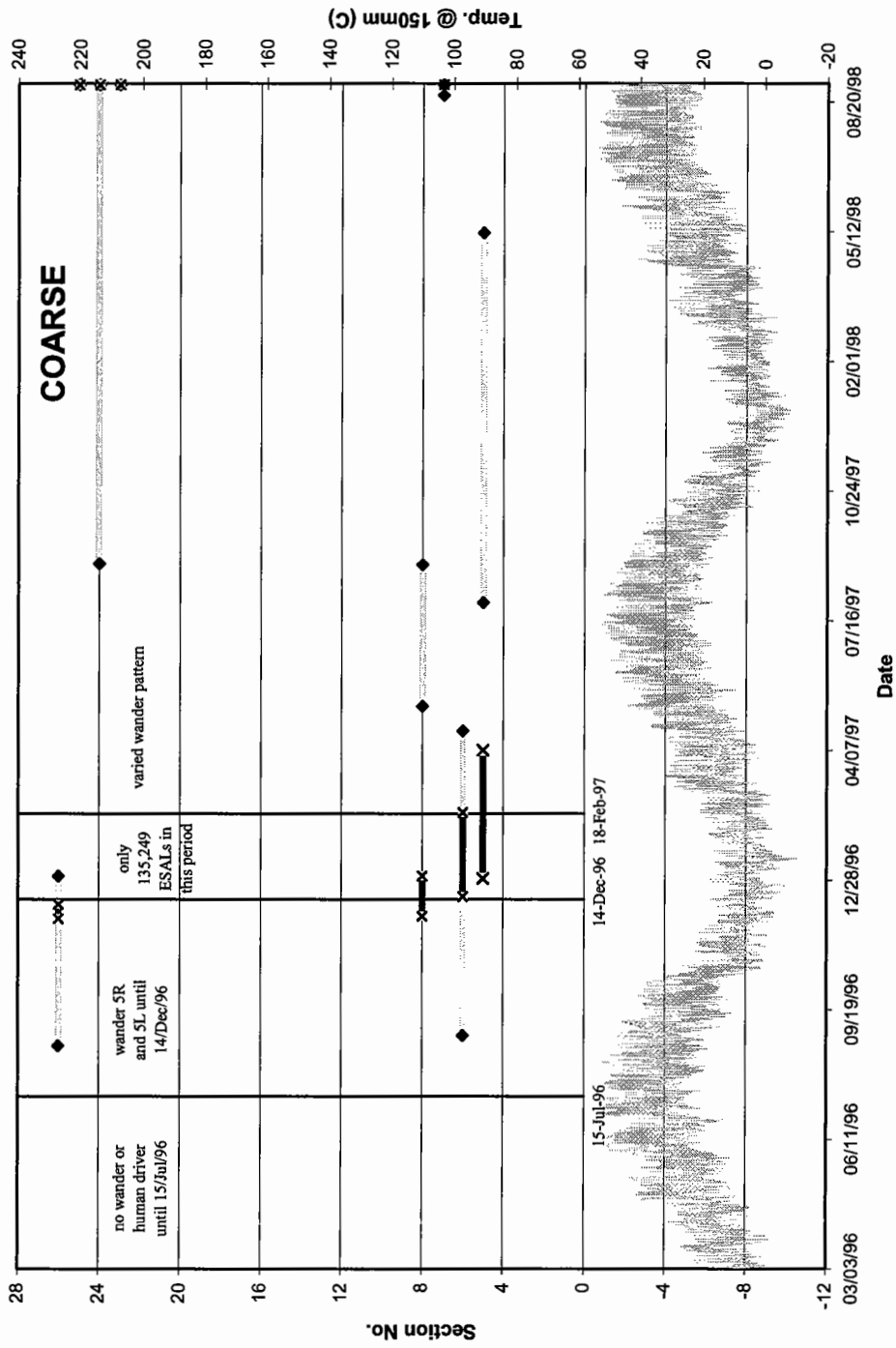


Figure 6.21. Simulation results of fatigue performance prediction and condition survey of coarse mixes of the WesTrack project. (Note: the left \diamond means the result of no wander; the right \diamond is the result of no wander; the left \times means the result of 10 % fatigue cracking and the right \times is the 50 % fatigue cracking.)

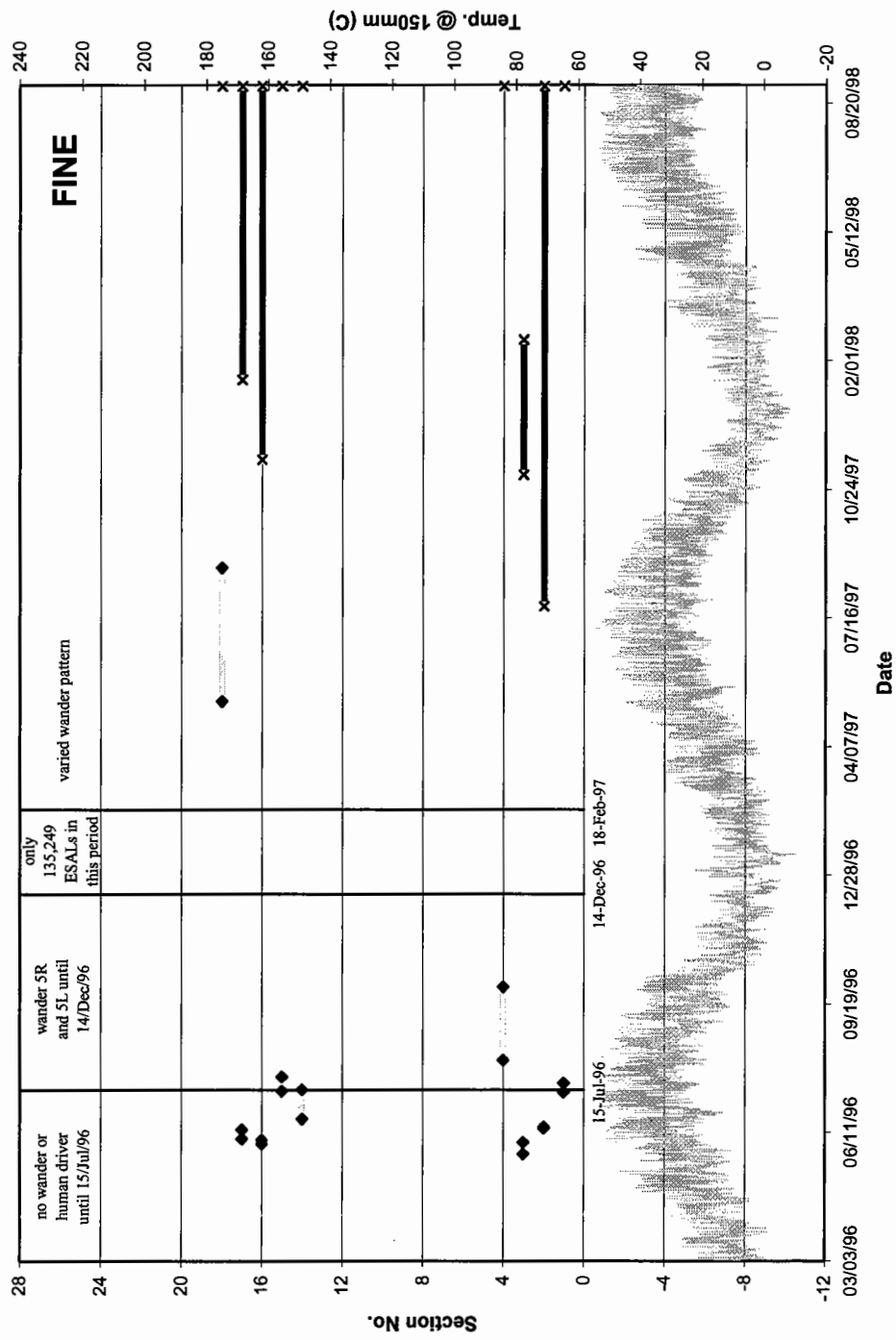


Figure 6.22. Simulation results of fatigue performance prediction and condition survey of fine mixes of the WesTrack project. (Note: the left ♦ means the result of no wander; the right ♦ is the result of 10 % fatigue cracking and the right x is the 50 % fatigue cracking.)

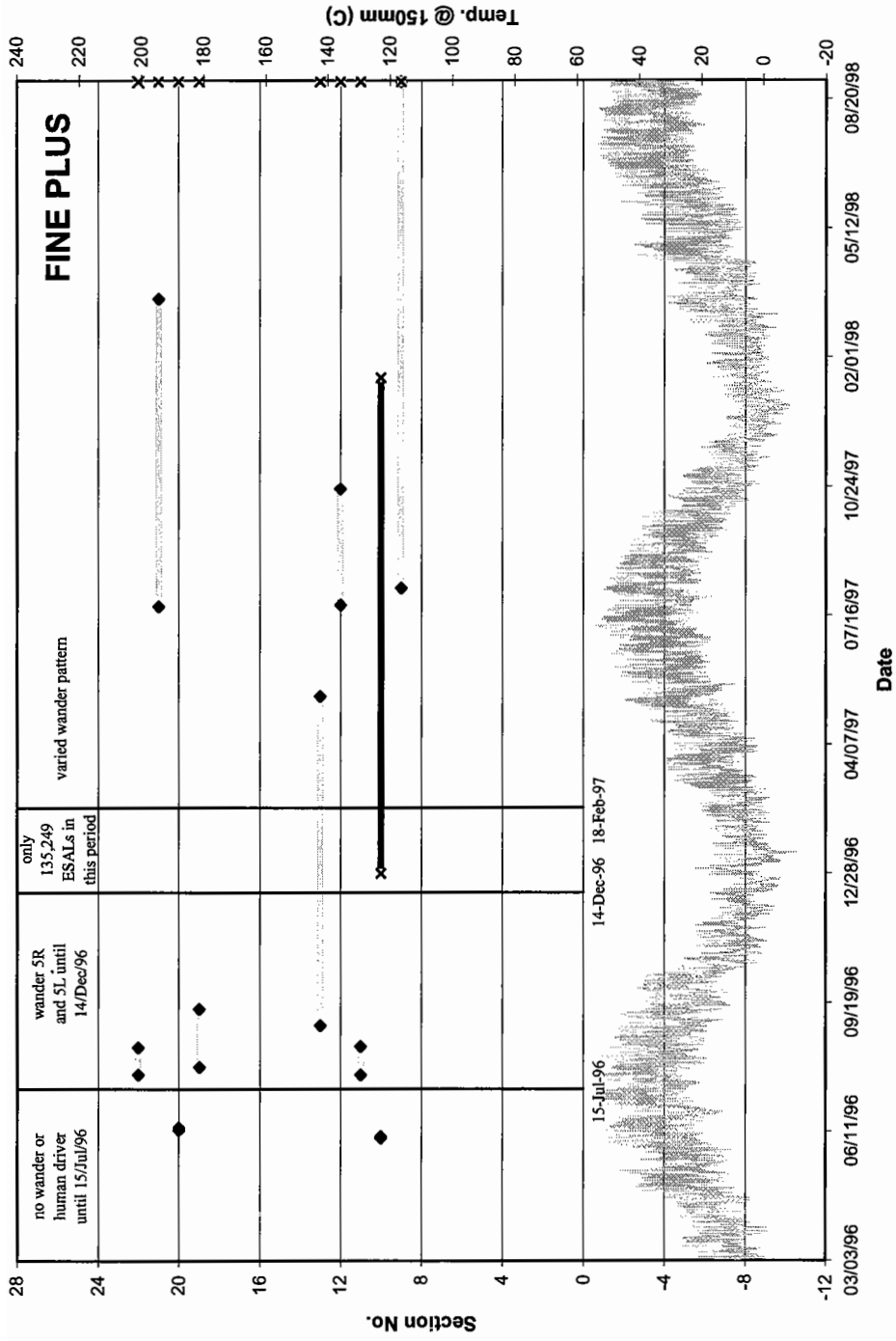


Figure 6.23. Simulation results of fatigue performance prediction and condition survey of fine-plus mixes of the WesTrack project. (Note: the left \blacklozenge means the result of no wander; the right \blacklozenge is the result of no wander; the left \times means the result of 10 % fatigue cracking and the right \times is the 50 % fatigue cracking.)

7.0 WEIBULL SIMULATION

7.1 General Considerations

A *Weibull* program that is coded and entitled according to the Weibull theory, as discussed in Chapter 5, was used to conduct the Weibull simulation to predict the fatigue performance (crack initiation, at present) of an in situ pavement. The paragraphs to follow give a brief introduction to the Weibull program and the related factors affecting fatigue performance that are incorporated into the program.

7.1.1 Algorithm of Weibull Program

Before describing the algorithm of the Weibull program, the assumptions postulated in Chapters 4 and 5 will be restated, i.e.,

1. *For every testing situation containing many variables, there exists one and only one associated stiffness deterioration curve in the SR-N space. If the testing situation changes from one state to the other at a given instant (repetition), the stiffness deterioration rate will follow the rate of the new state, starting immediately at that specific instant (repetition).*
2. *The SR cannot be increased.*

In addition another two additional assumptions will be postulated to complete the basis for the algorithm of the *Weibull* program.

3. *If there is no traffic, even though daily or seasonal temperature variations exist, the SR remains unchanged; i.e., aging and thermal effects have no effect on fatigue performance.*
4. *During each hour (WesTrack specific), the fatigue damage caused by traffic application at random wander positions is equivalent to the fatigue damage accumulated by applying traffic in a sequential and sorted order of wander positions.*

Using assumptions 1 and 2 above, we have already stated in Chapter 5 how to construct the compound stiffness deterioration curve in terms of a stiffness ratio and changes in material or environment variables. Assumptions 3 and 4 will now be incorporated to complete the Weibull dynamic algorithm to include traffic wander and environment factors in compliance with specific WesTrack data. This algorithm can be termed "hour-by-hour" or "node-by-node."

Each node in Figure 7.1 represents a wander position that has been subjected to traffic loading. Each hour consists of several or no nodes. For the specific wander pattern at WesTrack, each hour will consist of at most 11 nodes (each node representing a specific wander location of WesTrack). Each hour will be characterized by a set of environmental variables. The execution flow is wander-oriented, i.e., in a sequential and sorted order as shown by the direction of the arrow in Figure 7.1, i.e., "node-by-node" and "hour-by-hour" complying with assumptions 3 and 4. Notice that the stiffness will be changed node by node due to the stiffness deterioration calculated from the Weibull regression equation (assumptions 1 and 2); hence, the ELSYM5 layered-elastic theory

program will be called up to analyze strain at each node. The environmental situation is assumed to remain the same during each hour.

7.1.2 Program Elements and Flow Charts

The central parts of the *Weibull* program are the "ELSYM5 strain engine" and the Weibull algorithm that has been discussed in previous sections. The strain engine is a modification of the original ELSYM5 program (Ahlborn 1972) to create an independent subroutine that can be called by the *Weibull* program to return the values of tensile strain whenever the layer stiffness is varied due to a change of the pavement temperature and stiffness deterioration. The *Weibull* program was written in FORTRAN 90 and compiled by the Microsoft FORTRAN Power Station 4.0. The following briefly describes the modules and their corresponding major subroutines. Figure 7.2 illustrates the relationship between the modules and subroutines.

- *Module Strain_Engine*

```
Module Strain_Engine
  use ELSYM5_Program
  use Link_List

  subroutine strain_calculation(infile_unit, infile, center, wander, nnz, &
                               stn, avgstn)
  subroutine make_image(center, old_x, old_stn, new_x, new_stn, d)
  subroutine mirror_array(center, n, old_array, new_array)
  function interpolation(point1, point2, xpos)
  subroutine reduce_matrix(nnz, nnxy, pe_array, new_array)
  subroutine find_array_strain(n, list, x, stn)
  subroutine find_array_maxpos(n, list, maxpos)
  subroutine find_array_avgstn(nz, nxy, list, avgstn)
```

This module calls up the other two modules, namely ELSYM5_Program and Link_List. This module provides a main subroutine, `strain_calculation()`, to calculate the intended maximum principal tensile strains.

- *Module ELSYM5_Program*

```
Module ELSYM5_Program
  subroutine tensile_strain(infile_unit,infile,nnz,nnxy,pe_array)
```

The main subroutine of this module is `tensile_strain()`. This subroutine is obtained by modifying the original ELSYM5 program to take the same ELSYM5 input file and return an array consisting of the principal tensile strains (including ϵ_1 , ϵ_2 , and ϵ_3) at the locations specified in the input file.

- *Module Link_List*

```
Module Link_List
  subroutine DelList(list)
  subroutine InsertFront(head,a,b)
  subroutine InsertBack(head,a,b)
  subroutine InsertBetween(head,PredPtr,CurrPtr,temp)
  subroutine InsertSort(head,a,b)
  subroutine WriteList(head)
```

This is the utility module that consists of several useful subroutines to manipulate the linked list. The six subroutines `DelList()`, `InsertFront()`, `InsertBack()`, `InsertBetween()`, `InsertSort()`, and `WriteList()` make up this module.

- *Module Equations*

```
Module equations
  subroutine read_in_equations(infile_unit,infile,wbl,stif)
  subroutine weibull_function(coef_wbl,n0,av,ac,vma,temp,rs4s50,m200,stn,delta_n,phi,dsr)
```

```

subroutine sum_table(coef_wbl,n,av,ac,vma,temp,rs4s50,m200,stn,sum,gamma)
subroutine stiffness_function(coef_stif,av,ac,vma,temp,stif)

```

The main purpose of this module is to read in and perform the calculation of the Weibull and stiffness regression equations. The disadvantage of this module resides in its inflexible arrangement of variables within regression equations. For the Weibull regression equation, we can only include the constant term `CONST` and the covariates (or independent variables) `AV`, `AC`, `VMA`, `TEMP`, `RS4S50`, `M200`, `LN(STN)`, `LN(N)`, and `LN(LN(N))`. As with the stiffness regression equation, the covariates included are `AV`, `AC`, `VMA`, and `TEMP`. The sequence of these covariates is very important because the input file of the regression equations is coded according to this order. And, the input format will be presented as a symmetrical matrix to incorporate the interaction terms.

- *Module ELSYM5_File_Modify*

```

Module ELSYM5_File_Modify

subroutine change_ELSYM5_input(infile_unit,infile,outfile_unit,outfile,stif)
subroutine go_through_ELSYM5(infile_unit,infile,center,nxy,nz,zout)
subroutine convert_char_to_number(string,number)

```

This module serves the purpose of changing the layer stiffness in the ELSYM5 input file whenever factors that affect stiffness exist, such as changes in temperature or traffic application.

- *Main Program Weibull_Simulation*

```

Program Weibull_Simulation

Use equations

```

```

Use Strain_Engine
Use ELSYM5_File_Modify

subroutine process_one_hour(infile_unit,infile,center,nz,nout,&
                           tb,g,sg,base,av,ac,vma,rs4s50,m200,&
                           coef_wbl,coef_stif,n0,traffic,&
                           cum_reps,phi,sr_old,sr_new,&
                           sr_old_nowander,sr_new_nowander,&
                           sr_old_avg,sr_new_avg,&
                           sr_old_nw_avg,sr_new_nw_avg)

subroutine process_one_node(infile_unit,infile,center,wander,&
                            sg,base,av,ac,vma,temp,rs4s50,m200,s0,&
                            nxy,nz,n0,dn,coef_wbl,cum_reps,phi,&
                            sr_old,sr_new,sr_old_avg,sr_new_avg,&
                            sr_old_nowander,sr_new_nowander,&
                            sr_old_nw_avg,sr_new_nw_avg)

```

The main program `Weibull_Simulation` utilizes three modules; `Equations`, `Strain_Engine`, and `ELSYM5_File_Modify`. It also contains two subroutines called `process_one_hour()` and `process_one_node()`.

The flowchart of the main program is briefly illustrated in Figure 7.3. As can be seen from this flowchart, the essential part is the subroutine `process_one_hour()`, which conducts all the calculations of stiffness ratio. The detailed flowchart of `process_one_hour()` is listed in Figure 7.4. From Figure 7.4, it is easy to see why these two main subroutines `process_one_hour()` and `process_one_node()` are named in such a way, for the algorithm is executed "hour-by-hour" and "node-by-node".

7.1.3 Scope of Simulation

- Pavement structure and range of simulation

Figure 7.5 represents the corresponding pavement structure, the loading configuration of a dual-tire, coordinate setup, and the intended strain-calculation points. Notice that the origin of this coordinate system is under the center of left tire. The depths used to calculate the strain are 1, 3, 5, and 5.99 inches below the surface (English units

are used here because of limitations of the ELSYM5 code). The horizontal points are located at 8, 9, 10, 11, 12, 13, 14, 15, 17, and 19 inches off the origin. In this chapter, the fatigue damage results for the asphalt layer will be presented in terms of a two-dimensional image-and-contour plot based on a total of 40 points, containing four depths multiplied by ten horizontal points.

- Simulation cases

The simulation cases cover only the 26 originally constructed test sections of the WesTrack project; the overlap and replacement sections are not included here. In addition, several simulation cases were run to verify the effect of traffic pattern, weather pattern, construction variability, and the correction factor. Construction variations include the effects of compaction, thickness, and asphalt content.

- Initial stiffness equations

The regression equation for initial stiffness used for the coarse gradation is

$$E(\ln \text{stif}) = 10.6586 - 0.2211 ac - 0.0607 av - 0.0633 temp + 0.0703 vma$$

(0.7081)
(0.0927)
(0.0095)
(0.0029)
(0.0306)

$$R^2 = 0.88.$$

The regression equation for initial stiffness utilized for the fine and fine-plus gradations is as follows:

$$E(\ln \text{stif}) = 11.3220 - 0.2133 ac - 0.0808 av - 0.0548 temp$$

(0.1941)
(0.0304)
(0.0055)
(0.0021)

$$R^2 = 0.87.$$

- Weibull equations

Two Weibull regression equations will be applied in the simulation, one for coarse gradation, the other for fine and fine-plus gradations.

For the coarse gradation, we have

$$\begin{aligned}
 E(\ln(-\ln(SR))) = & 105.8248 - 1.8679 av + 17.4844 \ln stn + 1.1902 temp - 10.3682 rs4s50 \\
 & \quad (8.6671) \quad (0.0793) \quad (0.8926) \quad (0.1702) \quad (1.2809) \\
 & - 8.8144 m200 + 4.8639 \ln(\ln(n)) - 0.1674 av \cdot \ln stn - 0.0110 av \cdot temp \\
 & \quad (0.6664) \quad (0.1027) \quad (0.0075) \quad (0.0009) \\
 & + 0.2041 av \cdot rs4s50 - 0.0237 av \cdot \ln(\ln(n)) - 0.0786 \ln stn \cdot temp \\
 & \quad (0.0097) \quad (0.0076) \quad (0.0030) \\
 & - 1.5698 \ln stn \cdot rs4s50 - 1.3200 \ln stn \cdot m200 - 0.2416 temp \cdot rs4s50 \\
 & \quad (0.1303) \quad (0.0701) \quad (0.0262) \\
 & - 0.1082 temp \cdot m200 - 0.0534 temp \cdot \ln(\ln(n)) \\
 & \quad (0.0129) \quad (0.0036)
 \end{aligned}$$

$$R^2 = 0.83.$$

For the fine and fine-plus gradations, we have

$$\begin{aligned}
 E(\ln(-\ln(SR))) = & -55.4911 + 7.0102 ac + 0.6083 av + 0.4755 temp - 1.3899 \ln stn \\
 & \quad (4.2948) \quad (0.5779) \quad (0.0558) \quad (0.0922) \quad (0.3329) \\
 & + 7.0609 rs4s50 + 0.9143 m200 + 8.0053 \ln(\ln(n)) - 0.0528 ac \cdot av \\
 & \quad (1.0012) \quad (0.2540) \quad (0.4530) \quad (0.0027) \\
 & - 0.0753 ac \cdot temp + 0.1186 ac \cdot \ln stn - 1.0103 ac \cdot rs4s50 \\
 & \quad (0.0035) \quad (0.0214) \quad (0.1395) \\
 & - 0.2657 ac \cdot m200 + 0.0908 ac \cdot \ln(\ln(n)) - 0.0045 av \cdot temp \\
 & \quad (0.0292) \quad (0.0241) \quad (0.0003) \\
 & + 0.0177 av \cdot \ln stn - 0.0266 av \cdot rs4s50 - 0.0057 av \cdot m200 \\
 & \quad (0.0040) \quad (0.0111) \quad (0.0026) \\
 & + 0.0340 av \cdot \ln(\ln(n)) - 0.0776 temp \cdot \ln stn - 0.1069 temp \cdot rs4s50 \\
 & \quad (0.0045) \quad (0.0017) \quad (0.0169) \\
 & - 0.0296 temp \cdot m200 - 0.0661 temp \cdot \ln(\ln(n)) + 0.4191 \ln stn \cdot rs4s50 \\
 & \quad (0.0054) \quad (0.0019) \quad (0.0705) \\
 & + 0.1871 \ln stn \cdot m200 + 0.5835 \ln stn \cdot \ln(\ln(n)) + 0.8220 rs4s50 \cdot m200 \\
 & \quad (0.0192) \quad (0.0307) \quad (0.0329) \\
 & + 0.2449 rs4s50 \cdot \ln(\ln(n)) + 0.1018 m200 \cdot \ln(\ln(n)) \\
 & \quad (0.0879) \quad (0.0230)
 \end{aligned}$$

$$R^2 = 0.91.$$

- Traffic file

Please refer to Appendix E for the details of input format. The traffic file contains the hourly magnitude and wander positions of trafficking, from 3/3/96 to 9/3/98, for a total of 21,943 hours.

- Environment and material file

The input format of the environment and material file is described in Appendix E. It contains the information of material properties, such as *av*, *ac*, *vma*, *rs4s50*, and *m200*, and the environmental variables, such as temperature at the bottom of asphalt concrete layer, the temperature gradient, and the stiffness of base and subgrade. The duration of the file is the same as that of the traffic file. The material properties of the Weibull simulation are listed in Table 7.1.

- Correction factor

The correction factor that adjusts for the difference of boundary conditions between laboratory and field is assumed to be 1.0, for there is no way to confirm this factor from the WesTrack data. The effect of the correction factor on fatigue performance predictions will be discussed later in this chapter.

7.1.4 Failure Criterion

Conventionally, the fatigue life in the laboratory fatigue test is defined as the number of repetitions at the time when the stiffness reaches its 50 % deduction. It is also believed that the distinguishable macrocrack might initiate at this moment based on the experience of conducting the fatigue tests and according to the SHRP fatigue report-A404 (Tayebali 1994). The main goal of using the dynamic approach of Weibull is to determine the crack initiation time of a crack forming from the bottom up to the surface of an asphalt concrete pavement. Since the outcome of the Weibull approach can be expressed with a two-dimensional stiffness ratio image-and-contour plot, it makes it possible to identify the location and time of crack initiation, if the failure criterion is defined as the stiffness ratio reaching 0.5.

7.1.5 Stiffness, Temperature, and Stiffness Ratio

In this Weibull approach, the stiffness ratio is used as an index of fatigue damage. Once the stiffness ratio reaches a certain level, it is said that the crack initiation will occur. The assumption postulated in this Weibull approach is that the fatigue damage of asphalt concrete cannot be recovered once damaged. However, keep in mind that the stiffness ratio is defined as $S(n, \underline{X}, T)/S(0, \underline{X}, T)$, where $S(n, \underline{X}, T)$ is the stiffness of asphalt concrete with mix properties \underline{X} at loading repetition n subjected to temperature T ; when n equals zero means the initial stiffness at temperature T .

It has been identified that temperature affects the stiffness of asphalt concrete. The asphalt concrete loses stiffness at higher temperatures and conversely gains strength when the temperature cools down. Thus both temperature and stiffness varies with time, and the value of stiffness is a relative quantity rather than an absolute one. The Weibull

approach utilizes, instead of an absolute stiffness, the stiffness ratio. But, in the calculation of tensile strain, the ELSYM5 program needs an absolute stiffness as an input. To solve this discrepancy, an algorithm needs to be provided to take into account not only the temperature variation but also the stiffness deterioration. It is important to note that this algorithm must be developed maintaining the first assumption above.

Figure 7.6 will be used to demonstrate the relationship between stiffness ratio and initial stiffness. Two stiffness deterioration curves of laboratory fatigue tests with the same mix are shown in this figure. One is the $S^*(n, \underline{X}, T_2)$ curve at temperature T_2 and the other is the $S(n, \underline{X}, T_1)$ curve at temperature T_1 . Now, if the fatigue test starts at the $S(n, \underline{X}, T_1)$ curve and stops after n_1 applications, then the stiffness ratio will decrease from 1.0 to, say, R_1 . Afterward, if the temperature changes from T_1 to T_2 , then the stiffness will jump from $S(n, \underline{X}, T_1)$ to $S^*(n, \underline{X}, T_2)$. However, before any loading is applied, the stiffness ratio is assumed to maintain at R_1 , that is, the stiffness $S^*(n_1, \underline{X}, T_2)$ equals to $S^*(0, \underline{X}, T_2) \cdot R_1$. Notice that $\Delta S = S^*(n_2, \underline{X}, T_2) - S^*(n_1, \underline{X}, T_2)$. When we divide this equation by $S^*(0, \underline{X}, T_2)$, we obtain the difference of stiffness ratio ($\Delta R_{1 \rightarrow 2}$) along the $S^*(n, \underline{X}, T_2)$ curve after applying $n_2 - n_1$ loading repetitions. Hence, at loading repetition n_2 , the stiffness ratio will be $R_2 = R_1 + \Delta R_{1 \rightarrow 2}$. One thing should be pointed out; most of time the conventional stiffness equation obtained from laboratory fatigue tests is meant to be the "initial stiffness", defined as the stiffness at repetition 50 and a function of either material or environmental variables. In the Weibull program, the stiffness at any loading repetition and any temperature will be calculated based on the

present stiffness ratio and the conventional initial stiffness regression equation described above.

7.1.6 Stiffness as an Input

One of the drawbacks of utilizing the linear layered-elastic program is that it can only input one stiffness value to represent the stiffness of the entire layer. This ignores the fact that, because of distance from the load, temperature, or the wander effect, the strains experienced in the layer are varied point by point; consequently, the stiffness deterioration should be diverse point by point as well. To mend this inconsistency, it was decided to use the average strains in one layer to calculate the stiffness deterioration for the Weibull regression equation and then to convert the stiffness ratio into stiffness based on the stiffness equation. The stiffnesses obtained were input for the next loading cycle. In sum, the Weibull program is compromised because of the restrictions of the linear layered-elastic program. However, instead of using the minimum strain or the maximum strain to calculate the input stiffness, the mean strain utilized here should be more statistically appropriate.

7.1.7 Wander Consideration

Instead of having channelized traffic, the wander distribution of tires on a highway cross section is distributed normally. For a specified position at the bottom of asphalt concrete layer, the tensile strain encountered will vary with time and wander position. The difference in fatigue damage that is accumulated due to the various strains encountered, compared with the constant strain of the no-wander case, is therefore termed

as the "wander effect". The effect of wander on the fatigue performance is significant; this has already been demonstrated in the discussion in Chapter 6 utilizing the Miner's law. However, without considering the stiffness deterioration of the pavement itself and including high temperature fatigue information, it seems the Miner's approach is too conservative. That is to say, the correction factor for wander, defined as the ratio of repetitions of no-wander divided by repetitions of wander, tends to be too high. Here, the author would like to further extend the definition of the correction factor of wander effect in the following way:

Definition: wander effect

For two given associated stiffness deterioration curves and a specific SR, the wander effect will be measured with the magnitude of the correction factor of wander that is defined as $\phi_w = \frac{N_{wander}}{N_{no\ wander}}$, where N_{wander} is the repetitions at the specific SR of wander curve; $N_{no\ wander}$ the repetitions at the specific SR of no wander curve.

The term "associated" in this definition means that the stiffness deterioration curves are calculated for the same location in the pavement structure for comparison. For the simulations of WesTrack, the location was chosen as the weakest point of the no-wander case after the whole simulation.

The *Weibull* program will take traffic and wander as input along with the other input files and compute the stiffness ratios both for the wander and no-wander cases. The way to calculate the tensile strain due to the wander at a specified position has already been illustrated in Figure 6.18 of Chapter 6.

7.1.8 Vehicle Speed and Stiffness

The frequency sweep test is utilized to define the master curves of the material of interest, especially an assumed thermorheologically simple material such as asphalt concrete. A typical result from the frequency sweep test is schematically shown in Figure 4.28, which illustrates the relationship between loading frequency (or loading time) and complex moduli at various reference temperatures. Thus, for a specific asphalt mix, the complex modulus depends not only on the temperature but also on the loading time. On highways, the various vehicle speeds will result in different loading times on the asphalt pavement; accordingly, the asphalt pavement will respond differently in stiffness, if temperature remains unchanged.

As shown in Figure 4.28, loading time or frequency and the stiffness of asphalt concrete exhibit a nonlinear relationship, which is characteristic of a viscoelastic material. This nonlinear relationship seems to be appropriately described by the Gamma function presented in Chapter 4.9.2. Note that these complex moduli could be regarded as the initial stiffness without any consideration of deterioration due to traffic loading, because the curves were from the nondestructive frequency sweep test. Once the initial stiffness was represented by the material variables, temperature, and loading time (vehicle speed which can be fit using a gamma distribution as discussed in Chapter 4.9.2), the same issue arose as discussed in Chapter 7.1.5: initial stiffness versus stiffness ratio, and its affect on the fatigue performance of asphalt concrete. In this study, the effect of loading time (or vehicle speed) is not corrected during the simulation.

7.1.9 Traffic Wander, Traffic Composition, and Vehicle Speed

The traffic encountered on a highway, which includes many types of trucks, many tire configurations, and varying speeds over its service life, has randomness as its chief characteristic. The traffic features most related to the design of pavement, in general, are traffic wander, traffic composition (including truck type, tire configuration, tire pressure, etc.), and vehicle speed. The Weibull dynamic approach introduced in this study improves the prediction of the fatigue performance in a step-by-step recursive way and makes it possible to integrate the traffic characteristics into the simulation. The details of constructing a random sequence of traffic are demonstrated in Appendix E: *The Weibull User's Manual*. However, generating a random pattern of traffic is not included in this version of *Weibull* program, since the main goal of this study is to attempt to reproduce by analytical means the phenomenon observed in WesTrack.

7.2 Simulation Results of WesTrack

For this version of the *Weibull* program, the stiffness deterioration history of every point described in the ELSYM5 input file is monitored. Figure 7.7 gives a wander example of all the stiffness deterioration curves arranged in various depths at different offsets of Section 3. As seen in this figure, at offsets of 8, 9, 10, and 19 inches, more stiffness deterioration has accumulated at a depth of 1 inch than at a depth of 3 inches. This indicates that at those offsets the material experiences tensile strain on top of asphalt concrete layer and thus accumulates more fatigue damage. The *Weibull* program makes it possible to monitor the stiffness deterioration history of any point in pavement. Also

note how the stiffness curves show rapid deterioration at the early trafficking stage and slowing thereafter.

The temperatures at the bottom of the asphalt concrete at WesTrack are plotted against the cumulative traffic in Figure 7.8a. The horizontal sections of the cumulative traffic curve are when no traffic has been applied during those time periods. The slope of the cumulative traffic curve represents the rate of cumulative traffic. The steeper the slope, the more traffic was applied. The weakest point of the wander case is located at an offset of 12 inches and a depth of 5.99 inches. Its stiffness deterioration curve is plotted with the cumulative traffic curve in Figure 7.8b. It should be noted that almost 30 % of stiffness deduction occurs at the first two months which cover the temperatures from 0°C to 30°C. After this period, the rate of stiffness deterioration slows even if there is a combination of hot temperature and heavy trafficking.

The image-and-contour plots of SR of the 24 WesTrack sections (Sections 3 and 8 excluded) after 21943 hours of simulation with wander and no wander are presented and attached in Appendix B from Figure B.7.1 through Figure B.7.24. Figures 7.9 and 7.10 display the image-and-contour plots of SR of Sections 3 and 8 respectively. For all the 26 test sections, the values of SR at the weakest points of the wander and no wander cases after simulation are listed in Table 7.2. Bear in mind that the simulations were conducted with a correction factor of 1.0.

For the WesTrack traffic pattern, the stiffness deterioration pattern at the bottom of the asphalt concrete layer seems to be no difference for the wander and no-wander cases no matter which mixes are used. By inspecting the stiffness deterioration curves of all 26 test sections at the weakest points of the no-wander cases, as seen in Figures 7.11

through 7.13, it was found that no obvious wander effects exist in the mixes of coarse gradation and only slight wander effects are observed in the mixes of fine and fine-plus gradations.

This contradicts the results observed in Miner's approach of Chapter 6. The wander effect is hardly perceived; the correction factor for the wander effect, ϕ_w , is always greater than 1.0 and close to 1.0 for these simulations. This can also be seen in Table 7.2 where the final SR values of the wander cases are always higher than the values of the no-wander cases. As a weak inference, this suggests that traffic with wander will cause less fatigue damage as compared to channelized traffic. It might be conjectured that, for the specific traffic pattern at WesTrack, the main reason for no obvious wander effect is because about one-tenth of traffic was applied at the central position (no-wander position), which resulted in no difference between wander and no-wander during the early service-life of the pavement when fatigue damage accumulates quickly whatever the environment and material factors.

Another interesting phenomenon observed is that the final stiffness deterioration patterns for the wander and no-wander cases for a given section look very similar. The only perceived difference is that less fatigue damage accumulated under the tire of the no-wander cases. When looking at the image-and-contour plots, something that should be in mind is that stiffness deterioration is caused by fatigue damage and the fatigue damage is caused by the tensile strain. This phenomenon also gives indirect support to the proposed explanation of the lack of wander effect. Because the traffic was applied at the central position in the early service life of pavement, most of the fatigue damage was

accumulated there and a stiffness deterioration pattern was set in place. The extra trafficking thereafter had less effect in determining the stiffness deterioration pattern.

The condition survey data of fatigue damage at the WesTrack project and the final SR deterioration results from Weibull simulation are listed in Table 7.3. In addition, the Table 7.3 also lists the date and hour when the SR reached 0.8 and 0.6. According to the condition survey data and the SRs at 0.8 and 0.6, three figures were plotted to explore the relationship between the predictions and the condition survey. For the sections with the coarse gradation, several findings were observed:

1. As seen in Figure 7.14, the 10 % fatigue cracking occurred only at the sections with air-void contents greater than 8.0 % and at the first winter. The 50 % fatigue cracking was developed quickly once the 10 % fatigue cracking had been reached. It implies that the cold weather is an important factor in crack propagation. The Weibull simulation fails to describe the quick crack propagation during winter for the coarse mixes and the importance of including a crack propagation model in the Weibull simulation is clearly demonstrated.
2. The rankings of the simulation results for those sections with cracks, if one looks carefully at Table 7.3, is almost the same for those with 10 % cracking and 50 % cracking.
3. For the simulation results of SR, if 0.5 is the value set for the failure criterion, then none of the simulation results of SR show the failure. This indicates that a Weibull simulation without an additional model will not model the crack propagation phenomenon, especially during a cold winter. Although it can be

argued that the simulation results of SR are capable of being modified by the correction factor, the prominent fact is that the lack of crack propagation model is a significant deficiency for the Weibull dynamic approach.

For the fine and fine-plus gradations (as illustrated in Figures 7.15 and 7.16), the observations can be summarized in the following:

1. The 10 % fatigue cracking only occurred on the sections with air-void contents greater than 10 % for both the fine and fine-plus gradations. A notable counterexample is fine-plus test section 20 which had a 10.9 % air-void content but no cracking.
2. The 10 % fatigue cracking was observed at the second or the third year for the fine gradation but it occurred at the first winter for the fine-plus gradation. Notice that all the cracking sections had air-void contents greater than 10 %.
3. The 50 % fatigue cracking only occurred at Sections 3 and 10 in the second winter.
4. The ranking of the final SR values is not consistent with the ranking of the 10 % and 50 % cracking-developed time.
5. The fine-plus gradation takes longer time to have the crack propagation to go from 10 % cracking to 50 % cracking as compared with the fine gradation.

These observations reinforce the importance of the incorporation of a crack propagation model. The mechanism of crack propagation is not so simple as the crack

initiation. The crack propagation rate may be a complex function of temperature, traffic, material properties, and pavement structure.

In sum, the lessons that have been learned from this simulation are as follows:

1. The rate of stiffness deterioration is higher in the early trafficking stage and slows thereafter.
2. Fatigue damage accumulates quickly at the early stage of trafficking. Thus, long-term fatigue performance may be determined significantly by the temperature range and the pattern of trafficking in the early service life of the newly constructed pavement.
3. No obvious wander effect was observed for this specific WesTrack traffic pattern.
4. The Weibull simulation results are generally consistent with the condition survey data for the fatigue damage within the same gradation type.
5. It seems that the Weibull dynamic approach cannot capture the mechanism of surface cracking because the approach, for the time being, only includes the consideration of the crack initiation and excludes the crack propagation. From this simulation, it was recognized that a combination model of crack initiation and crack propagation should be seriously considered in the future.

Conclusions (1) and (2), although contradicted in beam tests, match well to, for example, Chapter 5.7.3 from the 503RF study.

7.3 Traffic Pattern and Simulation

The term “traffic pattern” might be seen elsewhere with different definitions. The definition the author uses herein is as follows:

A traffic application can be characterized by three variable elements: loading configuration, wander location, and vehicle speed. Where the total number of traffic applications remains constant for a fixed time interval, a “traffic pattern” will consist of sequentially ordered traffic applications with any combination of these three variable elements.

A term “modified traffic pattern” will be utilized along with “original traffic pattern” to emphasize the differences in loading sequences. To confirm the hypothesis in Chapter 7.2 that no wander effect is observed because the traffic was applied in the center position at the early service life of the pavement, two simulations with a correction factor of 1.0 were run at Sections 3 and 8 respectively. From the laboratory fatigue tests, it is recognized that the stiffness deterioration curve accumulates the fatigue damage quickly in the early loading stage, especially for the tests with higher strain level. Thus, it is naturally inferred that the early traffic pattern applied on the pavement will control the damage rate of the pavement for the rest of its life.

To further explore this, a “modified traffic pattern” was formed by moving the data for the first 3,000 hours from the beginning to the end of the traffic file. The proportion of the traffic applications during this 3,000-hours period is about one tenth of the total applied traffic. For this case, the total applied traffic remains unchanged and the pavement will not experience channelized traffic at the beginning of its service life.

The results of the modified traffic pattern applied to the Section 3 final stiffness deterioration data are shown in Figures 7.17a and 7.17b, separately, for wander and no-wander cases. As compared with the results of original and modified traffic patterns, several observations of the final stiffness deterioration patterns of wander and no-wander cases can be summarized below:

1. In sum, the modified traffic pattern causes less deterioration of the asphalt concrete layer.
2. The SR values that occur at a 1-inch depth with wander seem to have a decreasing trend from left to right; but, the fatigue damage caused by original traffic pattern at this depth deteriorates more at the two far ends.
3. The modified traffic pattern created a very different pattern of stiffness deterioration with wander, as visualized in Figure 7.9a.

The difference that appeared in the no-wander cases, as seen in Figures 7.17b and 7.9b, is primarily in the degree of deterioration; the final stiffness deterioration patterns are similar.

Figure 7.18 presents the plot of SR against time at the location with an offset of 12 in. and depth of 5.99 in. This is the weakest point that occurs in a no-wander case subjected to the original traffic pattern. As can be clearly viewed in this figure, there is a wander effect under the modified traffic pattern. The stiffness deterioration curves also vary at the early trafficking stage for the original and modified traffic patterns.

The same conclusions obtained from test section 3 apply to test section 8. The stiffness deterioration patterns of final SR values, with wander and no-wander cases, are

illustrated separately in Figure 7.19a and 7.19b. The only difference is that for the modified traffic pattern, no wander effect can be seen (Figure 7.20). In other words, the mix at test section 8, is insensitive to the wander effect of that traffic pattern.

Therefore, two general conclusions can be made from this simulation:

1. The traffic pattern will affect the stiffness deterioration curve and the final stiffness deterioration pattern.
2. The asphalt-aggregate mix can be either sensitive or insensitive to the wander effect caused by various traffic patterns.

Therefore, the hypothesis proposed at the beginning of this chapter—that no obvious wander effect is observed because a significant portion of the traffic was applied in the center position during the early service life of the pavement—has been supported through the application of a modified traffic pattern analysis.

7.4 Weather and Simulation

The fatigue test results of this study show that the stiffness deteriorates quickly at low to intermediate temperatures and that most fatigue damage accumulates during the early loading stage. Consequently, it is suspected that the start time of trafficking after the construction of a pavement is significantly associated with the fatigue performance over its life span for the two year life span of WesTrack. To verify such a hypothesis, the original temperature spectrum of WesTrack was modified so that the traffic loading was presumed to start in the early summer. In doing so, the first 1,440 hours of temperature data (i.e., the first 2 months) was eliminated from the original temperature file. To utilize

the full traffic load spectrum, those blank temperatures were supplied with the temperatures from the same dates in the previous year.

As previously, the simulations were applied to Section 3 (fine gradation) and the Section 8 (coarse gradation). The applied correction factor remained one. The original traffic pattern was utilized herein so as to verify the main effect of the weather pattern.

As discussed in the previous section, the traffic pattern will affect the final pavement deterioration pattern. For the original traffic pattern, the channelized traffic applied in the early service life of the pavement makes no obvious wander effect. Although the weather pattern has been modified, the final pavement deterioration patterns, as seen in Figures 7.21 and 7.23, still look quite similar for the wander and no-wander cases. It implies that the final pavement deterioration pattern is mainly determined by the traffic pattern.

While subjected to the original traffic pattern, the modified weather pattern deteriorates the stiffness of both Sections 3 and 8 more quickly than the original weather pattern, as can be seen in Figures 7.22 and 7.24. Also note that there is almost no wander effect for both mixes.

7.5 Traffic and Weather Effects

From the simulation of the ELSYM5 results, it was found that the relationship among temperature, stiffness, and fatigue life is usually as follows:

1. In general, for a mix, the high temperatures will cause low stiffnesses and thus induce a high strain level at the bottom of the asphalt concrete layer.
2. Low temperatures will cause high stiffnesses and thus induce low strains.

However, it can also be recognized from the fatigue analysis of Chapter 4 that the same mix experiences less fatigue damage, meaning longer fatigue life, at higher temperatures; vice versa, more fatigue damage occurs at lower temperatures for a given strain. In addition, the fatigue test results show that a low strain level always accompanies a longer fatigue life. It is confusing that the fatigue test results seem to contradict the statements from the ELSYM5 analyses. To resolve this confusion, it is better to examine fatigue life from the viewpoint of temperature effect and strain effect rather than from the viewpoint of literal understanding. In other words, for any mix, its fatigue life is determined by temperature and strain. Both effects and, if possible, the interaction of the two need to be estimated quantitatively to determine which effect is dominant. Thus, it is important to take into account both traffic and weather effects in running a simulation or designing a pavement. It should be noted that the traffic pattern is strain-related and the weather pattern is temperature-related.

To further verify the main and/or interaction effects made by the traffic and weather on fatigue performance, several simulations were conducted. Sections 3 and 8, were chosen as representative sections. The applied correction factor remained one. The modified traffic pattern was the same file defined in Chapter 7.3. The modified weather file is the same file utilized in Chapter 7.4.

In Figure 7.25a, the final pavement deterioration pattern for Section 3 is similar to the pattern with modified traffic only, as shown in Figure 7.17a. The only deviance is that the pavement deteriorates more under the combined effect. From Figure 7.25b, no considerable difference is perceived in the final pavement deterioration pattern of the no-

wander case. It is interesting to note that the final pavement deterioration pattern seems to be affected only by the type of traffic pattern and not by the weather pattern.

Figure 7.26 illustrates the stiffness deterioration curves under the effect of either traffic, weather, both, or none in the same figure. The same location, which is the weakest point of the no-wander case with the original traffic and weather patterns, was chosen for comparison for all these stiffness deterioration curves. Several findings shown in this figure can be summarized :

1. With the modified traffic alone, the stiffness deterioration is less than that without any traffic or weather effects.
2. With the modified weather alone, the fatigue damage is greater than that without any traffic or weather effects.
3. When both the modified traffic and weather patterns are applied, the fatigue damage is the greatest among all the simulation cases.
4. The wander effect is prominent only in those simulations with the modified traffic pattern. That with the weather effect alone does not show any wander effect.
5. Under the application of original weather pattern, the modified traffic pattern reduces the fatigue damage, whereas the modified traffic pattern accelerates the fatigue damage when subjected to the modified weather pattern. This indicates that the traffic and weather patterns must be considered simultaneously when a pavement is designed.

As for Section 8, Figure 7.27 plots the pavement deterioration of the wander and no-wander cases and Figure 7.28 presents the stiffness deterioration curves with traffic and weather effects. The same conclusions from Section 3 apply to Section 8. One obvious discrepancy is that no wander effect is perceived, no matter which type of traffic or weather pattern is applied. Again, the simulation results tell us that the wander effect is mix-dependent.

7.6 Construction Variability and Simulation

Construction variability can be attributed to variations in the degree of compaction, reflecting differences in the percent of air-void content, the thickness of asphalt concrete layer, and the percent of asphalt content. In the following sections, these construction variations will be discussed with the Weibull simulation results. The simulations were applied to the Sections 3 and 8 with a correction factor of 1.0. The modified traffic pattern and the original weather pattern were utilized in the simulations.

7.6.1 Degree of Compaction

Among the construction variables, the degree of compaction is the most susceptible to construction practices. Generally, the percent air-void content may be reduced to some degree by traffic, resulting in a more capable fatigue-resistant mix. This is so called "traffic compaction". Shin (1999) inspected the air-void contents of WesTrack field cores and found out that the air-void contents were considerably reduced after 9 months of traffic loading (as listed in Table 7.4). As can be seen in the table, the

fine-plus gradation had the most percentage reduction among the gradations and in general the bottom lift had less reduction of air-void content than the top.

Table 7.4. Percentage reduction of air-void contents of WesTrack after 9 months of traffic loading.

	Coarse		Fine		Fine-plus	
	mean	Std. Dev.	mean	Std. Dev.	mean	Std. Dev.
AV_TOP (75mm)	39.5	20.1	35.7	13.1	48.7	16.7
AV_BOTTOM (75mm)	29.2	10.7	32.0	14.4	38.6	13.5

Although this phenomenon can be simulated in this version of Weibull program, here the author will focus on the simulation of the initial degree of compaction. The WesTrack Sections 3 (fine, AV = 12.4, AC = 4.97) and 8 (coarse, AV = 8.5, AC = 5.47) will be used as the demonstration examples of the AV effect. Two air-void contents, 10.4 % and 14.4 %, will be applied to Section 3, i.e., ± 2 % off the original air-void content. Two air-void contents, 6.5 % and 10.5 %, will be applied to Section 8.

The pavement deterioration results of various air-void contents are shown in Figure 7.29 and Figure 7.30, respectively, for 10.4 % and for 14.4 %. In general, the pavement with high air-void content displays more fatigue damage than that with low air-void content.

Figure 7.31 displays the stiffness deterioration curves with various air-void contents for Section 3. With a difference of only 2 % in air-void content, the stiffness deterioration could be very different. In general, higher air-void contents causes more fatigue damage.

The pavement deterioration patterns of Section 8 at various air-void contents are displayed in Figure 7.32 and Figure 7.33, separately, for 6.5 % and 10.5 %. It is obvious that fatigue damage at 10.5 % is more considerable than that at of 6.5 %.

The stiffness deterioration curves with various air-void contents are drawn and summarized in Figure 7.34. Notice that no wander effect is presented for various air-void contents, although the same modified traffic pattern has caused the wander effect for Section 3. The degree of stiffness deterioration seems to be proportional to the value of air-void contents. The higher the air-void content, the greater the stiffness deterioration. Accordingly, it is recognized that quality control of compaction in constructing the pavement is very important, as many previous researchers have pointed out. It should be noted that in this simulation case the traffic compaction is not considered.

7.6.2 Thickness of the Asphalt Concrete Layer

The designed thickness of asphalt concrete layer of WesTrack is 6 inches. Now, it is assumed that the thickness is ± 1 inch from the designed value due to the construction variation. Herein, the temperature at the bottom of the asphalt concrete layer and its corresponding temperature gradient remain unchanged whatever the thickness will be. The depths of the ELSYM5 input are then 1.0, 3.0, 4.5, and 4.99 inches for a 5-inch layer; 1.0, 3.0, 5.5, and 6.99 inches for a 7-inch layer. The 5-inch layer contains three sublayers with the thickness, 2.0, 2.0, and 1.0 inches from surface below. The 7-inch layer has three sublayers with thickness 2.0, 2.0, and 3.0 inches from surface below.

The image-and-contour plots of the final pavement deterioration of WesTrack Section 3 of various thicknesses with wander and no wander are presented in Figures 7.35 through 7.37. Figures 7.39 through 7.41 illustrate the corresponding image-and-contour plots of pavement deterioration of WesTrack Section 8. An interesting phenomenon extracted from these figures is that the pattern of stiffness deterioration at depth 1.0 inch for each section is similar along the horizontal direction no matter what thickness. In general, the fatigue damage at the bottom of the asphalt concrete layer depends on the thickness of the layer. The thinner the layer, the more the fatigue damage at its bottom.

The stiffness deterioration curves at an offset of 12 inches and at the bottom of the asphalt concrete layer are plotted in Figures 7.38 and 7.42 for Sections 3 and 8 respectively. It was found that the wander effect in Section 3 not only varies with time but also changes with the thickness of the asphalt concrete layer. On the contrary, in Section 8, no wander effects are perceived no matter what thickness. In addition, the results also show that the stiffness deterioration curves of Section 8 have only little fluctuation relative to the thickness variation, whereas the curves of Section 3 vary significantly relative to the thickness variation; the magnitude of variation is inversely proportional to the thickness of the asphalt concrete layer.

In sum, the findings of the thickness simulations can be listed below:

1. The thickness effect due to construction variation is mix-dependent.
2. A thinner layer displays exaggerated wander effect and deteriorates faster.
3. The coarse mix seems to have the better capacity to resist the thickness effect.

Finding 3 above, may be due to the higher stiffness of the coarse mix and thus smaller strains. To further verify this point, Section 15 (fine) was selected as a comparison with Section 8 (coarse) because both sections have similar air-void contents and asphalt contents. Figures 7.43 and 7.44 display the average tensile strains at the bottom of the asphalt concrete layer with the modified traffic pattern. As seen in these figures, the strain patterns are matched to the temperature pattern, i.e., a higher temperature results in a higher tensile strain. Also, with the consideration of stiffness deterioration, the strain at hot weather increases as the damage increases; the strain at cold weather decreases as the damage increases. Section 15 generally showed higher strains than those of Section 8; however, the difference reduces as the damage increases (as seen in Figure 7.45). Also, the difference of strains is larger in cold weather than in hot weather.

7.6.3 Asphalt Content

A variation of ± 0.5 % asphalt content off the designed value was applied to simulations of Sections 3 and 8 so as to simulate fluctuation of asphalt content due to construction variation. The original designed values of asphalt content for Sections 3 and 8 were 4.97 % and 5.47 % respectively.

Figure 7.46 displays the final pavement deterioration of Section 3 with AC = 4.47 %. As compared with the no wander case, the wander case has less fatigue damage along the bottom of the asphalt concrete layer. For this specific traffic pattern, the serious damage of the wander case occurs at a location of offset = 8 inch, depth = 5.99 inch; for the no-wander, it happens at a location of offset = 12 inch. The same observation, as

visualized in Figure 7.47, is applied to Section 3 with AC = 5.47 %. While comparing these two figures, it is found that the Section with less asphalt content has less fatigue damage. When the stiffness deterioration curves with asphalt contents of 4.47 %, 4.97 %, and 5.47 % are plotted together in Figure 7.48, it is easy to identify the effect of asphalt content caused by construction variation. The distance between the wander and no-wander curves seems to be proportional to the value of the asphalt content.

Unlike the clear pavement deterioration patterns of various asphalt contents for Section 3, it is hard to tell the difference of fatigue damage developed along the bottom of the asphalt concrete for the wander and no-wander cases of Section 8, as seen in Figure 7.49 and 7.50. The same conclusion can be drawn if plots are jointly made of the stiffness deterioration curves with asphalt contents 4.97 %, 5.47 %, and 5.97 %. In Figure 7.51, the stiffness deterioration curves with various asphalt contents are overlapped indistinctly. Therefore, the effect of asphalt content to the fatigue performance is definitely mix-dependent.

7.7 Correction Factor and Simulation Results

To accurately predict the surface cracking due to fatigue damage is the ultimate goal of utilizing the laboratory fatigue test results and conducting a simulation such as the Weibull dynamic approach proposed herein. The use of the correction factor to bridge the difference between laboratory test results and in situ performance is unavoidable. The crack development due to fatigue damage consists of two phases, crack initiation and crack propagation. Therefore, the correction factors should be applied at each stage, for it is suspected that the mechanism of crack propagation is different from the mechanism

of crack initiation. However, at present there is a lack of both an appropriate test setup and the associated fatigue test results for analyzing crack propagation so it is beyond the scope of this research.

Table 7.5, lists the most likely components of a correction factor for the crack initiation and crack propagation. The correction factor for crack initiation can be decomposed into the following components: temperature, strain, mix properties (mainly the AV) or traffic compaction, support conditions, loading frequency, loading configuration, rest period, wander, aging, and water damage. The most significant correction factors for crack propagation might be thermal strain and stiffness damage. In addition, all the factors for crack initiation might apply; however, this needs to be confirmed in future studies. For every component listed in Table 7.5, a suitable correction factor should be applied in the prediction procedure. Note that the three categories are listed in Table 7.5, namely accelerated controlled-strain laboratory fatigue test, full-scale pavement test, and in situ pavement. Generally, the correction factor is applied in one way, i.e., from the laboratory test to full-scale pavement test, from laboratory test to in situ pavement, or from full-scale pavement to in situ pavement. It is not reasonable to apply a correction factor in a reverse way such as from in situ pavement to laboratory test. As for the magnitude of the correction factor, it could be varied component by component and case by case.

Now, if the total correction factor of a simulation case can be represented as a function of various sub-correction factor, i.e., $\phi_{Total} = f(\phi_{ij})$, where $i = 1, \dots, n$ and $j = 1, \dots, n$, assuming that the relationship is restricted to the main effect and two-term interaction effects. Then the question raised will be, what are the relationships among the

correction factors ϕ_y s. The possible relationship among these correction factors, would need to be systematically verified by data from either full-scale pavement testing or an instrumentation-monitored in-field pavement.

In Chapter 5, a correction factor derived by the Weibull accelerated failure time model is given to indicate the difference caused by the boundary conditions provided that the in situ fatigue damage also follows the Weibull assumption. Actually, this “boundary conditions” correction factor is an ambiguous aggregated factor. Rather than give the complete details of all correction factors, the purpose of utilizing the Weibull accelerated failure time model is to propose a possible way to correct the “boundary conditions”. The simulation here is restricted to only the correction factor of the “boundary conditions” up to crack initiation, and does not include any correction factor for crack propagation.

The simulations were conducted with Sections 3 and 8 with the correction factors 0.8 and 1.2. The modified traffic pattern and the original weather pattern will be applied in the simulations.

Figure 7.52 plots the final pavement deterioration of SR of Section 3 with a correction factor of 0.8 for both the wander and no-wander cases. Figure 7.53 illustrates the pavement deterioration with a correction factor of 1.2. As visualized in these figures, the higher the value of the correction factor the less the fatigue damage. The corresponding stiffness deterioration curves of Section 3 for various correction factors are displayed in Figure 7.54. The stiffness deterioration curve with a correction factor of 0.8 has an astonishing shape, starting with a sharp drop and then suddenly turning to a flat

line around $SR = 0.45$. The smaller correction factor will cause more fatigue damage. Meanwhile, the wander effect is exaggerated by the smaller correction factor.

The same simulation results and conclusions can also be fitted to Section 8. As seen in Figure 7.57 the stiffness deterioration curves for various correction factors, unlike the curves of Section 3, have a mild variation. So, it is believed that the effect of correction factor is truly mix-dependent. The smaller the correction factor, the greater the wander effect. Figures 7.55 and 7.56 illustrate the final pavement deterioration of SR of Section 8 with the correction factors 0.8 and 1.2 respectively.

As can be seen in the simulations, the correction factor, just like the traffic and weather patterns, has a tremendous effect on the stiffness deterioration curve. More importantly, it is hard to establish any general rule to guide pavement design because the fatigue performance is really affected by all these unavoidable random variables in the correction factors. It should be recognized that the fatigue damage is a stochastic process. Instead of producing a determinate answer to a pavement design question, it should be considered as reliability or risk analysis. Furthermore, since the fatigue damage is a stochastic process, it is better to predict the fatigue performance in a dynamically-simulated way, such as the proposed Weibull dynamic approach, to truly reflect the fluctuations of material and environment variables .

7.8 Findings and Discussions

Findings from the various types of simulations are summarized below. However, bear in mind that the findings made are subject to several limitations of the Weibull program, such as: (1) a crack propagation model is not included, (2) it uses one stiffness

to represent the stiffness of an entire layer, and (3) the correction factor is set to be 1.0 for simulations because of lack of information.

1. Wander effect is mix-dependent, traffic-dependent, and also time-dependent; however, it is shown that the wander effect is not weather-dependent in the simulations of the two WesTrack Sections 3 and 8.
2. One problem encountered with use of the Weibull program is that the linear-elastic layered program ELSYM5 only accepts one stiffness value for representing the stiffness of the entire layer. This does not comply with the fact that the degree of stiffness deterioration varies point-by-point in the in situ pavement. But, it is possible to read in multiple ELSYM5 input files and use the strain engine as necessary to conduct a finite-element-method-like performance; however, it looks awkward as compared with the average strain in the current version of the Weibull program. The best solution is to replace the ELSYM5 strain engine with a finite element strain engine and incorporate the necessary information on stiffness deterioration, especially the crack propagation, in the simulation program. However, the most important task following this study should be the development of a model of crack propagation. In addition, it was found that the simulation result is sensitive to the stiffness equations obtained from the regression analysis. To improve the accuracy of simulation results, it is important to carefully assess the stiffness equation, especially at high temperatures.
3. The correction factors need to be found from field data. The correction factor derived from the Weibull accelerated failure time model needs to be further

verified. A combination model of crack initiation and crack propagation is needed.

4. Theoretically (from the simulation results), the coarse mixes seem to have the better capacity to resist the thickness effect, the traffic effect, and the weather effect; however, this is contradicted in practice. From the condition survey data, it was noted that several coarse sections had serious cracking in the first winter. The field observation indicates the importance of including the crack propagation model in the Weibull dynamic approach.